

Silicon Micro-photonic Implementation of Parallel-Serial Filter to Compensate Residual Dispersion in Optical Communication Systems

vorgelegt von
M.Sc
Abdul Rahim
geb. in Bahawalpur (Pakistan)

von der Fakultät IV – Elektrotechnik und Informatik
der Technischen Universität Berlin
zur Erlangung des akademischen Grades

Doktor der Ingenieurwissenschaften
- Dr.-Ing. -

genehmigte Dissertation

Promotionsausschuss:

Vorsitzender: Prof. Dr.-Ing. Klaus Petermann

Gutachter: Univ.-Prof. Dr.-Ing. C. G. Schäffer

Gutachter: Dr. Lars Zimmermann

Tag der wissenschaftlichen Aussprache: 12. Mai 2014

Berlin 2014

Contents

Acknowledgements	xiv
Declaration of contributions	xvi
Preamble.....	1
1.	5
Dispersion in Optical Fibers	5
1.1. Dispersion	5
1.2. Dispersion in Optical Fibers	6
1.3. Dispersion Induced Impairment in Optical Communication Systems	8
1.4. Residual Dispersion.....	10
1.5. Electrical vs. Optical Residual Dispersion Compensation Techniques.....	15
2.	17
Optical Residual Dispersion Compensation Schemes	17
2.1. Optical Solutions for Chromatic Dispersion Compensation	17
2.1.1. Free Space Optical Solutions	17
2.1.2. Optical Fiber Based Dispersion Compensators	19
2.1.3. Integrated Photonics Dispersion Compensators	21
2.1.3.1. Lattice filters as Dispersion Compensators	21
2.1.3.2. AWG Based Dispersion Compensator.....	22
2.1.3.3. Ring Resonator Based Dispersion Compensators	26
2.1.3.4. Integrated Bragg Grating Based Dispersion Compensators	27
2.2. Comparison of Different Dispersion Compensators in Different Platforms.....	27
2.3. Comparison of Different Integrated Dispersion Compensating Filters.....	29
2.4. Parallel-Serial Filter Approach- A New Paradigm.....	32
3.	37
Parallel-Serial filter for Residual Dispersion Compensation.....	37
3.1. Fundamentals of Optical Filters.....	37
3.2. 2-Port MZI as an FIR Filter	39
3.3. Generalized Description of a Delay line FIR Filter for Residual Dispersion Compensation.....	45
3.4. Higher Order FIR Filters for Residual Dispersion Compensation.....	49
3.5. Parallel-Serial Filter Approach for Residual Dispersion Compensation	50

3.6.	Parallel-Serial Filter vs. AWG and Lattice Filter based Residual Dispersion Compensators	53
3.7.	Choice of MMI Couplers for Parallel-Serial Filter	53
3.8.	6th order Parallel-Serial FIR Filter with Static Couplers	54
3.9.	6th Order Parallel Serial FIR Filter with Enhanced Tuning Range	59
4.	65
	Design and Fabrication of Parallel-Serial Filter	65
4.1.	Material Platform	65
4.2.	MMI Couplers	67
4.3.	Integrated Waveguides in SOI	73
4.4.	Thermo-optic Effect for Phase Shifting	76
4.4.1.	Optimized Design of the Heater for Phase Shifting	79
4.4.2.	Power Requirements of the Heater	82
4.4.2.1.	Optimization of the Heater Design	84
4.4.2.2.	Power Requirements for the Phase Shifting Elements	88
4.5.	Designed Devices	89
4.6.	Fabrication	95
5.	103
	Characterization of Parallel-Serial Filters	103
5.1.	Measurement Setup	103
5.2.	Dispersion Measurement Techniques	105
5.3.	Measurement Method	106
5.4.	Device Preparation for Measurements	107
5.5.	Single Stage Parallel-Serial Filter Characterization	110
5.5.1.	Transmission and Group Delay Characterization	111
5.6.	Two Stage Parallel-Serial Filter Characterization	118
5.7.	Enhanced Two Stage Parallel-Serial Filter Characterization	126
5.8.	Effect of Polarization	127
5.9.	Transforming Integrated Micro-Optic Parallel-Serial Filter to Nano-photonic Parallel-Serial Filter	130
	Conclusion and Research Forecast	134
	Scientific Contributions	137
	APPENDIX I	a
	Fabrication Process for the parallel-serial filter devices	a

APPENDIX II.....	g
Relationship of filter order R with maximum achievable dispersion D_{max}	g

Table of figures

Figure 1.1: Simplistic representation of a single span optical communication system.....	10
Figure 1.2: Dispersion accumulation and compensation by DCF for the single span optical communication system.....	10
Figure 1.3: Schematic depiction of variation in fiber chromatic dispersion dD due to temperature variation dT	12
Figure 1.4: Equivalent of a single span optical communication system with an adaptive dispersion compensator	13
Figure 1.5: Dispersion profile for the single span optical communication system with a tunable dispersion compensator which overcomes the over-compensation of chromatic dispersion.	13
Figure 1.6: Schematic representation of an N span WDM system with a TRDC to mitigate residual chromatic dispersion.	13
Figure 1.7: Exemplary transmission (top), group delay (middle) and dispersion (bottom) response of an ideal dispersion compensator.	14
Figure 2.1: VIPA architecture [2].....	17
Figure 2.2: Light propagation in VIPA based dispersion compensator [2]	18
Figure 2.3: Single Gires-Tournos etalon.....	18
Figure 2.4: Principle of chirped fiber Bragg grating for dispersion compensation	20
Figure 2.5: Schematic of a typical lattice filter using static couplers with fixed coupling coefficients.....	21
Figure 2.6: Block level representation of a lattice filter based dispersion compensator	21
Figure 2.7: A simplified schematic of an AWG.....	23
Figure 2.8: Principle of AWG based dispersion compensator.	24
Figure 2.9: Schematic of an AWG based dispersion compensator.....	24
Figure 2.10: AWG with a thermal lens to compensate fiber chromatic dispersion [17].....	25
Figure 2.11: Principle of thermal lens in AWG based dispersion compensator [17]	26
Figure 2.12: Ring resonator based dispersion compensator	27
Figure 2.13: Generalized layout of the parallel-serial filter for residual dispersion compensation (unit cell corresponds to single stage of the filter).....	32
Figure 3.1: Black box representation of an optical filter.	37
Figure 3.2: Block level representation of a single stage FIR(left) and a single stage IIR(right) filter.	38
Figure 3.3: 2-port MZI as a simple FIR filter	39
Figure 3.4: z-domain equivalent of a 2-port MZI	41
Figure 3.5: Position of through- and cross- port zeros for a 2-port MZI comprising ideal equal splitting 2-port MMI couplers	43
Figure 3.6: Position of through- and cross- port zeros for a 2-port MZI comprising 2-port MMI couplers with splitter with unequal coupling coefficients.....	43
Figure 3.7: Transmission (top) and dispersion (middle) of a 2-port MZI comprising ideal 2-port MMI couplers but an amplitude imbalance of 0.02 dB on the delay lines.	45

Figure 3.8: Normalized dispersion of a single zero with an arbitrary magnitude ρ and phase ψ	46
Figure 3.9: Influence of magnitude ρ_m of m^{th} zero on the normalized dispersion D_N (phase $\psi_m=0$).....	47
Figure 3.10: Influence of phase ψ_m of m^{th} zero on the normalized dispersion D_N (magnitude $\rho_m=2$).....	47
Figure 3.11: Superposition of normalized dispersion of two hypothetical zeros to deliver constant dispersion.....	48
Figure 3.12: Relationship of maximum achievable dispersion D_{max} for group delay ripple < 3 ps and useful bandwidth Δf (RBWU) > 40 GHz for a filter with N number of stages and $FSR = 100$ GHz (see appendix II).	50
Figure 3.13: Generalized layout of an N stage parallel-serial filter of order $R = NM - 1$ using M -port couplers.....	51
Figure 3.14: A 6 th order parallel-serial filter comprising two stages ($N=2$) using 4-port MMI couplers and a unit delay $\tau = 10$ ps for $FSR = 100$ GHz.....	54
Figure 3.15: Transmission (top) and group delay (bottom) for the 6 th order parallel-serial comprising ideal 4x4 MMI couplers and lossless delay lines for an $FSR = 100$ GHz.....	57
Figure 3.16: Parallel-serial filter tuned for negative (red), zero (green) and positive (black) dispersion. Simulation is performed using ideal MMI couplers and delay lines. Filter $FSR = 100$ GHz and group delay ripple is maintained below 3 ps.	58
Figure 3.17: Generalized MZI as a tunable power splitter	60
Figure 3.18: Enhanced two stage parallel-serial filter with a tunable coupler	61
Figure 3.19: Simulation result for the tunability of the enhanced two stage parallel-serial filter. The simulation is performed for filter with $FSR = 100$ GHz and by using ideal MMI couplers with lossless waveguides. The group delay ripple is < 0.25 ps.....	62
Figure 3.20: Compromise between the RBWU and Group delay ripple.....	62
Figure 4.1: Architecture of SOI material system used for the implementation of parallel-serial filter for residual dispersion compensation	66
Figure 4.2: Simplified schematic of an MMI coupler. The input and output single mode waveguides are connected by a central multimode waveguide section, where the self-imaging takes place (see figure 4.3).....	68
Figure 4.3: Self-imaging in the multimode waveguide section of an MMI coupler. Four images f_{out} of the input field f_{in} are produced at length $z=L_{MMI}$	68
Figure 4.4: MMI coupler with $j=M$ input and $k=M$ output ports.....	70
Figure 4.5: Different geometries of waveguides in different SOI platform	74
Figure 4.6: Geometrical description of a rib waveguide.....	74
Figure 4.7: Heater placed on top of a nano-wire (left) and beside a rib waveguide (right) with typical dimensions	78
Figure 4.8: Configuration of a heater as a phase shifting element for rib waveguides.....	78
Figure 4.9: Simulation scenario to evaluate diffused heat in silicon slab of a rib waveguide. 80	
Figure 4.10: Profile of temperature on a silicon rib waveguide.....	80
Figure 4.11: Mode profile for TE and TM polarized light in a rib waveguide. Dotted region shows the cross-section of the slab and rib section of the waveguide. All dimensions are in μm	81

Figure 4.12: Magnitude of heater induced loss in the rib waveguides.....	82
Figure 4.13: Electrical equivalent of a heater placed on a slab of a rib waveguide	82
Figure 4.14: Direction of heater flux from heater into the substrate and in the Silicon slab. ..	84
Figure 4.15: Combination of trenches and under-etched silicon substrate direct the heater thermal flux towards rib waveguide for improved efficiency of the heater	85
Figure 4.16: Schematic of the thermo-electric model to determine the effect of trenches on P_{elec}	86
Figure 4.17: Influence of trench depth on the power requirements to produce π phase shift. The wafer had a total substrate thickness of $500 \mu\text{m}$	86
Figure 4.18: Under-etched substrate to minimize P_{elec} (Courtesy: Frau. Evelin Brose of HFT, TU Berlin).....	87
Figure 4.19: Heater design used as a phase shifting element on the delay lines of the parallel-serial filter. For all designs, the length of heater is always greater than $700 \mu\text{m}$ and thickness of the heater metal is between 100 nm and 200 nm	87
Figure 4.20: Waveguide layout of the 2-port MZI to determine the power requirements for the heaters (inset shows the configuration of trenches and heater).....	88
Figure 4.21: Power requirements for a non-trenched (top) vs trenched (bottom) heater as a phases shifting element of a 2-port MZI.....	88
Figure 4.22: S-bends to separate the in-/out-coupling waveguides of an MMI coupler. All bends have been designed to have equal length.	90
Figure 4.23: Mask design for the single stage of a parallel-serial filter (left) and two adjacent delay lines with heaters for phase shifting (right).....	91
Figure 4.24: Mask design for the two stage parallel-serial filter (left), Heater design with trenches (right) along two adjacent delay lines	91
Figure 4.25: Enhanced two stage parallel-serial filter (left), two adjacent delay lines with completely etched silicon (yellow area) between delay lines for an improved design of the heaters (right).....	92
Figure 4.26: Mask file for a single chip showing the implantation of an enhanced two stage filter with test structures	93
Figure 4.27: Full wafer mask layout for the single stage implementation of a parallel-serial filter	94
Figure 4.28: Two and enhanced two stage parallel-serial filter mask	95
Figure 4.29: SEM image of the fabricated rib waveguide and an MMI coupler [8].....	96
Figure 4.30: Typical heater structure	97
Figure 4.31: Measured sheet resistance R_s for Titanium, Platinum and Aluminum sheets of different thickness.....	97
Figure 4.32: Heater resistance vs. length of heater	98
Figure 4.33: SEM images of a delay line with a heater and trenches beside the heater and the delay line	99
Figure 4.34: Photograph of the fabricated enhanced two stage parallel-serial filter	99
Figure 5.1: F2F insertion loss (left) and the GD (right) for the measurement loop.....	104
Figure 5.2: Schematic for the measurement of F2F loss and GD.....	104
Figure 5.3: Setup for the adjustment of TE/TM polarization at the tip of the in-coupling lensed fiber	104

Figure 5.4: Block level representation of the measurement setup for transmission and GD characterization of the parallel-serial filter. Excluding the DUT, all the other components are embedded inside the PDLA.	106
Figure 5.5: Schematic of the SOI chip mounted on an Aluminum carrier with an electrical PCB.....	108
Figure 5.6: Interfacing heaters on SOI chip to the electrical PCB for DC biasing	109
Figure 5.7: Steps involved in the preparation of SOI chip for measurement	109
Figure 5.8: A prepared SOI chip placed on measurement setup for characterization	110
Figure 5.9: Schematic representation of a single stage (4-arm MZI) of a parallel-serial filter	110
Figure 5.10: Measured Transmission (left) and Group delay (right) for the 4-arm MZI after phase tuning by using heaters on the delay lines.....	111
Figure 5.11: Top row shows the transmission and group delay for an ideal 4-arm MZI, Bottom row shows a comparison of the simulated transmission and group delay of the 4-arm MZI with and without phase error on the delay lines.....	112
Figure 5.12: Deviation in the response of a 4-arm MZI due to variation in MMI coupler performance.....	113
Figure 5.13: Measured vs. simulated transmission and group delay for the single stage of the parallel-serial filter	113
Figure 5.14: A test heater placed at a distance equal to the pitch of the delay lines (275 μm) of a 4-port MZI to quantify the effect of thermal-cross talk	114
Figure 5.15: Dependence of thermal cross-talk between the delay lines on transmission (left) and group delay (right) for single stage of a parallel-serial filter shifts the transmission and group delay response of the filter.....	115
Figure 5.16: Wavelength shift in the transfer function for the single stage parallel-serial filter with an increase in the applied power on the heater.....	115
Figure 5.17: Shift in the transmission response of the single stage filter with an increase in the temperature of the chip holder.....	116
Figure 5.18: Comparison of Transmission (left) and group delay (right) with simulation (dashed-black) and measurement (solid-black) with phase shift on delay lines.....	116
Figure 5.19: Comparison between experimental (Solid-black) and simulated (Red-Square) phase shift φ_{1-1} to match the simulated and experimental transmission and group delay for single stage of the parallel-serial filter (360° phase shift has required 180 mW).....	117
Figure 5.20: Single stage serial parallel filter tuned to nearly linear positive (left) and negative (right) group delay (dashed-red) and transmission (solid-black).....	117
Figure 5.21: A two stage serial-parallel filter	118
Figure 5.22: Wire-bonded heater for on-chip to off-chip interfacing of heaters.....	118
Figure 5.23: Measured (solid-red) transmission (a, c, e) and group delay (b, d, f) compared with the calculated (dotted-black) transmission and group delay for the two stage filter. ..	120
Figure 5.24: Linear fit (a, c, e) for the linear group delay slope and group delay ripple (b, d, e) in the region of linear group delay	121
Figure 5.25: Measured (solid) and calculated (dotted) positive, zero and negative group delay slopes for the two stage filter (Filter FSR = 100 GHz)	122

Figure 5.26: Transmission (a) for negative dispersion slope (b), variation in dispersion (c) and group delay bandwidth, which is the fraction of filter FSR with linear group delay slope (d) over the C-band for the two stage parallel-serial filter.....	123
Figure 5.27: Emulation setup to test the performance of the two stage parallel-serial filter.....	124
Figure 5.28: Constellation for 28 Gbaud QPSK after transmission through 100 km of SSMF (top) without compensation of +176 ps/nm residual dispersion and (bottom) after compensation of residual dispersion using two-stage parallel-serial filter	125
Figure 5.29: OSNR penalty for the two stage parallel-serial filter	125
Figure 5.30: Waveguide layout (left) for the enhanced two stage filter and the fabricated device (right) with heaters shown in red-dashed regions and the anti-reflected coated waveguide facets in the yellow-dotted region.....	126
Figure 5.31: Characterization of the enhanced two stage filter (Filter $FSR=100$ GHz).....	127
Figure 5.32: TE (solid-black) and TM (solid-red) characterization for the two stage parallel-serial filter when tuned for positive group delay slope. The PDFS is depicted by the 120pm shift between the top and bottom wavelength axis.	128
Figure 5.33: TE (solid-black) and TM (solid-red) characterization for the two stage parallel-serial filter when tuned for negative group delay slope. The PDFS is depicted by the 120pm shift between the top and bottom wavelength axis.	129
Figure 5.34: Birefringence tuned transmission (top) and group delay (bottom) for the TE (solid-red) and TM (solid-black) polarization for an un-tuned two stage parallel-serial filter	130
Figure 5.35: Mask layout of single stage parallel-serial filter for nano-photonic implementation	131
Figure 5.36: Transmission (top) and group delay (bottom) compared with ideal (solid-black) and measured (solid-red) for a nano-photonic implementation of a single stage parallel-serial filter.....	132

Table of tables

Table 2.1: Qualitative matrix for chromatic dispersion compensators realized in different platforms	28
Table 2.2: Comparison of photonic integrated dispersion compensators.....	31
Table 3.1: Zeros of the 6 th order parallel-serial filter to deliver the transmission and group delay response shown in figure 3.15	58
Table 4.1: Specifications of the SOI wafer used for the fabrication of parallel-serial filter for residual dispersion compensation.....	66
Table 4.2: Performance specifications for MMI couplers used in the implementation of parallel-serial filter for residual dispersion compensation	73
Table 4.3: Excess Loss, Imbalance, Phase Errors and Bandwidth of 4 x 4, 8 x 8, 12 x 12 and 16 x 16 MMI couplers in SOI platform [32]	73
Table 4.4: Selected Geometry of the Rib waveguide	75
Table 4.5: Summarized mask specifications for single, two and enhanced two stage filter....	92

List of Acronyms

AR	Auto Regressive
ARC	Anti-Reflection coating
ASE	Amplified Spontaneous Emission
AWG	Arrayed Waveguide Grating
B2B	Back to Back
CBG	Chirped Bragg Grating
CD	Chromatic Dispersion
CFBG	Chirped Fiber Bragg Grating
CMOS	Complementary Metal Oxide Semiconductor
DCF	Dispersion Compensating Fiber
DoF	Degree of freedom
DSF	Dispersion Shifted Fiber
DTFT	Discrete Time Fourier Transform
EDFA	Erbium Doped Fiber Amplifier
EOP	Eye Opening Penalty
FBG	Fiber Bragg Grating
FIR	Finite Impulse Response
FPR	Free Propagation Region
FSR	Free Spectral Range
GD	Group Delay
GDR	Group Delay Ripple
GT	Gires-Tournois etalons
GVD	Group Velocity Dispersion
HOM	Higher Order Mode
IIR	Infinite Impulse Response
ISI	Inter Symbol Interference
MA	Moving Average
MMI	Multimode Interference
MZI	Mach-Zhender Interferometer
OFDM	Orthogonal Frequency Division Multiplexing
PIC	Photonic Integrated Circuit
PMD	Polarization Mode Dispersion
QAM	Quadrature Amplitude Modulation
QPSK	Quadrature Phase Shift Keying
RBWU	Relative Bandwidth Utilized
RDS	Ratio Dispersion Slope
Rx	Receiver
SDM	Spatial Division Multiplexing
SiON	Silicon Oxynitride
SOI	Silicon on Insulator
SPM	Self Phase Modulation

SSMF	Standard Single Mode Fiber
TRDC	Tunable Residual Dispersion Compensation
Tx	Transmitter
VIPA	Virtually Imaged Phase Array
WDM	Wavelength Division Multiplexing
WGR	Waveguide Grating Router
XPM	Cross Phase Modulation

List of Symbols

$\frac{\sigma^2}{\sigma_0^2}$	Broadening factor
\bar{n}	Mode index (effective index)
a_i	Complex filter coefficients
B	Bit rate
b	Thickness of buried oxide (BOX)
c	velocity of light in free space
D	Dispersion
f	Un-scaled absolute Frequency (Hz)
h	Thickness of silicon slab
h(n)	Impulse Response
H(z)	Transfer Function
k_0	Free space wave number
k_{oxide}	Thermal conductivity of Silicon oxide
k_{si}	Thermal conductivity of Silicon
L	Fiber Length
L_d	Diffusion length
L_H	Length of heater
M	Grating or MMI Order
N	Number of stages in a filter
n	refractive index of a medium
n_{eff}	Effective index of a waveguide
n_g	Group Index
\bar{n}	Modal index of fiber mode
P_{elec}	Power required by the electrical heater
p_n	nth filter pole
R	Filter order
r	Ring Resonator radius
S	Dispersion slope
S_0	Dispersion slope at zero wavelength
t	Propagation time in fiber
T_B	Time for a bit slot
T_B	Bit slot
T_D	Depth of thermal isolation trench
T_H	Temperature of heater
v	velocity of light in a medium
W_H	Heater width
x_d	Distance between heater and the waveguide rib
x_d	Distance between the edge of the waveguide and heater
z	Z-domain
z_m	mth filter zero

β	Propagation constant
β	Propagation Constant
β_2	Group velocity dispersion
β_3	Higher order dispersion
Δf	Useful bandwidth of dispersion Compensator
$\Delta\lambda$	Spectral bandwidth (nm)
$\Delta\omega$	Spectral bandwidth
Λ	Grating Period
λ_B	Bragg Wavelength
λ_0	Zero Dispersion wavelength
$\rho_{m/n}$	Magnitude of zero/pole
σ	Broadening of optical pulse
τ_N	Normalized Group Delay
ν	Normalized frequency
ν_g	Group Velocity
Φ	Phase introduced by metallic heater
$\Psi_{m/n}$	Phase of the zero/pole
Ω	Normalized angular frequency ($\Omega=2\pi\nu$)
ω	Angular Frequency ($\omega=2\pi f$)

Acknowledgements

First and foremost is to thank Allah SWT that he has given me the energy and life enough to complete this part of work. Life is His blessing.

I am thankful to Professor Klaus Petermann for his guidance and supervision that led to the completion of this work. Working with him enabled me to improve myself not only academically but personally also. I would also like to acknowledge the guidance and support I received the daily supervision of Dr. Juergen Bruns. His openness to discuss ideas and willingness to try them always injected extra motivation in me. He was always kind in listening me with his always open door for me. Apart from technical stuff, he helped me with many administrative stuff. I am very thankful for his kindness in this regard.

This research work was in collaboration with Helmut Schmidt University Hamburg (Germany). There my interaction with Professor Christian G. Schaeffer was always very fruitful and many ideas implemented in this work are a consequence of that interaction. I am also thankful to him for providing me a feedback about my thesis. I later used his input to improve the quality of this work. I would like to mention the contribution of his research associate Stefan Schwarz. He did analytical calculation related to the devices implemented. He was very generous in sharing those results with me. This helped me in determining the performance of the devices realized in this work.

At Technische Universitaet Berlin, I had one of the best times I had spent as a foreigner. Although my colleagues never make me feel like a foreigner. The people in the clean room, Beatrice, Eveline, Mallice and Micheal were always very supportive. Many times they did an extra mile to support the timely completion of my work. People in the workshop, Chrstian Birr and Günther Falk and Thomas Kiekbusch always managed to find time to do various mechanical assemblies for me. I am thankful to Mr.Lindner, who provided me IT related support and always met with a smile on his face.

On the first floor of HFT Institute, Dr. Zimmermann (presently on the 3rd floor) was very kind in reading this manuscript. His suggestions led to an improvement of this work. Apart from that he was generous in sharing his vast set of experiences related to Silicon Photonics, which later saved me from many pitfalls. I am very thankful to him in this regard. Benjamin made me learn Ansys and later helped me in some of administrative problems. His company was always enjoyable and pleasing. Karsten gave me some of his initial devices to kick start my work. This helped in enhancing my understanding of few building blocks that were later used in my research work. Gerorg Winzer shared the laboratory equipment with me happily and helped me with wirebondings. Apart from that there are so many things in which he was always supportive. It was pleasure working beside him on the work benches. Ivano and Andrzej were kind in happily sharing the measurement tools with me. In the beginning they helped me in understanding the measurement mechanism, which later I used to characterize my devices.

On the third floor, my office mate Georg Rademacher always provided an enabling environment for research. He always provided an extra-motivation to work. Provided me and all other colleagues with the best coffee possible. The non-technical geo-political discussions with him are an integral part of my memory. Dimitar (now Dr. Kroushkov)

helped me with VPI simulations. Always welcomed me in his office to discuss ideas. His wisdom, popularly known as Dimi's wisdom, was worth listening to. I hope I could get a grab of few of his wise advises. His office mate and the Syedi for me, Mahmud, provided a good company and shared many ideas of his own with us. With Dr. Stefan Warm, my office neighbor, was always ready to share with me my excitement with some the results I have obtained. His input helped me in improving those results even further. Mathias Jaeger was kind in letting his student Dany Volkmann to provide me support related to LabView. I am thankful to both of them. Adrian helped me to introduce with the topic of OFDM, which later led me to develop some devices. I thank him for his openness in sharing ideas. Edgar came when I was about to leave. He was kind in listening to some of my long and noisy phone calls. I hope I did not bother him much. I think the same holds for Frau. Zötl, who was my neighbor on the other side of my office. Frau. Hamer and later Frau. Schiffer, the secretaries of Professor Peterman were always kind in solving various administrative issues for me. That definitely made my life easier. Student workers Tareq and Jalil helped me with measurements. They never looked at their watches and did lot of extra hours to support me. I am thankful to them also. After work, friends like Ahmed Al-Tanany, Khaled and Sajjad gave enjoyable companies. That helped me relax after work. Similarly back home in Pakistan, many friends who encourage and motivated me. I am very thankful to them also. I am thankful to all my teachers. They definitely helped me in reaching this milestone. I have no words to thank my mother. She spent whole her life on me. Her sacrifice is enormous. I hope someday I can do something for her. I am very thankful to my sisters Nabila, Saima and Mamoonah. They provided me with lot of motivation to complete this work. I am sure that my father in heavens must also be feeling proud of all of us. My wife Saima, is a real blessing I got from the Almighty. She helped me in overcoming all the thick and thin during this time. Waited for me for long hours alone when I missed so many of my promises to come home early. Took care of our daughter Zainab when I was having official trips. Managed all the household stuff single handed and kept her studies also on track. I am thankful to her and Zainab who joined me on weekends for the measurements. I find no words to thank her either. I am thankful to little Zainab also. She must have missed me.

Abdul Rahim
Somewhere over the Atlantic Ocean
Nov. 6th 2014

Declaration of contributions

This research work has been done in collaboration with the High-Frequency Engineering research group headed by Professor Christian G Schaeffer at Helmut-Schmidt University (Hamburg, Germany).

The analytical calculations and the matching of measurement results using these analytical calculations have been done by Mr. Stefan Schwarz of High-Frequency Engineering research group headed by Professor Christian G Schaeffer at Helmut-Schmidt University (Hamburg, Germany).

The German Research Foundation provided financial support to carry out this work.

Preamble

Optical Fiber is a key element of an optical communication system. Over the time, the optical communication systems have advanced to best use the enormous bandwidth available with optical fiber, which is on the order of 1000 GHz.km [1] at zero dispersion wavelength ($\lambda = 1.3 \mu\text{m}$) of an optical fiber. The evolution of optical communication has benefited tremendously from the technological inventions such as the development of low loss fibers, the ability to operate a semiconductor laser at room temperature, Erbium Doped Fiber Amplifiers (EDFA) for compensation of fiber loss, Wavelength Division Multiplexing (WDM) for effective use of the fiber bandwidth. This evolution has not stopped so far. Recently, coherent detection and enhanced modulation formats such as Quadrature Phase Shift Keying (QPSK) and Quadrature Amplitude Modulation (QAM) are proposed to meet the data rates of future optical networks. For example, NEC and Verizon have demonstrated a field trial to transmit a world record 21.7 Tb/s over 1503 km in SSMF using a flexible modulation scheme comprising dual polarization QAM and QPSK at the same time [2]. Although, WDM is the most widely deployed multiplexing technology, but more spectrally efficient modulation formats such as Optical Orthogonal Frequency Division Multiplexing (O-OFDM) and Nyquist multiplexing are also been actively researched. Recently a lot of research interest has undergone to investigate the potential of using Spatial Division Multiplexing (SDM) by using multicore or multimode fiber [3]. In 2012, NEC and Corning have already demonstrated Pb/s transmission in a multicore fiber [4].

Although, there are multitude of possibilities to enhance the transmitted data rates. A bottleneck comes from the electronics. Therefore, alternate technologies are being actively developed to replace or work in proximity with electronics to process the huge data rates. Integrated optics has been considered as a key technology in this regard. Various material platforms for integrated optics have been used. To name few are silica, Indium Phosphide, Silicon Nitride and Silicon-on-Insulator (SOI). Each material system has its own advantages and disadvantages. For the last few years, the SOI platform has gained a lot of attention because it can provide small form factors, compatibility with CMOS technology, possibility of high quality optical components such as splitters, combiners, waveguides, gratings and so on [5].

The availability of high performance components in SOI have been employed to demonstrate various applications ranging from (de)multiplexers, filters, modulators, tunable delay lines, heterogeneously integrated lasers and many more. The SOI based applications, perform equally well as compared to other technologies and sometimes even out-perform as compared to the others. In comparison to electronics, they overcome the speed limit and are energy efficient. It has already been demonstrated that the devices and modules demonstrated in SOI are assembled to deliver fully integrated optical systems [6].

In spite of new multiplexing and modulation schemes being employed in the current and next generation high speed optical communication schemes, the linear and non-linear fiber

impairments have always been a problem and hamper the transmission capacity of an optical communication system. Such impairments include Chromatic Dispersion (CD), Polarization Mode Dispersion (PMD), Self-Phase Modulation (SPM) and Cross Phase Modulation (XPM) [7]. Electrical filters and sophisticated digital signal processing are deployed for this purpose in modern optical communication systems. An integrated optical filter in SOI technology for the signal processing of fiber impaired signals is very beneficial. They are compact in size, require electrical power independent of the bit-rate, CMOS compatible and are feasible for mass production. Apart from integrated optical solutions for signal processing, bulk optics and fiber optics solutions are also prevalent.

Chromatic dispersion in standard single mode fiber of an optical communication system originates from the wavelength dependence of the refractive index. As a result of this, different spectral components of the laser source, which constitute the input optical pulse propagating in an optical fiber, travel at different speeds (group velocities). In time domain, the ultimate result is the broadening of the input optical pulses beyond their allocated time slots. Consequently a fraction of each transmitted optical pulse overlaps its neighboring pulses. Consequently, the correct detection of the received signal becomes difficult if the two consecutive pulses are very close to each other. This phenomenon is commonly referred as Inter Symbol Interference (ISI). Therefore, it is mandatory for any optical communication system to compensate chromatic dispersion to circumvent dispersion induced limit on the information carrying capacity of an optical fiber.

Photonic Integrated Circuits (PICs) for dispersion compensation are elegant, cheap and energy efficient, but they can only compensate few hundreds of ps/nm of dispersion. Therefore, they are not useful for the compensation of the accumulated dispersion over the span of a long haul transmission system. In the case of direct detection systems, the mostly employed method for the compensation of a major fraction of fiber dispersion is the Dispersion Compensating Fiber (DCF) or Fiber Bragg Gratings (FBGs). For coherent systems, electrical digital signal processing can compensate the accumulated dispersion. Apart from this accumulated dispersion, which is the major fraction of dispersion, the changes in the routing of optical signal and temperature fluctuations introduce a small and time varying fraction of dispersion. This can be termed as residual dispersion. This fraction becomes important when high data rates (> 40 Gbps) are used [8]. The few hundreds of ps/nm dispersion delivered by the PICs are ideally suited for the compensation of residual dispersion.

Variety of integrated optical filters for residual dispersion compensations have been previously proposed. They include lattice filters, Bragg grating based filters, Arrayed Waveguide Grating (AWG) based filters with thermal lens, ring-resonator based filters and many more [7]. Those implementations of the filters in which the optical signal propagate only in the forward direction belong to the FIR* class. While, the ones in which the optical signal has been fed backwards belong to the IIR class of the filter.

*A more detailed explanation of FIR filters is outlined in chapter 2.

As mentioned earlier, SOI is a very versatile material platform for the implementation of PICs. In this work, a new type of filter is proposed, designed, characterized and tested for the residual dispersion compensation in 28 Gbaud QPSK optical communication system using SOI platform. Unlike other implementations, this filter is based on higher order MMI couplers. Due to its architecture, it is termed as "Parallel-Serial filter". The key to the performance of the proposed filter is the quality of the components used in its implementation. The key component in this regard is the higher order MMI coupler. Such couplers with very good performance are available in the SOI platform. Not only that, low loss waveguides for optical delay lines and high thermo-optic effect are also available in SOI platform. These factors make SOI platform ideally suitable for the demonstration of this new filter concept.

In the scope of the work presented here, the design, principle, fabrication and characterization of parallel-serial filters for residual dispersion compensation is addressed. The breakdown of the presented work is as follows:

- The fundamentals of dispersion and the impairment it induces on high speed optical communication system is presented in Chapter 1.
- Existing dispersion compensating schemes in different platforms, their principle, pros and cons are highlighted in Chapter 2.
- The basic theory of FIR filter and the principle of the parallel-serial filter are presented in Chapter 3.
- Brief basic theory of building blocks, fabrication process and the layouts of the various fabricated devices are described in Chapter 4.
- Measurement scheme for the characterization of the fabricated parallel-serial filters and their measurement results are summed up in Chapter 5. The measurement results are evaluated by performing emulation and the key results are highlighted in this chapter.

References:

- [1] Cohen, L.G., "Comparison of single-mode fiber dispersion measurement techniques," *Lightwave Technology, Journal of*, vol.3, no.5, pp.958,966, October 1985.
- [2] T. Xia, G. Wellbrock, Y. Huang, M. Huang, E. Ip, P. Ji, D. Qian, A. Tanaka, Y. Shao, T. Wang, Y. Aono, and T. Tajima, "21.7 Tb/s Field Trial with 22 DP-8QAM/QPSK Optical Superchannels Over 1,503-km of Installed SSMF," in *National Fiber Optic Engineers Conference, OSA Technical Digest (Optical Society of America, 2012)*, paper PDP5D.6.
- [3] R. W. Tkach, "Scaling Optical Communications for the Next Decade and Beyond," *Bell Labs Tech. J.* 14(4) 3-9 (2010).
- [4] http://www.corning.com/opticalfiber/news_and_events/news_releases_2013/20130115_01.aspx accessed on 15.09.2013.
- [5] Soref, R., "The Past, Present, and Future of Silicon Photonics," *Selected Topics in Quantum Electronics, IEEE Journal of*, vol.12, no.6, pp.1678,1687, Nov.-Dec. 2006

- [6] Narasimha, A.; Analui, B.; Yi Liang; Sleboda, T.J.; Gunn, C., "A Fully Integrated 4 x 10Gb/s DWDM Optoelectronic Transceiver in a standard 0.13 μ m CMOS SOI," Solid-State Circuits Conference, 2007. ISSCC 2007. Digest of Technical Papers. IEEE International , vol., no., pp.42,586, 11-15 Feb. 2007
- [7] Govind P. Agrawal, Fiber-Optic Communication Systems, 3rd Edition, John Wiley & Sons, 2002.
- [8] A. E. Willner, I. P. Kaminow and T. Li. "Planar lightwave circuits in fiber-optic communication," in Optical Fiber Telecommunications, 5th ed. New York: Academic, 2008, vol. A: Components and Subsystems.

1.

Dispersion in Optical Fibers

1.1. Dispersion

The interaction of light with bulk matter has always been a topic of great interest. The speed of light c in free space is given by:

$$c = \frac{1}{\sqrt{\epsilon_0 \cdot \mu_0}} \quad (1.1)$$

where ϵ_0 and μ_0 are electric permittivity and permeability in free space. The phase velocity v of light on interaction with a bulk and homogenous media in free space is different and is given by:

$$v = \frac{1}{\sqrt{\epsilon \cdot \mu}} \quad (1.2)$$

The ratio of the speed of light in free space and the speed of light in matter is known as absolute index of refraction n , given by:

$$n = \frac{c}{v} \quad (1.3)$$

The above relation holds true only for some simple gasses e.g, Helium and Hydrogen for which $n \approx \sqrt{k_E}$ where $\sqrt{k_E}$ is the static dielectric constant [1]. Most of the other materials are dispersive. Dispersion is a phenomenon that corresponds to the frequency ω dependence of the index of refraction n of a medium. Therefore, it also referred as chromatic dispersion.

$$n = n(\omega) \quad (1.4)$$

The physical origin of dispersion is the interplay of various electric polarizations contributing at a certain frequency ω . An analytical expression relating the frequency ω dependence of the n is given by the dispersion relation [1]:

$$n^2(\omega) = 1 + \frac{N \cdot q_e^2}{\epsilon_0 \cdot m_e} \left(\frac{1}{\omega_0^2 - \omega^2} \right) \quad (1.5)$$

where N is the number of electrons in unit volume of matter, ω_0 , q_e and m_e are the resonant frequency, charge and mass of an electron. It is clear from dispersion equation that for $\omega_0^2 - \omega^2 < 0$, the refractive index of the media will be less than 1. For $\omega_0^2 - \omega^2 > 0$, the refractive index of the media will be greater than 1. The frequency region in which

$(dn/d\omega) > 1$ is called region of normal dispersion and the region with $(dn/d\omega) < 1$ is called region of anomalous dispersion. With increasing frequency ω , several transitions from $n > 1$ to $n < 1$ takes place, which attributes to several resonance frequencies ω_0 at which the system resonates. A more elaborate and very elegant physical description of the dispersion in dielectrics is available in [1]. A different convention that will be described later (see section 1.2) is used to define normal and anomalous dispersion in the field of optical fiber communications.

1.2. Dispersion in Optical Fibers

Like other media, optical fiber, which is the guiding media for an optical communication system has dispersion. The consequence of dispersion is the broadening of an optical pulse after propagation through the optical fiber. In geometrical optics, chromatic dispersion can be explained by the difference in the arrival time of multiple rays from the input to the output of the optical fiber due to different path lengths followed by them. This multipath dispersion is true for the multimode fibers, which support more than one guided mode and each of which has a different modal index \bar{n} , which is given as:

$$\bar{n} = \frac{\beta}{k_o} \quad (1.6)$$

where β is the propagation constant and k_o is the free space wavenumber and is given by:

$$k_o = \left(\frac{\omega}{c}\right) = \left(\frac{2\pi}{\lambda}\right) \quad (1.7)$$

Different modal indices for different modes in a multimode fiber result in different group velocities v_g , which is the velocity at which the envelope of a pulse propagates in a medium, for each mode.

$$v_g = \frac{c}{n_g} = \left(\frac{d\beta}{d\omega}\right)^{-1} \quad (1.8)$$

where n_g is the group index and is given by:

$$n_g = \bar{n} + \omega \left(\frac{d\bar{n}}{d\omega}\right) \quad (1.9)$$

Different group velocities in different modes result in different arrival times at the end of the fiber. This is commonly referred as intermodal dispersion and is the dominant part of dispersion in multimode fibers.

Apart from most recent research interest in the field of multimode fibers [2] to enhance the capacity of optical communication systems, presently most of the optical communication systems utilize single mode fibers, in which the energy of the optical signal is carried by a single mode. For the rest of the discussion, the focus will be on single mode fibers, in which the phenomenon of inter-modal dispersion is irrelevant but the phenomenon of dispersion is still relevant due to frequency dependence of propagation constant β , which is given by [3]:

$$\beta(\omega) = \bar{n} \cdot k_o = \bar{n} \cdot \left(\frac{\omega}{c}\right) = \bar{n} \cdot \left(\frac{2\pi}{\lambda}\right) \quad (1.10)$$

The wavelength dependence of the propagation constant β for the fundamental mode of the single mode fiber results in different arrival times for different spectral components of the input optical pulse. This phenomenon corresponds to Group Velocity Dispersion (GVD) or intra-modal dispersion.

For a pulse with spectral width $\Delta \omega$, the difference in the arrival time Δt for different spectral components of the pulse is given by:

$$\Delta t = \left(\frac{dt}{d\omega}\right) \cdot \Delta\omega \quad (1.11)$$

Where Δt is the difference in the arrival times t for different spectral components. t is the time taken by a specific spectral component ω to traverse the length L of the fiber and is given by:

$$t = \frac{L}{v_g} \quad (1.12)$$

Substituting of equation 1.8 and equation 1.12 in equation 1.11 results in:

$$\Delta t = L \cdot \beta_2 \cdot \Delta\omega \quad (1.13)$$

where β_2 is called the group velocity dispersion (GVD) parameter, which is a measure of broadening of an optical signal due to propagation in an optical fiber and is given by:

$$\beta_2 = \frac{d^2\beta(\omega)}{d\omega^2} \quad (1.14)$$

Since, it is customary in optical communication to employ wavelength spread $\Delta\lambda$ instead of frequency spread $\Delta\omega$, Δt can be re-written as:

$$\Delta t = \left(\frac{dt}{d\lambda}\right) \cdot \Delta\lambda = D \cdot L \cdot \Delta\lambda \quad (1.15)$$

where $D = \frac{d}{d\lambda} \left(\frac{1}{v_g}\right) = \frac{-2\pi c}{\lambda^2} \cdot \beta_2$ and is known as the dispersion parameter. It is expressed in the units of ps/(nm.km), which corresponds to the broadening of an optical pulse with a spectral width of 1nm after propagating thorough 1km long fiber. A positive value of D ($\beta_2 < 0$) corresponds to anomalous and a negative value of D ($\beta_2 > 0$) represents normal dispersion.

In conclusion, like any other material system, optical fibers also have dispersion. In multimode fibers this originates due to different group velocities for different modes supported by the multimode fiber and it is referred as intermodal dispersion. For single mode fiber, the wavelength dependence of the propagation constant results in different spectral components to be dispersed and is referred as GVD. A positive or negative value of GVD leads to broadening or compression of an optical pulse propagating through the optical fiber. GVD exists for all modes of the multimode fiber but the intermodal dispersion dominates in multimode fibers.

1.3. Dispersion Induced Impairment in Optical Communication Systems

So far, the phenomenon of dispersion has been explained in optical fibers. As mentioned earlier, the consequence of dispersion in optical fiber results in broadening of the optical signal propagating through it. The change in the width of the optical signal after propagating through the fiber is given by the broadening factor. The broadening factor $\frac{\sigma^2}{\sigma_0^2}$ for an optical pulse from a narrow linewidth optical source on propagating through an optical fiber with length L , is given by [3]:

$$\frac{\sigma^2}{\sigma_0^2} = (1) + \left(\frac{\beta_2 \cdot L}{2 \cdot \sigma_0^2}\right)^2 + \left(\frac{\beta_3 \cdot L}{4 \cdot \sqrt{2} \cdot \sigma_0^3}\right)^2 \quad (1.16)$$

where β_3 corresponds to the higher order dispersion, which is related to the dispersion slope and is obtained by the Taylor expansion of the wavelength dependent propagation constant $\beta(\omega)$.

$$\beta(\omega) = \beta_0 + \beta_1(\Delta\omega) + \frac{\beta_2(\Delta\omega)^2}{2} + \frac{\beta_3(\Delta\omega)^3}{6} + \dots \quad (1.17)$$

where ω_0 is the center frequency of the pulse spectrum and $\beta_m = \left. \frac{d^m \beta}{d\omega^m} \right|_{\omega=\omega_0}$.

The broadening σ leads the optical pulse to extend beyond the bit slot T_B . The result of that is Inter Symbol Interference (ISI). Therefore, dispersion puts a limit on the maximum bit rate $B = \frac{1}{T_B}$ transmitted over length L of the fiber.

Ignoring higher order dispersion such as β_3 in the above equation and considering a simplistic approximation of dispersion limited bit rate B for On-Off Keying (OOK) given by [3]:

$$\sigma \leq \frac{1}{4B} \quad (1.18)$$

It is possible to show that [3]:

$$B^2 \cdot |\beta_2| \cdot L \lesssim \frac{1}{16} \quad (1.19)$$

or for a system penalty of 1 dB, the dispersion D , bit rate B and transmission length L can be related as [9]:

$$B^2 \cdot |D| \cdot L \sim 1 \cdot 10^5 \text{ (ps/nm)} \left(\frac{\text{Gb}}{\text{s}}\right)^2 \quad (1.20)$$

which means that for every doubling of the bitrate B , the allowable cumulative dispersion $|D| \cdot L$ over the same propagation length has to be reduced by four times. In other words, a bit rate of 10 Gb/s can tolerate 1000 ps/nm of accumulated dispersion which reduces to 250ps/nm when the bit rate is doubled. Assuming nominal dispersion value of 17 ps/nm.km in a SSMF at $\lambda=1550\text{nm}$, 10 Gb/s signal will travel only 60 km and 20 Gb/s can travel only 15 km.

Similarly, assuming $\beta_2 = 0$ in the above equation will result in:

$$B^3 \cdot |\beta_3| \cdot L \leq 0.034 \quad (1.21)$$

where $\beta_3 = \frac{d\beta_2}{d\omega}$ is the third order dispersion parameter. It is related to the dispersion slope S by:

$$S = \left(\frac{2\pi c}{\lambda^2}\right) \cdot \beta_3 + \left(\frac{4\pi c}{\lambda^3}\right) \cdot \beta_2 \quad (1.22)$$

Equivalently, 1.21 can be re-written as:

$$B \cdot |S|(\Delta\lambda^2) \cdot L < 1 \quad (1.23)$$

From equation 1.21 and 1.23, it is clear that the higher order dispersion have less significant effect on limiting the bitrate of an optical communication systems as compared to the first order dispersion D . Commercially available SSMF have $S=+0.057$ ps/(nm².km) at 1550 nm). It is highly desirable to mitigate dispersion and dispersion slope in an optical fiber to ensure that the optical communication system is able to deliver high data rates. The term high data rate always refers to data rates beyond 40 Gb/s in the scope of this work.

The first solution which one would imagine is to change the dispersion behavior of the fiber itself so that the bit rate limitation induced by dispersion can be mitigated. This is possible because the total dispersion D_{tot} of a fiber is the sum of the material dispersion and the waveguide dispersion.

$$D_{tot} = D_{Material} + D_{Waveguide} \quad (1.24)$$

The material dispersion originates from the change of refractive index of the fiber material (silica) with wavelength ($n=n(\omega)$) and the waveguide dispersion comes from the geometry of the fiber. By using multiple cladding layers and proper tailoring of the dispersion profile, it is possible to implement a fiber termed as “Dispersion Shifted Fiber (DSF)”, which has zero dispersion in the region of 1550 nm (the region of lowest loss in optical fibers), which is commonly employed wavelength regime used for long haul optical communication. But, for such DSF fibers, different spectral components travel at the same group velocity. As a result of that, the phase matching condition is fulfilled for the spectral contents of different channels and leads to non-linear signal impairments such as four wave mixing (FWM) and cross-phase modulation (XPM).

The most commonly employed mechanism to overcome the dispersion induced impairments is the deployment of a dispersion compensating fiber DCF, which has a standard dispersion value to mitigate the positive dispersion accumulated over the length L of the fiber. The classical design [3] of DCF has a weakly confined fundamental mode which penetrates the low index fiber cladding to deliver large negative dispersion (i.e. -100 ps/nm). Another approach presented in [4] uses the parabolic shaped core region with a depressed cladding region to engineer the dispersion of the fiber. It provides a broadband all-optical solution to compensate fiber chromatic dispersion but at the cost of large loss of 0.4 to 0.64 dB/km [4]. Loss in fibers has no longer been a problem due to the advent of the

Erbium Doped Fiber Amplifier (EDFA). This in return adds noise in the form of Amplified Spontaneous Emission (ASE) from the amplifier. Another problem is associated to the small effective mode area of $\sim 20 \mu\text{m}^2$ for DCFs [3]. This results in an enhanced non-linear effect. This can be avoided by keeping the average optical power to smaller values. Figure 1.1 shows the schematic representation of a simplistic single span optical communication system. The typical span length and dispersion values for the SSMF and the DCF are also mentioned in Figure 1.1. A split EDFA approach is used to compensate propagation loss in the SSMF and the DCF, which has a typical value of 5 dB. Figure 1.2 shows the accumulation of chromatic dispersion on propagation of an optical signal along the SSMF and its compensation by the DCF. In a multi-span optical communication system, a DCF module can either be added on transmitter side (pre-compensation), before receiver (post-compensation) or in each span (in-line compensation) of dispersion.

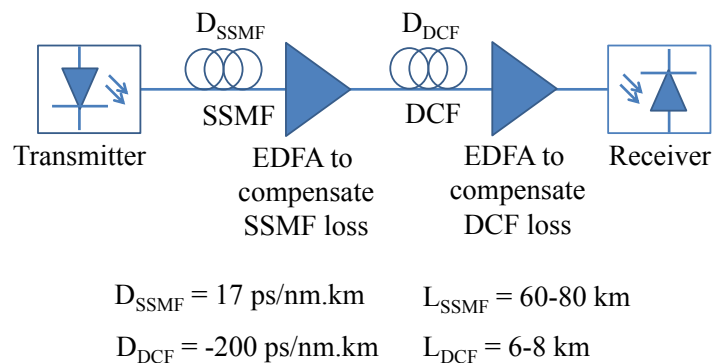


Figure 1.1: Simplistic representation of a single span optical communication system

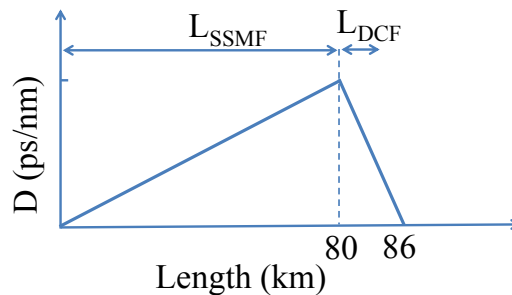


Figure 1.2: Dispersion accumulation and compensation by DCF for the single span optical communication system

1.4. Residual Dispersion

As shown by equation 1.20, at increasingly high data rates (such as beyond 40 Gb/s), the tolerance of the transmission systems becomes smaller and smaller and even few ps/nm of dispersion becomes vital. The tolerance to dispersion D_{tol} is defined as the maximum amount of dispersion that a transmission system can tolerate without degrading the performance of the communication system with reference to a Back to Back (B2B) system. For example, a measure of performance degradation can be Eye Opening Penalty (EOP), which is a ratio of the eye opening for a B2B and a system with transmission fiber. Other

measure can be the additional *OSNR* that is required with reference to the B2B system to ensure a certain *BER* in a transmission system with optical fiber.

The dispersion in an optical communication system is not always static and can be expressed as follows:

$$D_{system} = D_{span} + D(t) \quad (1.25)$$

D_{span} represents the intrinsic static dispersion in a standard single mode fiber (SSMF) and as already mentioned it has a value of 17ps/nm.km at a wavelength of 1550 nm. The other part, $D(t)$ also referred as residual dispersion, is not static and varies due to the temperature dependence of the dispersion parameter D or due to the different routes followed by an optical pulse in a reconfigurable optical network to reach the receiver. The effect of residual dispersion can be ignored at small data rates (up to 40 Gb/s) but at high data rates it adds to a significant system penalty. It has been shown by the results presented in [7] that a 40 Gb/s transmission system using SSMF has 1 dB EOP for 50 ps/nm, when pulses with a duty cycle, which is the ratio of pulse duration to bit duration, of 0.6 are transmitted and the amplifier noise is ignored. At 160 Gb/s, this value reduces to only ~ 3.3 ps/nm for the same EOP.

Normally, a directly buried optical fiber is installed at a depth of around 0.8 m to 1 m [8]. The temperature variation over 24 hours can penetrate only 0.45m deep and therefore do not bring an effect on the dispersion of the buried optical fiber. Unfortunately, this is not the case for the seasonal change in temperature, which penetrates several meters into the ground. This effectively changes the dispersion behavior of the fiber and brings degradation to the system performance. Apart from that, the fibers which are not buried are also influenced by the climate but no concrete study exists to account its effect on fiber chromatic dispersion.

The temperature dependent dispersion variation is given by [7,10]:

$$\frac{dD}{dT} = 0.25 \left(\lambda - \frac{\lambda_0^4}{\lambda^3} \right) \frac{dS_0}{dT} - \frac{S_0 \cdot \lambda_0^3}{\lambda^3} \cdot \frac{d\lambda_0}{dT} \quad (1.26)$$

where $\lambda_0=1310$ nm is the zero dispersion wavelength, $\frac{dS_0}{dT}$ has a value of -2.46×10^{-6} (ps-°C)/(nm-km) [10], $S_0=9.352 \times 10^{-2}$ (ps)/(nm-km) is the dispersion slope at λ_0 and dT is the change in temperature. The term $\frac{d\lambda_0}{dT}$, the thermal coefficient of zero dispersion wavelength, is independent of the fiber type and has a value of 0.021-0.028 nm/°C [10]. Therefore, the variation in dispersion due to temperature is predominantly affected by S_0 . Figure 1.3 depicts the variation in fiber chromatic dispersion dD when the temperature changes from T_1 to T_2 .

To emphasis the criticality (importance) of temperature dependent variation in dispersion, in [7] it has been shown that temperature variations of 10°C reaches the 1 dB EOP threshold of 50 ps/nm for a data rate of 40 Gb/s after ~ 900 km of transmission through a SSMF. For 160 Gb/s the reach drops to only 100 km for the same EOP. Therefore, small variations in channel dispersion can become very important at high data rates and it is essential to adaptively manage the channel dispersion to a value below certain threshold.

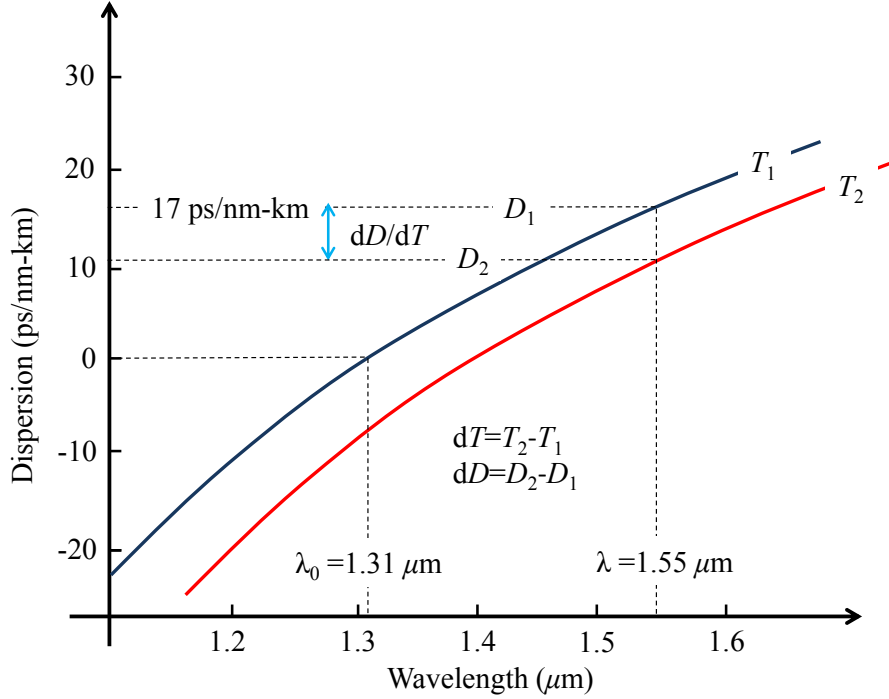


Figure 1.3: Schematic depiction of variation in fiber chromatic dispersion dD due to temperature variation dT

A perfect dispersion compensating systems which caters for both dispersion and dispersion slope can be defined by the following two conditions:

- The Ratio-Dispersion-Slope (RDS) of the transmission fiber and the compensating mechanism are equal [7].

$$RDS_{fiber} - RDS_{DCSystem} = 0 \quad (1.27)$$

$$RDS = \frac{S}{D} \quad (1.28)$$
- The dispersion compensating system has to deliver adaptive performance to nullify the temperature or routing induced dispersion variations.

Therefore, the simple model shown in Figure 1.1 equivalently becomes as the one shown in Figure 1.4, with the dispersion profile for a single span optical communication system utilizing a Tunable Residual Dispersion Compensator (TRDC) shown in Figure 1.5. Due to variation in channel dispersion, the DCF can over compensate the channel dispersion resulting in negative channel dispersion. This case has been shown in figure 1.5. It is also possible that the variation in channel dispersion results in under compensation of the channel dispersion. The TRDC ensures that the over- or under- compensation of fiber chromatic dispersion compensation due to variation in the channel dispersion is effectively mitigated in an adaptive way.

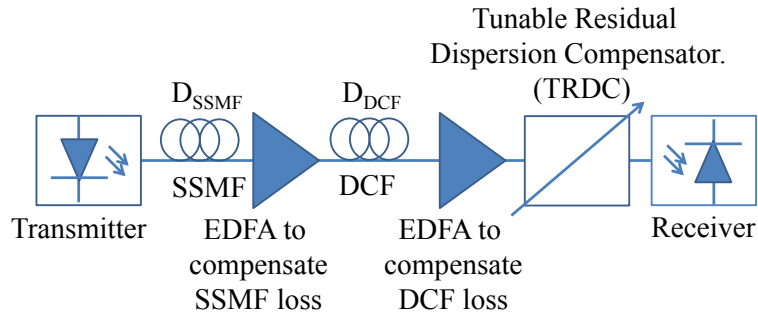


Figure 1.4: Equivalent of a single span optical communication system with an adaptive dispersion compensator

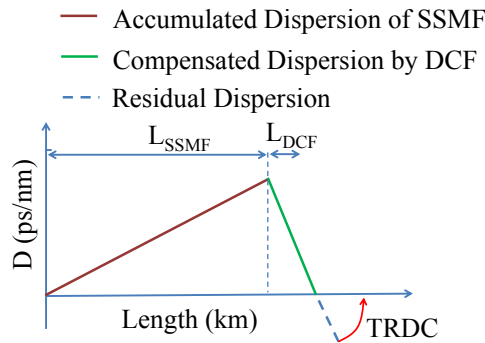


Figure 1.5: Dispersion profile for the single span optical communication system with a tunable dispersion compensator which overcomes the over-compensation of chromatic dispersion.

The second condition (2) mentioned above is the one where the limitation of the DCF becomes evident. Although, it handles the bulk or the intrinsic dispersion of the fiber but its response cannot be made adaptive. Techniques for adaptive dispersion compensation have gained a lot of research interest and many schemes have been developed and mentioned in literature (see reference 2–23 of chapter 2). The above discussion has also emphasized that adaptive management of residual dispersion is mandatory for high speed optical communication systems. Figure 1.6 shows a schematic for a multi-span WDM system with a DCF between two fiber spans and a TRDC before the demultiplexer.

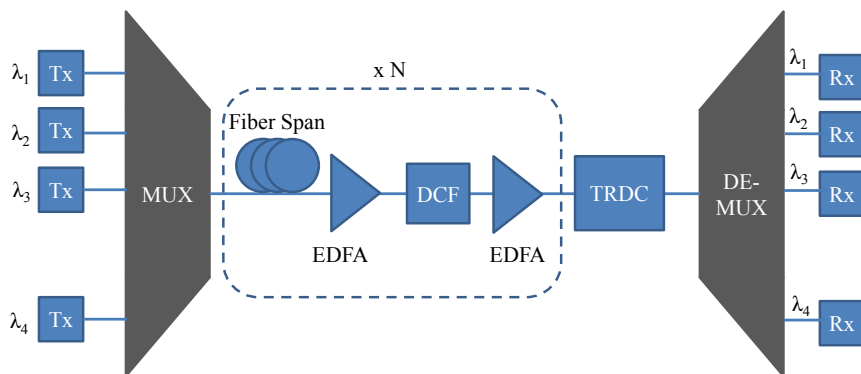


Figure 1.6: Schematic representation of an N span WDM system with a TRDC to mitigate residual chromatic dispersion.

Figure 1.7 shows the exemplary desired response for an adaptively tunable residual dispersion compensator. The following requirements need to be met:

- The dispersion compensator with a periodic frequency response over the entire C-band is highly desirable to simultaneously mitigate the dispersion for multiple channels of the Wavelength division multiplexed (WDM) transmission system. The periodicity of the filter response should be compatible with the specifications of WDM ITU grid. The wavelengths $\lambda_1, \lambda_2 \dots \lambda_m$ in the figure 1.7 correspond to the center frequencies of the WDM channels.
- An ideal dispersion compensating filter should have an all-pass transmission response for a certain fraction of each FSR.

$$|H(\omega)| = 1 \quad (1.29)$$

- This all pass response prevents any signal attenuation of the WDM channels during dispersion compensation. The flat top transmission in the shaded section of figure 1.7 shows the all pass response for each channel of the dispersion compensator.
- The slope of the group delay response $\frac{d\tau}{d\lambda}$ determines the amount of dispersion D delivered by the filter. A linear slope leads to a constant dispersion D .

$$D(\omega) = \frac{d\tau}{d\omega} = D \quad (1.30)$$

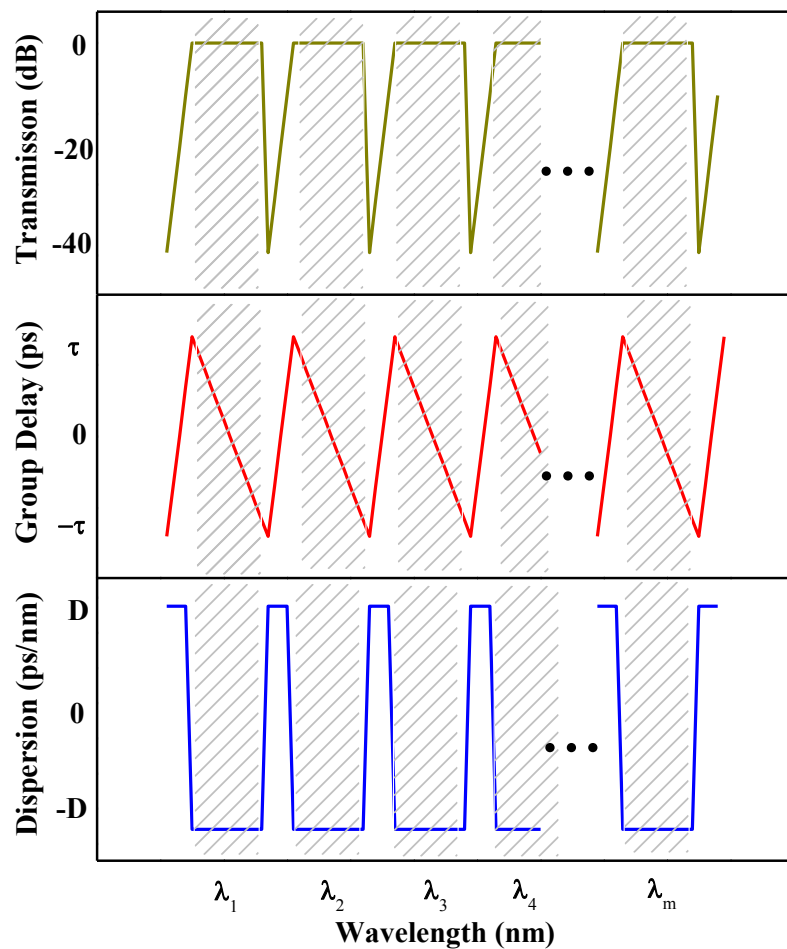


Figure 1. 7: Exemplary transmission (top), group delay (middle) and dispersion (bottom) response of an ideal dispersion compensator.

Therefore, the dispersion compensating filter should deliver a linear low ripple group delay response for first order dispersion compensation. Low ripple is desired because the deviation from that results in an incomplete regeneration of the optical pulses leading to degraded *BER*. Linear group delay and constant dispersion have been depicted by the shaded sections of the middle and bottom plots shown in figure 1.7.

1.5. Electrical vs. Optical Residual Dispersion Compensation Techniques

The main factors which contribute to the residual dispersion in an optical communication system are:

- Different path lengths over which an optical pulse might propagate in a reconfigurable optical network.
- Variation of the fiber dispersion due to bending or fiber manufacturing imperfections.
- Temperature or other environmental factors can also bring an effect on the fiber chromatic dispersion.

Various schemes in both electrical and optical platforms have been presented in the past. As compared to electrical schemes, the optical schemes have following advantages:

- The optical schemes can circumvent the bandwidth limits imposed by the speed of electronics.
- The amount of electrical power needed for electrical solutions is bitrate dependent, which is not the case for optical solutions.
- The electrical solutions are implemented after photo detection, which results in the loss of phase information. As a result of that the electrical solutions suffer from large signal-to-noise penalty when compensating very large values of dispersion.
- Integrated solutions have more potential of integration in the optical receiver module.
- The performance of electrical solutions for dispersion compensation is hampered in the presence of non-linearity and noise, which is not the case for optical solutions.

References:

[1] E. Hecht, "Optics" Addison Wesley, Fourth Edition, 2002.

[2] Ryf, R.; Randel, S.; Gnauck, A.H.; Bolle, C.; Essiambre, R.; Winzer, P.J.; Peckham, D.W.; McCurdy, A.; Lingle, R., "Space-division multiplexing over 10 km of three-mode fiber using coherent 6×6 MIMO processing," Optical Fiber Communication Conference and Exposition (OFC/NFOEC), 2011 and the National Fiber Optic Engineers Conference, vol., no., pp.1,3, 6-10 March 2011.

[3] Gvoind P. Agrawal, "Fiber Optic Communication Systems" Third Edition, "Wiley Series in Microwave and Optical Engineering, 2002.

- [4] Antos, A.J.; Smith, D.K., "Design and characterization of dispersion compensating fiber based on the LP₀₁ mode," *Lightwave Technology, Journal of* , vol.12, no.10, pp.1739,1745, Oct 1994.
- [5] Jensen, J.B.; Tokle, T.; Yan Geng; Jeppesen, P.; Serbay, M.; Rosenkranz, W., "Dispersion Tolerance of 40 Gbaud Multilevel Modulation Formats with up to 3 bits per Symbol," *Lasers and Electro-Optics Society, 2006. LEOS 2006. 19th Annual Meeting of the IEEE* , vol., no., pp.494,495, Oct. 2006.
- [6] Essiambre, R.; Kramer, G.; Winzer, P.J.; Foschini, G.J.; Goebel, B., "Capacity Limits of Optical Fiber Networks," *Lightwave Technology, Journal of* , vol.28, no.4, pp.662,701, Feb.15, 2010.
- [7] Vorbeck, S.; Leppla, R., "Dispersion and dispersion slope tolerance of 160-Gb/s systems, considering the temperature dependence of chromatic dispersion," *Photonics Technology Letters, IEEE* , vol.15, no.10, pp.1470,1472, Oct. 2003.
- [8] http://csmedia.corning.com/CableSystems/%5CResource_Documents%5CSRPs_rl%5C005-012.pdf accessed on 17.09.2013.
- [9] C. K. Madsen and J. H. Zhao, "Optical Filter design and Analysis - A signal processing approach", *Willey Series in microwave and optical engineering*, 1999.
- [10] P. S. André, A. N. Pinto, J. L. Pinto, "Effect of temperature on the single mode fibers chromatic dispersion", *Journal of Microwaves and Optoelectronics*, Vol. 3, No 5, July 2004.

2.

Optical Residual Dispersion Compensation Schemes

2.1. Optical Solutions for Chromatic Dispersion Compensation

Various optical schemes for the efficient compensation of chromatic and residual chromatic dispersion have been demonstrated. The classification of these approaches can be done on the basis of implementation platform or filter architecture. Three broad classes in terms of platform are free space optical solutions, fiber based solutions and integrated photonic solutions. On the basis of filter architecture, two broad categories are Finite Impulse Response (FIR) or Infinite Impulse Response (IIR) filter (FIR and IIR filters are explained in chapter 3).

Few of the most prominent schemes for dispersion compensation are briefly mentioned in this chapter. Apart from the schemes mentioned in this chapter, a large variety of other approaches also exists but they are beyond the scope of discussion in this chapter.

2.1.1. Free Space Optical Solutions

The free space optical solutions provide the highest dispersion values but at the cost of bulky size. The most prominent free space solution is the Virtually Imaged Phase Arrays (VIPA). It can compensate as much as ~ 3000 ps/nm of chromatic dispersion with a pass bandwidth of up to 68 GHz [1]. Figure 2.1 shows the schematic representation of the VIPA based dispersion compensator. The light propagation in a VIPA based dispersion compensator is depicted in figure 2.2.

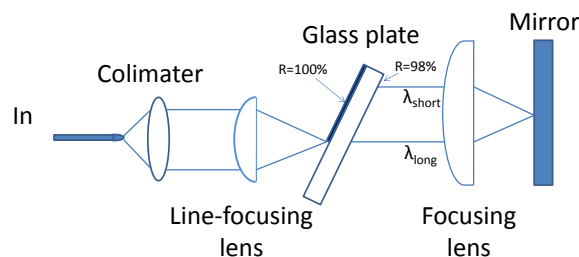


Figure 2. 1: VIPA architecture [2]

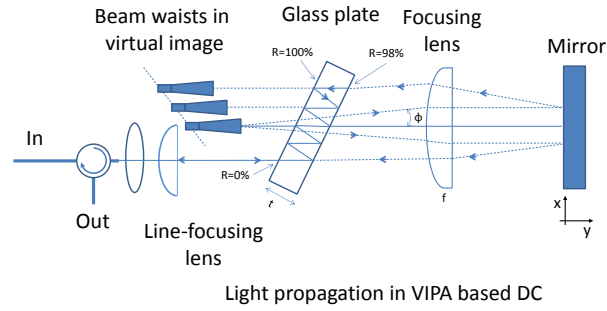


Figure 2.2: Light propagation in VIPA based dispersion compensator [2]

VIPAs generate large wavelength dependent dispersion angles (angular dispersion). The multiple beams that appear on the partially reflecting side (right side) of the glass plate interfere with each other. As a result of this interference, collimated light is produced which travels at an angle that varies with the wavelength of the light (i.e. angular dispersion). By using a focusing lens and a mirror after the VIPA, this angular dispersion can be translated into chromatic dispersion due to different propagation lengths for the longer and shorter wavelengths. It is important to mention that the angular dispersion is produced by the interference of the multiple beams at the right side of the glass plate and not by the glass plate itself, which is normally misunderstood due to ray optic description of figure 2.2. The dispersion can be tuned by tilting the mirror after the focusing lens or by sliding the so called “3D-mirror” along x-axis [3], which has a special profile unlike the flat surface of the mirror.

Another free space optical solution has been proposed in [5]. The main idea of this scheme is based on the use of cascaded Gires-Tournois (GT) etalons with equal Free Spectral Range (FSR). A GT etalon is a special type of Fabry-Perot etalon with one side fully reflective and the other side is partially reflective [6] as has been depicted in figure 2.3.

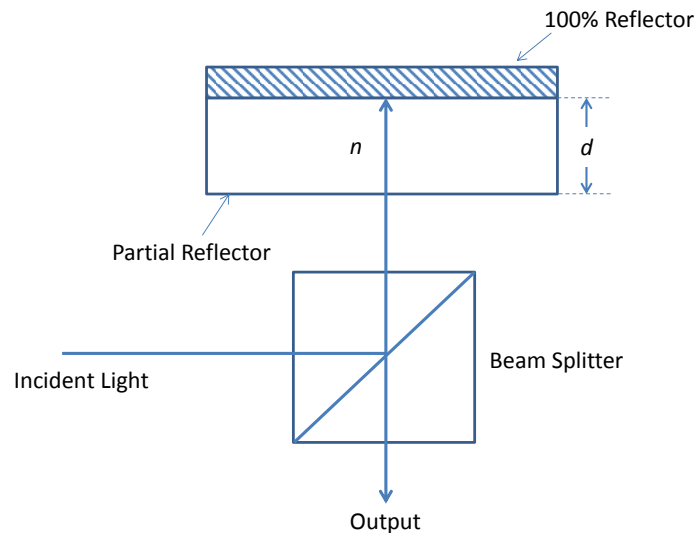


Figure 2.3: Single Gires-Tournois etalon.

Illuminating the GT at a small angle results in a beam, which can be separated out and used as an output. This output can be fed to another GT to make a cascaded GT based dispersion

compensator. The FSR , which is matched to the channel spacing of the WDM system defined by the ITU grid, is given by:

$$FSR = \frac{c}{2 \cdot n_g \cdot d} \quad (2.1)$$

where c is the free space speed of light, n_g is the group index of the etalon and d is the cavity spacing. Each GT has a single group delay (GD) peak in each FSR and the superposition of these GD peaks leads to a linear GD for a certain fraction of the FSR . The amount of dispersion and the GD ripple can be adjusted by choosing the reflection coefficients of the etalons. The GT etalon based solutions have shown to deliver up to 3400 ps/nm of chromatic dispersion but for a narrow bandwidth of only 18 GHz. The thermal tuning of the GTs results in a tunable dispersion compensator [6].

2.1.2. Optical Fiber Based Dispersion Compensators

Most prominent fiber based solutions include the Dispersion Compensating Fibers (DCF) and Fiber Bragg Gratings (FBG).

Ignoring the effect of higher order dispersion, the broadening σ of an optical pulse per unit of the source bandwidth after propagation through a SSMF of length L and dispersion D is given by:

$$\sigma = D \cdot L \quad (2.2)$$

This broadening can be eliminated by propagating the broadened optical pulse through a compensating fiber (DCF) whose length L_c and dispersion D_c are related by:

$$L_c = -\left(\frac{D}{D_c}\right) \cdot L \quad (2.3)$$

DCF has a negative dispersion value to mitigate the positive dispersion accumulated over a span L constituting SSMF. For practical reasons, the dispersion D_c from the DCF needs to have a large value to keep the L_c as short as possible.

DCF is an all optical, all fiber solution to compensate chromatic dispersion. It provides a broadband solution but at the cost of large insertion loss of typically 0.4-0.65 dB/km, which is mitigated by using an optical amplifier. This in return adds noise in the form of Amplified Spontaneous Emission (ASE) from the amplifier. Another problem is associated to the small mode diameters of DCFs, which result in an enhanced non-linear effect. This can be avoided by keeping the average optical power at smaller values. Mostly a DCF is deployed in optical communication systems to mitigate chromatic dispersion. To the best of my knowledge, viable solution exhibiting the tunability of dispersion in a DCF has not been reported so far.

Another promising fiber based solution to compensate chromatic dispersion is by using Fiber Bragg Gratings (FBGs). They are basically wavelength dependent reflective optical

filters. The wavelength of the reflected light (Bragg wavelength) λ_B is related to the average mode index \bar{n} and the grating period Λ by:

$$\lambda_B = 2 \cdot \bar{n} \cdot \Lambda \quad (2.4)$$

A grating with uniform grating period over the length of the grating is referred as a linear grating. For dispersion compensation, Chirped Fiber Bragg Gratings (CFBGs) are employed. The grating period for CFBG varies along the length of the fiber. This results in multiple locations where the Bragg condition is satisfied. Therefore, it serves as a reflector for multiple wavelengths from different positions of the grating.

Chromatic dispersion is produced because the longer and shorter wavelengths are reflected at different position from the CFBG and hence have different propagation lengths. The same has been depicted in figure 2.4. The maximum achievable dispersion D_{max} from a CFBG is related to the length L_g of the grating by:

$$D_{max} = \frac{\Delta\tau_{max}}{\Delta\lambda} = \frac{2 \cdot n_g \cdot L_g}{c \cdot \Delta\lambda} \quad (2.5)$$

where $\Delta\tau_{max}$ is the maximum achievable group delay and $\Delta\lambda$ is the difference between the shortest and the longest wavelength reflected by the CFBG and c is the speed of light in free space. Evident from equation 2.5, large L_g is desired to have large achievable dispersion from a CFBG.

The tuning of the CFBG based dispersion compensators requires a variation in the degree of chirp. This is achieved by various schemes such as by using thermo-optic effect, transverse loading on a polymer package, stacks of polymer actuators, or by bending the uniform grating to achieve a certain chirp [7].

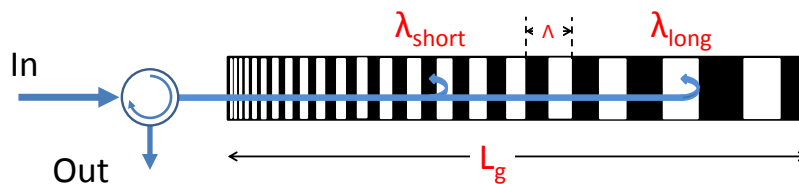


Figure 2.4: Principle of chirped fiber Bragg grating for dispersion compensation

The fiber based dispersion compensators are not limited to the above mentioned two techniques. Other techniques such as Higher Order Mode (HOM) dispersion compensating fibers [3], and fiber based GT etalons have also been demonstrated [8]. HOM is an attempt to mitigate large insertion loss associated with DCFs and in [8] CFBGs are used as GT etalons for tunable dispersion compensation for up to 32 WDM channels. Another very interesting approach is the use of fiber based delay line 2nd order FIR filters [9], which can compensate dispersion for multiple WDM channels and the tuning is achieved by changing the phase on the delay lines connecting the two 3x3 fiber couplers. The realized device with an FSR of 100 GHz has shown a tunability of ± 50 ps/nm and group delay ripple of as small as 1 ps over a bandwidth of 50 GHz to compensate residual dispersion for 42.464 Gb/s NRZ multi-channel transmission system.

2.1.3. Integrated Photonics Dispersion Compensators

Integrated photonics has provided a variety of passive devices for signal processing in optical communication systems. Among them, many dispersion compensating FIR and IIR filters have also been presented. Various photonic components such as ring resonators, integrated Bragg gratings, MMI couplers and AWGs have been utilized for the implementation of these filters. A very brief explanation of the most prominent implementations using these building blocks is given here.

2.1.3.1. Lattice filters as Dispersion Compensators

Lattice or Fourier filters are multiport filters typically comprising a concatenation of 2-port asymmetrical MZIs. The input optical signal propagates only in the forward direction and hence it belongs to the FIR class of the filters. The delay length ΔL connecting the two 2-port couplers constitutes the asymmetrical MZI, which represents a single stage of the lattice filter. A typical structure of lattice filter comprising N -stages is shown in figure 2.5.

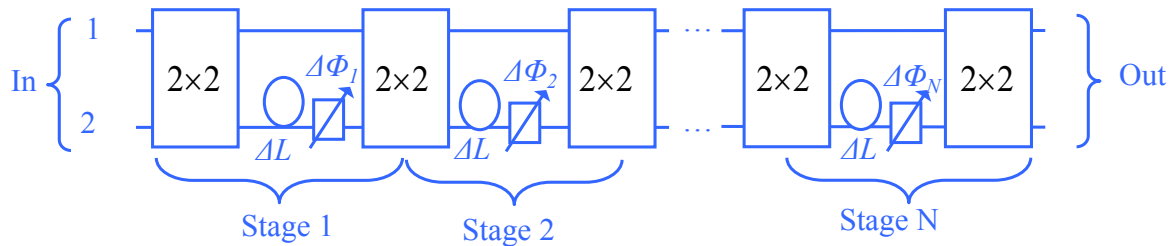


Figure 2. 5: Schematic of a typical lattice filter using static couplers with fixed coupling coefficients

In [17-20], lattice filters are demonstrated as dispersion compensators by using concatenation of $(p+1)$ symmetric and p asymmetric MZIs. Each symmetric MZI is interleaved by an asymmetric MZI. A set of symmetric and asymmetric MZI constitute a single stage of the lattice filter for dispersion compensation. Figure 2.6 shows a schematic representation of an N -stage lattice filter for residual dispersion compensation.

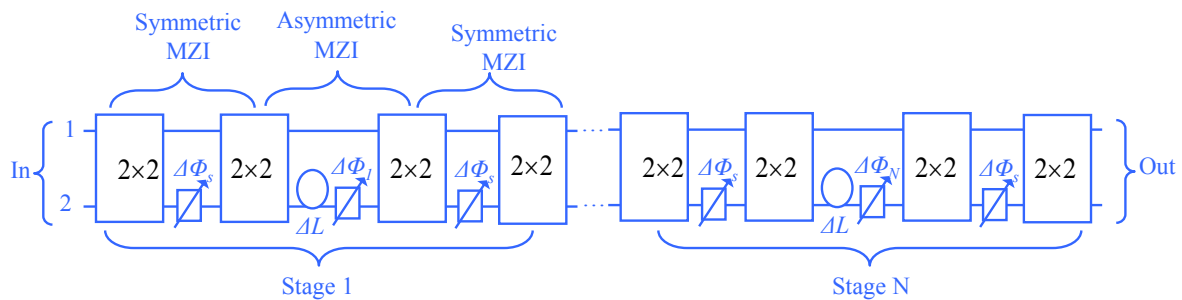


Figure 2.6: Block level representation of a lattice filter based dispersion compensator

The symmetric MZI of each stage of the dispersion compensator shown in figure 2.6 acts as a tunable coupler and enhances the degree-of-freedom to accurately tune the achievable dispersion of the filter. The two tunable couplers are connected to each other by a delay length ΔL , which determines the *FSR* of the filter. The lattice filter gives periodic frequency response with periodicity equal to the *FSR* of the filter. This enables compensation of multiple WDM channels at the same time. The unit delay length ΔL is related to the *FSR* of the filter by:

$$FSR = \frac{c}{n_g \cdot \Delta L} \quad (2.6)$$

The filter can be tuned to deliver a linear group delay by adjusting the coupling coefficients of the tunable coupler and the frequency dependent interference of multiple light beams passing through the cascaded asymmetrical MZIs [12]. This can be achieved by embedding a phase shifting element on the arms of the symmetric and asymmetric MZIs.

The maximum dispersion, which can be compensated by the filter, is related to the number of the stages N and in [12] it has been shown that this value is limited by the total length difference $N \cdot \Delta L$ between the arms of the asymmetrical MZI. By making a compromise for the allowable amount of group delay ripple, the maximum dispersion values from the filter can be enhanced.

In [12], which is one of the pioneering works on integrated lattice filters for residual dispersion compensation, an 8th order lattice filter that can compensate -681ps/nm to 786 ps/nm of chromatic dispersion over a bandwidth of 16.3 GHz has been demonstrated using silica material platform. Later on, [17, 18] have shown a 6th order filter in SiON, which can compensate only +100 ps/nm to -100 ps/nm of chromatic dispersion but over a much broader bandwidth of 62 GHz as compared to [12] and a small group delay ripple of 1 ps. A reflective implementation [13] of the lattice filter has shown 460 ps/nm of tuning range for dispersion for a bandwidth sufficient for compensation of chromatic dispersion in 40 Gb/s transmission system. This is also a silica based implementation of a residual dispersion compensator. The reflective approach doubles the achievable dispersion from the filter and also circumvents the polarization dependence.

2.1.3.2. AWG Based Dispersion Compensator

Arrayed Waveguide Gratings (AWGs), which are also termed as Waveguide Grating Routers (WGR) or Phased Arrays (PHASAR) have also been used for the implementation of residual dispersion compensating filters. A simplified schematic of an AWG is shown in figure 2.7.

An AWG comprises an input waveguide, which is connected to a Free Propagation Region (FPR). An array of waveguides (waveguide grating) connects this FPR with another FPR region on the right side. The output of the second FPR is connected to the output waveguides. The schematic in figure 2.7 shows a 1x3 AWG (one input and 3 outputs).

Depending on the application, single-input-single-output, single-input-multiple-outputs or multiple-inputs-single-output configurations are possible.

In an AWG, light is guided through the input waveguide to the first FPR. In the FPR, the lateral confinement of light vanishes and it diffracts. This diffracted light is coupled to the waveguide grating. The waveguides in the waveguide grating are arranged on a circle of radius R . The N waveguides of the waveguide grating have a pitch (center to center distance) of d . The combination of input waveguide with a FPR and waveguide grating effectively constitute a $1 \times N$ star coupler. The N waveguides in the waveguide grating have a linearly incremental optical path length difference ΔL , which is equal to an integer multiple of the center wavelength λ_c and is given by:

$$\Delta L = L_M - L_{M-1} = \frac{m \cdot \lambda_c}{n_{eff}} \quad (2.7)$$

L_M and L_{M-1} is the length of the M^{th} and $(M-1)^{\text{th}}$ waveguide of the waveguide grating. n_{eff} is the effective refractive index of the waveguide modes in the waveguide grating and m is an integer multiple and is termed as the grating order of the array. At λ_c (λ_2 in Figure 2.7), the light in the waveguide grating arrive with an equal phase shift at the output aperture. Therefore, the field distribution at the input aperture (see figure 2.7) is reproduced at the output aperture with an amplitude and phase distribution equal to the input field. Therefore, after propagation through the second FPR, the input field at the object plane (see figure 2.7) is reproduced at the image plane, which follows a circular path with radius R , on which the output waveguides are arranged.

For input light at $\lambda \neq \lambda_c$, the wavelength dependent phase difference $\Delta\phi$ produced by the wavelength dependent optical path length difference ΔL introduces a wavelength dependent tilt of the outgoing beam from the waveguide grating. This leads to a wavelength dependent shift of the focal point (image) formed on the image plane. This spatial dispersion produced by the AWG is the underlying principle of dispersion compensation by using AWGs.

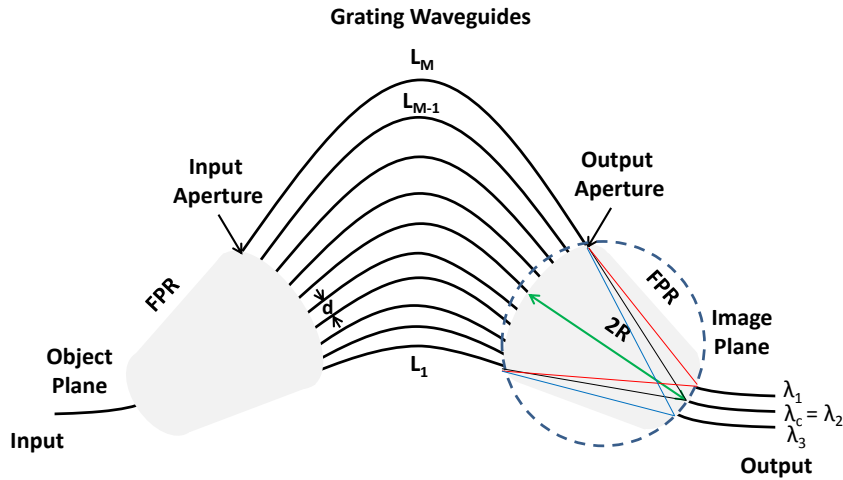


Figure 2. 7: A simplified schematic of an AWG

The AWG based implementation of a dispersion compensator can be treated as an integrated photonic implementation of the VIPA scheme presented in section 2.1.1. Both approaches use the spectral decomposition of the chromatically dispersed input signal to compensate dispersion. The AWG based dispersion compensator comprises two identical AWGs and a spatial phase filter. The principle of the AWG based dispersion compensator, as explained in [29] is as follows. The spatially dispersed input pulse at the output of the first AWG (input pulse is decomposed into its spectral components at the output of the first AWG). A spatial phase filter is placed at the output image plane of the first AWG to compensate the phase of each spectral component. The phase compensated wavelength components are recombined in the second AWG to regenerate the dispersion compensated optical pulse. Figure 2.8 shows a block level representation and waveguide layout of a typical dispersion compensator as proposed by [29].

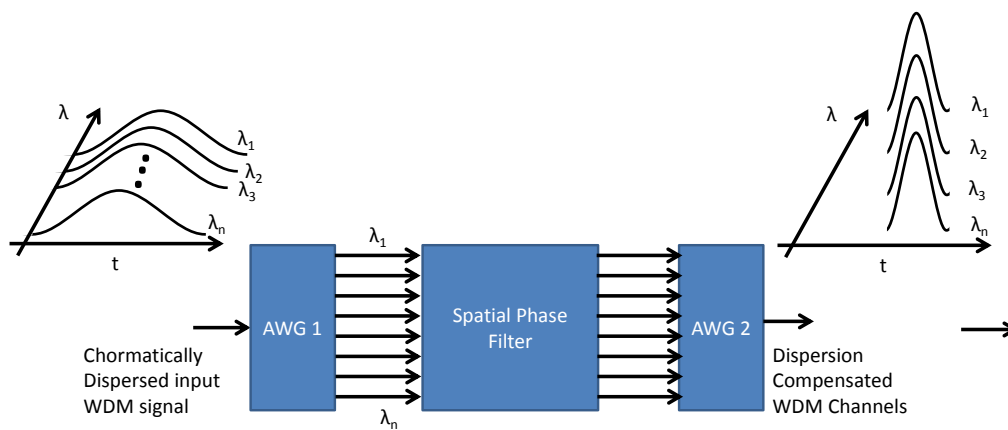


Figure 2. 8: Principle of AWG based dispersion compensator.

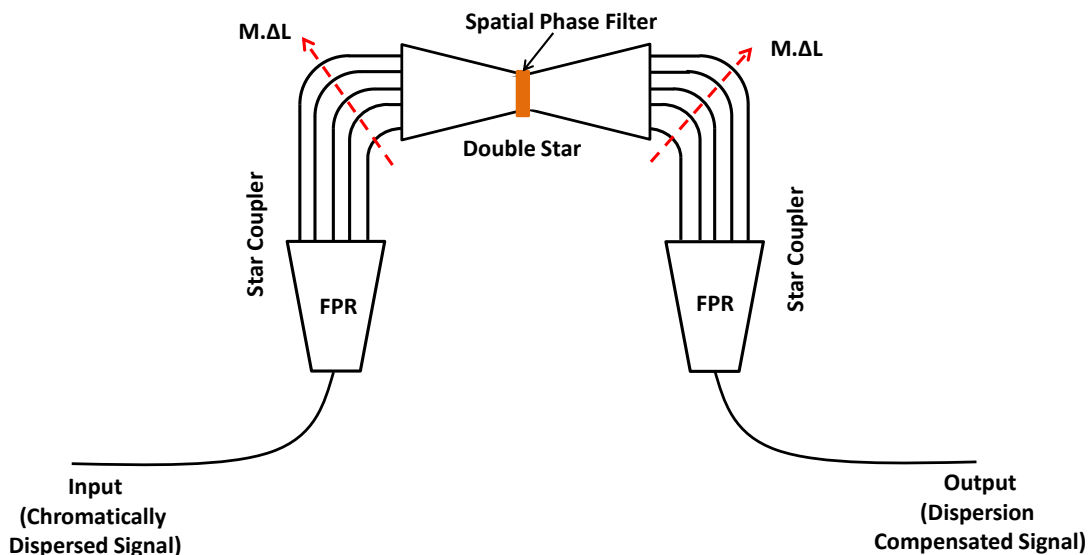


Figure 2. 9: Schematic of an AWG based dispersion compensator

A typical implementation of the AWG based dispersion compensator is shown in figure 2.9. As mentioned earlier and depicted by figure 2.8, the AWG based approach for dispersion compensation uses two AWGs, which are joined at the end of their second star coupler in

the so called “double star” configuration (see figure 2.9). In the middle of this double star (the imaging plane of the first AWG), a spatial phase filter is placed that provides a controllable quadratic phase distribution. Practically, this is implemented by using an array of thermo-optic phase shifters and is referred as a “thermal lens”. Intrinsically the AWG shows negative dispersion, which is given by [17]:

$$D_{int} = -\frac{2 \cdot M \cdot b \cdot c}{d \cdot (\lambda_c \cdot FSR)^2} \quad (2.8)$$

where M is the number of arms in the waveguide grating (grating order), d is the grating waveguide pitch at the double star, λ_c is the center wavelength, b is the spatial “channel” width at the double star, c is the free space speed of light. FSR determine the periodicity of the dispersion compensator and it is matched to the WDM channel grid. The origin of negative dispersion (see equation 2.7) comes from the fact that the shorter wavelengths from the signal decomposed by the first AWG are imaged on the longer grating arms of the second AWG and the longer wavelengths are imaged on the shorter arms. For positive dispersion, the temperature profile of the “thermal lens” is adjusted to deliver a phase profile that can focus the shorter wavelengths towards the shorter grating arms of the second AWG and the longer wavelengths towards the longer grating arms. Hence, longer wavelengths travel longer distance and shorter wavelengths travel shorter distance, which results in positive dispersion. For zero dispersion, the “thermal lens” is adjusted in such a way that the spectral components are converged to center of the inlets for the second AWG, where the recombination of the dispersion compensated signal takes place.

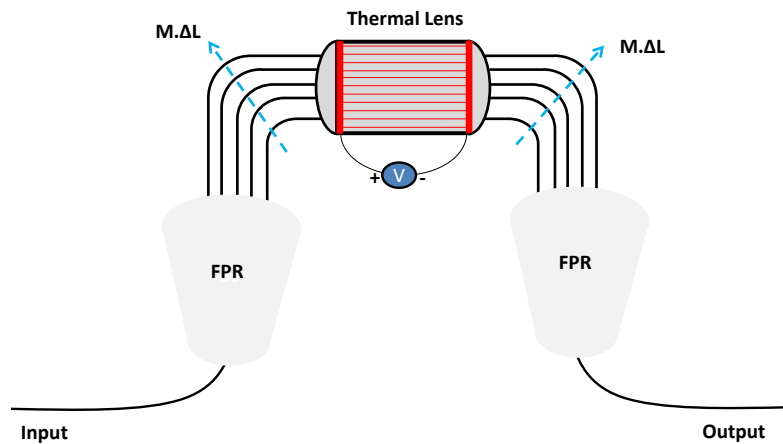


Figure 2.10: AWG with a thermal lens to compensate fiber chromatic dispersion [17]

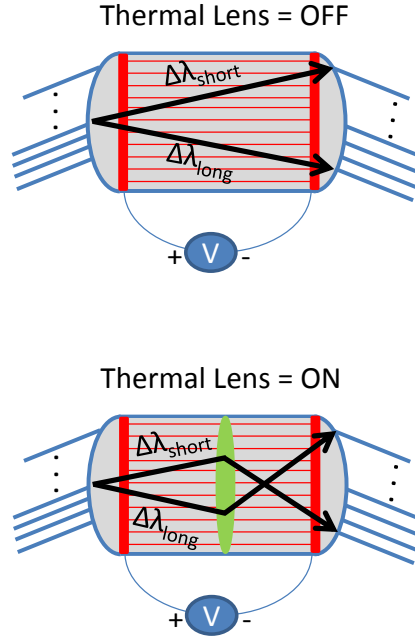


Figure 2.11: Principle of thermal lens in AWG based dispersion compensator [17]

[14-20] have shown the implementation of AWG based dispersion compensator. The standard two AWG configuration for dispersion compensation has a large footprint and thermal lens, which comprises an array of heaters, requires as much as 7.3 W to tune the dispersion from ~ -200 ps/nm to $+200$ ps/nm [17] over a bandwidth of 48 GHz. Both drawbacks have been mitigated by using a reflective configuration, which uses a single AWG and a mirror with an off-chip polymeric thermo-optic lens to tune the dispersion over a range of 1300 ps/nm over a bandwidth of >39 GHz by using ~ 74 mW of electrical power [19]. In [18] a reflective AWG based filter for residual dispersion compensator is presented with an on-chip thermal lens. The drawback of the reflective approach is the requirement of an off-chip circulator, which contributes to an additional loss of the device. The problem has been resolved by [27], which use two AWGs in reflective configuration. The fabricated device has shown to compensate $+142$ ps/nm to $+1148$ ps/nm over a bandwidth of 29 GHz by using 3.8 W of electrical power. The device has an insertion loss of 16.5 dB.

2.1.3.3. Ring Resonator Based Dispersion Compensators

A ring resonator based dispersion compensating filter can be considered as an integrated equivalent of the GT etalon based approach. A typical approach comprises several rings which are coupled to a single bus waveguide as demonstrated by figure 2.12. The single stage of the filter comprises a single ring coupled to the waveguide. If the frequency of the input signal matches the resonance frequency of the ring, then the signal will take longer time to pass through the waveguide. Therefore, each *FSR* of the ring will have a single group delay peak. Cascading various rings together brings flexibility to the design. The coupling coefficient k and the phase associated with each ring is adjusted in such a way to get linear group delay response for a certain fraction of the overall *FSR* of the filter.

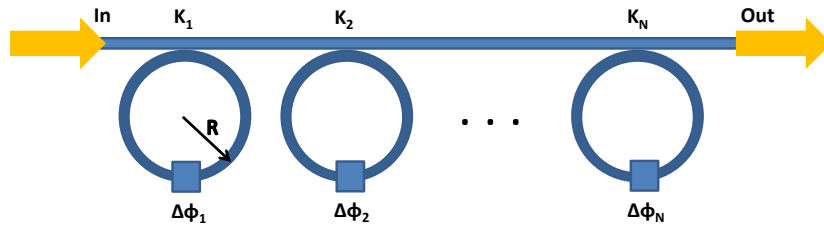


Figure 2.12: Ring resonator based dispersion compensator

Recently, some other filter approaches have also been proposed that use a combination of ring resonators and MZI to perform various signal processing applications and can be used for dispersion compensation [21]. In [26], a dispersion compensator comprising 8 rings has been fabricated using SiON to compensate ± 760 ps/nm of chromatic dispersion over a bandwidth of 25 GHz for 16 WDM channels. The group delay ripple is ~ 20 ps.

2.1.3.4. Integrated Bragg Grating Based Dispersion Compensators

An integrated equivalent of the CFBG based dispersion compensator has been demonstrated in [22]. Like CFBGs, an integrated CBG can reflect different wavelengths from different positions of the grating. This phenomenon can be used for the compensation of dispersion. The grating length to reflect an input signal can either be controlled by changing the width of the grating waveguide or the period of the grating. The grating period variation brings a stronger effect as compared to the waveguide width but due to tight fabrication requirements the waveguide width variation is more realistic. The integrated Bragg grating based devices have shown the compensation of 500 ps/nm of chromatic dispersion over a bandwidth of 1 nm. An added feature of such devices is the possibility of an on-chip integrated circulator to separate the compensated signal. The circulator comprises a pair of equal gratings and two 2x2 MMI couplers [23].

Recently, an apodized version [24] of the integrated Bragg grating based dispersion compensator has also been demonstrated. This implementation attempts to minimize the large group delay ripples in the un-apodized implementation. A reduction by a factor of 5 has been demonstrated by this implementation [24].

2.2. Comparison of Different Dispersion Compensators in Different Platforms

In the previous section, different dispersion compensators in free space, fiber and integrated optics have been discussed. In this section a comparative analysis of different approaches is provided.

As mentioned earlier, the free-space solutions such as VIPA have shown a large equalization range for chromatic dispersion. VIPAs designed with large angular dispersion can compensate chromatic dispersion for 100km long fibers. An obvious drawback of the VIPA or any free space approach is its bulky size and costly process of assembling various parts.

Fiber based CFBG deliver smaller dispersion values as compared to VIPA. The main limitations for fiber based devices are the large group delay ripple (\sim tens of ps) [30]. The impact of large group delay ripple on the performance of a dispersion compensator is mentioned in section 5.6. In general, it prevents the perfect regeneration of the chromatically dispersed optical pulse and leads to higher BER. The group delay ripple induced distortion is proportional to the peak-to-peak group delay ripple and also on the frequency of the group delay ripple [31]. Apart from that, the fiber based dispersion compensators show tendency towards lower insensitivity to temperature fluctuations [4].

Lastly, the integrated optical solutions are very compact in size and can be produced on mass-scale. A compromise exists for all integrated implementations between the achievable dispersion D_{max} in ps/nm and the useful bandwidth Δf in GHz. Integrated solution can deliver large dispersion values but at the cost of reduced bandwidth. The bandwidth can be enhanced by compromising the amount of dispersion. Therefore, it is realistic to say that the integrated solutions cannot replace fiber based or free space solutions due to the $D_{max} \sim 1/(\Delta f)^2$ compromise. Their true potential lies in using them for the compensation of residual dispersion. This residual dispersion originates either due to temperature fluctuations or the routing of the optical signal (see section 1.4). A qualitative matrix, which summarizes the important features of tunable dispersion compensators in free space, fiber or integrated platforms, has been shown in the following table 2.1 (VIPA is considered as a benchmark for fiber based and integrated dispersion compensators).

Table 2.1: Qualitative matrix for chromatic dispersion compensators realized in different platforms

Approach	Dispersion Value (ps/nm)	Bandwidth	Group Delay Ripple	Size	Multichannel Operation
Free Space (VIPA)	Large	Large	Small	Bulky	Compatible
Fiber (CFBG)	Large	Small	Large*	Large	Not compatible
Integrated Optics (Lattice or AWG Filter)	Small/Large	Large/Small	Small	Compact	Compatible

2.3. Comparison of Different Integrated Dispersion Compensating Filters

To further narrow down the comparison, in this section a comparative analysis of only the integrated approaches for dispersion compensation is provided.

The main limitation of the lattice filter, which has been the first integrated dispersion compensator reported, is the large number of coupling elements required to build a filter with certain order R . As shown in figure 2.6, an N -stage filter of order $R=N$ will require $2(N+1)$ 2×2 couplers. A large order R of the filter is highly desirable to deliver large dispersion (more detail is in section 3.5). This happens only at the cost of large filter size and cumbersome tuning because a change of phase on one of the delay arms or a change in the coupling coefficients of one of the tunable couplers affects all zeros of the filter, which determine the overall response of the filter.

AWG based approaches for dispersion compensation have shown a lot of promising results. The double AWG approach suffers from the reduced transmission bandwidth for the dispersion compensators. This originates from the fact that the longer and shorter wavelengths suffer from higher loss due to their non-zero angle on the output waveguides. A possible solution to solve this problem is to use another AWG in the middle with twice the delay length as compared to the outer two AWGs. The amount of achievable dispersion for a given bandwidth can be increased by increasing the grating order M of the AWG or by increasing the number of stages N . In [13] it has been shown that a device with larger N is more desirable as compared to a device with higher M because a device with larger N will be more tolerant to phase errors in the WGR arms [19, 20] as compared to a device with large M . Also a device with smaller M and larger N (more serial device) can deliver higher dispersion values as compared to a device with larger M and smaller N (more parallel device) [13].

Generally, AWGs have phase errors across the arrayed waveguides. These errors are associated with either fabrication (random) or design (systematic) of the AWG. The fabrication based phase errors originate from various factors such as the limited resolution of the mask used for photolithography, side wall roughness of the waveguides and variation in the refractive index or thickness of the guiding layer (top silicon of the SOI wafer). The variation in the effective refractive indices, which is a function of the bending radius of the waveguides, in the waveguide grating has phase errors associated in the waveguide grating. Therefore, from fabrication and design aspect, the devices with higher M are less tolerant as compared to devices with smaller M . Another drawback of the AWG based approach is the high power (\sim couple of Watts) requirements to tune the filter to various dispersion values.

The most eminent limitation of the ring resonator based approach is the dependence of FSR of the filter on the ring radius r .

$$FSR = \frac{\lambda^2}{n_{eff} \cdot L} = \frac{\lambda^2}{n_{eff} \cdot (2 \cdot \pi \cdot r)} \quad (2.9)$$

Since the *FSR* of the filter has to be matched to the WDM grid, small ring radii will be required for dense WDM systems. This will make the radiation losses from the ring high and will also put tight technological requirements.

Integrated Bragg gratings suffer from the same problem as their fiber counterpart and that is the large group delay ripple. Apodized Bragg grating approaches have minimized the group delay ripples to around 20 ps [24], which is still very large as compared to the other integrated approaches [11].

In table 2.2 a comparison of different photonic integrated dispersion compensators is provided.

Table 2.2: Comparison of photonic integrated dispersion compensators

Configuration	Tunable range ΔD (ps/nm)	Range (ps/nm)	B.W@ Dmax (GHz)	Ripple (ps)	FOM	Tuning Mech.	Tuning Power	Mutichannel	Insertion Loss (dB)
AWG [18]	-1523-+207	1730	29	20	93	Off-chip polymeric Thermo-Optic Lens	74 mW	Yes	7
AWG [27]	+142-+1148	1006	29	--	54	Thermo Optic	Less than 5 W	yes	16.5
Integrated Bragg Gratings[22]	-	500	-	100	-	-	Not Tuned	No	1.7
Ring Resonators [26]	+/- 760	1520	25	10	60	Thermo Optic	-	yes	--
Lattice Filter [12]	-681/+786	1467	16.3		25	Thermo Optic	--	Yes	14.4
Lattice Filter [10]	-120/+120	240	60	1.5	55	Thermo Optic		Yes	

$$\text{Figure of Merit } FOM = (B.W)^2 \cdot \Delta D \cdot \frac{\lambda^2}{c_0}$$

2.4. Parallel-Serial Filter Approach- A New Paradigm

From the discussion in section 2.3, it can be concluded that a major impediment faced by future high speed optical communication systems is the chromatic dispersion. With increasing data rates (especially beyond 40 Gb/s), the tolerance to fiber chromatic dispersion is reduced and even small values of dispersion need compensation. Integrated optical solutions are best suited for compensating such small and residual dispersion in an optical communication system. A large number of solutions have already been demonstrated in integrated optics. Each solution has its own advantages and disadvantages as discussed in section 2.3. Therefore, the quest to circumvent and nullify the limitations of existing filter architectures by novel filter architectures is still continuing.

On the basis of architecture, coherently connected FIR filters for residual dispersion compensation can be classified into either parallel filters or serial filters. Parallel filters are the ones which use parallel filtering elements. An example of that is the AWG based filters with thermal lens (see section 2.1.3.2). The lattice filters belong to the serial architecture as it uses a cascade of 2-port MZIs (see section 2.1.3.1). The advantages and disadvantages of both approaches are detailed in section 2.3.

A higher order filter is, generally, required to perform complex signal processing tasks such as dispersion compensation. This fact will be elaborated in more detail in Chapter 3. Both parallel and serial filter architectures for dispersion compensation provide only a single degree-of-freedom (DOF) to enhance the order R of the filter. For example, a large number of stages N are required to increase the order R of the serial filter (increased serialization of the serial filter). Similarly, the parallelism of the parallel filter is enhanced to increase the order R of the parallel filter.

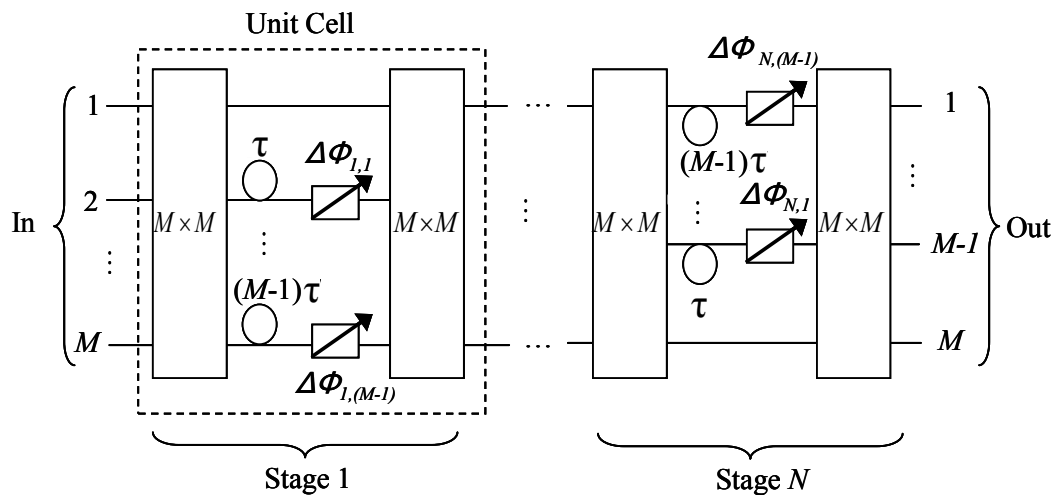


Figure 2. 13: Generalized layout of the parallel-serial filter for residual dispersion compensation (unit cell corresponds to single stage of the filter).

One of the main attributes of the work presented in this research is to bring a paradigm shift by introducing new filter architectures. This architecture is termed as Parallel-Serial filter architecture. The name attributes the fact that the order R of the filter is increased by either increasing the number of stages N (serialism) or by using parallel filtering elements in each stage of the filter (parallelization) of the filter. As a result, unlike the existing filter architectures there are two DOF available to enhance the order R of the parallel-serial filter. Figure 2.13 shows the block level representation of a generalized parallel-serial filter. The order R of the parallel-serial filter is given by $N(M-1)$, where N is the number of stages and M is the order of the parallel filtering elements in each stage of the parallel-serial filter. Therefore, this scheme has a potential to provide more delay while keeping the number of coupling elements small (see Figure 2.13). Like lattice filter, a single stage (unit cell) of the parallel-serial filter consists of an M -port MZI. The unit delay τ produced by the delay length ΔL determines the *FSR* of the parallel-serial filter. Total delay $N(M-1)\tau$ produced by parallel-serial filter determines the maximum dispersion produced by the parallel-serial filter. Furthermore, phase shifting elements are placed on the delay lines to tune the response of the parallel-serial filter. A more detailed description and principle of the parallel-serial filter is topic of discussion for Chapter 3.

To elaborate further the advantage of parallel-serial filter over its counter parts (i.e. lattice and AWG based filters), consider the implementation of a 14th order FIR filter. In the case of a lattice filter (see figure 2.6), $2(N+1)=30$ 2-port couplers are required. AWG based filter will have only one stage ($N=1$) (see figure 2.10) with waveguide grating order $M=15$. In the case of parallel-serial filter, the number of stages in the filter will depend on the choice (parallelism) of the filtering element in each stage. For example, if filtering elements with $M=8$ are used, then $N=(M-1)/R=2$ are required and only 3 coupling elements will be required. This reduced number of coupling elements as compared to the serial filter makes the filter footprint compact.

To achieve a certain transfer function, each stage of the filter has to be appropriately tuned. The overall response of the filter is the cumulative effect of all these contributions from each stage of the filter. This will be explained in more detail in chapter 3. A smaller number of stages by using parallel-serial filters will require optimization of less number of these stages. Therefore, the tuning of the parallel-serial filter is less cumbersome compared to a completely serial filter with a large number of stages.

As highlighted in section 2.3, AWGs which are used in the implementation of the parallel filters, are known for their low tolerance to fabrication inaccuracies and dependence on the layout of the device [28]. On the other hand, a parallel-serial filter is capable of using filtering elements (such as MMI couplers) that are more tolerant to fabrication errors and layout. Apart from that, the parallel-serial filter does not require a complex thermal lens design, which is employed for the implementation of a tunable residual dispersion compensator using AWGs.

In conclusion, a parallel-serial filter provides an attractive alternative to the existing filter architectures, which are used for the implementation of a dispersion compensator. This filter approach provides a compact, easy to tune, robust and low power approach to implement a residual dispersion compensator.

In the scope of this work, parallel-serial filters for residual dispersion compensation are presented. But the filter architecture is versatile and can be used for the implementation of other signal processing tasks [32].

References:

- [1] Gvoind P. Agrawal, "Fiber Optic Communication Systems" Third Edition, " Wiley Series in Microwave and Optical Engineering, 2002.
- [2] Yamauchi, Y.; Sonoda, H.; Furukawa, H.; Kubota, Y., "Variable dispersion compensator using a VIPA with an extended bandwidth," Optical Communication, 2005. ECOC 2005. 31st European Conference on , vol.4, no., pp.821,822 vol.4, 25-29 Sept. 2005.
- [3] H. Ooi, K. Nakamura, Y. Akiyama, T. Takahara, T. Terahara, Y. Kawahata, H. Isono, and G. Ishikawa, "40-Gb/s WDM Transmission With Virtually Imaged Phased Array (VIPA) Variable Dispersion Compensators," J. Lightwave Technol. 20, 2196- (2002).
- [4] M. Shirasaki, "Virtually Imaged Phase Array" Fujitsu Science Technology Journal, Vol. 35, Issue 1, 1999.
- [5] Shabtay, G.; Mendlovic, D.; Itzhar, Y., "Optical single channel dispersion compensation devices and their application," Optical Communication, 2005. ECOC 2005. 31st European Conference on , vol.3, no., pp.321,322 vol.3, 25-29 Sept. 2005.
- [6] Paul Coulbourne et al., "Tunable Dispersion Compensator" US Patent US 6,654,564 B1.
- [7] Song, Y. W.; Starodubov, D.; Pan, Z.; Xie, Y.; Willner, A.E.; Feinberg, J., "Tunable WDM dispersion compensation with fixed bandwidth and fixed passband center wavelength using a uniform FBG," Photonics Technology Letters, IEEE , vol.14, no.8, pp.1193,1195, Aug. 2002.
- [8] Doucet, S.; LaRochelle, S.; Morin, M., "Reconfigurable Dispersion Equalizer Based on Phase-Apodized Fiber Bragg Gratings," Lightwave Technology, Journal of, vol.26, no.16, pp.2899,2908, Aug.15, 2008.
- [9] Duthel, T.; Otto, M.; Schäffer, C.G., "Simple tunable all-fiber delay line filter for dispersion compensation," Photonics Technology Letters, IEEE , vol.16, no.10, pp.2287,2289, Oct. 2004.
- [10] M. Bohn, W. Rosenkranz, and P. Krummrich, "Adaptive distortion compensation with integrated optical finite impulse response filters in high bitrate optical communication systems," IEEE J. Sel. Topics Quantum Electron., vol. 10, no. 2, pp. 273-280, Mar./ Apr. 2004.

- [11] F. Horst, R. Germann, U. Bapst, D. Wiesmann, B. Offrein, and G. Bona, "Compact tunable FIR dispersion compensator in SiON technology," *IEEE Photon. Technol. Lett.*, vol. 15, no. 11, pp. 1570–1572, Nov. 2003.
- [12] K. Takiguchi, K. Jinguji, K. Okamoto, and Y. Ohmori, "Variable group-delay dispersion equalizer using lattice-form programmable optical filter on planar lightwave circuit," *IEEE J. Sel. Topics Quantum Electron.*, vol. 2, no. 2, pp. 270–276, Jun. 1996.
- [13] C. Doerr, S. Chandrasekhar, M. Cappuzzo, A. Wong-Foy, E. Chen, and L. Gomez, "Four-stage Mach-Zehnder-type tunable optical dispersion compensator with single-knob control," *IEEE Photon. Technol. Lett.*, vol. 17, no. 12, pp. 2637–2639, Dec. 2005.
- [14] F. Kerbstadt and K. Petermann, "Analysis of adaptive dispersion compensators with double-AWG structures," *J. Lightw. Technol.*, vol. 23, no. 3, pp. 1468–1477, Mar. 2005.
- [15] C. Doerr, D. Marom, M. Cappuzzo, E. Chen, A. Wong-Foy, L. Gomez, and S. Chandrasekhar, "40-Gb/s colorless tunable dispersion compensator with 1000-ps/nm tuning range employing a planar lightwave circuit and a deformable mirror," in *Proc. Opt. Fiber Commun. Conf./NFOEC*, Mar. 2005, vol. 5, pp. 1–3.
- [16] D. Marom, C. Doerr, M. Cappuzzo, E. Y. Chen, A. Wong-Foy, L. Gomez, and S. Chandrasekhar, "Compact colorless tunable dispersion compensator with 1000-ps/nm tuning range for 40-Gb/s data rates," *J. Lightw. Technol.*, vol. 24, no. 1, pp. 237–241, Jan. 2006.
- [17] Doerr, C.R.; Stulz, L.W.; Chandrasekhar, S.; Pafchek, R., "Colorless tunable dispersion compensator with 400-ps/nm range integrated with a tunable noise filter," *Photonics Technology Letters, IEEE*, vol.15, no.9, pp.1258,1260, Sept. 2003.
- [18] Y. Ikuma and H. Tsuda, "AWG-Based Tunable Optical Dispersion Compensator With Multiple Lens Structure," *J. Lightwave Technol.* 27, 5202-5207 (2009).
- [19] Doerr, C.R.; Blum, R.; Buhl, L.L.; Cappuzzo, M.A.; Chen, E.Y.; Wong-Foy, A.; Gomez, L.T.; Bulthuis, H., "Colorless tunable optical dispersion compensator based on a silica arrayed-waveguide grating and a polymer thermo-optic lens," *Photonics Technology Letters, IEEE*, vol.18, no.11, pp.1222,1224, June 2006.
- [20] N. Fontaine, J. Yang, W. Jiang, D. Geisler, K. Okamoto, R. Huang, and S. Yoo, "Active arrayed-waveguide grating with amplitude and phase control for arbitrary filter generation and high-order dispersion compensation," in *34th Eur. Conf. Opt. Commun.*, Sep. 2008, pp. 1–2.
- [21] Ibrahim, S.; Luo, L.W.; Djordjevic, S.S.; Poitras, C.B.; Zhou, L.; Fontaine, N.K.; Guan, B.; Cheung, S.; Ding, Z.; Okamoto, K.; Lipson, M.; Yoo, S. J B, "Fully reconfigurable silicon photonic lattice filters with four cascaded unit cells," *Optical Fiber Communication (OFC), collocated National Fiber Optic Engineers Conference, 2010 Conference on (OFC/NFOEC)*, vol., no., pp.1,3, 21-25 March 2010.

- [22] I. Giuntoni, D. Stolarek, A. Gajda, J. Bruns, L. Zimmermann, B. Tillack, and K. Petermann, "Integrated Dispersion Compensator Based on SOI Tapered Gratings," in 37th European Conference and Exposition on Optical Communications, OSA Technical Digest (CD) (Optical Society of America, 2011), paper Th.12.LeSaleve.4.
- [23] Giuntoni, I.; Stolarek, D.; Gajda, A.; Winzer, G.; Bruns, J.; Tillack, B.; Petermann, K.; Zimmermann, L., "Integrated drop-filter for dispersion compensation based on SOI rib waveguides," Optical Fiber Communication (OFC), collocated National Fiber Optic Engineers Conference, 2010 Conference on (OFC/NFOEC) , vol., no., pp.1,3, 21-25 March 2010.
- [24] Giuntoni, I.; Stolarek, D.; Bruns, J.; Zimmermann, L.; Tillack, B.; Petermann, K., "Integrated Dispersion Compensator Based on Apodized SOI Bragg Gratings," Photonics Technology Letters, IEEE , vol.25, no.14, pp.1313,1316, July15, 2013.
- [25] T. Schlipf, M. Street, J. Pandavenes, R. McBride, and D. Cumming, "Design and Analysis of a Control System for an Optical Delay-Line Circuit Used as Reconfigurable Gain Equalizer," J. Lightwave Technol. 21, 1944- (2003).
- [26] K. Suzuki, I. Nakamatsu, T. Shimoda, S. Takaesu, J. Jushioda, E. Mizuki, M. Horie, Y. Urino, H. Yamazaki, "WDM tuneable dispersion compensator with PLC ring resonator" OFC 2004, pp. 746, Feb. 2004.
- [27] Y. Ikuma, T. Mizuno, H. Takahashi, H. Tsuda, "Circulator-free reflection type tunable optical dispersion compensator using cascaded arrayed waveguide gratings" in 36th European Conference and Exhibition on Optical Communication, Sep. 2010.
- [28] Nur Ismail, Fei Sun, Gabriel Sengo, Kerstin Wörhoff, Alfred Driessen, René M. de Ridder, and Markus Pollnau, "Improved arrayed-waveguide-grating layout avoiding systematic phase errors" Vol. 19, No. 9, Optics Express, 25 April 2011.
- [29] Hiroyuki Tsuda, Hirokazu Takenouchi, Akira Hirano, Takashi Kurokawa, Katsunari Okamoto, "Performance Analysis of a Dispersion Compensator Using Arrayed Waveguide Gratings", Journal of Lightwave Technology, Vol. 18, No. 8, Aug. 2000.
- [30] Sumetsky, M.; Litchinitser, N.M.; Westbrook, P.S.; Reyes, P.I.; Eggleton, B.J.; Li, Y.; Deshmukh, R.; Soccolich, C.; Rosca, F.; Bennike, J.; Liu, F.; Dey, S., "High-performance 40 Gbit/s fibre Bragg grating tunable dispersion compensator fabricated using group delay ripple correction technique," Electronics Letters , vol.39, no.16, pp.1196,1198, 7 Aug. 2003.
- [31] Xiang Lu, Linn F. Mollenauer, Xing Wei, "Impact of group-delay ripple in transmission systems including phase-modulate formats", Photonics Technology Letters, Vol. 16, No. 1. Jan. 2004.
- [32] A. Rahim et al., "Terabit Optical OFDM demultiplexer in Silicon Photonics", in Optical Fiber Communication Conference/National Fiber Optic Engineers Conference 2013, OSA Technical Digest (online) (Optical Society of America, 2013), paper JTh2A.28.

3.

Parallel-Serial filter for Residual Dispersion Compensation

Finite Impulse Response (FIR) and Infinite Impulse Response (IIR) are the two distinct types of optical filters. The architecture of the proposed Tunable Residual Dispersion Compensating (TRDC) filter proposed in the scope of this work allows the propagation of the chromatically dispersed optical signal only in the forward direction. Therefore, it belongs to the FIR class (finite number of terms that contributes to the impulse response of the filter). In this chapter, a fundamental theoretical description of a classical FIR filter is revisited. Later on, this is extended to give a theoretical account of the proposed Tunable Residual Dispersion Compensating Filter, which is elaborated by the ideal model for the proposed filter architecture.

3.1. Fundamentals of Optical Filters

Before dealing with FIR filters, some basic concepts of the filter theory are mentioned. Figure 3.1 shows the black box representation of an optical filter. Eq. (3.1) relates the transfer function $H(z)$ to the output $Y(z)$ and input $X(z)$ of an optical filter.

$$H(z) = \frac{Y(z)}{X(z)} \quad (3.1)$$

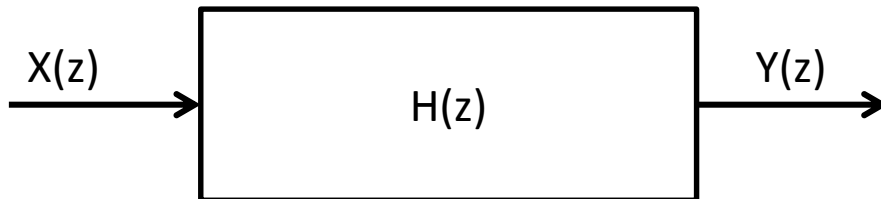


Figure 3. 1: Black box representation of an optical filter.

Certain architectures for the filter are employed depending on the application of the filter. Broadly, any filter architecture belongs to one of the two fundamental categories, namely the FIR or IIR architecture. An FIR filter is also sometimes referred as a Moving Average (MA) or no-pole filter and the IIR filter as Auto Regressive (AR) filter. The FIR filter comprises only the feed forward paths. This is not the case with IIR filter, which has a feedback loop. Figure 3.2 shows the block level representation of delay line based single stage FIR and IIR filter. The terms a_0, a_1 are the filter coefficients and Γ is the gain

coefficient and cannot be larger than 1 for passive optical filters. z^{-1} is the z-domain representation of a delay line (this concept will be explained further in section 3.2).

The definition of FIR and IIR filter mentioned here is more architectural. An analytical definition of the FIR and IIR filter is mentioned next.

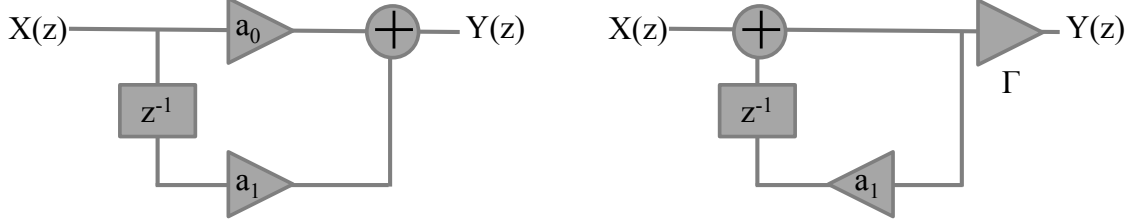


Figure 3. 2: Block level representation of a single stage FIR(left) and a single stage IIR(right) filter.

By treating the optical filter as a lossless discrete linear system with a discrete input signal [1], the transfer function of a filter can be expressed in terms of its complex roots as follows:

$$H(z) = \frac{\prod_{k=1}^K (1 - z_m \cdot z^{-1})}{\prod_{p=1}^P (z - p_n \cdot z^{-1})} \quad (3.2)$$

In (3.2), the roots in the numerator z_m are called the zeros and the roots in the denominator p_n are the poles of the transfer function $H(z)$. Unlike electrical filters, the optical filters have complex values for the poles and the zeros [17] and are equivalently written as:

$$\begin{aligned} z_k &= \rho_k \cdot e^{j\psi_k} \\ p_p &= \rho_p \cdot e^{j\psi_p} \end{aligned} \quad (3.3)$$

where ρ_k and ρ_p are the magnitude of the k^{th} zero and p^{th} pole of the filter. Similarly ψ_k and ψ_p is the phase of the k^{th} zero and p^{th} pole of the filter respectively. If the transfer function of a filter involves poles then it belongs to the IIR filter category. A filter whose transfer function is expressed in terms of zeros only is an FIR filter. Consequently, the generalized transfer function of an FIR filter with K -zeros is expressed as:

$$H(z) = \prod_{k=1}^K (1 - z_m \cdot z^{-1}) \quad (3.4)$$

Both FIR and IIR filters can be described in terms of their zeros and poles respectively. The poles and zeros determine the behavior of the filter which includes the magnitude

$|H(z)|$ and phase response $\varphi = \tan^{-1} \left[\frac{\text{Imag}(H(z))}{\text{Real}(H(z))} \right]$ of the filter. The negative derivative

with respect to the angular frequency ω determines the group delay τ of the filter.

$$\tau = -\frac{d}{d\omega}(\varphi) \quad (3.5)$$

For any filter to perform a certain signal processing functionality, it must deliver a certain magnitude and phase response. For example, a bandpass filter must have a small insertion loss and linear phase in the pass band. On the other hand, a dispersion compensating filter needs to have a certain dispersion value (quadratic phase function) that can mitigate the dispersion accumulated over the transmission length of the fiber (see figure 1.6).

As mentioned in chapter 2, the optical implementations of filters are limited not only to the free space or fiber optics, but integrated implementations of optical filters are getting lot of attention for various signal processing applications due to their compact size. In the scope of this work, the focus is laid on the implementation of an integrated FIR filter for residual dispersion compensation (see section 2.4) in high speed optical communication systems using a new and versatile parallel-serial filter approach (described in section 2.4). As explained in section 1.5 and elaborated in figure 1.6, the dispersion compensating filter is required to have a periodic all-pass transmission response with a constant dispersion D ($D \sim \frac{d}{d\omega}(\tau)$) for a certain fraction of the filter FSR .

3.2. 2-Port MZI as an FIR Filter

In order to explain the principle and basic concepts related to an FIR filter, we consider the example of an asymmetric 2-port MZI in integrated optics, which is the simplest possible FIR filter. Schematically it is shown in figure 3.3.

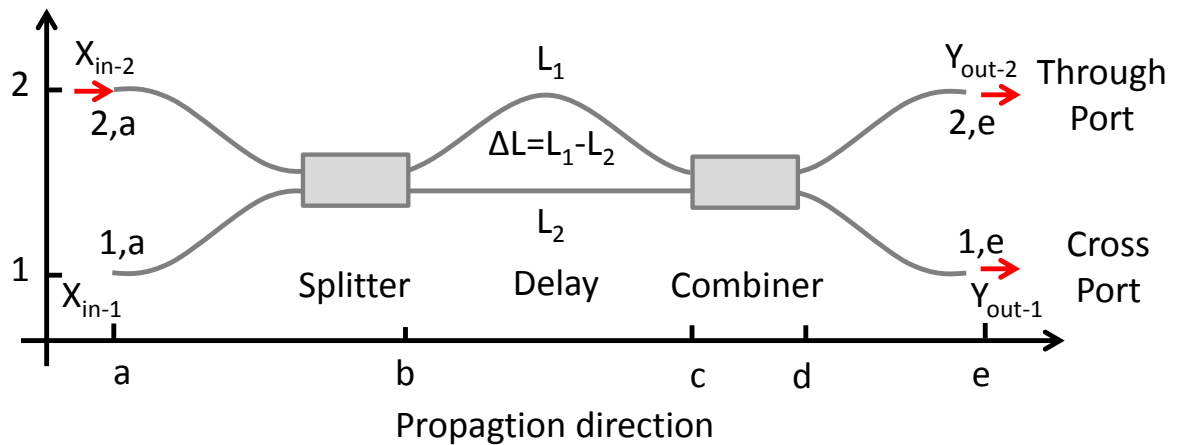


Figure 3. 3: 2-port MZI as a simple FIR filter

An asymmetric MZI is composed of two couplers, which are connected by a pair of waveguides. For the MZI shown in figure 3.3, the input signal is applied at one of input ports of the first coupler (left side of figure 3.3). In this case it is applied at the second port (2,a) of the first coupler. The first port (1,a) is idle. The couplers are connected by two waveguides with lengths L_1 and L_2 respectively. The term asymmetric refers to the unequal waveguide lengths connecting the two couplers. The relative length difference of the two waveguides is:

$$\Delta L = L_1 - L_2 \quad (3.6)$$

The waveguides connecting the two couplers are referred as delay lines due to the difference in the propagation length ΔL . The couplers can be directional couplers based on the overlapping of evanescent field from one waveguide to the core of the other waveguide [2] or Multimode Interference (MMI) couplers (see chapter 4 for more detailed description of MMI couplers), which are based on the principle of self-imaging [3]. At this moment, it is assumed that the two couplers do not introduce any additional phase shift. The amplitude of the input signal at the input port (2,a) of the first coupler is split in two parts. Therefore, the first coupler is referred as splitter. The two parts travel along the delay lines. The phase of the signal traveling along the two waveguides is given by:

$$\begin{aligned} \phi_1 &= \beta \cdot L_1 \\ \phi_2 &= \beta \cdot L_2 \end{aligned} \quad (3.7)$$

Assuming that the delay lines are dispersive ($n_g = \bar{n} + \omega \left(\frac{d\bar{n}}{d\omega} \right)$) then the differential phase $\Delta\phi$ for the two signals traveling along the delay lines will consequently be given by:

$$\Delta\phi = \beta \cdot \Delta L = \bar{n} \cdot k \cdot \Delta L = \bar{n} \cdot \frac{2\pi}{\lambda} \cdot \Delta L \quad (3.8)$$

For a dispersive delay line, $\Delta\phi$ becomes:

$$\Delta\phi(\omega) = n_g \cdot \frac{\omega}{c} \cdot \Delta L = \omega \cdot \Delta\tau(\omega) \quad (3.9)$$

The above equation shows that the relative phase difference $\Delta\phi$ between the two signals traveling along the delay lines is frequency dependent. Also the group delay $\Delta\tau(\omega) = \frac{d}{d\omega}(\Delta\phi(\omega)) = n_g(\omega) \cdot \frac{\Delta L}{c}$ introduced by the delay lines is frequency dependent due to the dispersive nature of the delay lines. The two signals travelling along the delay lines are recombined in the second coupler, which is referred as combiner in figure 3.3.

Assuming that the through- and cross-port transmission for the splitter and coupler is given by the coefficients a and b respectively. The resulting transfer matrix for them can be written as follows:

$$[S_s] = \begin{pmatrix} a_s & b_s \\ b_s & a_s \end{pmatrix} \text{ and } [S_c] = \begin{pmatrix} a_c & b_c \\ b_c & a_c \end{pmatrix},$$

where $[S_s]$ and $[S_c]$ refer to the transfer matrix for the splitter and the combiner respectively. The sub-scripts s and c refer to the splitter and the combiner.

As explained earlier, a delay line only produces a relative phase shift. Therefore, the transfer matrix for a lossless delay line can be represented as:

$$[S_{DL}] = \begin{bmatrix} e^{-j\Delta\phi(\omega)} & 0 \\ 0 & 1 \end{bmatrix} \quad (3.10)$$

The term $e^{-j\Delta\phi(\omega)}$ corresponds to the relative phase shift added by the delay length ΔL .

By using the definition of z-transform ($z = e^{j\Delta\phi}$), the transfer matrix for an ideal lossless delay line is given as:

$$[S_{DL}] = \begin{bmatrix} z^{-1} & 0 \\ 0 & 1 \end{bmatrix} \quad (3.11)$$

The transfer matrix $[H_{MZI}]$ for the 2-port MZI of figure 3.2 can be obtained by the multiplication of the transfer matrix of the combiner, delay line and the splitter (Transfer matrix method).

$$[H_{MZI}] = S_c \cdot S_{DL} \cdot S_s = \begin{bmatrix} a_s a_c z^{-1} + b_s b_c & a_s b_c z^{-1} + b_s a_c \\ b_s a_c z^{-1} + a_s b_c & b_s b_c z^{-1} + a_s a_c \end{bmatrix} \quad (3.12)$$

Each element $H_{MZI}^{i,o}$ of the transfer matrix $[H_{MZI}]$ represents the transfer function of the 2-port MZI for an input at port i and output port o . The transfer function $H_{MZI}^{i,o}$ is a polynomial of the form:

$$H_{MZI}^{i,o} = A + B \cdot z^{-1}, \quad (3.13)$$

where the coefficients A and B are the product of the elements from the combiner and the splitter scattering matrices. Moreover, $H_{MZI}^{i,o}$ is a polynomial of first order and hence has a single zero of the form $z=B/A$. Therefore, a 2-port asymmetrical MZI is also called as a single zero FIR filter and is considered as the simplest possible FIR filter. A z-domain functional equivalent of the 2-port MZI is shown in figure 3.4.

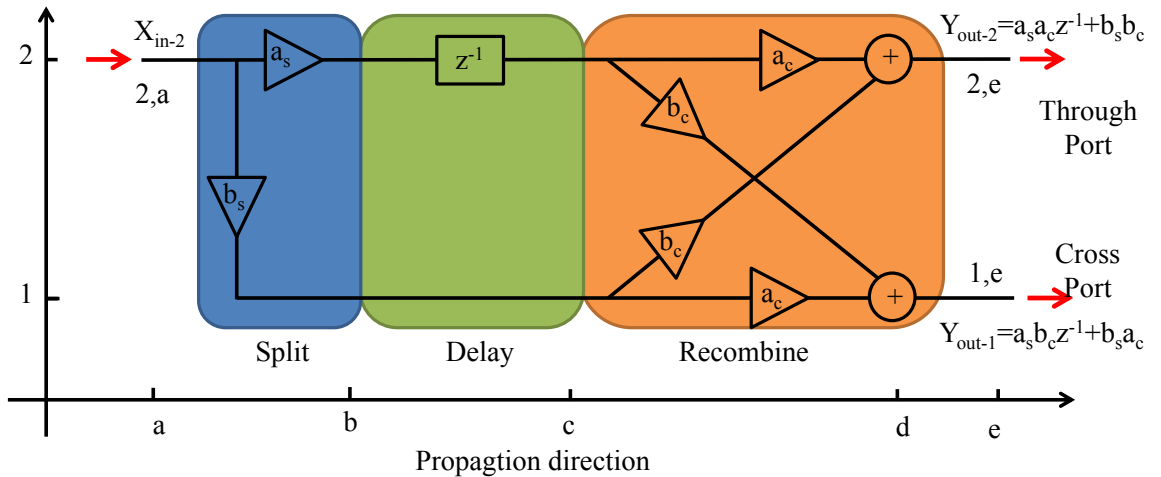


Figure 3.4: z-domain equivalent of a 2-port MZI

The recombination of the two signals in the combiner will lead to interference if the two signals have the same frequency, same polarization and retain the temporal coherence over the longest delay line. Relative phase of the recombining signals determine if the interference will be constructive or destructive. The resulting frequency response of the filter is periodic due to frequency dependence of the phase. The periodic response of the filter is referred as the Free Spectral Range (*FSR*) and is given by [19]:

$$FSR = \frac{1}{\Delta\tau} = \frac{c}{n_g \cdot \Delta L} \quad (3.14)$$

where c is the velocity of light in vacuum and n_g is the group index as defined earlier in equation (1.9).

To elaborate further, consider the example of a 2-port MZI comprising two MMI couplers and delay lines. The principle of the MMI will be dealt in chapter 4. Two identical and ideal MMI couplers with equal splitting and loss less delay lines are assumed. The transfer matrix of a lossless 3dB (2-port) MMI coupler is given by:

$$[S_s] = \begin{pmatrix} a_s & b_s \\ b_s & a_s \end{pmatrix} = \frac{1}{\sqrt{2}} \cdot \begin{pmatrix} 1 & j \\ j & 1 \end{pmatrix} = [S_c] \quad (3.15)$$

It is evident from the transfer matrix for the 2-port MMI couplers (equation 3.15) that the cross-port transmission has a 90° relative phase shift between the through- and cross-port, which is contrary to the discussion earlier.

By using equation (3.11) and (3.15), the overall transfer matrix for a 2-port MZI comprising MMI couplers and a lossless delay lines is given by:

$$[H_{MZI}(z)] = \begin{bmatrix} H_{MZI}^{1,1} & H_{MZI}^{2,1} \\ H_{MZI}^{1,2} & H_{MZI}^{2,2} \end{bmatrix} = \begin{bmatrix} z^{-1} - 1 & j(z^{-1} + 1) \\ j(z^{-1} + 1) & -z^{-1} + 1 \end{bmatrix} \quad (3.16)$$

For this special case of identical ideal 3-dB couplers with $|a_s| = |b_s| = \frac{1}{\sqrt{2}}$, the zeros for the diagonal (through ports) and off-diagonal (cross-ports) components of the transfer matrix $[H_{MZI}]$ lie on the unit circle of the pole-zero diagram, which is a standard way to represent the position of poles and zeros for a filter. Figure 3.5 shows the magnitude ρ and phase ψ for the through- and cross-port zeros.

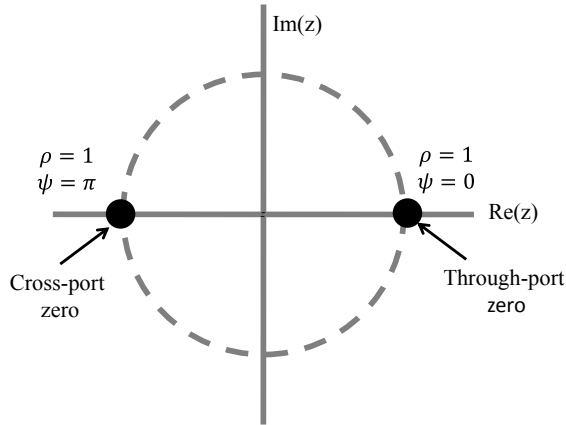


Figure 3.5: Position of through- and cross- port zeros for a 2-port MZI comprising ideal equal splitting 2-port MMI couplers

In reality, the couplers and the delay lines are not ideal. Waveguides have losses and the couplers have deviation from the ideal splitting ratios (imbalance in magnitude and phase) and excess loss (see chapter 4 for more details about imbalance, phase errors and excess loss in MMI couplers). These deviations are not desired and originate from the imperfections in the fabrication process (details about fabrication process are in chapter 4). On the other hand, sometimes the characteristics of the components comprising an integrated filter (i.e. delay lines and MMI couplers in this case) are intentionally modified to deliver a filter with desired filter transfer function. For example, consider a case in which the input MMI coupler (splitter) and the output MMI coupler (combiner) of the 2-port MZI has coupling coefficients that are different (see equation 3.17) from the ideal coefficients shown in equation (3.15).

$$[S_s] = [S_c] = \begin{pmatrix} a_s & b_s \\ b_s & a_s \end{pmatrix} = \begin{pmatrix} 0.67 & 0.74j \\ 0.72j & 0.69 \end{pmatrix} \quad (3.17)$$

The unequal splitting performed by the splitter modifies the transfer matrix of the 2-port MZI and the zeros are no longer located on the unit circle (see figure 3.6). ρ and ψ denote the magnitude and phase of the through- and cross-port zeros.

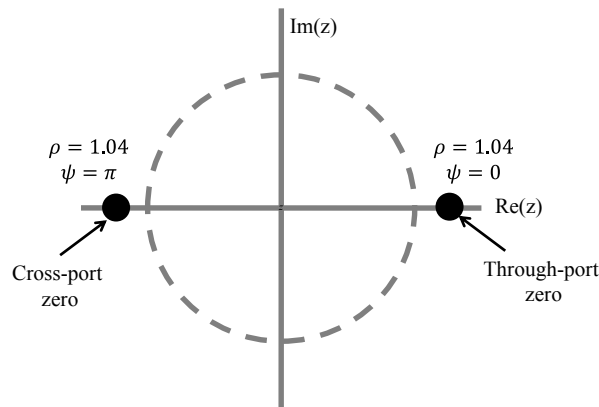


Figure 3.6: Position of through- and cross- port zeros for a 2-port MZI comprising 2-port MMI couplers with splitter with unequal coupling coefficients

Figure 3.7 shows the through- and cross-port transmission and dispersion (wavelength derivative of group delay is dispersion and group delay is the negative wavelength derivative of filter phase) of a 2-port MZI comprising an equal splitting ratio combiner, splitter with unequal splitting ratios and lossless waveguides. Since the focus of this work is on the implementation of a novel integrated dispersion compensator, therefore, dispersion is shown instead of phase for consistency of discussion. The MZI shows a periodic response ($FSR = 100$ GHz). The through- and cross-port show orthogonal transmission. A 2-port MZI is a single zero filter and the dispersion response is equivalent to the dispersion response of a single zero. Like transmission, the dispersion is also periodic ($FSR = 100$ GHz). In section 3.3 a more detailed investigation of the response and behavior of a single zero will be presented.

From the above example, one can understand that a change in the characteristics (for example, coupling coefficients of a coupler or additional phase shift on the delay lines) of the elements constituting an integrated optical FIR filter change the position of filter zeros. As a result the transmission and dispersion, which are determined by the filter zeros, can be adjusted to the desired response depending on the filter application. Similarly, an adaptively tunable filter transfer function is achievable by adaptively tuning the filter components (such as by using a tunable phase shift on delay lines or couplers with tunable coupling coefficients).

As explained earlier in this section, a 2-port asymmetrical MZI is the simplest possible delay line FIR filter. In its standalone form it finds application for simple filtering, demodulation and sensing of signals. On the other hand, its unity order is not sufficient to deliver transfer functions required to perform complex signal processing tasks such as dispersion compensation.

Higher order filters are desired for that. Such filters have been employed for various applications such as multiplexing and demultiplexing of WDM channels [4], OFDM demultiplexing [5], gain equalization for amplifiers [6], optical delay lines [7] and so on. The generalized transfer function $H(z)$ for the higher order FIR filters is already mentioned in equation (3.4).

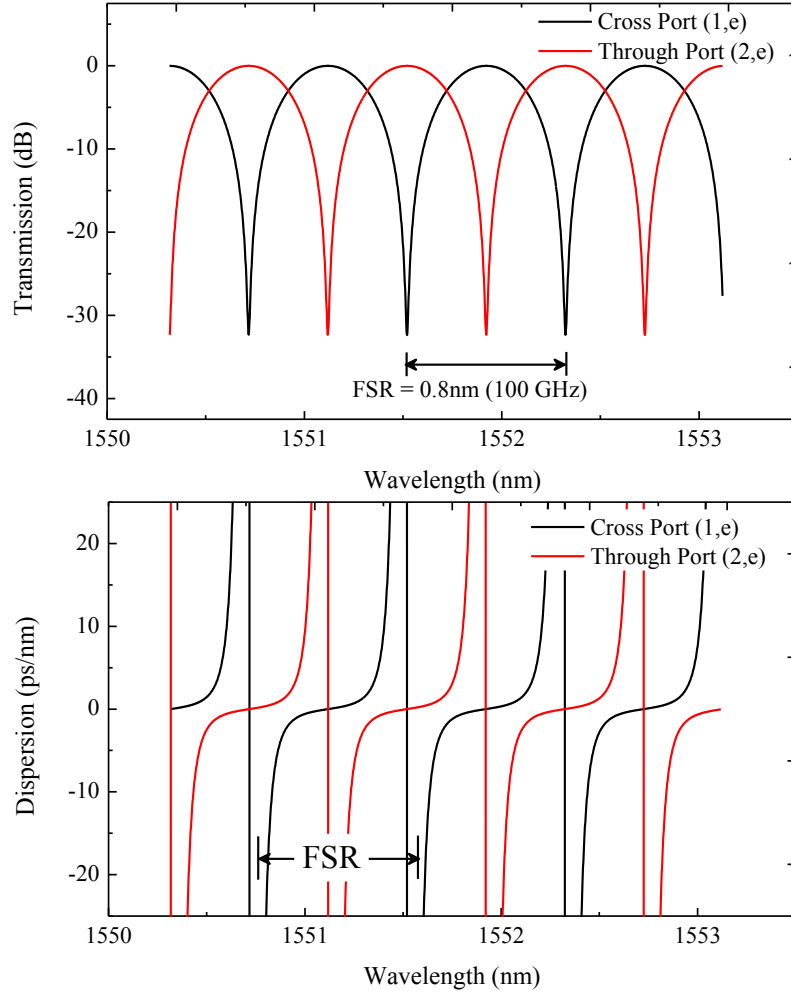


Figure 3.7: Transmission (top) and dispersion (middle) of a 2-port MZI comprising ideal 2-port MMI couplers but an amplitude imbalance of 0.02 dB on the delay lines.

3.3. Generalized Description of a Delay line FIR Filter for Residual Dispersion Compensation

A filter with constant dispersion is needed to compensate the chromatic dispersion of a fiber (see figure 1.6). The main attributes for a dispersion compensating filter have already been outlined in section 1.5.

If the normalized frequency Ω is given by (λ_c is the center wavelength):

$$\Omega = 2\pi \left[\frac{1}{FSR} \left(f - \frac{c}{\lambda_c} \right) + 0.5 \right] \quad (3.18)$$

then the normalized dispersion D_N is given by:

$$D_N = 2\pi \frac{d\tau_n(\Omega)}{d\Omega} = -D \cdot \frac{FSR^2 \cdot \lambda_c^2}{c} \quad (3.19)$$

where $\tau_N = \tau \cdot FSR$ is the normalized group delay, λ_c is the center wavelength and c is the speed of light.

It has been shown that the overall phase response of the filter is the superposition of the phase response of all the zeros of the filter. The phase response of the m^{th} zero is given by [18]:

$$\varphi_m(\Omega) = \arctan \left[\frac{\rho_m \cdot \sin(\Omega - \psi_m)}{1 - \rho_m \cdot \cos(\Omega - \psi_m)} \right] \quad (3.20)$$

The corresponding normalized group delay $\tau_{N,m}$ for the m^{th} zero is obtained by negative derivative of the phase $\varphi_m(\Omega)$ of the zero and is given by [18]:

$$\tau_{N,m} = -\frac{d}{d\Omega} \varphi_m(\Omega) = \left[\frac{\rho_m^2 - \rho_m \cos(\Omega - \psi_m)}{1 - 2\rho_m \cdot \cos(\Omega - \psi_m) + \rho_m^2} \right] \quad (3.21)$$

Dispersion is obtained by the derivative of the group velocity and the normalized value D_N for the m^{th} zero, given by [18]:

$$D_{N,m} = 2\pi \frac{d\tau_{N,m}}{d\Omega} = \frac{2\pi \cdot \rho_m (1 - \rho_m^2) \cdot \sin(\Omega - \psi_m)}{1 - 4\rho_m \cos(\Omega - \psi_m) + 4\rho_m^2 \cos(2\Omega - 2\psi_m) - 4\rho_m^3 \cos(\Omega - \psi_m) + \rho_m^4} \quad (3.22)$$

In the last section (section 3.2), the dispersion for a 2-port MZI has been shown, which has only one zero. The dispersion of a single zero is an odd function and has a saw tooth like shape and repeats for each FSR of the filter. This has been depicted in figure 3.8 where the black solid line shows the normalized dispersion for a single zero and the dotted black line shows the approximated saw tooth behavior of the zero. The dispersion response of a single zero has three distinct features [13,18]. They are the peak-to-peak (maximum) amplitude of the dispersion D_{max} , drop width w and the zero crossing along the wavelength axis for the dispersion value.

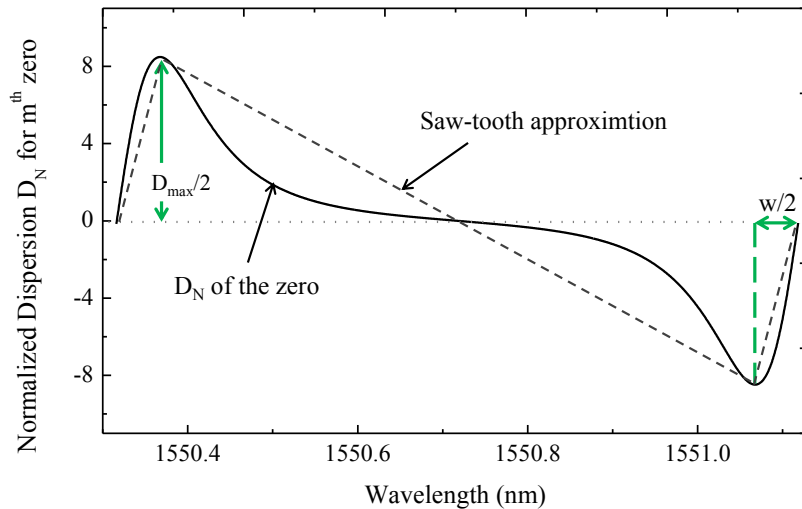


Figure 3.8: Normalized dispersion of a single zero with an arbitrary magnitude ρ and phase ψ .

D_{max} and the frequency for the zero crossing $\Omega(D_N=0)$ for a single zero are given by [18]:

$$D_{max} = \pi(\rho_m^4 - 1) \cdot \left[\frac{\sqrt{2(s-1) + (s-10)\rho_m^2 - \rho_m^4}}{3s-5 + (3s-26)\rho_m^2 - 5\rho_m^4} \right] D \quad (3.23)$$

where $s = \sqrt{\rho_m^4 + 34\rho_m^4 + 1}$ and $\Omega(D_N) = \varphi_m$

It is clear from equation (3.23) that a change in the magnitude of the zero ρ changes the peak dispersion value $D_{max}/2$ and the drop width w for the zero. The peak values show an inversion for the magnitude values smaller and larger than 1. Figure 3.9 shows the change in the maximum value of dispersion for different values of the magnitude ρ of the zero. Similarly, the zero crossing of the dispersion for a zero is affected by the phase ψ of the zero, as shown in figure 3.10.

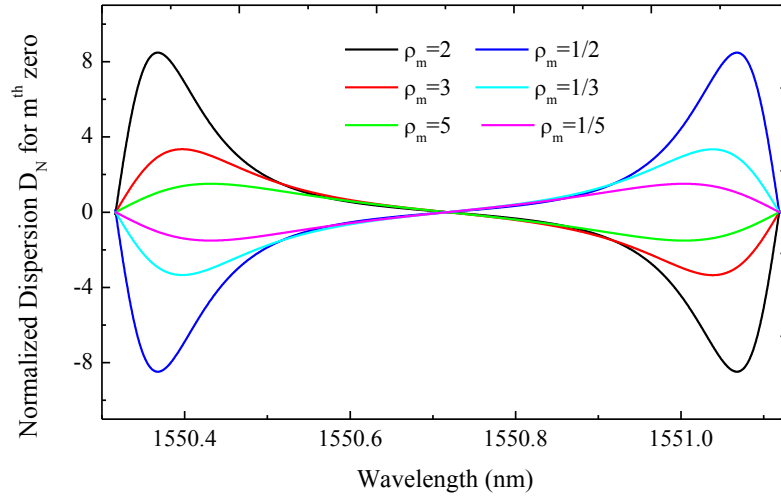


Figure 3.9: Influence of magnitude ρ_m of m^{th} zero on the normalized dispersion D_N (phase $\psi_m=0$)

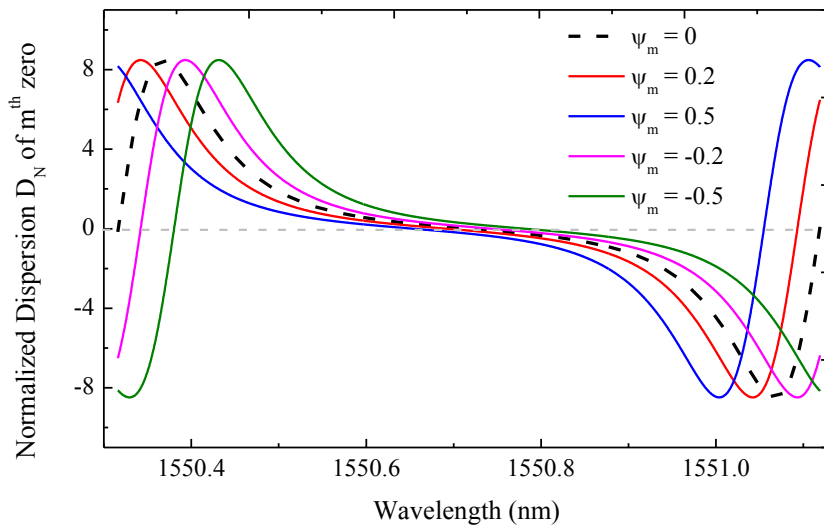


Figure 3.10: Influence of phase ψ_m of m^{th} zero on the normalized dispersion D_N (magnitude $\rho_m=2$)

Due to complex nature of filter zeros, each zero has two Degrees-of-Freedom (DoF) associated with the magnitude ρ and phase ψ of the zero. By moving the zero in the complex plane, it is possible to adopt the behavior of the filter to the desired transfer function. For example, in [18], a hypothetical scenario to implement a dispersion compensator using two zeros (z_1 and z_2) is presented. A dispersion compensator needs to have a constant dispersion for a fraction of the filter FSR (In literature, the fraction of filter FSR which has a constant value is also referred as Relative Bandwidth Utilized (RBWU). In this work the term useful bandwidth Δf and RBWU are used interchangeably). Two conditions must be fulfilled to accomplish that [20]:

- (a) The saw-tooth shaped dispersion for the two zeros have an even symmetry in the center of the filter FSR .
- (b) The dispersion for the two zeros is shifted by $\pm\pi \cdot (1 - RBWU)$ from each other along the FSR of the filter.

When these two conditions are fulfilled by adjusting the position of zeros on the complex plane then the dispersion for the two zeros result in a constant dispersion for a fraction of the filter FSR , as shown in figure 3.11. Condition (a) above requires that the two zeros for the hypothetical filter are related as shown in equation (3.24).

$$z_1 = \frac{1}{z_2} \quad (3.24)$$

The region with constant dispersion is the useful bandwidth of the dispersion compensator. It determines the bandwidth of the WDM channel over which the dispersion can be compensated. One can also observe from Figure 3.9 that the dispersion for the two zeros, which are reciprocal to each other, will have a cumulative zero average value over the FSR (see (3.25)). Therefore, it is possible to only have a fraction of filter FSR with constant non-zero dispersion. Moreover, the RBWU (or useful bandwidth Δf) of a filter can be increased by comprising the maximum achievable dispersion. More discussion about this compromise will be discussed in the next sections (see section 3.9).

$$\int_0^{FSR} (\sum_{m=0}^M D_m) d\Omega = 0 \quad (3.25)$$

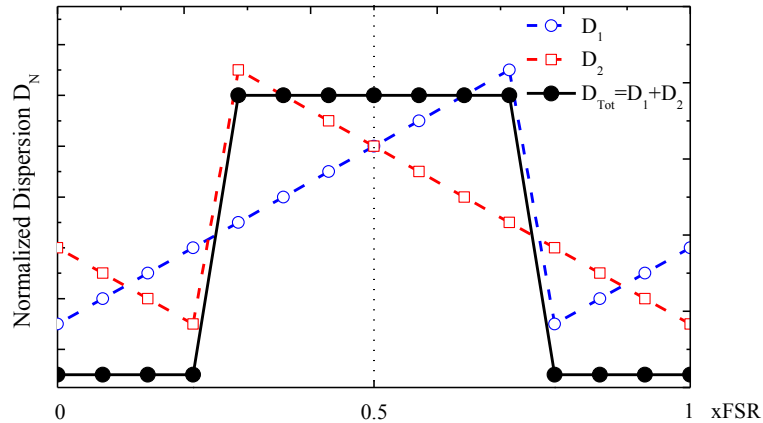


Figure 3.11: Superposition of normalized dispersion of two hypothetical zeros to deliver constant dispersion

3.4. Higher Order FIR Filters for Residual Dispersion Compensation

The discussion in the section 3.3 gave a very simplistic view to synthesize a dispersion compensating filter. In section 1.5, the key performance parameters of any dispersion compensating filter are its bandwidth for which it has constant dispersion (RBWU or useful bandwidth Δf), periodicity for compensating dispersion of multiple WDM channels, group delay ripple, maximum achievable dispersion and dispersion tuning to dynamically adapt to variation in residual dispersion. As mentioned in section 3.2, higher order delay line FIR filters are highly desirable to fulfill the requirements of a complex signal processing task such as a dispersion compensator.

For a given order R of the filter, a compromise exists between the maximum achievable dispersion, useful bandwidth Δf (or RBWU) and group delay ripple GDR of the filter. A filter can generate larger dispersion values by compromising the RBWU and flatness of the dispersion curve (increase group delay ripple), which results in increased OSNR penalty for the system [9]. Treating the RBWU and group delay ripple as the benchmark for a filter performance, then the maximum achievable dispersion D_{max} from the filter depends on the order R of the filter. Limiting the GDR to small values with enhanced RBWU (larger Δf) for a dispersion compensating filter, the maximum attainable dispersion value can be increased with an increase in the order R of the filter. In order to have a linear group delay for 40 % of the filter FSR and a group delay ripple of less than ± 3 ps. Figure 3.12 shows the relationship of the achievable filter dispersion and the order R of the filter [10]. Each stage N of the filter comprises a 3rd order FIR filter with a maximum delay of $\tau=30$ ps. So $N=2$ corresponds to $R=6$.

One benchmark of the filters for residual dispersion compensation is $D_{max} \cdot (\Delta f)^2$ where D_{max} is the maximum achievable dispersion and Δf is the bandwidth of filter. For a given group delay ripple, a compromise exists between D_{max} and Δf for residual dispersion compensator of certain order R . More discussion about this compromise is mentioned in section 3.9. From figure 3.12, it is evident that a higher order R is desired to achieve larger D_{max} without compromising the useful bandwidth Δf or maximum group delay ripple of a residual dispersion compensator. In appendix II, the relationship between the filter order R and the maximum achievable dispersion D_{max} is presented.

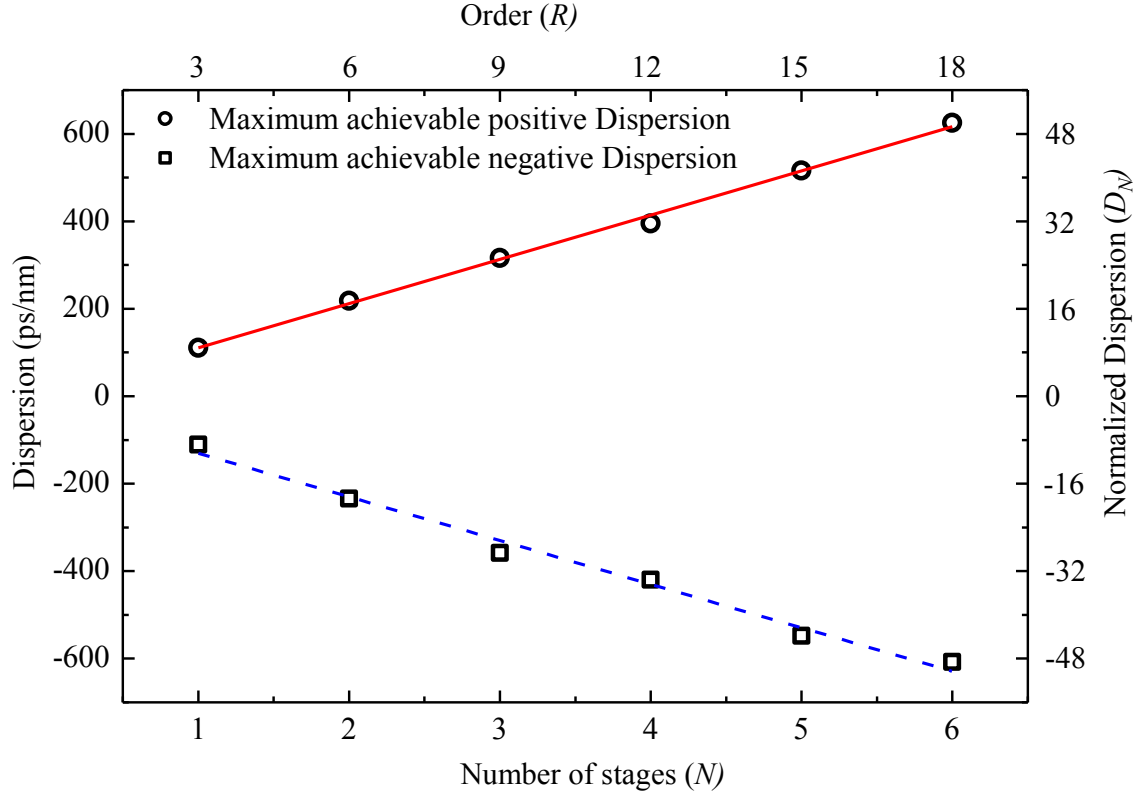


Figure 3.12: Relationship of maximum achievable dispersion D_{max} for group delay ripple < 3 ps and useful bandwidth Δf (RBWU) > 40 GHz for a filter with N number of stages and $FSR = 100$ GHz (see appendix II).

3.5. Parallel-Serial Filter Approach for Residual Dispersion Compensation

As mentioned in section 3.4, higher order FIR filters are highly desirable to deliver residual dispersion compensating filters with good performance. The two most renowned approaches to deliver higher order FIR filters for dispersion compensation are the lattice filters [11] and the AWG based filters with a thermal lens [12]. The main principle of both approaches has already been described in section 2.1.3.1 and 2.1.3.2, respectively. The order R of the lattice filter is increased by cascading more and more asymmetrical MZIs, which comprises delay lines and tunable couplers. In other words the lattice filter scales serially. The terms serial filter and lattice filter attribute to the same architecture in this work and both terms are used interchangeably.

The other approach of AWGs (section 2.1.3.2) uses an increase in the number of grating arms. This enhances the parallel processing of the optical signal to supplement the order of the filter by resolving the input signal into larger number of spectral components. Therefore the approach is referred as parallel in this work. The pro and cons for both approaches are already highlighted in chapter 1. In terms of scalability, both approaches are limited to only one dimension which is either serial or parallel to enhance the order of the filter. This puts a limit on the scalability of the filter architecture.

To overcome the limitation of both approaches (section 2.3), a new filter approach is presented, which is the main highlight of this work. Due to its architecture, it is termed as the Parallel-Serial filter. The name attributes to the fact that the filter has parallel processing units, which are cascaded to each other in series and is, hence, referred as the Parallel-Serial Filter architecture. Figure 3.13 shows the generalized schematic of the Parallel-Serial filter architecture.

Parallel-Serial filters consist of higher order MMI couplers. Unlike lattice filters, where the unit cell of the filter is a two port MZI, the unit cell of a Parallel-Serial filter is a generalized MZI. The dotted region in figure 3.13 depicts a unit cell of the Parallel-Serial filter. Each unit cell comprises two $M \times M$ MMI couplers, where M is the number of input/output port of the MMI coupler (order of the MMI coupler). The higher order MMI couplers are connected to each other by delay lines with unit delay τ , which determines the FSR of the filter. The maximum delay from a unit cell equals $(M-1)\tau$. The MMI couplers can have static coupling coefficients or they can be tunable (more details in section 3.9). As explained in section 3.3, a filter can be adjusted to a desired transfer function by adopting the magnitude ρ and phase ψ of the zeros. This is possible by using tunable MMI couplers in the unit cell and by embedding phase shifting elements $\Delta\phi_{x,y}$ on the delay lines. The coefficients x,y correspond to the filter stage N and the time delay produced by the delay line respectively. For example, $\Delta\phi_{2,3}$ implies to the phase element in the second stage on the 3rd delay line. Since it is enough to change the relative phase difference between the delay lines, therefore phase shifting elements on only $(M-1)$ delay lines are sufficient.

The first MMI coupler of the unit cell of the Parallel-Serial filter performs the splitting of the incoming chromatically dispersed optical signal. Each component is delayed by the delay lines and an additional phase shift on the delay lines acts as a weight function. The delayed and the weighed components are recombined in the second MMI coupler.

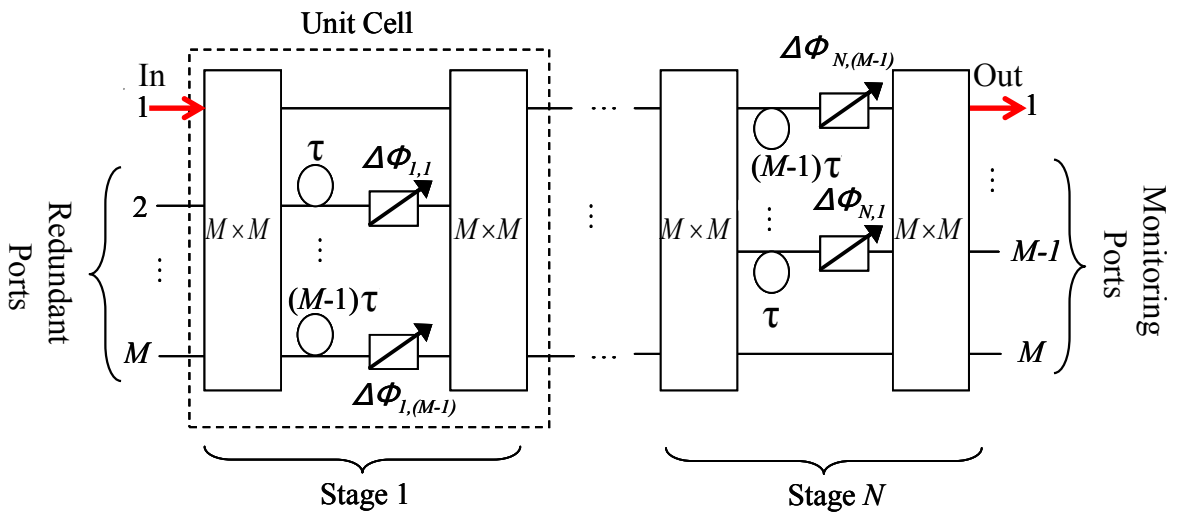


Figure 3.13: Generalized layout of an N stage parallel-serial filter of order $R = N(M - 1)$ using M -port couplers

A unit cell corresponds to a single stage of the Parallel-Serial filter. The transfer matrix for the unit cell $[H_{unitcell}]$ of the Parallel Serial filter comprising $M \times M$ MMI couplers is obtained by the multiplication of the transfer matrices for the two MMI couplers $[S_{MMI}]$ comprising the unit cell, transfer matrix for the delay lines $[S_{DL}]$, transfer matrix for the additional phase shifters embedded on the delay lines $[S_\phi]$.

$$[H_{unitcell}(z)] = [S_{MMI-2}] \cdot [S_{DL}] \cdot [S_\phi] \cdot [S_{MMI-1}] \quad (3.26)$$

$[S_{MMI-1}]$ and $[S_{MMI-2}]$ correspond to the transfer matrix for the first and the second MMI coupler of the unit cell respectively. The transfer matrices for the $M \times M$ MMI couplers are of the form:

$$[S_{MMI}] = \begin{bmatrix} s_{11} & \cdots & s_{1M} \\ \vdots & \ddots & \vdots \\ s_{M1} & \cdots & s_{MM} \end{bmatrix} \quad (3.27)$$

where $s_{ij} = |s_{ij}| \cdot e^{j\phi_{ij}}$ is the coupling coefficient of the MMI coupler. The subscripts i and j denote the input and output port of the MMI coupler and $j = \sqrt{-1}$.

Assume that the M delay lines connecting the MMI couplers of the unit cell have a unity incremental delay τ . The maximum delay in the unit cell is $(M-1)\tau$. The transfer matrix for the delay lines and the phase shifting elements on the delay lines are given by:

$$S_{DL} = \begin{bmatrix} 1 & \cdots & 0 \\ \vdots & \ddots & \vdots \\ 0 & \cdots & z^{-(M-1)} \end{bmatrix} \quad (3.28)$$

$$S_\phi = \begin{bmatrix} 1 & \cdots & 0 \\ \vdots & \ddots & \vdots \\ 0 & \cdots & e^{-j\Phi_{M-1}} \end{bmatrix} \quad (3.29)$$

Cascading multiple unit cells will result in a higher order Parallel-Serial filter. The first MMI coupler of the first stage acts as a demultiplexer and the second MMI coupler of the last stage act as the multiplexer. The remaining MMI couplers and the delay lines act as a tunable delay line. An N stage Parallel-Serial filter results in a filter of order $R = N(M-1)$, and requires $\left\lceil \frac{R}{(M-1)} + 1 \right\rceil$ MMI couplers.

The generalized transfer matrix $[H_{PSF(R)}]$ for the parallel-serial filter of order $R = N(M-1)$ comprising N stages and $\left\lceil \frac{R}{(M-1)} + 1 \right\rceil$ number of MMI couplers of order M with total delay $\tau_t = N(M-1)\tau$ is given by $[H_{PSF(R)}]$.

$$[H_{PSF(R)}] = \left[S_{MMI-\left\lceil \frac{R}{(M-1)+1} \right\rceil} \right] \cdot \left[S_{\phi-\left\lceil \frac{R}{M-1} \right\rceil} \right] \cdot \left[S_{DL-\left\lceil \frac{R}{M-1} \right\rceil} \right] \cdots [S_{MMI-2}] \cdot [S_{\phi-1}] \cdot [S_{DL-1}] \cdot [S_{MMI-1}] \cdot \quad (3.30)$$

Although, the figure 3.13 shows an architecture with M inputs and M outputs but a dispersion compensating filter is a single input single output device. The extra input ports for the architecture shown in figure 3.13 provide redundancy and the extra output ports can be used for monitoring purpose [13].

$[H_{PSF(R)}]$ is an $M \times M$ matrix and its each element $H_{PSF(R)}^{i,o}$ is a transfer function for an input at port i (where $i=1$ to M) and output at port o (where $o=1$ to M) of the parallel-serial filter. $H_{PSF(R)}^{i,o}$ is a polynomial of order R with R zeros z_r (R solutions for the polynomial) and, as mentioned in section 3.1, can equivalently be expressed in terms of filter zeros as:

$$H_{PSF(R)}^{i,o} = \prod_{r=1}^R (1 - z_r \cdot z^{-1}) \quad (3.31)$$

3.6. Parallel-Serial Filter vs. AWG and Lattice Filter based Residual Dispersion Compensators

The Parallel-Serial filter architecture provides two Degree-of-Freedom (DoF) to enhance the order R of the filter. One possibility is to increase the order M of the MMI couplers, which results in an increased order R for the unit cell. The other possibility is to increase the number of stages N . This feature makes the Parallel Serial filter architecture more scalable as compared to the lattice or AWG based filters for dispersion compensation. The Parallel-Serial filter architecture requires reduced number of couplers as compared to lattice filters. Since the Parallel-Serial filter uses MMI couplers, the fabrication tolerance [14] of Parallel-Serial filter is better as compared to the AWG based filters. Apart from that, the AWG based filter requires a complex design for a thermal lens to tune the filter.

3.7. Choice of MMI Couplers for Parallel-Serial Filter

Attributes determining the performance of the parallel-serial filter, which include the maximum attainable dispersion, useful bandwidth and group delay ripple, are determined by the number of zeros (order of the filter). For a parallel-serial filter, there are two options to increase the number of zeros of the filter. One possibility is to increase the number of stages N of the parallel-serial filter and the other option is to increase the order M of the MMI couplers. The optimal choice depends on several aspects such as the size of the filter, the number of WDM channels for which the filter can compensate dispersion and the insertion loss for the filter. These factors bring an impact on the choice of the couplers to realize the parallel-serial filter.

If a filter is realized with couplers of lower order, the filter will become more and more serial. The size of the filter will be large and the insertion loss for the filter will be large due to overall larger waveguide lengths. The bandwidth of the MMI couplers is inversely influenced by the order of the MMI couplers [14] therefore a more serial filter is expected to compensate chromatic dispersion for more WDM channels.

Choosing higher order MMI couplers will bring parallelism to the filter. The resulting filter will have relatively shorter waveguide length and will bring the loss of the filter to smaller value. The wavelength dependence of the MMI coupler will reduce the total number of WDM channels for which the filter can compensate the residual dispersion for. Although, the MMIs are known for their high fabrication tolerance [14] but the tolerance reduces by increasing the order of the MMI couplers. A parallel-serial filter is expected to be more compact when implemented with higher order MMI couplers as compared to a more serial filter. Therefore, moving from a more serial to a more parallel parallel-serial filter brings a compromise between the loss, size, number of channel for which the filter can compensate dispersion. An analysis about how the filter performance is influenced by the performance of MMI coupler is left out to be discussed in one of the next chapters. Section 4.2 provides a discussion about the relationship between the order of the MMI couplers with excess loss, imbalance, phase errors and bandwidth of the MMI couplers.

3.8. 6th order Parallel-Serial FIR Filter with Static Couplers

To elaborate further, a 6th order parallel-serial FIR filter is presented in this section. It is assumed that the filter consist of two stages ($N=2$) and each stage consist of MMI couplers with $M=4$. A block level representation of the filter is shown in figure 3.14. It is composed of three symmetric 4×4 MMI couplers. The MMI couplers are connected by two sets of delay lines. In each set the delay lines have a time difference of $\tau = 10$ ps ($FSR = 100$ GHz). The filter has a total maximum delay $\tau_i = 60$ ps. Six phase tuning elements $\varphi_{1,1} \dots \varphi_{2,3}$ are embedded on the delay lines. Since, MMI couplers with static (fixed) coupling coefficients are used, therefore the phase shifting elements are used to manipulate the transfer function of the filter. In the case of a dispersion compensator, they are used to tune the filter for linear positive, zero or linear negative group delay slopes.

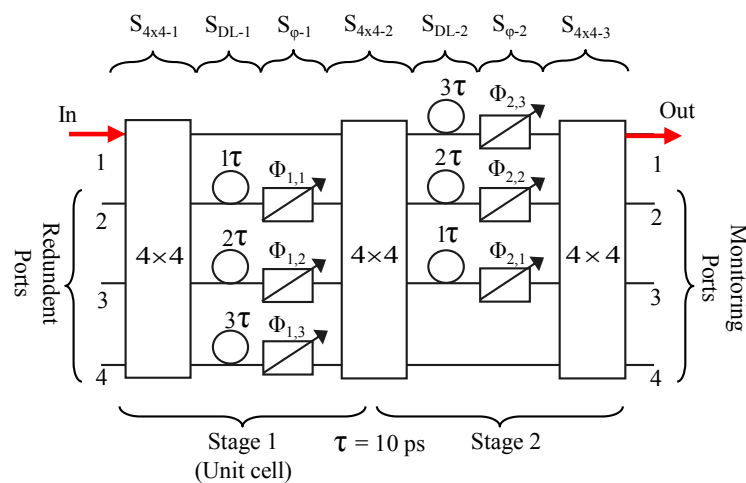


Figure 3.14: A 6th order parallel-serial filter comprising two stages ($N=2$) using 4-port MMI couplers and a unit delay $\tau = 10$ ps for $FSR = 100$ GHz

The unit cell for the 6th order parallel-serial filter shown in Figure 3.14 comprises a 4-port MZI.

Assume that the 6th order parallel-serial filter comprises ideal, identical and equal splitting MMI couplers with a transfer matrix of the form:

$$[S_{4 \times 4-1}] = [S_{4 \times 4-2}] = [S_{4 \times 4-3}] = 0.5 \begin{bmatrix} 1 & e^{j\frac{3\pi}{4}} & e^{j\frac{\pi}{4}} & 1 \\ e^{j\frac{3\pi}{4}} & 1 & 1 & e^{j\frac{\pi}{4}} \\ e^{j\frac{\pi}{4}} & 1 & 1 & e^{j\frac{3\pi}{4}} \\ 1 & e^{j\frac{\pi}{4}} & e^{j\frac{3\pi}{4}} & 1 \end{bmatrix} \quad (3.32)$$

The transfer matrix for the delay lines in the first stage S_{DL-1} and the delay lines in the second stage S_{DL-2} is given by:

$$[S_{DL-1}] = \begin{bmatrix} 1 & 0 & 0 & 0 \\ 0 & z^{-1} & 0 & 0 \\ 0 & 0 & z^{-2} & 0 \\ 0 & 0 & 0 & z^{-3} \end{bmatrix}, [S_{DL-2}] = \begin{bmatrix} z^{-3} & 0 & 0 & 0 \\ 0 & z^{-2} & 0 & 0 \\ 0 & 0 & z^{-1} & 0 \\ 0 & 0 & 0 & 0 \end{bmatrix}, \quad (3.33)$$

The transfer matrix for the phase shifting elements which are embedded on the delay lines in the first stage $S_{\Phi-1}$ and the transfer matrix for the ones which are embedded on the delay lines in the second stage $S_{\Phi-2}$ are of the form:

$$[S_{\Phi-1}] = \begin{bmatrix} 1 & 0 & 0 & 0 \\ 0 & \Phi_{1,1} & 0 & 0 \\ 0 & 0 & \Phi_{1,2} & 0 \\ 0 & 0 & 0 & \Phi_{1,3} \end{bmatrix} \text{ and } [S_{\Phi-2}] = \begin{bmatrix} \Phi_{2,3} & 0 & 0 & 0 \\ 0 & \Phi_{2,2} & 0 & 0 \\ 0 & 0 & \Phi_{2,1} & 0 \\ 0 & 0 & 0 & 1 \end{bmatrix} \quad (3.34)$$

The multiplication of the transfer matrices for the three MMI couplers (3.32), transfer matrix for the pair of delay lines connecting the MMI couplers (3.33) and the transfer matrix for the phase shifting elements on the delay lines (3.34) will result in the overall transfer matrix $H_{PSF(R=6)}$ for the 6th order ($R=6$) parallel-serial filter.

$$[H_{PSF(R=6)}] = [S_{4 \times 4-3}] \cdot [S_{\Phi-2}] \cdot [S_{DL-2}] \cdot [S_{4 \times 4-2}] \cdot [S_{\Phi-1}] \cdot [S_{DL-1}] \cdot [S_{4 \times 4-1}] \quad (3.35)$$

The subscripted 1, 2 and 3 in equation (3.34) correspond to the index of the MMI couplers, delay lines and phase shifting elements of stage 1 and stage 2 respectively.

$[H_{PSF(R=6)}]$ is a 4 x 4 matrix and its each element is a 6th order polynomial. The transfer function $H_{PSF(R=6)}^{i,o}$ for an input at port i ($i=1$ to 4) and output at port o ($o=1$ to 4) for the 6th order parallel-serial filter.

The equivalent transfer function $H_{PSF(R=6)}^{i,o}$ for input at port i and output at port o $H_{PSF(R=6)}$ in terms of filter zeros is given by:

$$H_{PSF(R=6)}^{i,o} = \prod_{m=1}^{m=6} (1 - z_m \cdot z^{-1}) \quad (3.36)$$

where z_m is the m^{th} zero of the filter, $z^{-1} = e^{-j\omega\tau}$ and $\tau=10\text{ps}$.

For the 6th order parallel-serial filter to deliver the transfer function required for dispersion compensation the six zeros have to satisfy the condition mentioned in equation (3.24) and the two conditions mentioned in section 3.3, which are highlighted by figure 3.11. By appropriately weighing the optical signal propagating on the delay lines using phase shifting elements, the six zeros of the filter satisfy (3.24) and are related as follows:

$$z_1 = \frac{1}{z_2}, \quad z_3 = \frac{1}{z_4}, \quad z_5 = \frac{1}{z_6} \quad (3.37)$$

As result of this relationship between zeros, the cumulative dispersion of three zeros provide a saw-tooth shaped dispersion with positive slope and the other three provide saw-tooth shaped dispersion with negative slope. With a shift of $\pm\pi \cdot (1 - RBWU)$ accomplished between these two saw-tooth shaped dispersion responses, a constant dispersion is delivered for a fraction of the FSR as explained in section 3.3 and depicted in figure 3.11. The relationship between zeros, which is given by equation (3.37), results in a symmetrical response (see figure 3.11) with respect to the filter FSR [15] for the dispersion compensator. The symmetry of the response is essential so that the filter response can be matched to the WDM grid so that the residual dispersion for all WDM channels can be mitigated at the same time. Equivalently, the generalized filter transfer function of a parallel-serial filter for residual dispersion compensation can be re-written as:

$$H_{PSF(R=6)}^{i,o} = \sum_{m=1}^{R/2} (1 - z_m \cdot z^{-1}) \cdot (1 - \frac{z^{-1}}{z_m}) \quad (3.38)$$

As already mentioned in section (3.3), each zero brings an independent group delay (dispersion) contribution to the overall group delay response of the filter. The group delay response for a single zero is computed by [18] and is given by:

$$\tau_m(\Omega) = T \cdot \left[\frac{\rho_m^2 - \rho_m \cos(\Omega - \psi_m)}{1 - 2\rho_m \cdot \cos(\Omega - \psi_m) + \rho_m^2} \right] \quad (3.39)$$

The overall group delay response from the 6th order parallel-serial filter is the superposition of all six group delay contributions from the six zeros of the filter and is given by:

$$\tau_t(\Omega) = \sum_{m=1}^6 \tau_m(\Omega) \quad (3.40)$$

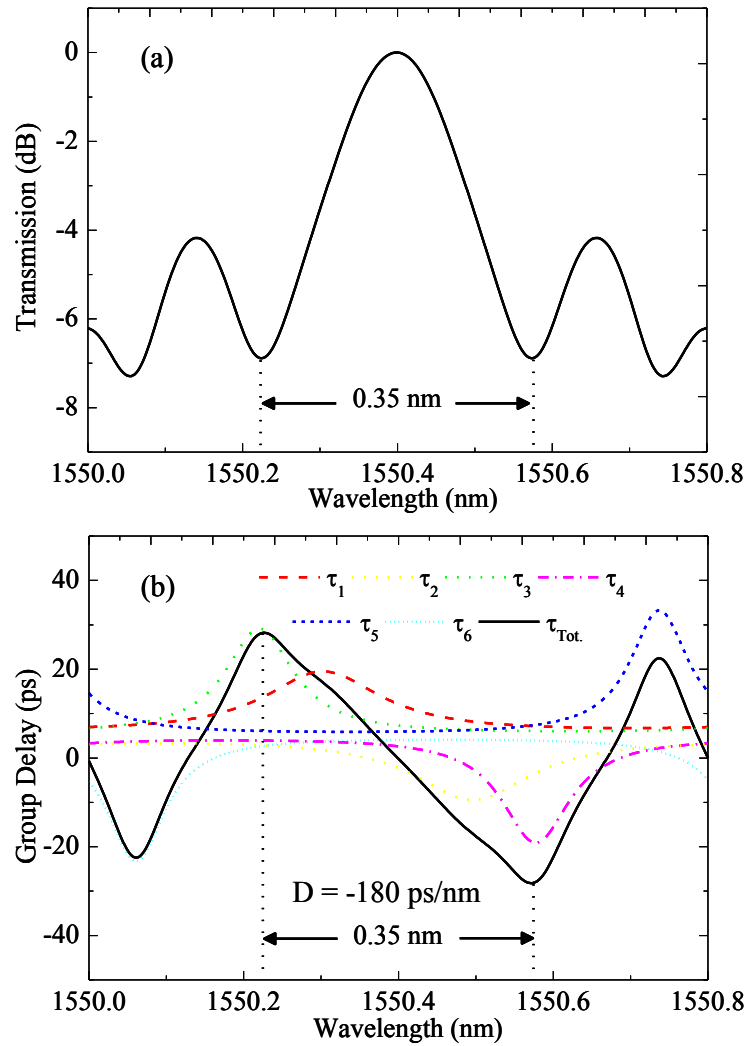


Figure 3.15: Transmission (top) and group delay (bottom) for the 6th order parallel-serial comprising ideal 4x4 MMI couplers and lossless delay lines for an $FSR = 100$ GHz

Assuming ideal and identical MMI couplers with a lossless filter structure, figure 3.15 shows the simulated transmission and group delay response for the 6th order parallel-serial filter structure shown in figure 3.14. The simulation is performed by using Transfer Matrix Method (TMM) by the project partners in Helmut-Schmidt University (Hamburg-Germany). The solid line shows the total group delay of the filter and the dotted lines show the group delay contributions from the individual zeros. Table 3.1 shows the values of the six zeros to achieve the transmission and group delay response shown in figure 3.15.

Table 3.1: Zeros of the 6th order parallel-serial filter to deliver the transmission and group delay response shown in figure 3.15

z_1	$0.083+j1.36$
z_2	$0.045-j0.73$
z_3	$-0.51+j1.56$
z_4	$-0.19-j0.58$
z_5	$-1.47+j1.33$
z_6	$-0.37-j0.34$

It is possible to tune the filter by changing the phase on the delay lines connecting the MMI couplers. The three phase shifting elements on the delay lines connecting MMI couplers of each stage are sufficient to bring a relative phase shift between the optical signals travelling along the delay lines. By appropriate adjustment of the phase on the delay lines, it is shown in the figure 3.16 that the positive group delay slope (black, solid) is changed to no (green, solid) and negative (red, solid) group delay slope.

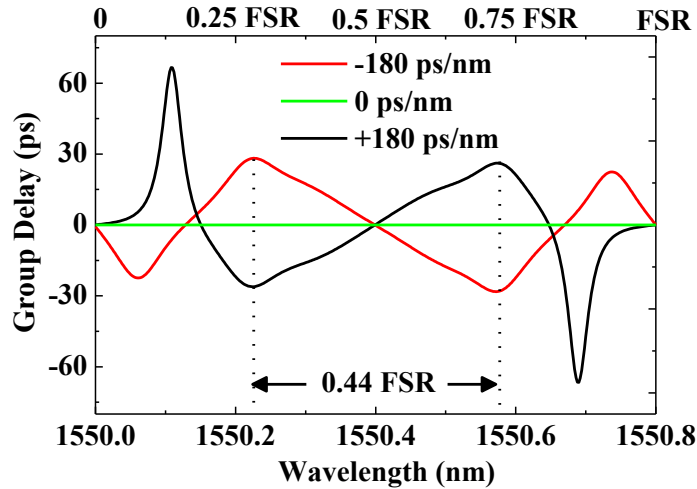


Figure 3.16: Parallel-serial filter tuned for negative (red), zero (green) and positive (black) dispersion. Simulation is performed using ideal MMI couplers and delay lines. Filter $FSR = 100$ GHz and group delay ripple is maintained below 3 ps.

The simulation results shown in figures (3.16) are for a filter with a unit delay $\tau = 10$ ps, which corresponds to an $FSR=100$ GHz. Each stage of the filter has a maximum delay of 30 ps and the total delay of filter is 60 ps. The positive and negative group delay slopes are linear for a bandwidth of ~ 44 GHz (0.35nm). For zero group delay slope (green, solid line in figure 3.16), the bandwidth is larger, which indicates that the filter's group delay bandwidth increases with a decrease in the group delay slope and vice versa. The positive, no and negative group delay slopes have shown a group delay ripple of < 3 ps. The simulation result has shown that the filter can compensate ± 180 ps/nm of residual

chromatic dispersion in an optical fiber. (Simulation results shown in figures (3.15) and (3.16) are in collaboration with Helmut-Schmidt University (Hamburg-Germany).

3.9. 6th Order Parallel Serial FIR Filter with Enhanced Tuning Range

The 6th order filter in section 3.5 comprising higher order ($M=4$) MMI couplers demonstrates the feasibility of parallel-serial filters for residual dispersion compensation. One limitation of that approach is the limited tuning range for the filter. Also, another drawback is the limited transmission bandwidth (6 dB transmission bandwidth of only 0.35 nm, see figure 3.15).

Both limitations are attributed to the MMI couplers with static (fixed) coupling coefficients. The 12 Degrees-of-Freedom (DoF) available from the six complex zeros of the filter with static MMI couplers (figure 3.14) cannot be placed at any arbitrary position in the complex z -plane by using only six phase shifting elements (which are embedded on the delay lines). This puts a limit on the possible number of transfer functions delivered by the parallel-serial filter and hence limits the performance of the filter in terms of transmission bandwidth, group delay bandwidth, group delay ripple and the tunable range for the filter.

The zeros can be placed at any arbitrary location in the z -plane by replacing the static MMI couplers with fixed coupling coefficients with tunable couplers. A tunable coupler is the one whose coefficients such as the splitting ratios can be adjusted to any arbitrary value. Symmetric generalized MZI with phase shifting elements is the most widely known technique to demonstrate a higher order tunable coupler [16]. A schematic representation of an $M \times M$ tunable coupler is shown in the figure 3.17. It comprises two MMI couplers which are connected by MZI arms with phase shifting elements. The weighing of the split input signal by the first MMI coupler before addition (recombination) in the second MMI coupler results in a tunable coupler with variable coupling coefficients. The principle of the tunable coupler can be explained from its transfer matrix, which is obtained by the multiplication of the transfer matrix for the two MMI couplers and the MZI arms with phase shifters.

$$S_{TunableCoupler} = S_{combiner} \cdot S_{MZI\ arms} \cdot S_{splitter}$$

where $T_{splitter}$ is the transfer matrix for the input MMI coupler, which acts as a splitter and $T_{combiner}$ is the transfer matrix for the output MMI coupler, which acts a combiner. The transfer matrices for the splitter and combiner is an $M \times M$ matrix of the form shown in equation (3.27) and with each element of the matrix is of the form $s_{ij} = |s_{ij}| \cdot e^{j\phi_{ij}}$, where i and j denote the input and output ports of the MMI coupler and bold $\mathbf{j} = \sqrt{-1}$. The transfer matrix for the phase shifters on the MZI arms $S_{MZI\ arms}$ is given by:

$$S_{MZI\ arms} = \begin{bmatrix} 1 & \dots & 0 \\ \vdots & \ddots & \vdots \\ 0 & \dots & e^{j\Delta\Phi_j} \end{bmatrix} \quad (3.41)$$

Using equation (3.41), each element s_{ik} of the matrix $S_{TunableCoupler}$ is obtained and is of the form:

$$s_{ik} = \sum_{j=1}^M |s_{ij}| \cdot |s_{jk}| \cdot e^{j(\varphi_{ij} + \varphi_{jk} + \Delta\Phi_j)} \quad (3.42)$$

Furthermore, the output intensity $P_{out(k)}$ at port k of the combiner is related to the input power $P_{in(i)}$ at port i of the splitter by:

$$P_{out(k)} = |s_{ik}|^2 \cdot P_{in(i)} \quad (3.43)$$

where $|s_{ik}|^2$ for ideal MMI couplers and ideal MZI arms is given by [16]:

$$|s_{ik}|^2 = \frac{1}{M^2} \{M + 2[\sum_{p=1}^{M-1} \sum_{q=p+1}^M \cos[(\varphi_{ip} - \varphi_{iq}) + (\varphi_{pk} - \varphi_{qk}) + (\Delta\Phi_p - \Delta\Phi_q)]]\} \quad (3.44)$$

where p and q refer to the arms j of the MZI. For input power $P_{in(i)}$ at port i of the splitter, by changing the applied phase values on the arms of the MZI, $|s_{ik}|^2$ is varied, which results in varying the output intensity $P_{out(k)}$ at port k of the combiner (see equation (3.43)). Therefore, the structure shown in figure 3.17 effectively works as a tunable coupler by tuning the phase shift on the symmetric arms of the MZI. In [16], a very detailed and comprehensive analysis of symmetric MZI based variable splitting ratio MMI couplers is presented.

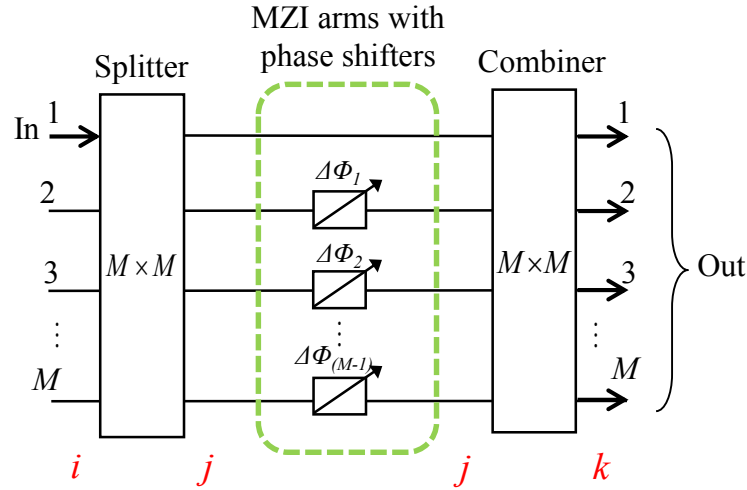


Figure 3.17: Generalized MZI as a tunable power splitter

Replacing each MMI coupler with fixed coupling coefficients in the filter shown in figure 3.14 with tunable couplers of the form shown in figure 3.17 will require $2 \cdot \left[\frac{R}{(M-1)} + 1 \right]$ MMI couplers. This implies that the required number of couplers will be doubled as compared to the filter with static couplers. Not only that, but that the number of phase shifting elements is also increased by 2.5 times. Consequently, the resulting filter will

become as bulky and complicated as a lattice filter. This is not desirable and most importantly not required to enhance the tuning range of the parallel serial filter.

An alternative approach is to replace only the middle MMI coupler of the 6th order parallel-serial filter by a tunable coupler. The resulting architecture of the filter is shown in the figure 3.18. In the scope of this work it is termed as the extended two-stage parallel-serial filter. It needs 4 MMI elements and only 9 phase shifting elements. The middle two MMI couplers act as the tunable coupler and connects the input and output MMI couplers with delay lines with a total delay of 60 ps (unit delay $\tau = 10\text{ps}$ for $FSR = 100\text{ GHz}$).

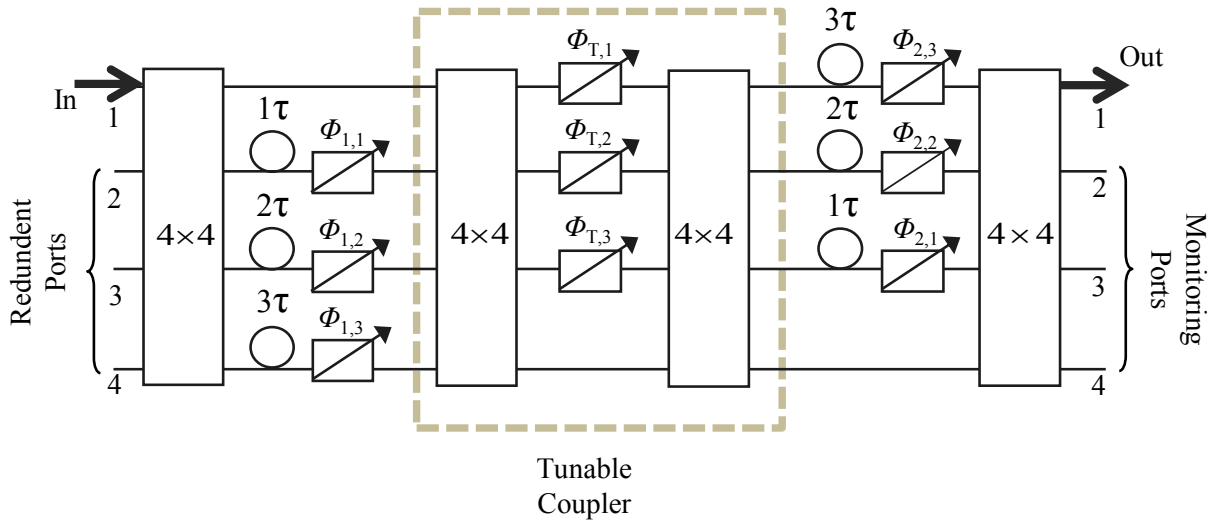


Figure 3.18: Enhanced two stage parallel-serial filter with a tunable coupler

The tunable coupler in the middle enables the six zeros of the filters to be placed more freely in the z -plane. This results in more flexibility in tuning the filter to various group delay slopes as shown by the simulation result shown in Figure 3.19. Clearly the limited tuning range of parallel-serial filter with static couplers (see figure 3.16) is improved by using a tunable coupler in the middle (Although this configuration still puts a limit on the values for achievable zeros). Since the use of a single tunable coupler in the middle is sufficient to provide “almost” continuous tuning of the group delay slope, therefore, it can be concluded that it is not necessary to replace all couplers of the static parallel-serial filter of figure 3.14 with their tunable counterparts. One can observe in figure 3.19 that as the group delay slope increases to achieve larger maximum achievable dispersion D_{max} while keeping the group delay ripple below certain value ($< 0.25\text{ ps}$ in this case), the useful bandwidth Δf (or RBWU) of the parallel-serial filter decreases. This verifies the compromise between the maximum group delay slope and the useful bandwidth of the filter for a maximum allowed group delay ripple, which was mentioned in section 3.3.

Figure 3.20 shows the relationship between the group delay ripple τ_{ripple} and the mean value of the dispersion D_{mean} for various fractions of the useful filter bandwidth Δf (or RBWU) for the extended two stage filter for residual dispersion compensation. The flatness of the dispersion curve (small τ_{ripple}) is least effected when the useful bandwidth

(or RBWU) is small. The dispersion values reach ± 200 ps/nm while keeping τ_{ripple} below 1ps. For an increased RBWU (i.e. 70 % of filter FSR, which is equal to a $\Delta f = 70$ GHz for a filter with $FSR = 100$ GHz), the value for τ_{ripple} ripple increases exponentially and the filter can deliver only ± 100 ps/nm for $\tau_{ripple} < 1$ ps. Lastly, it is evident that the relationship for τ_{ripple} and dispersion D_{mean} is axially symmetrical, meaning that the influence of group delay ripple is independent of the dispersion sign. So both positive and negative values can be achieved with the same flatness.

In comparison to the two stage parallel-serial filter comprising static couplers (figure 3.14, the enhance two stage parallel-filter (figure 3.18) has an improved tunability. For $D_{max} = 180$ ps/nm, a reduced group delay ripple τ_{ripple} (3 ps for the former and 0.25 ps for the latter), increased useful bandwidth ($\Delta f = 44$ GHz for the former and $\Delta f = 55$ GHz for the latter) is provided by the enhanced two stage parallel-serial filter as compared to the two stage parallel-serial filter with static MMI couplers (MMI couplers with fixed coupling coefficients).

Simulation results shown in figure 3.19 and figure 3.20 are performed by the project partners at Helmut-Schmidt University (Hamburg-Germany).

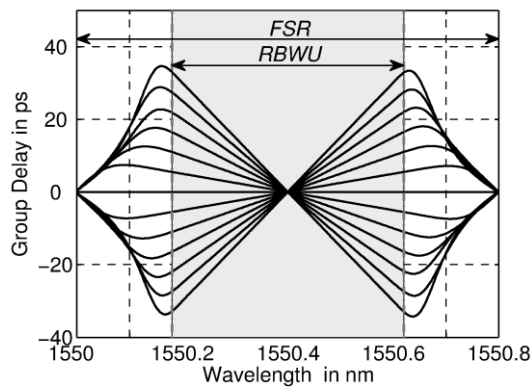


Figure 3.19: Simulation result for the tunability of the enhanced two stage parallel-serial filter. The simulation is performed for filter with $FSR = 100$ GHz and by using ideal MMI couplers with lossless waveguides. The group delay ripple is < 0.25 ps.

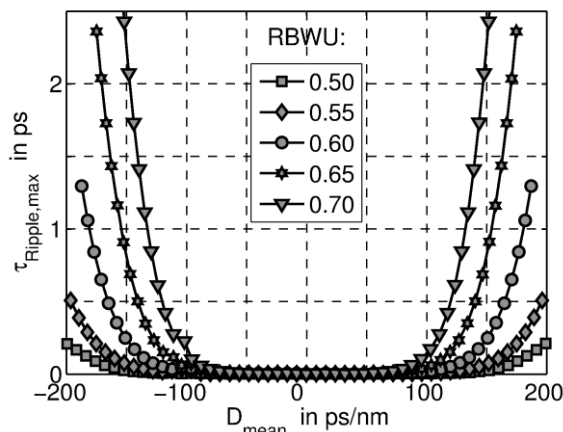


Figure 3.20: Compromise between the RBWU and Group delay ripple

References:

- [1] C. K. Madsen and J. H. Zhao, "Optical Filter design and Analysis - A signal processing approach", Wiley Series in microwave and optical engineering, 1999.
- [2] Trinh, P. D.; Yegnanarayanan, S.; Jalali, B., "Integrated optical directional couplers in silicon-on-insulator," *Electronics Letters* , vol.31, no.24, pp.2097,2098, 23 Nov 1995.
- [3] Soldano, L.B.; Pennings, E. C M, "Optical multi-mode interference devices based on self-imaging: principles and applications," *Lightwave Technology, Journal of* , vol.13, no.4, pp.615,627, Apr 1995.
- [4] Smit, M.K.; Van Dam, C., "PHASAR-based WDM-devices: Principles, design and applications," *Selected Topics in Quantum Electronics, IEEE Journal of* , vol.2, no.2, pp.236,250, Jun 1996.
- [5] A. Rahim, S. Schwarz, J. Bruns, C. Schäffer, and K. Petermann, "Terabit Optical OFDM demultiplexer in Silicon Photonics," in *Optical Fiber Communication Conference/National Fiber Optic Engineers Conference 2013, OSA Technical Digest (online) (Optical Society of America, 2013)*, paper JTh2A.28.
- [6] T. Schlipf, M. Street, J. Pandavenes, R. McBride, and D. Cumming, "Design and Analysis of a Control System for an Optical Delay-Line Circuit Used as Reconfigurable Gain Equalizer," *J. Lightwave Technol.* 21, 1944- (2003).
- [7] Hoang Manh Nguyen; Igarashi, K.; Katoh, K.; Kikuchi, K., "Continuously-tunable optical delay line using PLC-based optical FIR filter," *Lasers and Electro-Optics (CLEO) and Quantum Electronics and Laser Science Conference (QELS), 2010 Conference on* , vol., no., pp.1,2, 16-21 May 2010.
- [8] A. V. Oppenheim, R. W. Schafer and J. R. Buck, "Discrete time signal processing", 2nd Edition, Prentice Hall, 1999.
- [9] Xiang Liu; Mollenauer, L.F.; Xing Wei, "Impact of group-delay ripple in transmission systems including phase-modulated formats," *Photonics Technology Letters, IEEE* , vol.16, no.1, pp.305,307, Jan. 2004.
- [10] Rahim, A.; Schwarz, S.; Bruns, J.; Voigt, K.; Kroushkov, D.I.; Arnous, M.T.; Schäffer, C.G.; Petermann, K., "Finite Impulse Response Filter Using 4-Port MMI Couplers for Residual Dispersion Compensation," *Lightwave Technology, Journal of* , vol.30, no.7, pp.990,996, April1, 2012.
- [11] K. Takiguchi, K. Jinguji, K. Okamoto, and Y. Ohmori, "Variable group-delay dispersion equalizer using lattice-form programmable optical filter on planar lightwave circuit," *IEEE J. Sel. Topics Quantum Electron.*, vol. 2, no. 2, pp. 270-276, Jun. 1996.
- [12] C. Doerr, D. Marom, M. Cappuzzo, E.Chen, A. Wong-Foy, L. Gomez, and S. Chandrasekhar, "40-Gb/s colorless tunable dispersion compensator with 1000-ps/nm

tuning range employing a planar lightwave circuit and a deformable mirror," in Proc. Opt. Fiber Commun. Conf./NFOEC, Mar. 2005, vol. 5, pp. 1-3.

[13] N. Neumann , T. Schuster and C. Schäffer "Simple filter for dispersion estimation via optical VSB filtering", 35th Eur. Conf. Opt. Commun., pp.1 -2 2009.

[14] P. Besse , M. Bachmann , H. Melchior , L. Soldano and M. Smit "Optical bandwidth and fabrication tolerances of multimode interference couplers", J. Lightw. Technol., vol. 12, no. 6, pp.1004 -1009 1994.

[15] S. Schwarz, A. Rahim, C. Schäffer, J. Bruns, and K. Petermann, "Fully Adjustable Serial-Parallel FIR Filter for Compensation of Residual Chromatic Dispersion," in European Conference and Exhibition on Optical Communication, OSA Technical Digest (online) (Optical Society of America, 2012), paper We.1.A.1.

[16] Lagali, N.S.; Paiam, M.R.; MacDonald, R.I.; Worhoff, K.; Driessen, A., "Analysis of generalized Mach-Zehnder interferometers for variable-ratio power splitting and optimized switching," Lightwave Technology, Journal of , vol.17, no.12, pp.2542,2550, Dec 1999.

[17] M. Bohn, W. Rosenkranz, and P. Krummrich, "Adaptive distortion compensation with integrated optical finite impulse response filters in high bitrate optical communication systems," IEEE J. Sel. Topics Quantum Electron., vol. 10, no. 2, pp. 273-280, Mar./Apr. 2004.

[18] N. Neumann, T. Duthel, M. Haas, and C. Schäffer, "General Design Rules for the Synthesis of Dispersion and Dispersion Slope Compensation FIR and IIR Filters With Reduced Complexity," J. Lightwave Technol. 25, 3555-3562 (2007).

[19] Smit, M.K.; Van Dam, C., "PHASAR-based WDM-devices: Principles, design and applications," Selected Topics in Quantum Electronics, IEEE Journal of , vol.2, no.2, pp.236,250, Jun 1996.

[20] Duthel, T.; Fritzsche, D.; Michael, F.; Schaffer, C.G.; Breuer, D., "Quasi-Analytic Synthesis of Nonrecursive Optical Delay Line Filters for Reliable Compensation of Dispersion Effects," Lightwave Technology, Journal of , vol.24, no.11, pp.4403,4410, Nov. 2006.

4.

Design and Fabrication of Parallel-Serial Filter

This chapter provides fundamental information about the SOI material system and the photonic components used for the realization of a parallel-serial filter. Waveguides as delay lines, MMI couplers and phase shifting elements are the building blocks of the parallel-serial filter. This chapter is dedicated to the theoretical description of these elements. The thermo-optic effect using micro-heaters (metallic heaters) is used to provide a phase shift on the delay lines and the optimization of such phase shifting elements is also addressed in this chapter. In the last part of the chapter, the fabrication process and the designed parallel-serial filters are presented.

4.1. Material Platform

The principle of operation of the components used to implement the tunable residual dispersion compensation is independent of the material platform. But on the other side the design specification and performance are strongly dependent on the type of material platform used. Therefore it is important to highlight what type of material platform is used and why it has been considered useful for the implementation of the parallel-serial filter for residual dispersion compensation.

In this work, 4 μm SOI material is used for the implementation of the filter. It consists of a top silicon layer. An oxide layer, commonly referred as Buried Oxide (BOX) is sandwiched between the top silicon layer and the silicon substrate. The top silicon is the guiding layer for the light. In the simplest implementation, the top air and the sandwiched oxide layer act as the cladding layers. The substrate layer provides mechanical stability to the guiding and cladding layers. Figure 4.1 shows the layer architecture of the SOI material with dimensions marked on the left side and the index profile (excluding top and bottom air) is depicted on the right side of the figure. 4.1.

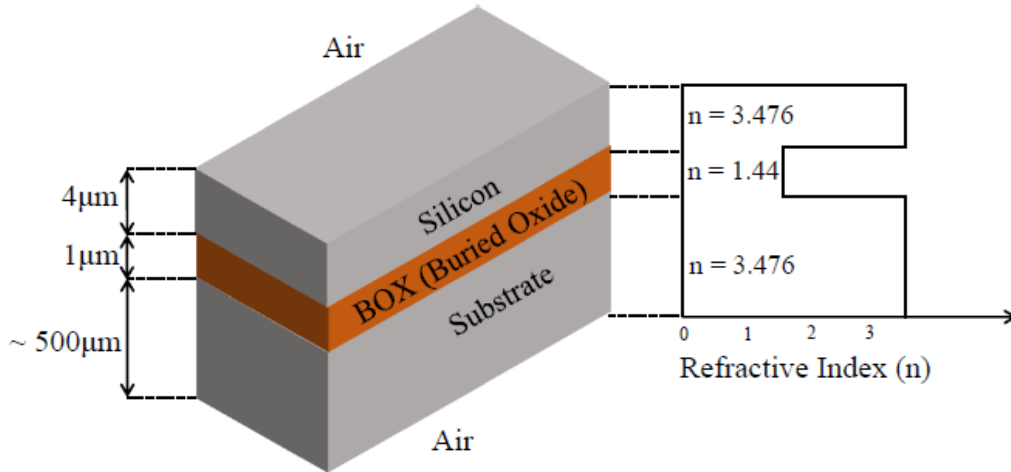


Figure 4.1: Architecture of SOI material system used for the implementation of parallel-serial filter for residual dispersion compensation

The SOI platform can be classified into various types. This classification can be done on the basis of the:

- Size of the wafer (i.e. 100 mm (4 inch) or 200 mm (8 inch) wafer)
- Thickness of the guiding silicon layer which ranges from few nanometers to a few microns
- Thickness of the BOX layer

In this work, SOI wafers with top (guiding) silicon thickness of $4\mu\text{m}$ are used. The BOX layer has a thickness of $1\mu\text{m}$. The size of the wafer is 100 mm (4 inch) and the total thickness of the wafer is $\sim 500\mu\text{m}$. Important features of the SOI wafer used for the fabrication of the devices are highlighted in the Table 4.1.

Table 4.1: Specifications of the SOI wafer used for the fabrication of parallel-serial filter for residual dispersion compensation

Size of the wafer	100 mm (4 inches)
Guiding Silicon thickness	$4\mu\text{m}$
BOX thickness	$1\mu\text{m}$
Variation of guiding silicon layer thickness	$\sim 0.05\mu\text{m}$ [1]

It must be mentioned that the most recent SOI based integrated devices are based on a nanowire SOI platform, which uses a silicon layer of 220nm thickness [24]. Due to the application (residual dispersion compensation) of the filter concept proposed in this work, $4\mu\text{m}$ SOI is considered a better platform. Few of these reasons are as follows:

- The main aim of the proposed filter concept is to use higher order coupling devices ($M>2$) for the implementation of a dispersion compensating filter. At the start of this work, the other SOI platforms were not yet able to provide very high quality higher order couplers. Recently, higher order MMI couplers with small excess loss, imbalance and phase accuracy are available also in nanowires [2].

- The proposed filter is an interferometric device and is implemented by using delay lines. 4 μm SOI provides waveguides with small loss and ensure small imbalance at the input of the intermediate coupling stages of the filter. This prevents degradation in the performance of the filter. Effect of MMI performance on the performance of the parallel-serial filter is addressed in chapter 5.
- The 3.5 μm rib waveguides in 4 μm SOI (discussed in section 4.3) have a small loss (~ 0.1 dB/cm) [8] as compared to the waveguides in 220 nm SOI platforms (~ 2 dB/cm for nanowires) [25]. Grating couplers are used in 220 nm SOI platform and they have a typical loss of 3 dB [26], which is ~ 3 dB higher than the butt coupling loss for 3.5 μm wide rib waveguides in 4 μm SOI technology (facet coupling for 3.5 μm wide rib waveguides in 4 μm SOI technology). Both factors contribute in the implementation of a low insertion loss parallel-serial filter using 4 μm SOI technology.
- The polarization independent behavior is another factor which leads to the selection of 4 μm SOI platform for this work [1].
- The proposed filter has to compensate dispersion over the C-band for a high bandwidth WDM system. Nanowire based devices have strong wavelength dependent gratings [4] for in-out coupling and it is challenging to operate them over the whole C-band without inducing significant penalty.
- An advantage of an integrated photonic residual dispersion compensator is its ability to be heterogeneously integrated with the receiver. The integration of dispersion compensators with wide waveguides, receivers with wide waveguides and photo-diodes is more feasible as compared to narrow waveguide dispersion compensators and receivers. The latter will require tapers for efficient flip-chip bonding of photo-diodes.

It is important to mention that during the course of this work, nanowire technology has improved tremendously and MMI couplers with good phase accuracy, low excess loss and small imbalance are available [2].

4.2. MMI Couplers

For the realization of a parallel-serial filter, the main component is a higher order MMI coupler (In this work, an MMI coupler with more than 2 output ports is considered as higher order).

An MMI coupler is a passive device with M_{in} input and M_{out} output waveguides (number of the output waveguides is the order M of the MMI coupler). The input and output waveguides are typically single mode. They are connected by a central multimode section [27]. Figure 4.2 shows a simplified schematic of an MMI coupler with $M_{in}=1$ and $M_{out}=4$.

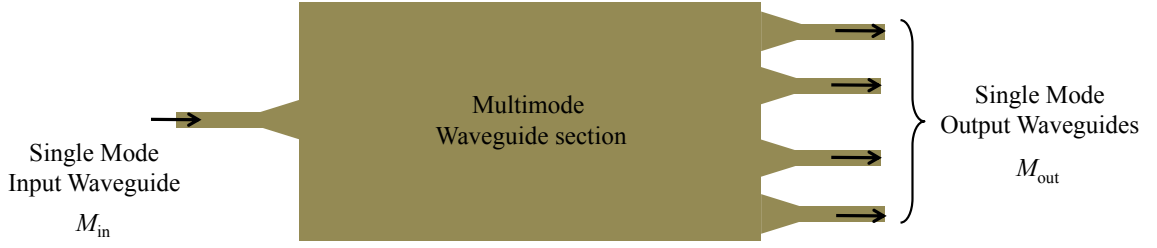


Figure 4.2: Simplified schematic of an MMI coupler. The input and output single mode waveguides are connected by a central multimode waveguide section, where the self-imaging takes place (see figure 4.3)

The main principle of the MMI coupler is based on the “self-imaging” which takes place in the multimode waveguide section. The term self-imaging implies that depending on how the guided modes in the multimode waveguide section interfere with each other in a multimode waveguide section of length $z=L_{MMI}$ and width W_{MMI} , a single or multiple replicas of the input field $f_{in}(x,0)$ are reproduced at periodic locations along the length of the MMI section. The replicas of $f_{in}(x,0)$ produced at the output of the multimode section $f_{out}(x,L_{MMI})$ might not be equally spaced from each other.

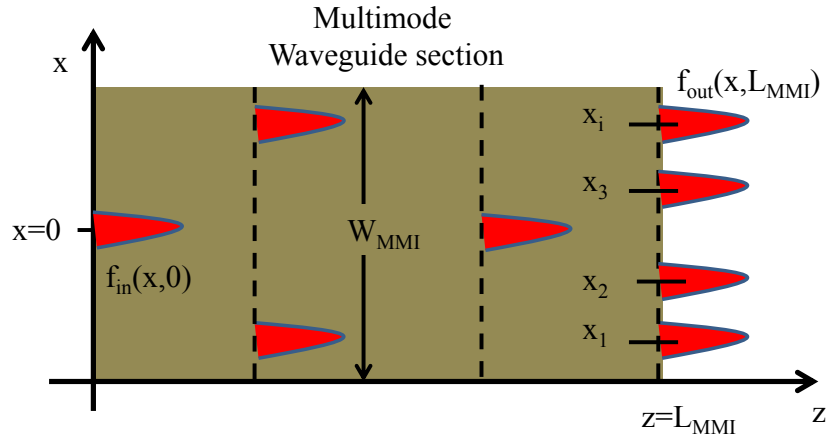


Figure 4.3: Self-imaging in the multimode waveguide section of an MMI coupler. Four images f_{out} of the input filed f_{in} are produced at length $z=L_{MMI}$.

Analytically the self-imaging the multimode section of an MMI coupler with M outputs (M images at $z=L_{MMI}$) is expressed as [27]:

$$f_{out}(x) = \frac{1}{C} \sum_{i=0}^{M-1} f_{in}(x - x_i) \cdot \exp(j\varphi_i) \quad (4.1)$$

where $f_{out}(x,L_{MMI})$ is the optical field distribution at length L_{MMI} of the multimode waveguide section of the MMI coupler, x is the lateral dimension of the multimode section, $|C| = 1/\sqrt{M}$ is a complex normalization constant, $f_{in}(x)$ is the input field distribution at $z=0$ for the multimode waveguide section of the MMI coupler. The terms x_i and φ_i determine the positions and phases of the M images formed at the output of the multimode section.

$$x_i = (2i - M) \frac{P}{M} W_{MMI} \quad (4.2)$$

$$\varphi_i = i(M - i) \frac{P}{M} \pi \quad (4.3)$$

W_{MMI} is the effective width of the multimode section and i represent each of the M images available at the $z=L_{MMI}$ of the multimode waveguide section.

Since the nature of imaging in the multimode waveguide section of the MMI coupler is periodic (due to periodicity of phase of the interfering modes in the multimode section), therefore the M images are available at multiple positions along the propagation direction z . This means that several lengths L_{MMI} for the multimode waveguide section are possible to design an MMI coupler with M images. Furthermore, the length L_{MMI} is influenced by the position of excitation of the input field $f_{in}(x,0)$. By exciting the input field at certain lateral positions of the multimode section, certain modes can be excited in the multimode section. Such MMI couplers in which only certain modes are excited for the self-imaging in the multimode section are called “restricted interference” MMI couplers. On the other hand, if MMI couplers are designed without any consideration for the type of modes excited in the multimode section, then they are termed “general interference” MMI couplers. The input field can be excited at any lateral position for such MMI couplers. Generally, shorter length L_{MMI} is possible with “restricted interference” MMI coupler.

The length L_{MMI} of the MMI coupler is related to the type of interference T_1 and periodicity P of imaging in the multimode section by the following expression:

$$L_{MMI} = \frac{3P}{T_1 \cdot M} L_c, \quad (4.4)$$

with $P \geq 0$, $M \geq 1$ and P and M have no common divisor. Here, P defines several possible lengths for the multimode section L_{MMI} to generate M images. $P=1$ allows the MMI couplers with smallest length. The term T_1 defines if the MMI coupler is general interference or restricted interference. In case of general interference, the term T_1 is equal to unity and for paired and symmetric restricted interference based devices, the factor T_1 is either equal to 3 or 4 respectively. Although the restricted interference devices have shorter length L_{MMI} they do not always result in shorter devices. The reason comes from the fact that the excitation of certain modes in the multimode section require an increased width W_{MMI} of the multimode section and that leads to increased length L_{MMI} , resulting in not necessarily small devices. L_c is the beat length of the two lowest order modes and is given by:

$$L_c = \frac{\pi}{\beta_0 - \beta_1} = \frac{\pi}{\Delta\beta_{01}} \quad (4.5)$$

and

$$\Delta\beta_{01} = \frac{3\pi^2}{2 \cdot n \cdot k_0 \cdot W^2} \quad (4.6)$$

where $k_0 = \frac{2\pi}{\lambda}$ is the propagation constant in vacuum.

To elaborate further, consider an MMI coupler with $M=4$. Assume, general interference ($T_I=1$), the length of the MMI coupler L_{MMI} is given by:

$$L_{MMI} = \frac{3P}{4} \cdot L_c, \text{ with } P=1,3,5 \dots$$

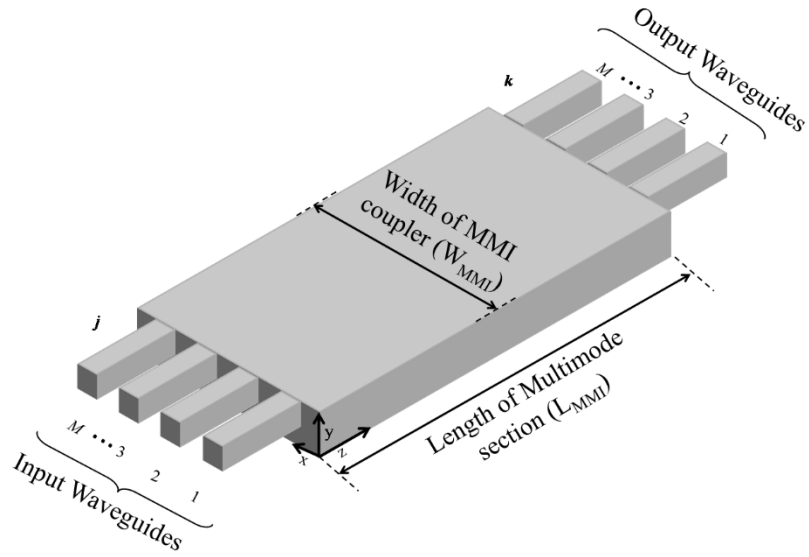


Figure 4.4: MMI coupler with $j=M$ input and $k=M$ output ports

Consider an $M \times M$ MMI coupler with $j=M$ input and $k=M$ output ports (see figure 4.4). As mentioned earlier in section 3.3, the input to output relationship of an MMI coupler can be written in the form of a transfer matrix S_{MMI} of the form shown earlier in equation (3.27). Each element s_{jk} in row j and column k of this transfer matrix relates the input at port i and output at port k of the MMI coupler and is of the form:

$$s_{jk} = a_{jk} \cdot e^{j\varphi_{jk}} \quad (4.7)$$

where a_{jk} is the real field amplitude transfer coefficient from input port j to output port k . $j=\sqrt{-1}$ and φ_{jk} is the relative phase associated with imaging an input at port j to an output at port k of the MMI coupler and is given by:

$$\varphi_{jk} = -\frac{\pi}{2}(-1)^{j+k+M} + \frac{\pi}{4M} \left[j+k-j^2-k^2 + (-1)^{i+j+M} \cdot \left(2jk - j - k + \frac{1}{2} \right) \right] \quad (4.8)$$

To use an MMI coupler in a filter device for residual dispersion compensation, the quality of the MMI coupler is pivotal. The quality of an MMI coupler is measured in terms of its performance specifications. It includes:

- *Excess Loss*: It is also termed as the insertion loss and it is a measure of the input intensity lost in imaging the input to the output ports of the MMI coupler. It is a ratio of the sum of all output intensities of the MMI coupler to the input intensity. For an input intensity a_j^2 at port j of the MMI coupler only, the excess loss (EL) of an MMI coupler is given by:

$$EL = 10 \log \left[\sum_{k=1}^M |a_{jk}|^2 \right] \left[- \right] (\text{in dB}) \quad (4.9)$$

where a_{jk} is the real field amplitude transfer coefficient from input port j to output port k . In chapter 3, a lossless MMI coupler is assumed. This mean $\sum_{k=1}^M a_{jk}^2 = 1$ and results in EL=0 dB. A small EL is desired to reduce the overall insertion loss of the fabricated parallel-serial filter.

- *Imbalance*: Imbalance in MMI couplers is a measure of the deviation of the intensity at a certain output port a_{jk} in relation to a reference output port $a_{jk(\text{ref})}$, where k_{ref} is the reference output port.

$$Imbalance = 10 \cdot \log \left(\frac{|a_{jk}|^2}{|a_{jk(\text{ref})}|^2} \right) (\text{in dB}) \quad (4.10)$$

Small and predictable imbalance is desired for MMI couplers used in the fabrication of the parallel-serial filter for residual dispersion compensation. As shown in section 3.3, the transfer function of the filter is the product of the transfer matrix S_{MMI} for the MMI couplers, delay lines S_{DL} and phase shifters S_{ϕ} on the delay lines. Large imbalance (deviation from equal splitting assumed for the implementation of the parallel-serial filter) will deviate the transfer function (position of filter zeros) of the parallel-serial filter from the expected response. This deviation might lead to a situation from where the filter cannot be tuned to deliver linear group delay slopes by adjusting the phase shift on the delay lines (see chapter 5 for more details).

- *Phase Accuracy*: The phase accuracy is a measure of the accuracy of the phase associated with imaging an input at port j to the output port k as given by equation (4.8). Like imbalance, the phase inaccuracy might result in difficulties in tuning the filter for residual dispersion compensation.
- *Polarization dependent loss (PDL)*: Polarization dependent loss is a difference in the maximum and minimum intensity of an image formed for an input at port j and output at port k of the MMI coupler for all states of polarization.

$$PDL = 10 \cdot \log \left(\frac{|a_{jk}^{\text{max}}|^2}{|a_{jk}^{\text{min}}|^2} \right)$$

Small PDL is desired for the MMI couplers so that the performance in terms of insertion loss for parallel-serial filter is independent of the state of the polarization.

- *Bandwidth of MMI Couplers:* Bandwidth of the MMI coupler is a measure of the wavelength range over which the values of excess loss, imbalance and phase accuracy remain within a certain margin from the designed specifications. In [6], it has been shown that the bandwidth of MMI couplers is inversely proportional to the number of ports and thus the length of the MMI coupler. For the application of residual dispersion compensation, the device should be able to compensate dispersion of all WDM channels over the C-band. Therefore, MMI couplers which give good performance in terms of excess loss, imbalance and phase accuracy are required. Table 4.2 compares the excess loss, imbalance and phase accuracy of 4x4, 8x8, 12x12 and 16x16 MMI couplers in silicon technology [32].

A very important feature of MMI couplers is that they are more tolerant to the fabrication errors compared to some other coupling devices. For example, MMI couplers are more tolerant to fabrication tolerances than directional couplers. $1 \times M$, $M \times M$ and $M_{in} \times M_{out}$ ($M_{in} \neq M_{out}$) MMI couplers have been demonstrated in the SOI platform with a performance better than their implementation in other platforms [8]. Generally, the excess loss, imbalance and bandwidth of the MMI couplers are dependent on the order of the MMI coupler (see Table 4.3). A higher order MMI coupler suffers from higher excess loss, imbalance and reduced bandwidth. As mentioned earlier, [6] has shown an inverse relationship between the port count of the MMI couplers and their bandwidth (Table 4.3 also proves that). On the other hand, the tolerance of the fabrication errors is independent of the order of the MMI coupler [6]. Within a certain limit (such as 4-port MMI) the SOI platform provides very high quality MMI couplers with very good performance. Such higher order MMI couplers have not been commonly employed for various applications. But, of course, there is a lot of potential in investigating the application of higher order MMI couplers for applications such as FIR filters for residual dispersion compensation. Apart from this application, recently in [28], we have shown how higher order MMI couplers can be used to implement higher order ($R=16$) FIR filters for the de-multiplexing of O-OFDM sub-channels.

In this work, 4-port MMI couplers are used to demonstrate an integrated optical filter to compensate residual dispersion for a high speed optical communication system. The design of the MMI coupler is outside the scope of this work. An existing MMI coupler with a performance required to demonstrate the filter concept is selected [7]. The main design and performance specifications are highlighted in the Table 4.2.

Table 4.2: Performance specifications for MMI couplers used in the implementation of parallel-serial filter for residual dispersion compensation

4-port MMI coupler	
Design Specifications	
Width of multimode section (μm)	32.1 μm
Length of multimode section (μm)	2400 μm
Interference Type	General
Performance Specifications (C-band)	
Excess Loss (dB)	< 0.3 dB
Imbalance (dB)	< 0.7 dB
Phase Accuracy (deg)	< 5°
Polarization Dependent Loss (PDL)	0.2 dB

Table 4.3: Excess Loss, Imbalance, Phase Errors and Bandwidth of 4 x 4, 8 x 8, 12 x 12 and 16 x 16 MMI couplers in SOI platform [32]

$M_{\text{in}} \times M_{\text{out}}$	Imbalance (dB) in C-band	Excess Loss (dB) in C-band	Bandwidth (nm) for phase error > 5°
4×4	0.7	0.3	35 nm (C-band)
8×8	1.18	1.25	29 nm
12×12	2.1 dB	1.87	16 nm
16×16	> 2.5 dB	> 2 dB	12 nm

4.3. Integrated Waveguides in SOI

Waveguides are the key component for any integrated optical device. They are used not only for routing an optical signal but for delaying an optical signal with reference to the other. In the latter case, they are called delay lines. They confine an optical signal for guiding. Their classification is very diverse and can be done on the basis of geometry, guiding modes and material. For example, figure 4.5 shows the geometries of rib waveguide in 4 μm SOI (a), rib waveguide in 1.4 μm SOI (b) and nano-wires in 220 nm SOI platform (c). In this work, non-planar rectangular single mode rib waveguides in 4 μm SOI are used (similar to (a) in Figure 4.5).

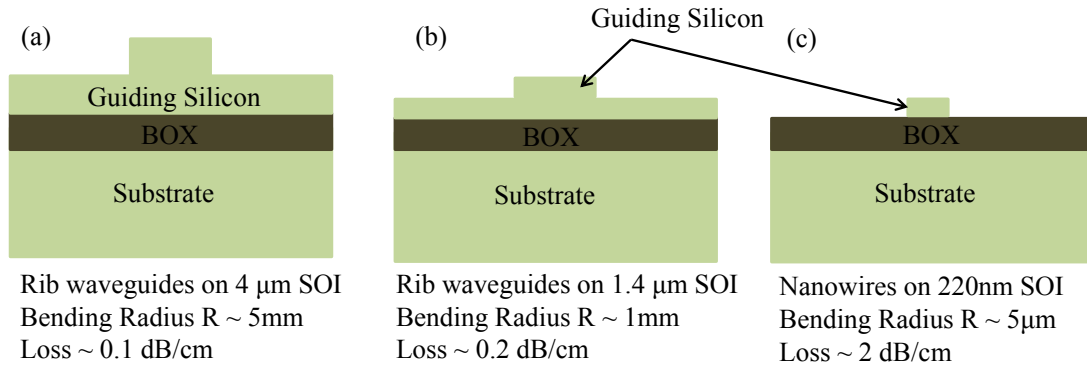


Figure 4.5: Different geometries of waveguides in different SOI platform

A cross-sectional view of the rib waveguide is shown in figure 4.6, in which the core of the waveguide comprises a high index strip and planar layer with equal index and is placed on top of a low index cladding. It is necessary that the waveguides for the implementation of photonic integrated circuits are single mode. This is necessary to overcome modal dispersion in photonic integrated devices. Modal dispersion arises due to different group velocities for different guided modes of the waveguide. The single mode condition for the rib waveguide on SOI platform is associated with the geometry of the rib waveguide by the following relationship [3]:

$$r \leq 0.5$$

$$\frac{W}{H} \leq 0.3 + \frac{r}{\sqrt{1-r^2}} \quad (4.11)$$

W , H and $r=h/H$ are shown in figure 4.6 and denote the width, rib height and normalized slab height, respectively. Table 4 presents the dimensions of the rib waveguide used in the realization of the parallel-serial filter.

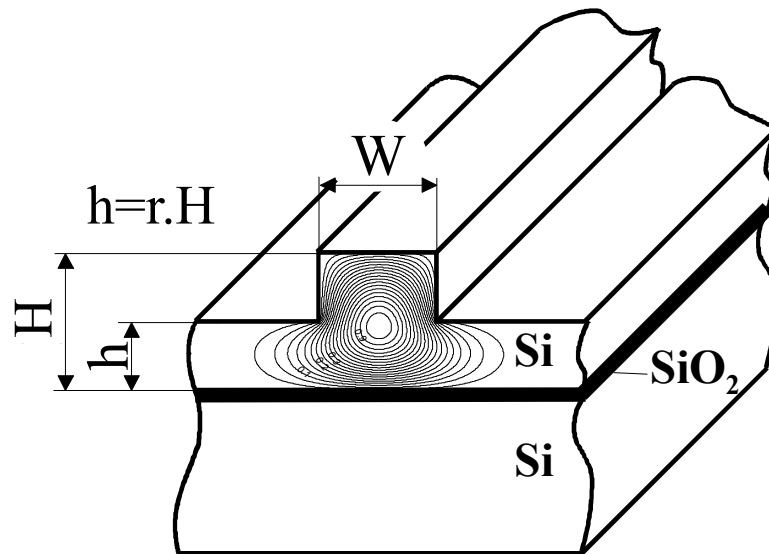


Figure 4.6: Geometrical description of a rib waveguide

Table 4.4: Selected Geometry of the Rib waveguide

<i>Selected geometry of the Rib waveguide</i>	
Width W	3.5 μm
Height of the guiding Silicon layer H	4 μm
Slab Height h	2 μm
Etch depth H-h	2 μm
Normalized slab height r	0.5

An important performance specification of the integrated waveguides is the optical loss. The loss in a waveguide can originate from the material or the geometry of the waveguide. Some materials have an intrinsically high absorption coefficient. The absorption coefficient (attenuation coefficient) α quantifies the degree to which the intensity of an optical signal is reduced as it propagates through the material. Intrinsic silicon has a small absorption coefficient in the telecom wavelength regime ($\lambda > 1.2 \mu\text{m}$). That makes it a suitable material to realize low loss waveguides for optical telecommunication applications as has been demonstrated by [3].

The magnitude of loss in waveguides is also influenced by the geometry of the waveguides. The three waveguide types shown in Figure 4.5 have been implemented in the same material (SOI) but they exhibit different loss due to different geometries of the waveguides. For example, nano-wires (strip waveguides) have shown higher loss values of $\sim 2 \text{ dB/cm}$, whereas rib waveguides in $4 \mu\text{m}$ SOI have shown loss value of $\sim 0.2 \text{ dB/cm}$ [8]. Stronger interaction of the optical mode field with the surface roughness of the waveguides in nano-wire waveguides results in higher losses [29] due to scattering or radiation of the optical field out of the waveguide as compared to the rib waveguides used in a $4 \mu\text{m}$ SOI implementation. When the period of surface roughness on waveguide walls, which originates from the fabrication process (lithography and etching) of the waveguides, becomes smaller than the wavelength of the optical signal, the scattering losses occur. Post processing of fabricated waveguides, such as thermal oxidation is used to reduce the scattering losses due to roughness of the waveguides.

To transport optical signals to different components placed on the chip, the waveguides have to be bent. Although the bends make the interconnection between different components on chip easy and results in a compact size of the chip, the bending of the waveguide introduces additional losses due to radiation of the optical field outside the guiding layer. Decreasing the bending radii result in an exponential increase in the bending losses. Therefore, it is important to determine the minimum bending radius for a waveguide. Figure 4.5 states the bending radii for different SOI waveguides, with nano-wires showing the smallest bending radii of $5 \mu\text{m}$ (promising for compact devices).

In this work rib waveguides with $3.5 \mu\text{m}$ width in $4 \mu\text{m}$ SOIs have been used. The minimum bending radius for these waveguides has previously been computed by [8]. It has been shown that a bending radius of at least 5 mm ($\times 1000$ times larger than nano-

wires) is required to keep bending losses to below 0.1 dB for both TE and TM polarized light. For straight waveguides, a low loss of 0.1 dB/cm to 0.2 dB/cm has been recorded by [8] and has been verified by the measurement performed in this work as well.

Unless otherwise mentioned, in this work, the term rib waveguide is attributed to the waveguide dimensions mentioned in the table 4.4. Such waveguides are used for in- and out-coupling of an optical signal from the parallel-serial filter for residual dispersion compensation. The delay lines connecting the MMI couplers are also using the 3.5 μm rib waveguides. The low loss (0.1 dB/cm) in the rib waveguides ensures that the delay lines do not introduce substantial imbalance at the input of the recombining MMI couplers of the parallel-serial filter.

The field size of rib-waveguides is ~ 2.5 times smaller than the mode field size of Standard Single Mode Fiber (SSMF), which is $\sim 10 \mu\text{m}$. Moreover, the mode profile of waveguides is non-circular and the mode profile of fiber is circular. These factor lead to a large coupling loss (estimated to be ~ 6 dB in [8]). Possible solution to avoid this large coupling loss is by either making the mode-field diameter of the waveguide compatible with the fiber or vice versa. The former requires a 3D taper, which will require careful designing to minimize loss introduced by them and precise fabrication. In this work, a lensed fiber is used to match its mode filed profile with the waveguide. A lensed fiber with a spot size of 3.3 μm has been used and it has reduced the coupling loss from ~ 6 dB to $\sim 0.2-0.3$ dB for waveguides with anti-reflection coated facets. Such a low coupling loss is only achieved by careful aligning of the fiber with the waveguide because this technique has small tolerance to misalignment.

4.4. Thermo-optic Effect for Phase Shifting

The drift in the position of zeros due to non-ideal elements, for example due to phase errors or imbalances in the MMI couplers, of a filter is not desired. On the other hand, to make the filters more adaptive and versatile, tunable couplers [9] and additional phase shifts [10] are introduced on the delay lines. In this way the transfer function of the filter can be adapted to the desired filter response. It has been explained in section 3.8 and 3.9 that the parallel-serial filter can deliver a linear group delay for a certain fraction of the *FSR* by adjusting the phase on the delay lines connecting the MMI couplers. The phase of an optical signal propagating through a waveguide is given by:

$$\Phi = n_{eff} \cdot k \cdot L \quad (4.12)$$

where n_{eff} is the effective refractive index of the waveguide mode, k is the free-space propagation constant and L is the length over which the optical signal is propagated. A change in the refractive index of the SOI waveguide leads to change in the phase Φ of the signal propagating through the waveguide. The differential phase $\Delta\Phi$ introduced by a change in the refractive index Δn_{eff} is given by:

$$\Delta\Phi = \Delta n_{eff} \cdot k \cdot L = \Delta n_{eff} \cdot \frac{2\pi}{\lambda} \cdot L \quad (4.13)$$

Silicon has a high thermo-optic coefficient of $1.86 \times 10^{-4} \text{ K}^{-1}$ at 1550 nm [29]. On the other hand, it does not have a linear electro-optic coefficient [12], therefore, the thermo-optic effect is a very commonly employed physical phenomenon, which is used to introduce a change in the refractive index to introduce a phase change in SOI based devices. Thermo-optic effect based phase change can be introduced by heating of the waveguide, which is accomplished by placing a micro-heater either on top [13] or beside the waveguide.

A micro-heater is an Ohmic metallic resistor to heat the waveguide. The high thermo-optic coefficient of silicon enables low power (tens of mW) to achieve a certain phase change [14, 15]. Furthermore, sub-microsecond time response is possible due to the high thermo-optic coefficient of Silicon [14, 15]. Important design requirements for the design of a micro-heater to introduce a phase shift is to ensure low power functionality without introducing any additional optical loss and without influencing the neighboring waveguides by introducing a thermal cross-talk.

As mentioned earlier, the heater can either be placed on top of the waveguide or beside the waveguide at a certain distance. The choice is influenced by the geometry of the waveguides. For rib waveguides, heaters can be placed beside the waveguide on the silicon slab (see figure 4.7). For nano-wires, the heaters can only be placed on top of the waveguides (see figure 4.7). In the latter case, it is necessary to ensure that the heater does not introduce any additional loss by the absorption of the optical signal in the metallic heater. This is achieved by typically using a buffer layer between the Silicon waveguide and the heater. Never-the-less, this approach is more prone to influence the optical properties of waveguides by either introducing optical loss or by changing the birefringence of the waveguide due to additional stress introduced by the buffer layer. The optimum thickness of the buffer layer depends on the waveguide geometry. A buffer layer of 500 nm is used by [13] and $1.5 \mu\text{m}$ is used by [16]. Placing heater at a certain distance is considered more appropriate for rib waveguides, which have a Silicon slab region with high thermal conductivity to conduct the heat to the waveguide rib, where the majority of the optical field is confined. Figure 4.7 shows the two heater configurations discussed here with typical dimensions.

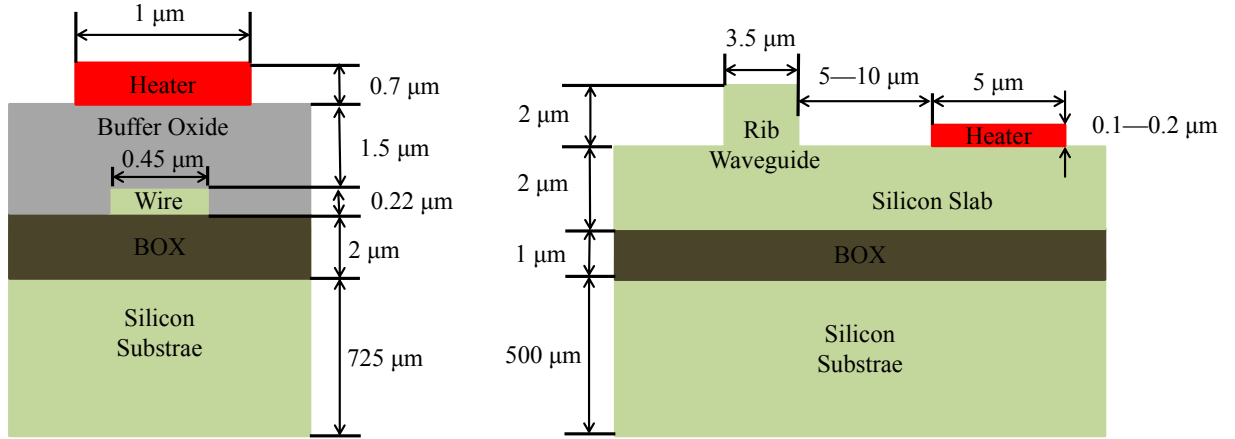


Figure 4.7: Heater placed on top of a nano-wire (left) and beside a rib waveguide (right) with typical dimensions

The amount of temperature change ΔT required to produce a phase change of $\Delta\Phi$ is given by:

$$\Delta T = \left(\frac{\partial n_{eff}}{\partial T} \right)^{-1} \cdot \frac{\lambda}{2\pi} \cdot \frac{\Delta\Phi}{L_H} \quad (4.14)$$

where $\left(\frac{\partial n_{eff}}{\partial T} \right)$ is the thermo-optic coefficient of silicon and L_H is the length of the heater. A schematic representation of a heater placed beside a waveguide is shown in figure 4.8, where h and b represent the thickness of the Silicon slab and BOX layer respectively. x_d denotes the distance at which the heater is placed from the silicon rib.

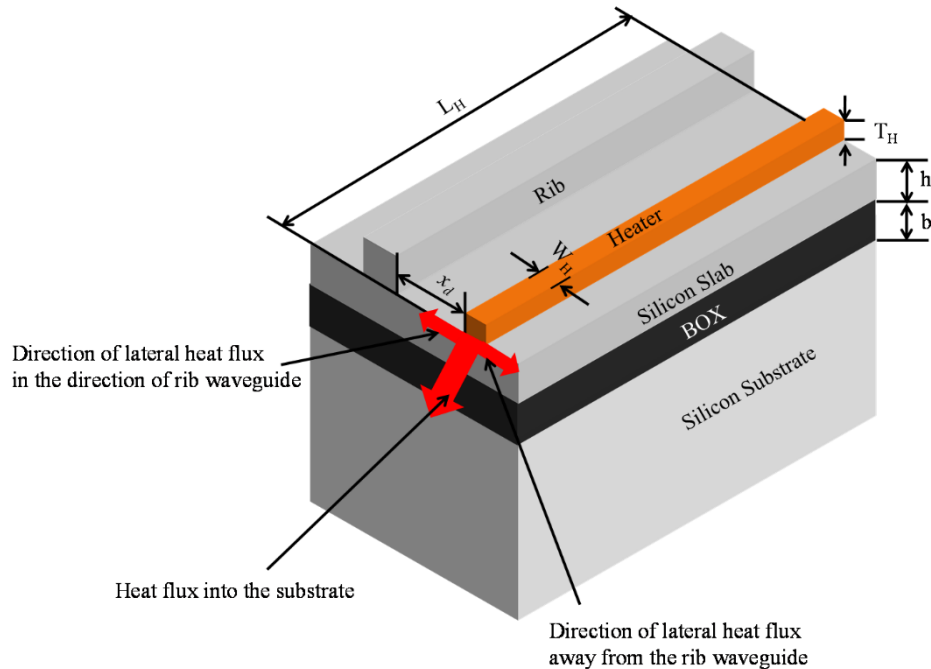


Figure 4.8: Configuration of a heater as a phase shifting element for rib waveguides

4.4.1. Optimized Design of the Heater for Phase Shifting

When electrical power P_{elec} is applied to the heater, the temperature T_H of the heater rises due to Ohmic losses. This rise in the temperature of the heater increases the temperature of the silicon slab due to conduction of heat from the heater to the silicon slab. This heat, which is conducted to the Silicon slab diffuses in all direction and it decays exponentially with distance from the heater (see figure 4.10).

The lateral diffusion of the heat in the direction of the rib waveguide in the silicon slab, which is marked with a red arrow (pointing towards waveguide) in figure 4.8, results in an increase ΔT in the temperature of the rib waveguide. Apart from that, the heat diffuses in the direction opposite to the waveguide and also a part of heat diffuses through the BOX into the substrate. The latter two diffusions (i.e. in silicon slab opposite to waveguide and in the substrate) will be topic of discussion in section 4.4.2.

Different models [13, 21, 22] are available to understand the conduction and spreading of heat in different material systems. The diffusion length L_d , which is the lateral distance from heater at which the temperature in the silicon slab has decayed by $1/e$, is related to the thickness and thermal conductivity of silicon and silicon dioxide [13]

$$L_d = \sqrt{\frac{h \cdot b \cdot k_{si}}{k_{oxide}}} \quad (4.15)$$

$k_{si} = 140 \text{ W/m.K}$ and $k_{oxide} = 1.2 \text{ W/m.K}$ represent the thermal conductivity of Silicon and Silicon dioxide respectively. Assuming $h = 2.2 \mu\text{m}$ and $b = 1 \mu\text{m}$ will result in $L_d = 16 \mu\text{m}$.

The optimum distance x_d between the heater and the waveguide is determined by the diffusion length L_d and the field profile of the waveguide. If a heater is placed far away from the waveguide, the laterally diffused heat (which decays exponentially) does not increase the temperature of the waveguide to produce the thermo-optic effect. On the other hand, a heater placed very close to the waveguide will increase the temperature of the waveguide but it might introduce optical losses due to the interaction of waveguide mode field with the heater. An optimum position of heater is the one which produces maximum ΔT at the waveguide without introducing any additional optical losses.

The value of L_d obtained analytically is further verified by performing a thermal simulation using ANSYS 11.0, which is based on Finite Element Method (FEM). The simulation scenario is schematically shown in the figure 4.9. A heater with width $H_w = 5 \mu\text{m}$ wide is placed on top of a Silicon slab with $h = 2.2 \mu\text{m}$ to determine the extent of lateral diffusion of heat in the silicon slab (The rib section is ignored in the simulation). The heater is placed in the middle of a silicon slab which is $1000 \mu\text{m}$ in length and width to prevent the effect of boundary conditions. The walls of the silicon slab, BOX and substrate are treated as thermal ground. The simulation is performed at the room

temperature of 25°C. No heat flow due to convection and radiation is assumed in this simulation.

Figure 4.10 shows the profile of the temperature in the silicon slab with distance D , which is measured from the edge of the heater. Due to the symmetry, the temperature profile is the same in both lateral directions. The temperature of the slab decays exponentially with distance from the heater and reaches to a value of $1/e$ at a distance of around $16.1 \mu\text{m}$, which is equal to the calculated value obtained by equation (4.15). Like lateral diffusion of heat, longitudinal diffusion of heat also takes place in the silicon slab. Due to this, a heater of length L_H , effectively heats waveguide of length L_H+2L_d .

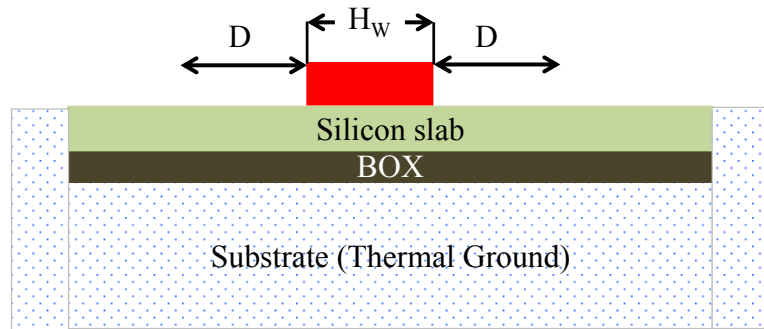


Figure 4.9: Simulation scenario to evaluate diffused heat in silicon slab of a rib waveguide

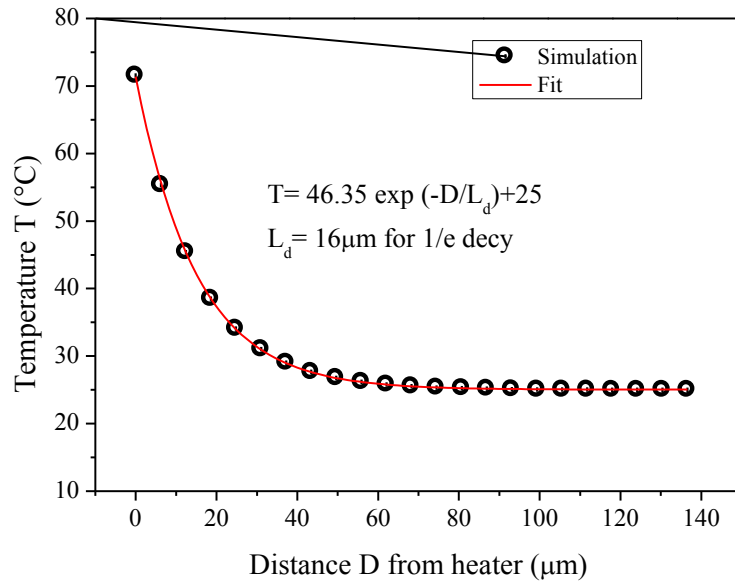


Figure 4.10: Profile of temperature on a silicon rib waveguide

From the above discussion it is clear that due to exponential decay of the heater temperature along the silicon slab, a heater placed at a distance $x_d \geq (L_d=16 \mu\text{m})$ will not be effective in achieving the temperature change ΔT to produce the phase shift $\Delta\Phi$. Therefore, the heater must be placed at $x_d \leq (L_d=16 \mu\text{m})$.

As mentioned earlier, a heater that is placed very close to the waveguide might introduce additional loss due to the interaction of mode field in the waveguide with the

metallic heater. The mode field profile in a waveguide gives a first level approximation to determine the optimum location of the heater. The mode profile for the TE and TM polarized optical signal in a rib waveguide is shown in the figure 4.11. Evidently, majority of the optical field is confined in the rib section of the waveguide. A fraction of the optical field extends $\sim 2-3 \mu\text{m}$ in the slab region. Therefore, a heater placed closer than $2 \mu\text{m}$ is susceptible to introduce additional loss in the waveguide.

To further verify this, a simple experiment is conducted by placing 2.8 mm long, $5 \mu\text{m}$ wide heaters at distance $x_d=0$ to $4 \mu\text{m}$ from the waveguides on a slab with height $h=2 \mu\text{m}$. The distance x_d between the heater and the waveguide is measured from the edge of the heater to the edge of the waveguide (see figure 4.12). $x_d=0$ means that the heater edge is directly in contact with the edge of the waveguide. The loss in these waveguides with heaters at $x_d=0$ to $4 \mu\text{m}$ is compared with the ones which have no heaters beside them. Any additional loss in waveguides with heater is attributed to the absorption of optical signal by the metallic heater. The experimental schematic is shown in the inset of the figure 4.12. The waveguides without heaters were measured to have a loss value of 0.17 dB/cm (intrinsic waveguide loss). The loss for the waveguides with heaters is normalized to the loss for the waveguide without heaters (i.e. 0.17 dB/cm). As shown in figure 4.12, a very large normalized loss of more than 16 dB/cm was measured for a heater directly in contact with the wall of the waveguide ($x_d=0$) due to absorption of optical field by the metallic heater. For heater that has $x_d=3 \mu\text{m}$ distance, no additional optical loss is observed.

Therefore, as estimated from the mode field profile for the rib waveguide and from the experiment, it is concluded that a heater placed at a distance of more than $3 \mu\text{m}$ will not introduce any additional loss in the rib waveguides. The loss measurements to determine the effect of heaters are performed for only TE polarization.

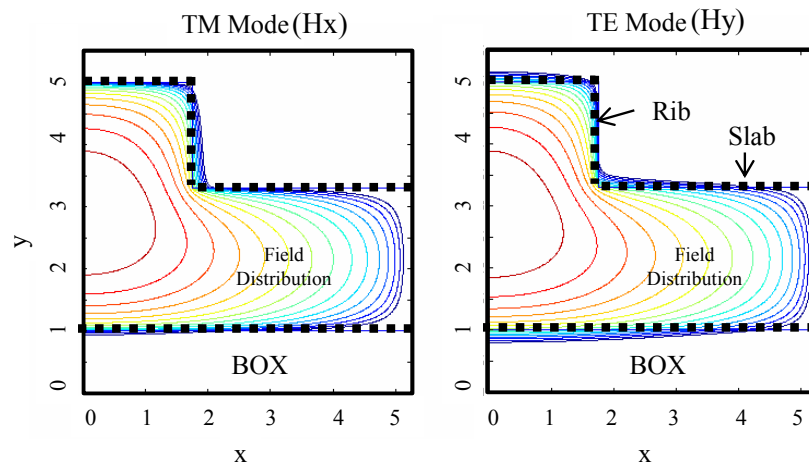


Figure 4.11: Mode profile for TE and TM polarized light in a rib waveguide. Dotted region shows the cross-section of the slab and rib section of the waveguide. All dimensions are in μm .

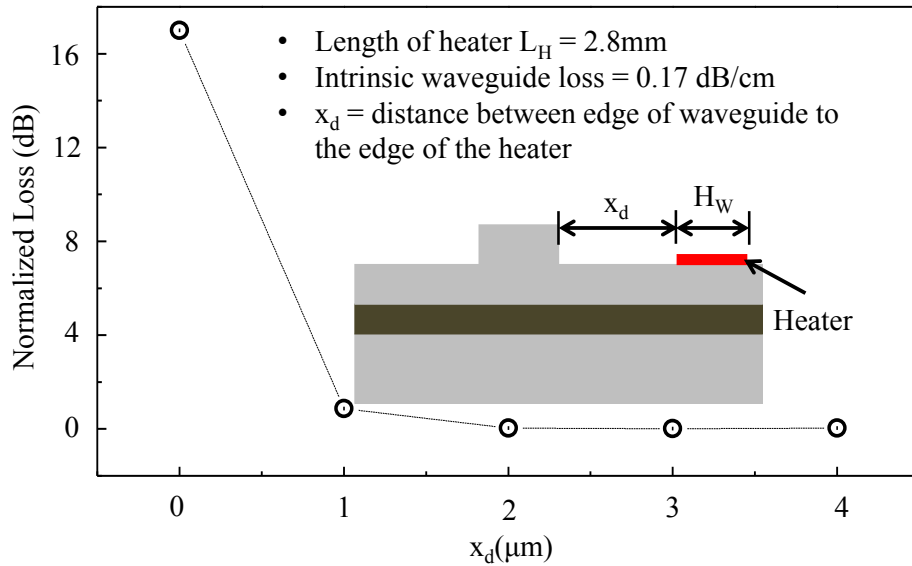


Figure 4.12: Magnitude of heater induced loss in the rib waveguides

On the basis of above discussion, it is concluded that it is safer to place the heaters at a distance of $3 \mu\text{m}$ from the edge of the waveguide. Along straight waveguides, the heaters are placed at a distance $x_d = 5 \mu\text{m}$ from the edge of the waveguide to provide some fabrication tolerance during the implementation of the parallel-serial filter. If the heaters are placed along the bent waveguides then $x_d = 10 \mu\text{m}$ is used.

4.4.2. Power Requirements of the Heater

An optimized position of the heater enhances efficiency of the heater, which is determined by the amount of electrical power P_{elec} required to achieve a certain phase shift $\Delta\Phi$. The electrical power applied to the heaters results in joule heating of the waveguide. In [17], an extensive thermal model is presented, which relates the amount of electrical power P_{elec} needed to achieve a certain phase shift $\Delta\Phi$. The thermal phenomenon resulting in raising the temperature of a waveguide from temperature T_1 to T_2 can be represented by an equivalent electrical circuit shown in the figure 4.11. Using the analogy between the electrical and thermal phenomenon, the heat flow rate Q is equivalent to the electrical power P_{elec} . The temperature change $\Delta T = T_2 - T_1$ is equivalent to electrical voltage V and electrical resistance is equivalent to the thermal resistance R .

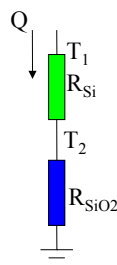


Figure 4.13: Electrical equivalent of a heater placed on a slab of a rib waveguide

$$Q = P_{elec} = \frac{\Delta T}{R_{eq.}} = \frac{\Delta T}{(R_{Si} + R_{SiO_2})} \quad (4.16)$$

In section 4.4.1, the discussion was focused only on the heat which diffuses laterally in the silicon slab. To take into account the heat which diffuses through the BOX into the substrate, consider the equivalent thermal resistance of both silicon slab R_{Si} and thermal resistance of oxide R_{oxide} are considered.

$$R_{Si} = \frac{h}{k_{Si}(H_w + 2L_d) \cdot L_H} \quad (4.17)$$

$$R_{SiO_2} = \frac{b}{k_{SiO_2}(H_w + 2L_d) \cdot L_H}$$

where H_w is the width of heater, L_d is the diffusion length and L_H is the length of the heater. The factor 2 takes into account the lateral diffusion in the direction of the waveguide and direction opposite to the waveguide. Using the above equations, the amount of electrical power P_{elec} required for generating phase shift $\Delta\Phi$ is given by:

$$P_{elec} = \frac{\lambda}{2\pi} \left(\frac{\partial n_{eff}}{\partial T} \right)^{-1} \Delta\phi(H_w + 2L_d) \left[\frac{h}{k_{Si}} + \frac{b}{k_{SiO_2}} \right]^{-1} \cdot \exp\left(\frac{x_d}{L_d}\right) \quad (4.18)$$

The factor $\exp\left(\frac{x_d}{L_d}\right)$ is a scaling factor which takes into account the exponential temperature decay along the slab section. It highlights the fact that as the distance between the heater and the waveguide increases (i.e. large x_d), more and more electrical power P_{elec} will be required to achieve an increase ΔT in temperature to achieve a phase shift $\Delta\Phi$. For $x_d = 0$, the heater is placed exactly beside the waveguide and the scaling factor is equal to 1 and requires the least amount of P_{elec} to produce a certain phase shift. As x_d (distance between heater and the waveguide) increases, the temperature decays exponentially and the amount of electrical power P_{elec} to increase ΔT for a phase shift of $\Delta\Phi$ has to be scaled to compensate for this temperature decay. Lastly, the term $\frac{h}{k_{Si}} \ll \frac{b}{k_{SiO_2}}$ and can be ignored and equation (4.18) reduces to:

$$P_{elec} = \frac{\lambda}{2\pi} \left(\frac{\partial n}{\partial T} \right)^{-1} \Delta\phi(H_w + 2L_d) \left[\frac{b}{k_{SiO_2}} \right]^{-1} \cdot \exp\left(\frac{x_d}{L_d}\right) \quad (4.19)$$

Small power P_{elec} to achieve a phase shift $\Delta\Phi$ requires small diffusion length L_D , narrow heater width H_w , and a large thickness b for the BOX. Intuitively, a thick BOX will prevent the heat to conduct through the oxide into the substrate and will effectively diffuse in the slab to heat the waveguide. Similarly, preventing heat to diffuse laterally in the direction opposite to the waveguide also results in an effective heating of the

waveguide. In [30], a comparison of different resistive heating mechanisms such as resistive heaters (which are used in this work), doped silicon, Nickel Silicide and Tungsten for silicon photonic circuits has been provided. It has been concluded in the work of [30] that the tuning efficiency, which is the amount of power needed to produce a certain phase shift, is independent of heating mechanism. Due to the ease of implementation of resistive heaters, this mechanism has been deemed the most suitable in the implementation of the parallel-serial filter.

4.4.2.1. Optimization of the Heater Design

From the discussion in section 4.4.2, it can be concluded that an efficient heater requires the optimization of the heater width H_w and diffusion length L_d . An efficient heater is the one which requires the minimum power P_{elec} to produce the desired phase shift $\Delta\Phi$.

To optimize the heater design, consider the direction of thermal flux (figure 4.14) from the heater towards the rib waveguide, BOX and the substrate. The large thermal conductivity of silicon allows the heat to reach the waveguide. The low thermal conductivity of oxide acts as barrier to prevent the heat flow into the substrate but a relatively thin BOX is not sufficient to prevent a significant fraction of the flux reaching the substrate. The lateral and the flux penetrating through the BOX into the substrate are shown by the yellow and red arrow respectively in figure 4.14. Clearly, the maximum flux ($2 \times 10^7 \text{ W/m}^2$) is downward into the substrate and the magnitude of lateral flux in the direction of waveguide and opposite to it is $\sim 1.6 \times 10^7 \text{ W/m}^2$.

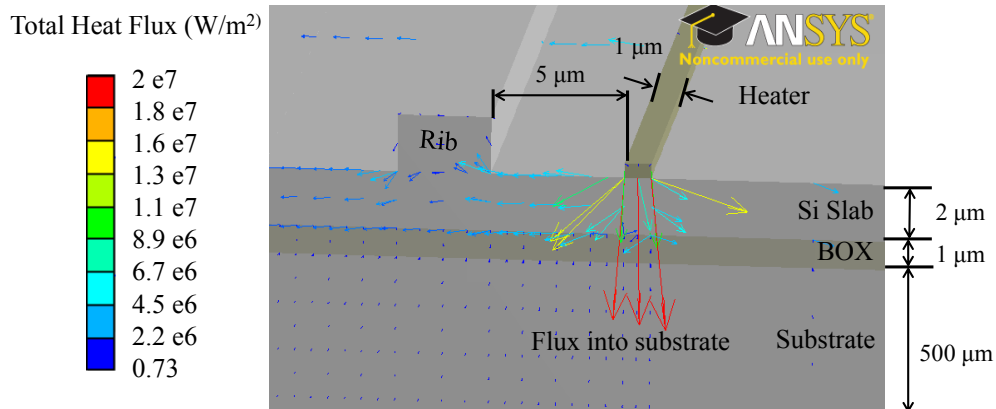


Figure 4.14: Direction of heater flux from heater into the substrate and in the Silicon slab.

To minimize the P_{elec} , the flux into the substrate and in the slab away from the waveguide has to be channeled (directed) towards the waveguide. A combination of grooves (trenches) by etching the silicon slab and an increased thickness b of the BOX can be used to channel the flux towards the waveguide. It is not practical to increase the thickness of the BOX. A more practical solution is to under-etch the silicon substrate under the heater [19,20]. This will be discussed in more detail in later part of this section. Figure 4.15 shows the simulation result for how thermal flux from heater is directed

towards the rib waveguide by combination of trenches (which are etched beside the heater and the rib waveguide) and the under-etching of the silicon substrate.

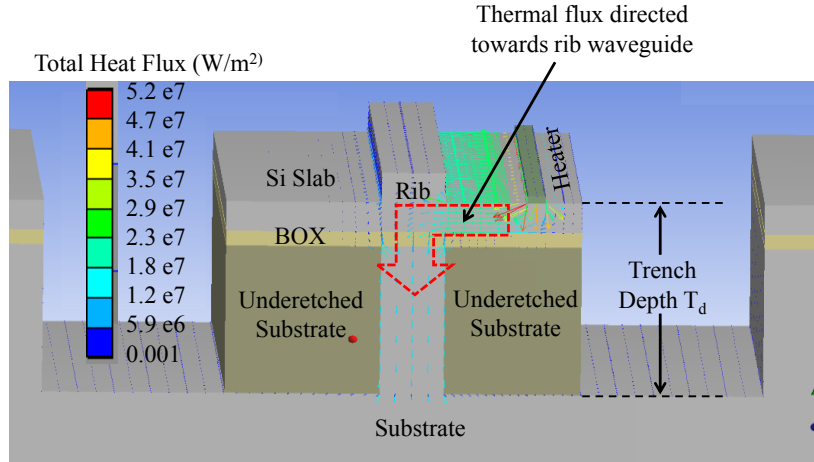


Figure 4.15: Combination of trenches and under-etched silicon substrate direct the heater thermal flux towards rib waveguide for improved efficiency of the heater

The etching of the trenches in the silicon slab limits the diffusion of heat across the trenches and thus limits the diffusion length L_d . Consequently, the amount of power P_{elec} to achieve a certain phase shift $\Delta\Phi$ (see equation 4.19) reduces. For an effective reduction of L_d , the location (position) and the depth of the trench needs to be determined.

A trench too close to the waveguide will result in reduced L_d to improve the power efficiency of the heater but will influence the optical properties of the waveguide. A simulation is performed by using the Beam Propagation Method (BPM) to estimate how far the optical field extends in the slab section. From the simulation result it has been found that the optical field does not extend beyond $6 \mu\text{m}$ in the silicon slab. Therefore, the trenches can be etched $x_{trench} > 6 \mu\text{m}$ from the edge of the rib waveguide. In section 4.4.1, it was found that the heater can be placed at $> 3 \mu\text{m}$ from the edge of the waveguide but for trenches the distance is doubled. The reason comes from the fact that the heater is placed on top of the slab region and the trenches are etched into the silicon slab. The optical field near the surface of the slab (where the heater is placed) is much smaller than the optical field inside the slab (see figure 4.11). Therefore, heaters can be placed closer than the trenches.

In order to optimize the depth T_D of the trench for the optimization of P_{elec} , a thermo-electric simulation is performed by using ANSYS 12.0. A schematic of the simulation setup is shown in the figure 4.17. The depth of the trench T_D is varied to determine an impact on the power requirements. A $5 \mu\text{m}$ wide heater is placed at a distance of $x_d = 5 \mu\text{m}$ from the rib waveguide. The trenches are $20 \mu\text{m}$ wide and are etched at a distance of $10 \mu\text{m}$ from the waveguide. Slightly larger separation between waveguide and heater (i.e. $2 \mu\text{m}$ more than minimum allowed separation between waveguide and heater) and waveguide and trenches (i.e. $4 \mu\text{m}$ more than minimum allowed distance between waveguide and trench) are assumed to ensure fabrication flexibility.

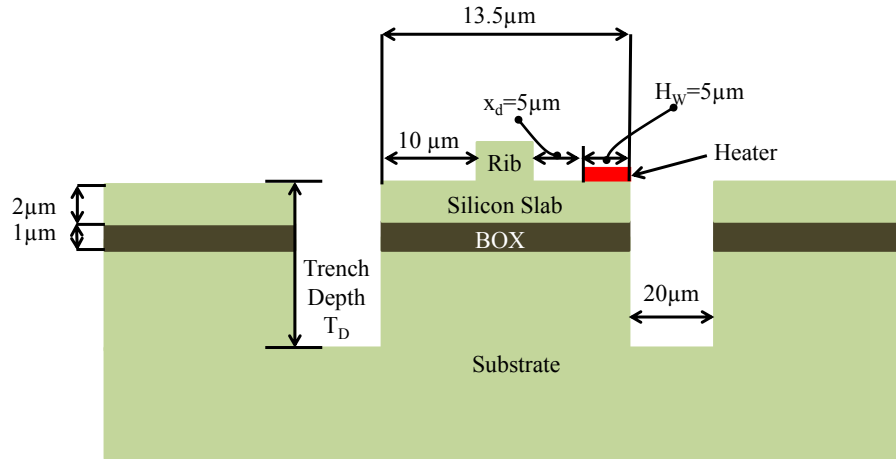


Figure 4.16: Schematic of the thermo-electric model to determine the effect of trenches on P_{elec}

The results from the simulation are presented in figure 4.18. The major effect of 48% reduction in the power requirement P_{elec} to produce a certain phase shift of $\Delta\Phi$ comes from etching the 2 μm thick silicon slab up to to the BOX layer. To check the accuracy of the simulation, it has been found that the first simulation point for the case of no trenches is in good agreement with the experimental value to achieve π phase shift in a 2-port MZI (see section 4.4.2.2). Etching of the BOX and deeper into the substrate further reduces the power requirements linearly (see figure 4.18). The power required to achieve a phase shift of π reduces from 136 mW for the no trench case to around 30 mW for trenches that are 200 μm deep. In the scope of this work, such deep trenches have not been implemented because the mechanical stability of SOI with very deep trenches has not been investigated. More over the deep etching took relatively large time.

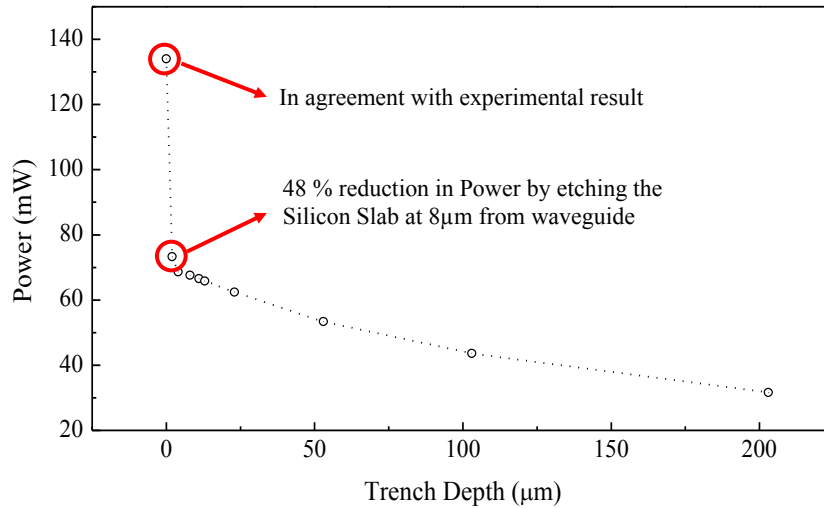


Figure 4.17: Influence of trench depth on the power requirements to produce π phase shift. The wafer had a total substrate thickness of 500 μm .

As discussed earlier, the etching of the trenches will limit the lateral conduction of heat in the silicon slab but it does not fully prevent the leakage of heat flux into the substrate. A possible solution is to etch the substrate under the heater. This is possible by back side etching of the substrate under the heater to ensure in-plane thermal conduction [19, 20].

This requires alignment from the back side of wafer, which is challenging. Another possibility is to use isotropic etching of substrate under the heater to avoid back side alignment. Simulation results have shown that $\sim 8\text{mW}$ of electrical power for π phase shift is required by using $100\mu\text{m}$ deep trenches and $8\mu\text{m}$ under-etching of substrate. In the scope of this work, such isotropic etching of the silicon substrate has not been used for the realization of the parallel-serial filter. Never-the-less, a recipe for the processing of such isotropic etches has been developed in the clean-room of TU Berlin. This development might be useful for some future activities involving thermo-optic effect in SOI devices. Figure 4.18 shows the SEM image of a $23\mu\text{m}$ deep trench with an isotropic etching of $\sim 8\mu\text{m}$.

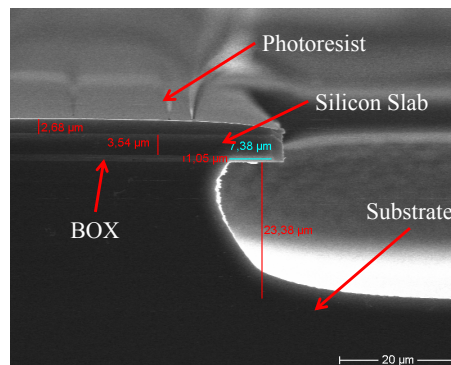


Figure 4.18: Under-etched substrate to minimize P_{elec} (Courtesy: Frau. Evelin Brose of HFT, TU Berlin)

Lastly, figure 4.19 shows the architecture of the heater which is used as a phase shifting element on the delay lines of a parallel-serial filter. In all designs for the parallel-serial filters, the length of the heater L_H is always more than $700\mu\text{m}$ and the thickness of the heater metal is between 100nm to 200nm (The choice of metal for heaters and choice of thickness will be discussed in section 4.6). Typically the top silicon is etched till the BOX layer to implement trenches. For some devices, trenches as deep as $10\mu\text{m}$ have been implemented.

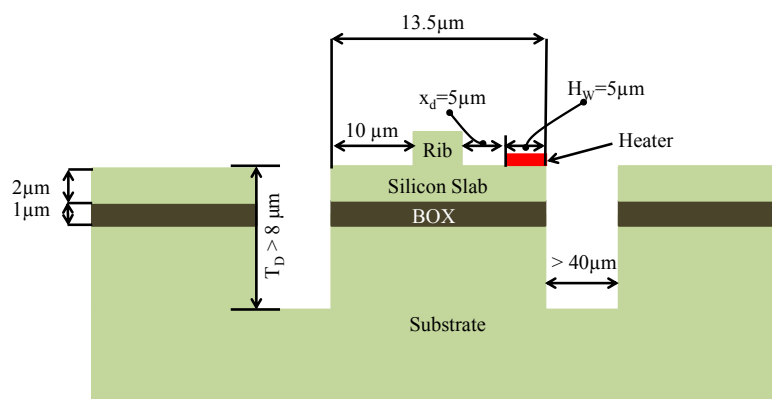


Figure 4.19: Heater design used as a phase shifting element on the delay lines of the parallel-serial filter. For all designs, the length of heater is always greater than $700\mu\text{m}$ and thickness of the heater metal is between 100nm and 200nm .

4.4.2.2. Power Requirements for the Phase Shifting Elements

For the experimental verification of the reduction of electrical power P_{elec} required to achieve a phase shift $\Delta\Phi$, measurements are performed on a simple 2-arm MZI with and without trenches. An existing design for the MZI is used which has previously been verified [8].

The MZI comprises two 2-port MMI couplers that are connected by waveguides having delay lengths of 25 ps (40 GHz). Heaters with width $H_W = 5\mu\text{m}$ are implemented at a distance of $10\mu\text{m}$ from the delay lines using 200 nm Titanium. The length of the heaters is $1400\mu\text{m}$. At a distance of $10\mu\text{m}$ from the heater and the delay lines Silicon slab of $\sim 2\mu\text{m}$ is etched to make trenches. Figure 4.20 shows the waveguide layout of the 2-arm MZI with heaters. The inset shows the configuration of the heater.

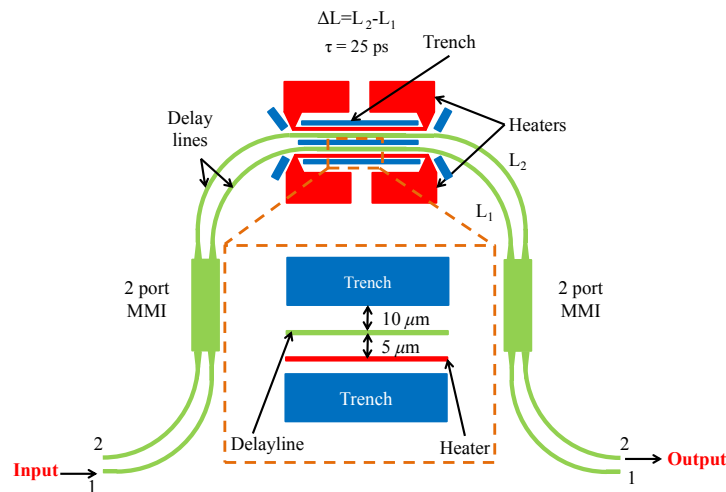


Figure 4.20: Waveguide layout of the 2-port MZI to determine the power requirements for the heaters (inset shows the configuration of trenches and heater).

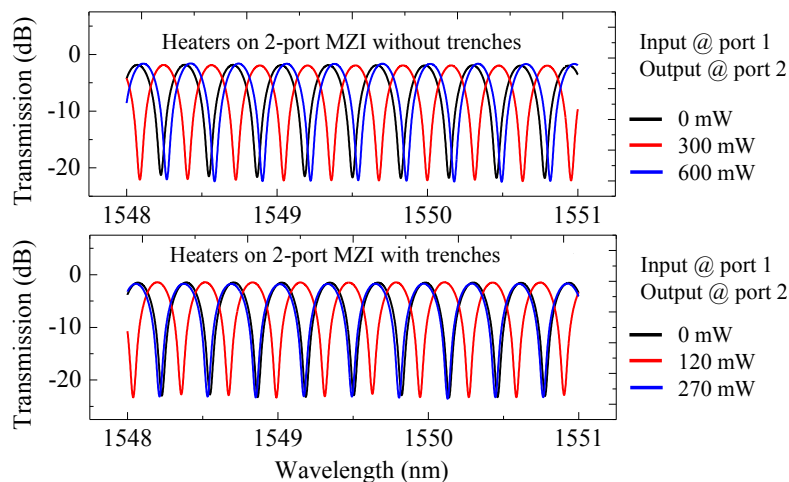


Figure 4.21: Power requirements for a non-trenched (top) vs trenched (bottom) heater as a phases shifting element of a 2-port MZI

The power requirement for an MZI with trenches is compared with the power requirement for an MZI without trenches. The input signal is applied at input port 1 and the output signal is received at output port 2 of the MZI (see figure 4.20). The measurement results for the two devices are shown in figure 4.21. The configuration of the heater for a trenched heater is shown in the insert of figure 4.20. For this experiment, trenches are implemented by etching the top silicon slab up to the BOX layer.

From the measurements, it was calculated that the non-trenched heater required P_{elec} of ~ 610 mW to produce 2π phase shift. By using equation 4.19 (section 4.4.2), which relates the power requirement P_{elec} of the heater to achieve phase shift $\Delta\Phi$, $P_{elec}=670$ mW is calculated. The difference between the measured and calculated value of values P_{elec} has less than 10% error and it might be associated to deviation of fabricated devices from the

values used in the calculation. For calculation, $\frac{\partial n_{eff}}{\partial T} = 1.86 \cdot 10^{-4}$ is assumed at 1550 nm.

$H_W = 5 \mu\text{m}$, $L_d=16 \mu\text{m}$, $b=1 \mu\text{m}$ and $K_{SiO_2}=1.2 \text{ W/m.K}$ is used.

The power was reduced to ~ 270 mW when trenches are implemented on the device. Although, the heater and trench dimensions are different from the simulation scenario of figure 4.15 but the 55 % reduction in power by etching the trenches matches well with 48 % reduction anticipated by the simulation result.

4.5. Designed Devices

In the last sections of this chapter, the components required for the implementation of the parallel-serial filter have been presented. Three different types of devices have been designed to demonstrate parallel-serial filters for residual dispersion compensation. They include a single stage of the parallel-serial filter (see figure 3.14), which is simply a 4-arm MZI comprising two 4x4 MMI couplers that are connected by delay lines. A two stage parallel-serial filter (see figure 3.14) and a two stage filter with enhanced tuning (see figure 3.18) are also designed.

The mask layouts for these three types of devices are shown in the figure 4.23, 4.23 and 4.24 respectively. The masks are designed by the using TexEDA LAYED, which is a commercial tool for mask layout of photonic circuits [31]. All masks have been designed by using a mask grid size of 1 μm . A small mask grid size is required to prevent phase errors on the delay lines due to variation in the path length of the delay lines during fabrication.

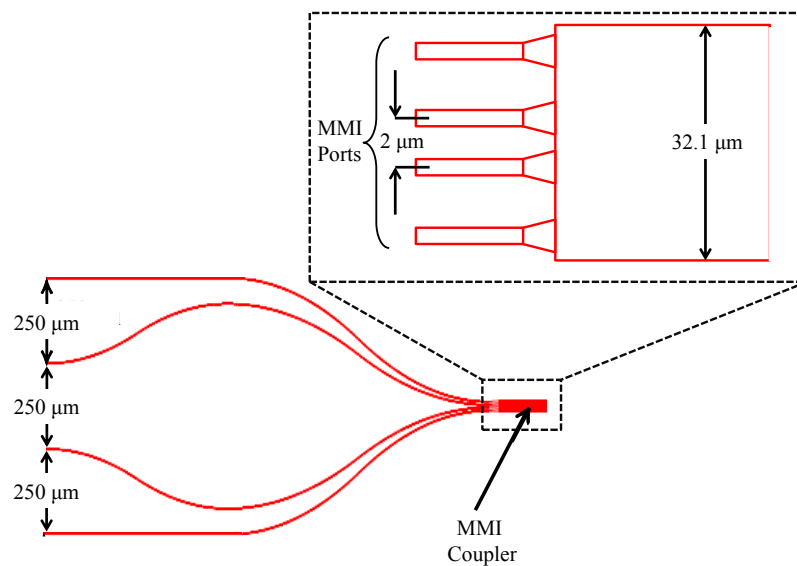
All designs are made for a FSR of 100 GHz ($\tau=10\text{ps}$), which requires a delay length of $\Delta L \sim 857 \mu\text{m}$ by using the expression [23]:

$$FSR = \frac{c}{n_g \cdot \Delta L} \quad (4.20)$$

where c is the speed of light in vacuum and n_g is the group index for the rib waveguide and has an assumed value of ~ 3.5 (a value higher than effective index n_{eff} and smaller

than simulated value of $n_g \sim 3.6$ is assumed to consider fabrication tolerances, see page 110).

The waveguide layout is designed considering the requirements related to space limitation of the measurement setup and the processing requirements of the devices. As mentioned in section 4.3, a minimum bending radius of 5 mm is used in all the designs to ensure low bending loss. Such a large value for the bending radius results in large sized devices. Folded waveguide layout design is used to reduce the size of devices. The 4-port MMI couplers used in this work have in- and out-coupling ports, which are very close (the central waveguides are only $2 \mu\text{m}$ apart) to each other. To relax the requirements of the fabrication process, the waveguides are separated from each other by using s-bends. A typical layout of MMI couplers with s-bends used in this work is shown in figure 4.22. The resulting pitch of the MMI ports after s-bends is $250 \mu\text{m}$.



The aspect ratio of the picture is changed for better clarity.

Figure 4.22: S-bends to separate the in-/out-coupling waveguides of an MMI coupler. All bends have been designed to have equal length.

Except for the single stage filter comprising a 4-arm MZI, all devices have an input and output waveguide pitch of $250 \mu\text{m}$, which is required for fiber-pig tailing of the devices. The pitch is only $50 \mu\text{m}$ for the single stage device.

On the basis of optimization performed in section 4.4, the phase shifting elements are placed at $5 \mu\text{m}$, when placed along a straight waveguide. When heaters are placed beside a bent waveguide then the distance is increased to $10 \mu\text{m}$. The width of the heater is $5 \mu\text{m}$. Trenches are etched at $10 \mu\text{m}$ from the walls of the waveguides (see figure 4.19).

The design for the trenches has evolved over the period of development for the devices. In the beginning, trenches were etched only beside the heaters to enhance the thermal efficiency of the heaters (see figure 4.24 (right)). For later designs, as shown by the design in figure 4.25, trenches are etched in such a way that the silicon slab in the neighborhood of the heaters is completely removed. This scheme is expected to minimize the effect of thermal cross-talk between the waveguide (specific data about thermal cross-talk is

presented in section 5.5). It is also ensured that the delay lines are as apart as possible (minimum value of $200\ \mu\text{m}$ is ensured for all designs of parallel-serial filter) so that the effect of thermal cross-talk is as small as possible. An added advantage of widely spaced delay lines is the availability of enough space to place large heater contact (in all designs, contact pads have a size of at least $150\ \mu\text{m} \times 150\ \mu\text{m}$). Large heater pads help in easier contacting and wire-bonding.

For all designs, the waveguide geometry and the MMI specifications mentioned in section 4.3 and section 4.2, respectively, are used. The sizes for the designed devices are $2.5\ \text{cm} \times 2\ \text{cm}$ (see figure 4.23), $2.8\ \text{cm} \times 2.4\ \text{cm}$ (see figure 4.24) and $3.7\ \text{cm} \times 2.5\ \text{cm}$ (see figure 4.25) for the single stage, two stage and enhanced two stage filters.

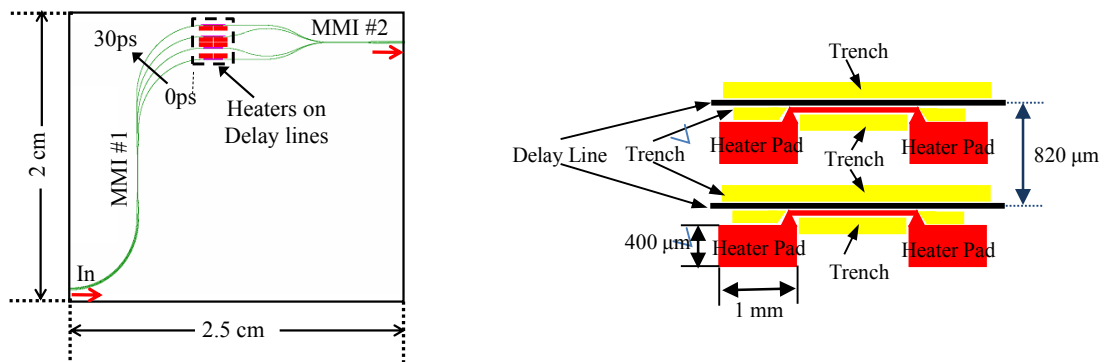


Figure 4.23: Mask design for the single stage of a parallel-serial filter (left) and two adjacent delay lines with heaters for phase shifting (right)

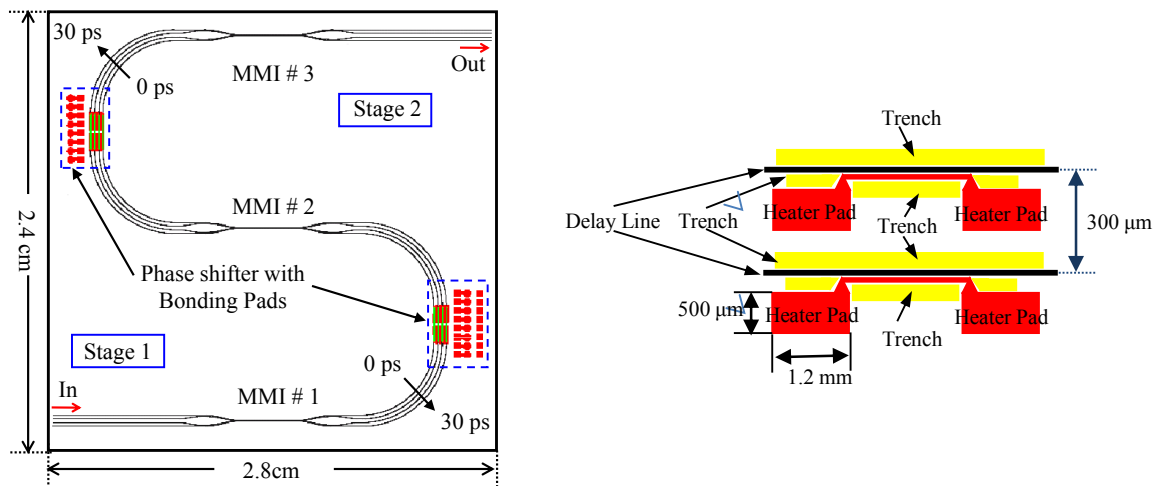


Figure 4.24: Mask design for the two stage parallel-serial filter (left), Heater design with trenches (right) along two adjacent delay lines

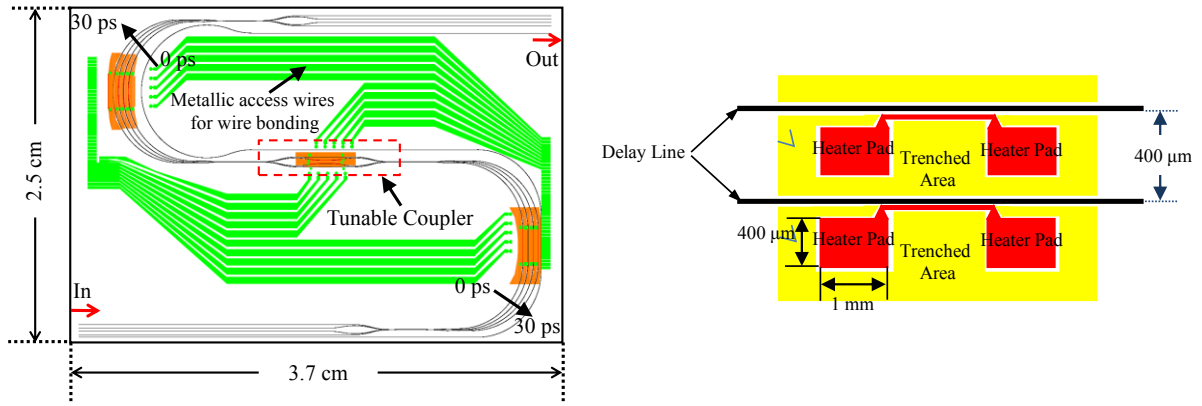


Figure 4.25: Enhanced two stage parallel-serial filter (left), two adjacent delay lines with completely etched silicon (yellow area) between delay lines for an improved design of the heaters (right)

Table 4.5 presents a summary of the important design specifications of the masks for single stage, two stage and enhanced two stage parallel-serial filter.

Table 4.5: Summarized mask specifications for single, two and enhanced two stage filter

Parameter	Single Stage SPF	Two Stage SPF	Enhanced two stage SPF
FSR	100 GHz	100 GHz	100 GHz
Delay Length for $\tau = 10$ ps	857 μm	857 μm	857 μm
Waveguide Width	3.5 μm	3.5 μm	3.5 μm
Bending Radii	> 5 mm	> 5 mm	> 5 mm
Waveguide pitch	50 μm	250 μm	250 μm
Heated Delay line pitch	820 μm	300 μm	400 μm
Size of the chip (including test structures)	2.6 cm x 2.6 cm	3.2 cm x 3.1 cm	3.7 cm x 3.2 cm
Minimum Heater Length	1.5 mm	2.5 mm	2.5 mm
Minimum Size of contact pad	400 μm x 1000 μm	1200 μm x 150 μm	250 μm x 250 μm

The layout of the devices has also considered placing maximum number of devices on a single chip. A snapshot of the single chip for a two stage parallel-serial filter device is shown in the figure 4.26. Straight waveguides, bent waveguides and MMI couplers are also placed on the chip for test purposes.

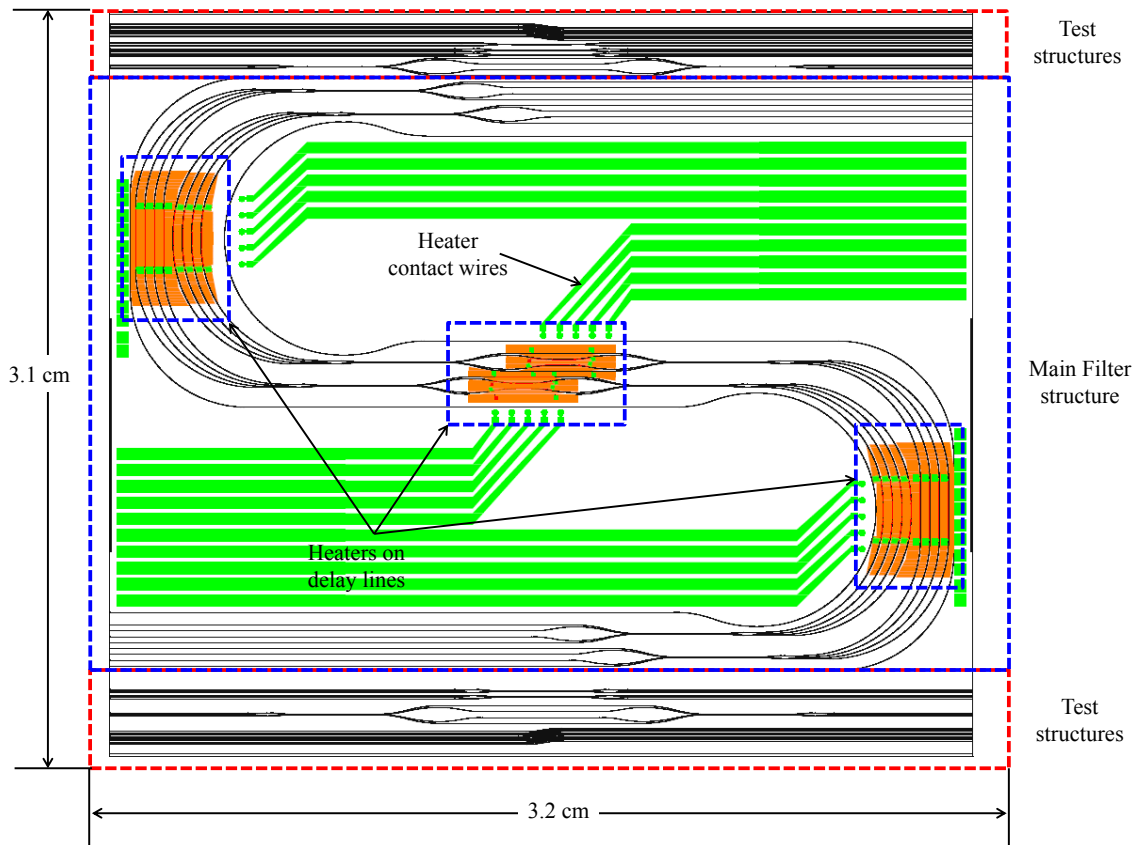


Figure 4.26: Mask file for a single chip showing the implantation of an enhanced two stage filter with test structures

Figure 4.27 and 4.28 show the wafer layout for the single stage and two stage devices on a 4 inch (100 mm) SOI wafer respectively. Apart from the main filter structures, test structures, structures for the alignment of different mask layers, structures for dicing the wafer into chips and for polishing of the chips are also placed on each mask.

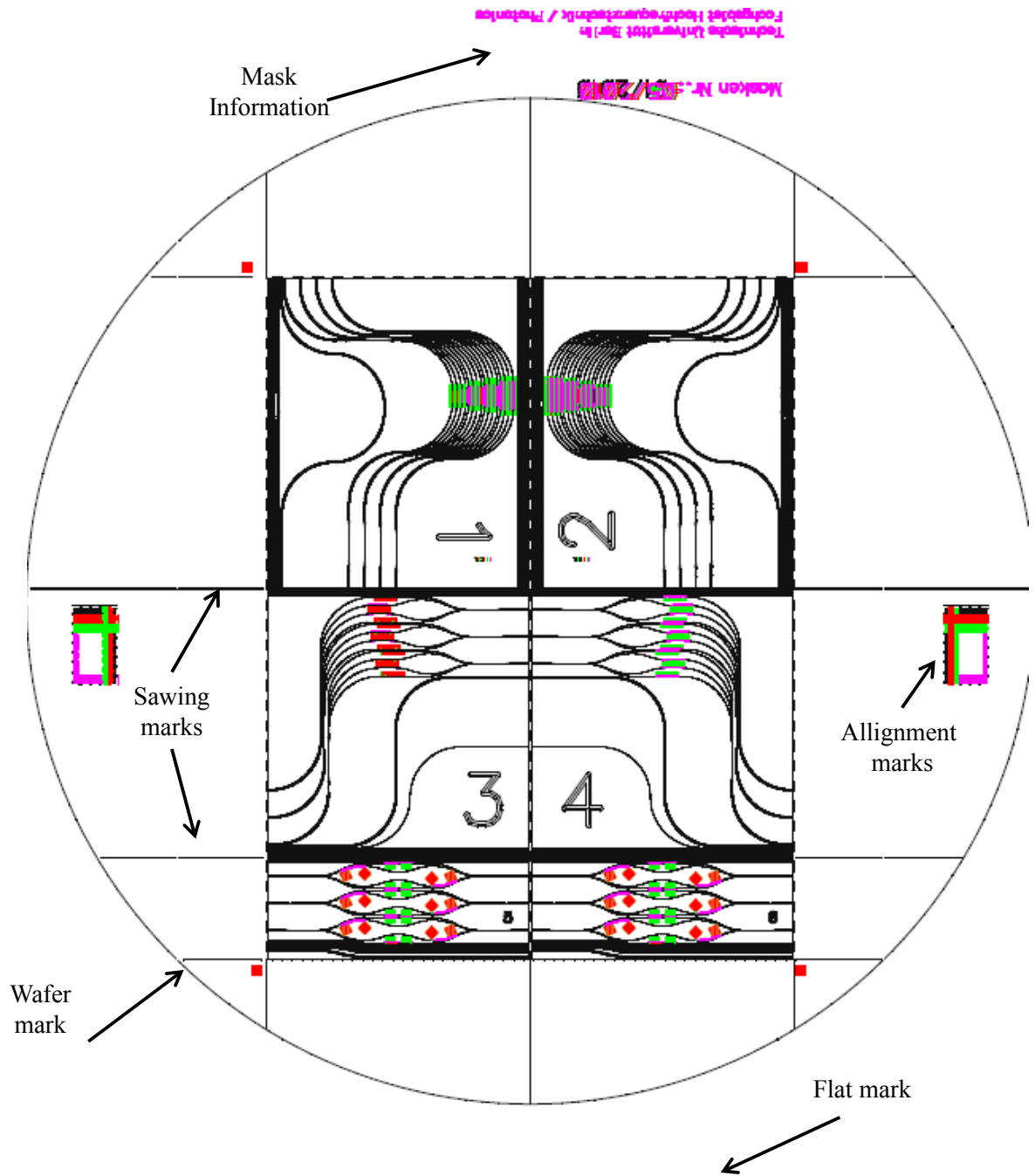


Figure 4.27: Full wafer mask layout for the single stage implementation of a parallel-serial filter

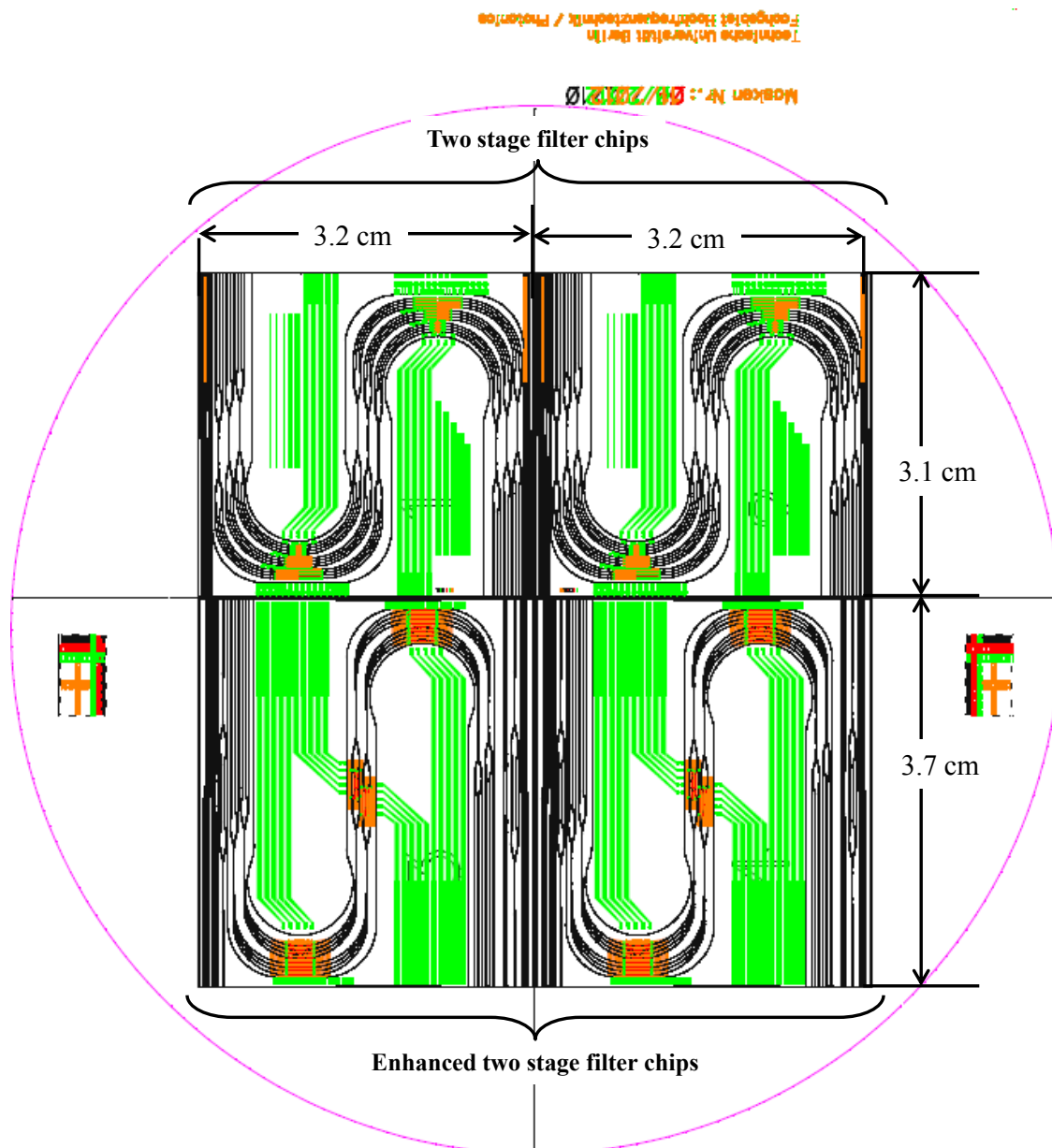


Figure 4.28: Two and enhanced two stage parallel-serial filter mask

4.6. Fabrication

The masks described in section 4.5 comprised four layers. The 1st includes the waveguide structures. The heaters are implemented using layer 2 and layer 3. The 2nd layer has heater structure and the 3rd layer has the contact pads for the heaters. The 4th layer has the trench structures.

E-beam writing of the 1st layer (waveguides) was carried out at the Heinrich Hertz Institute (Berlin). E-beam writing of the 2nd layer (heaters), 3rd layer (contact pads) and the 4th layer (trenches) was carried out in-house using the e-beam writing tool of Technische Universität Berlin. Masks for waveguides, heaters and contact pads are

bright field and the mask for the trenchesis the dark field mask. Depending on if the region with or without Chromium on the mask is used to define the structure determines if the mask is bright or dark field. A dark field mask is the one in which the region without Chromium is used to define the structure. Therefore, waveguide mask is bright field and the heater and contact pad masks are dark field.

The fabrication of the devices is carried out at the in-house clean-room of Technische Universitaet Berlin, which is a class 1000 clean room. 100 mm (4 inch) Bond and Back Etched SOI (BESOI) wafers with 4 μm Silicon layer and 1 μm BOX layer are used for the realization of the devices. BESOI wafers are developed by the Chemical Mechanical Polishing (CMP) to thin one of the two wafers which are bonded by oxidization. In this work, the top Silicon layer of the wafers used for the processing of the devices has a variation of ~ 500 nm in the thickness. Normally, the edges of the wafer are thinner than the middle region of the wafer.

The processing of the devices has four steps, which includes (1) the etching of the waveguides, (2) metallization for heaters, (3) metallization for heater pads and (4) etching of the trenches (grooves).

The first step is the patterning and etching of the rib waveguides and MMI couplers. A more detailed process is outlined in [8]. Here just a short description of the process is given:

For patterning positive photo-resist and contact lithography is used. The top silicon is etched by 1.8 μm with Reactive Ion Etching (RIE) at 200 K using SF_6 and CHF_3 . The developed waveguides have shown low surface roughness and anisotropic profile. Figure 4.29 shows the Scanning Electron Microscope (SEM) image for the cross section of a fabricated waveguide and the top view of a 4x4 MMI coupler. The more detailed processing steps related to the waveguide etching are presented in the section A and B of Appendix I.

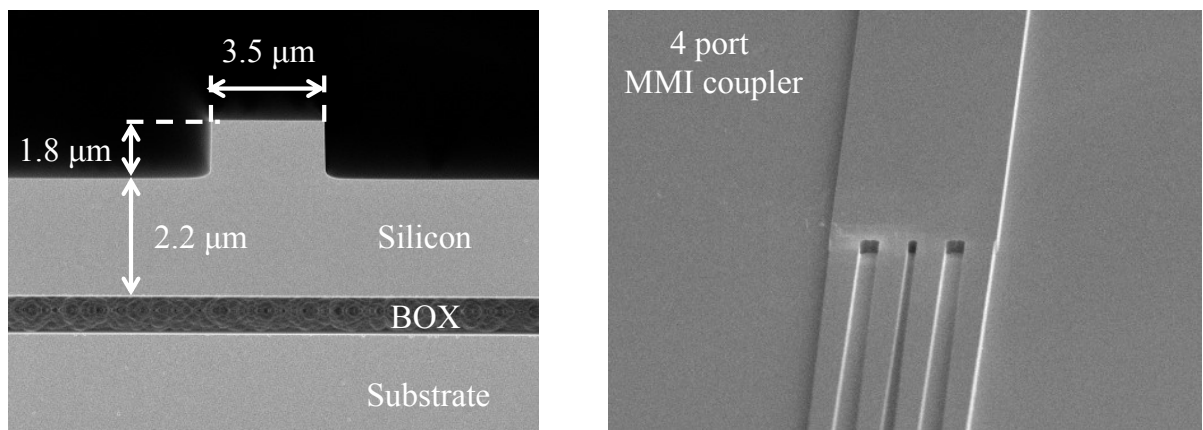


Figure 4.29: SEM image of the fabricated rib waveguide and an MMI coupler [8]

After the etching of the waveguides, heaters are implemented. The fabrication of the heater has two steps (i.e. step (2) and step (3)). The heater is composed of three parts, namely the (1) heating wire, (2) access arms and the (3) contact pads. An ideal heater

should have large resistance of the heating wire section and small resistance for the other parts. A typical heater structure used in the fabricated devices is shown in figure 4.30.

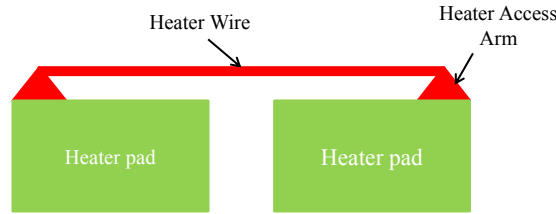


Figure 4.30: Typical heater structure

In step (2), the heater wire is implemented (thin metallization) and in step (3) the second (thick) metallization is performed for the implementation of the heater access arms and the contact pads. In both steps, metallization by evaporation is used. Three different metals, namely Titanium, Platinum and Aluminum are investigated for the implementation of the heaters. Sheet resistance R_s is used to determine the heater resistance delivered by each metal.

$$R = \frac{\rho L}{d W} = R_s \frac{L}{W} \quad (4.21)$$

Here, R is the resistance in Ω , R_s is the sheet resistance, ρ is the specific electrical resistance (resistivity) in $\Omega \cdot m$, L is the length of the metal and d is the metal thickness ($d \times W$ is the area of the cross-section).

To get the experimental data for R_s , different metals with various thicknesses of the metal are deposited on the Silicon wafer. 4 point probe is used to determine R_s . Experimental data of R_s for Titanium (Ti), Platinum (Pt) and Aluminum (Al) with layer thickness of 100nm, 200nm, 300nm, 400nm and 500nm are presented in figure 4.31.

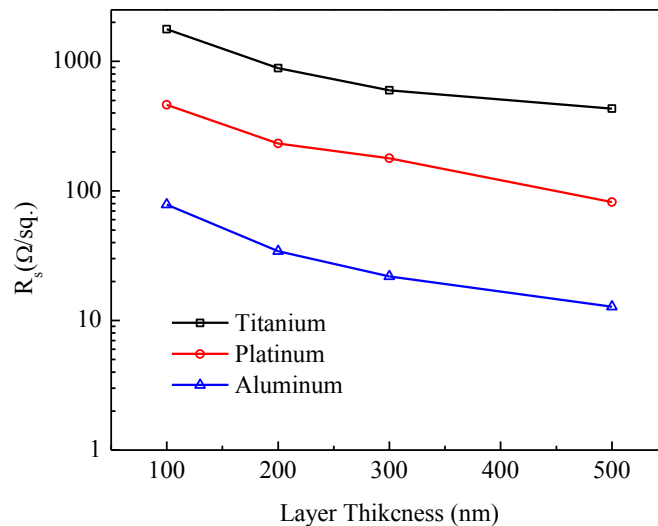


Figure 4.31: Measured sheet resistance R_s for Titanium, Platinum and Aluminum sheets of different thickness

By using the sheet resistance R_s for 100 nm Titanium, Platinum and Aluminum, the resistance values for 700 μm , 1400 μm , 2100 μm and 2800 μm long and 5 μm wide heater wires are presented in figure 4.32.

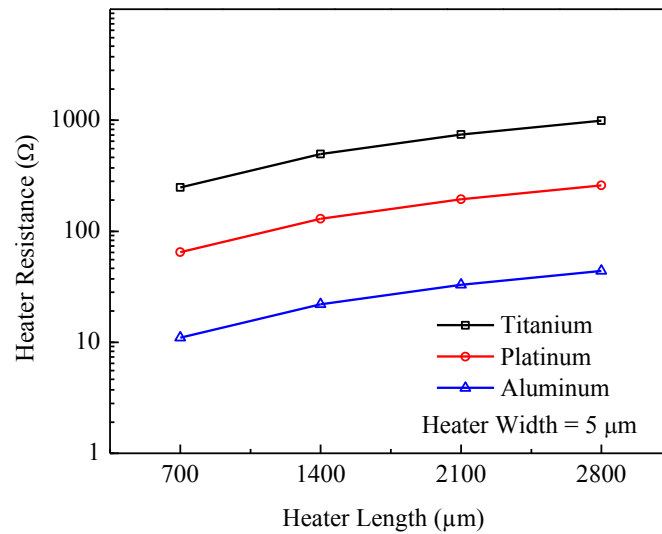


Figure 4.32: Heater resistance vs. length of heater

For the ease of processing and better compatibility with the wire-bonding system, Aluminum is chosen as the metal for the implementation of the heaters. By implementing heaters with different widths, it has been found that 5 μm wide heaters are most suitable to be implemented. Although narrow heaters (small H_W) increase the efficiency of the heater (see equation 4.19), the processing for heaters narrower than 5 μm was found to be challenging due to difficulties in the processing. 100 nm thick Aluminum layer is deposited by using Lift-off process. The deposition of metal is performed by using evaporation. For contact pads, a thicker Aluminum layer of 500 nm is used. The processing for both metallization steps is identical. More details about the metallization process are outlined in section C, D, E and F of Appendix I.

The last fabrication step (i.e. step (4)) is the formation of trenches for thermal isolation between delay lines and for improving the efficiency of the heaters. For the etching of Silicon slab, Inductively Coupled Plasma (ICP) etching using C_4F_8 and SF_6 is used. The BOX is etched by using RIE using CHF_3 and Ar at 288 K. To etch into the substrate, once again ICP is utilized. Typically, 8 μm –10 μm deep trenches are used for the implementation of parallel-serial filters. The detailed fabrication process for the etching of trenches is mentioned in section H of the appendix I. An SEM image of the waveguide with a heater and trench is shown in figure 4.33.

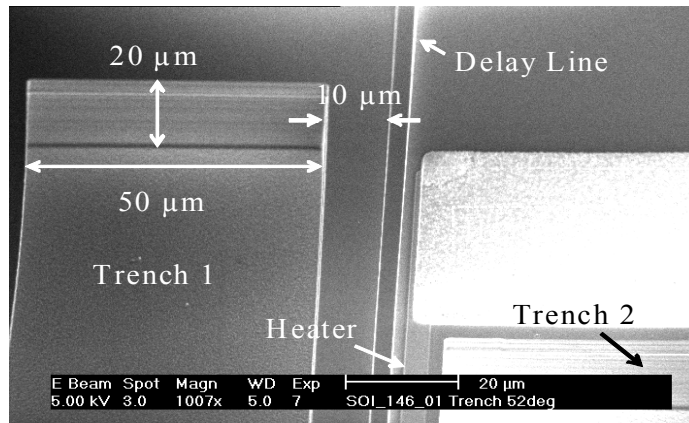


Figure 4.33: SEM images of a delay line with a heater and trenches beside the heater and the delay line

Later, the fabricated wafers are post-processed starting with the dicing of the wafer into chips. The chips are then grinded and polished to have smooth waveguide facets for efficient coupling. The chips are first grinded by using a high roughness Silicon Carbide (SiC) paper to reach the waveguide facets. On reaching there, reduced roughness SiC papers are used to smoothen out the surface, which makes the surface ready for polishing by using polishing suspension SF₁.

Unlike in [8], no SiO₂ is deposited on the chips for protection of the surface. The removal of SiO₂ layer requires Hydrofluoric (HF) acid, which removes the metallic heater structures also. Only thermo-plastic adhesives and glass dummies are used to protect chip surface end to provide extra mechanical strength to the SOI chips.

The polished chips are dipped in Acetone for at least 24 hours to remove thermo-plastic glue and later cleaned by using Acetone and Isopropanol.

Before, optical characterization of the fabricated parallel-serial filters, the facets of the in- and out-coupling waveguides are coated with 208 nm Silicon Nitride (Si₃N₄) at 208°C using PECVD. The nitride coating acts as an anti-reflection coating to reduce the in- and out- coupling from 1.5dB to less than 0.2 dB at $\lambda=1550$ nm [18]. Figure 4.34 shows fabricated enhanced two stage parallel-serial filters.

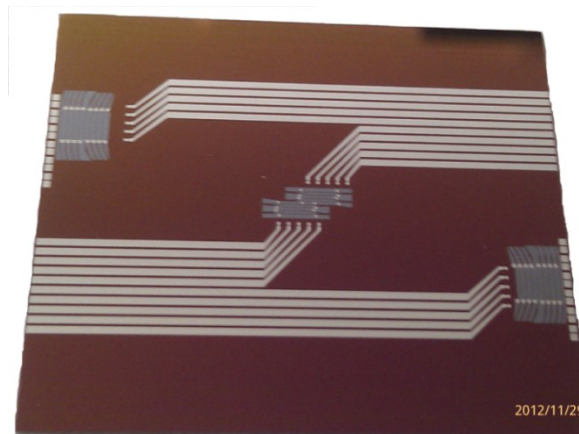


Figure 4.34: Photograph of the fabricated enhanced two stage parallel-serial filter

References:

- [1] Zimmermann, L.; Voigt, K.; Winzer, G.; Bruns, J.; Petermann, K., "Optimization considerations for 4 μm SOI-waveguide technology with respect to polarization dependence," Group IV Photonics, 2007 4th IEEE International Conference on , vol., no., pp.1,3, 19-21 Sept. 2007.
- [2] Voigt, K.; Zimmermann, L.; Winzer, G.; Hui Tian; Tillack, B.; Petermann, K., " C - Band Optical 90 °Hybrids in Silicon Nanowaveguide Technology," Photonics Technology Letters, IEEE , vol.23, no.23, pp.1769,1771, Dec.1, 2011.
- [3] Fischer, U.; Zinke, T.; Kropp, J.; Arndt, F.; Petermann, K., "0.1 dB/cm waveguide losses in single-mode SOI rib waveguides," Photonics Technology Letters, IEEE , vol.8, no.5, pp.647,648, May 1996.
- [4] G. Roelkens, D. Van Thourhout, and R. Baets, "High efficiency silicon-on-Insulator grating coupler based on a poly-silicon overlay," Opt. Express 14(24), 11622-11630 (2006).
- [6] P. Besse, M. Bachmann, H. Melchior, L. Soldano, and M. Smit, "Optical bandwidth and fabrication tolerances of multimode interference couplers," J. Lightw. Technol., vol. 12, no. 6, pp. 1004-1009, Jun. 1994.
- [7] Voigt, K.; Zimmermann, L.; Winzer, G.; Petermann, K., "SOI based 2x2 and 4x4 waveguide couplers - evolution from DPSK to DQPSK," Group IV Photonics, 2008 5th IEEE International Conference on , vol., no., pp.209,211, 17-19 Sept. 2008.
- [8] K. Voigt, "Interferometric devices based on 4 μm SOI material for application in optical telecommunications", PhD Thesis, Technische Universitaet Berlin, published 04.06.2012.
- [9] Leuthold, J.; Joyner, C.H., "Multimode interference couplers with tunable power splitting ratios," Lightwave Technology, Journal of , vol.19, no.5, pp.700,707, May 2001.
- [10] Lagali, N.S.; Paiam, M.R.; MacDonald, R.I., "Theory of variable-ratio power splitters using multimode interference couplers," Photonics Technology Letters, IEEE , vol.11, no.6, pp.665,667, June 1999.
- [11] J. Komma, C. Schwarz, G. Hofmann, D. Heinert and R. Nawrodt, "Thermo-optic coefficient of silicon at 1550nm and cryogenic temperatures" Appl. Phys. Lett. 101 , 041905 (2012).
- [12] V. Passaro, F. Magno, and A. Tsarev, "Investigation of thermo-optic effect and multi-reflector tunable filter/multiplexer in SOI waveguides," Opt. Express 13, 3429-3437 (2005).
- [13] U. Fischer, T. Zinke, B. Schüppert, K. Petermann Singlemoded optical switches based on SOI-waveguides with a large cross-section Electronics Letters, Vol. 30, No.5, pp.406-408, 1994.

- [14] M. Harjanne, M. Kapulainen, T. Aalto, and P. Heimala, "Sub- μ s Switching Time in Silicon-on-Insulator Mach-Zehnder Thermo-optic Switch," *IEEE Photon. Technol. Lett.* 16 , 2039-2041 (2004).
- [15] M. W. Geis, S. J. Spector, R. C. Williamson, and T. M. Lyszczarz, "Submicrosecond Submilliwatt Silicon-on-Insulator Thermo-optic Switch," *IEEE Photon. Technol. Lett.* 16 , 2514-2516 (2004).
- [16] Rahim, A. ; Schwarz, S. ; Bruns, J. ; Voigt, K. ; Winzer, G. ; Zimmermann, L. ; Schäffer, C. ; Petermann, K., "Silicon Photonic Implementation of a scalable OFDM Demultiplexer", *Photonics Technology Letters*, 2013.
- [17] U. Fischer, "Entwicklung und Optimierung eines integriert-optischen Schaltmoduls in Silizium", PhD Thesis, Technische Universität Berlin, 1995.
- [18] M. Schnarrenberger, "Optische Filter aus Silizium-Rippenwellenleitern", Ph.D Thesis, Technische Universität Berlin, Sept. 2008.
- [19] A. D McConnell and K. E. Goodson, "Thermal conduction in silicon micro- and nanostructures", in *annual review of heat transfer*, vol. 14, pp. 19-168, 2005.
- [20] X. Jack Hu, Ankur Jain, Kenneth E. Goodson, " Investigation of natural convection boundary condition in microfabricated structures", in *International of thermal sciences*, vol. 47, pp. 820-824, 2007.
- [21] B Vermeersch, B.; De Mey, G., "A Fixed-Angle Heat Spreading Model for Dynamic Thermal Characterization of Rear-Cooled Substrates," *Semiconductor Thermal Measurement and Management Symposium*, 2007. SEMI-THERM 2007. Twenty Third Annual IEEE , vol., no., pp.95,101, 18-22 March 2007.
- [22] Masana, F.N., "A closed form solution of junction to substrate thermal resistance in semiconductor chips," *Components, Packaging, and Manufacturing Technology, Part A, IEEE Transactions on* , vol.19, no.4, pp.539,545, Dec 1996.
- [23] Smit, M.K.; Van Dam, C., "PHASAR-based WDM-devices: Principles, design and applications," *Selected Topics in Quantum Electronics, IEEE Journal of* , vol.2, no.2, pp.236,250, Jun 1996.
- [24] Bogaerts, W.; Baets, R.; Dumon, P.; Wiaux, V.; Beckx, S.; Taillaert, D.; Luyssaert, B.; Van Campenhout, J.; Bienstman, P.; Van Thourhout, D., "Nanophotonic waveguides in silicon-on-insulator fabricated with CMOS technology," *Lightwave Technology, Journal of* , vol.23, no.1, pp.401,412, Jan. 2005.
- [25] H. Tian, G. Winzer, A. Gajda, K. Petermann, B. Tillack, and L. Zimmermann, "Fabrication of low-loss SOI nano-waveguides including BEOL processes for nonlinear applications," *J. Eur. Opt. Soc., Rapid Publicat.*, vol. 7, pp. 12032-12037, Aug. 2012.

- [26] circuit Roelkens, G. and Vermeulen, D. and Van Thourhout, D. and Baets, R. and Brisson, S. and Lyan, P. and Gautier, P. and Fédéli J.-M., "High efficiency diffractive grating couplers for interfacing a single mode optical fiber with a nanophotonic silicon-on-insulator waveguide" in Applied Physics Letters, 92, 131101 (2008).
- [27] Soldano, L.B.; Pennings, E. C M, "Optical multi-mode interference devices based on self-imaging: principles and applications," Lightwave Technology, Journal of, vol.13, no.4, pp.615,627, Apr 1995.
- [28] Abdul Rahim, Stefan Schwarz, Jürgen Bruns, Lars Zimmerman, Sheikh Jalil Ahmed, Christian G. Schäffer, Klaus Petermann, "16-Channel O-OFDM Demultiplexer in Silicon Photonics" accepted in OFC 2014, Th3F.2.
- [29] A. Densmore, S. Janz, R. Ma, J. Schmid, D. Xu, A. Delâge, J. Lapointe, M. Vachon, and P. Cheben, "Compact and low power thermo-optic switch using folded silicon waveguides," Opt. Express 17, 10457-10465 (2009).
- [30] A. Masood, M. Pantouvaki, G. Lepage, P. Verheyen, J. Van Campenhout, P. Absil, D. Van Thourhout, W. Bogaerts, Comparison of heater architectures for thermal control of silicon photonic circuits, Group IV Photonics, South Korea, p.ThC2 (2013).
- [31] <http://texeda.de/laytools.htm>
- [32] Internal Seminar Presentations by Dr. Karsten Voigt in Summer Semester 2013.

5.

Characterization of Parallel-Serial Filters

This chapter is dedicated for the characterization of the fabricated parallel-serial filter. Initially, the measurement setup and the measurement method are described. Later, the device preparation steps for fabrication and the results for characterization are presented for single, two and enhanced two stage parallel-serial filters.

5.1. Measurement Setup

The measurement setup for the characterization of the fabricated devices comprises the following components:

- Agilent Photonic Loss and dispersion analyzer (PDLA)
- Polarization filter
- Polarization Controller
- Lensed fibers

Before the characterization of the devices, some pre-adjustments are necessary to be made on the measurement setup. One such adjustment is the measurement of the fiber-fiber (F2F) loss and the group delay (GD). The insertion loss of the device is computed by normalizing with reference to the F2F loss. This also ensures good quality of optical connection between the optical source, receiver and the connecting fibers. Figure 5.1 shows the measured F2F loss and GD for the measurement loop over a bandwidth of 20 nm from 1540 nm to 1560 nm. F2F loss measurement takes into account the propagation loss in the lensed optical fibers, connectors which connect the fibers with the laser, polarization controller & the photo-detector, the insertion loss of the polarization controller and the coupling loss between in- and out-coupling lensed fibers. Figure 5.2 shows the measurement schematic for F2F loss and GD measurement.

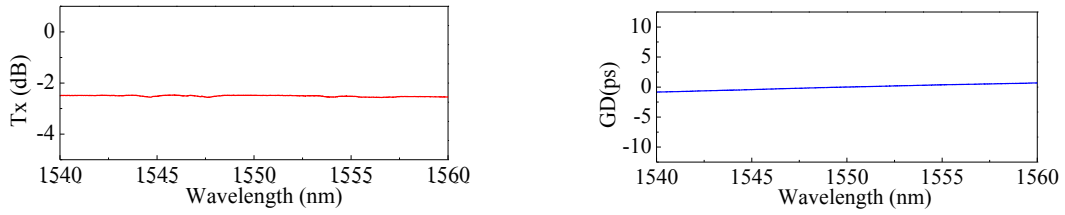


Figure 5.1: F2F insertion loss (left) and the GD (right) for the measurement loop.

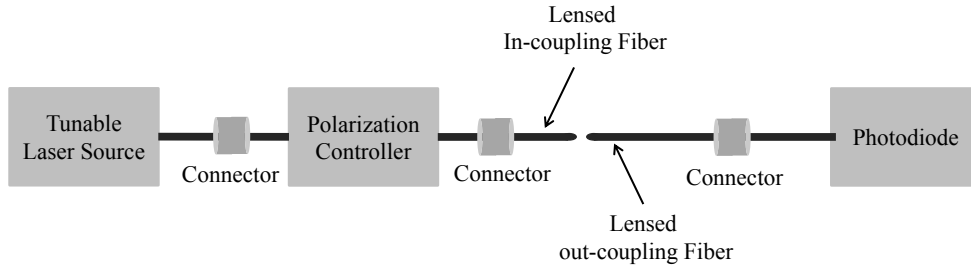


Figure 5.2: Schematic for the measurement of F2F loss and GD

A second pre-measurement step is the adjustment of the polarization to characterize the device for a certain polarization. The setup for the adjustment of the polarization is shown in the figure 5.3. The optical signal from the laser sources passes through a polarization controller before reaching the lensed in-coupling fiber. The light emerging from the lensed fibers is focused by using a focusing lens on the photodiode (PD) after passing through a chopper and a polarization filter. The electrical signal of the photodiode (PD) and the output of the chopper are observed on an oscilloscope.

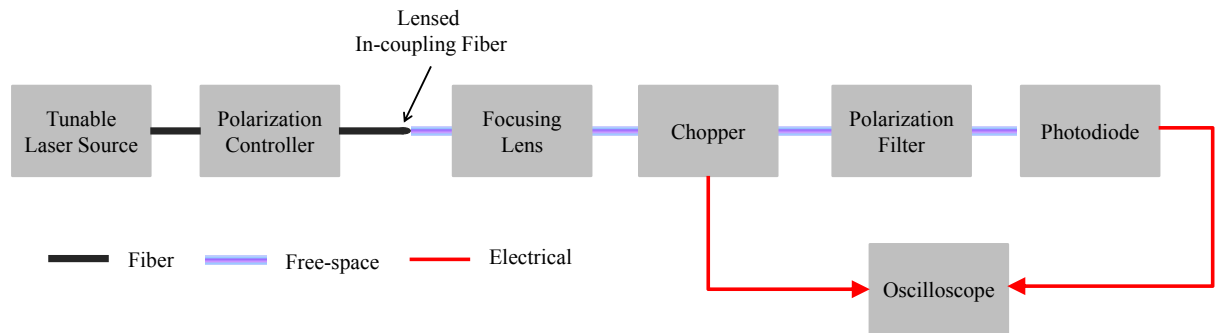


Figure 5.3: Setup for the adjustment of TE/TM polarization at the tip of the in-coupling lensed fiber

The combination of polarization controller and polarization filter enables the setting of a certain state-of-polarization (i.e. TE or TM) at the tip of the in-coupling fiber. The state-of-polarization at the tip of the in-coupling lensed fiber can be adjusted by changing the settings of the half wave plate and the quarter wave plate of the polarization controller. If the polarization of the optical signal coming from the in-coupling fiber is orthogonal to the settings of the polarization filter then no signal reaches the PD. If this signal has the same polarization as the polarization filter then the PD detects the maximum signal.

5.2. Dispersion Measurement Techniques

This work is focused on the measurement of dispersion from an integrated photonic filter. An existing technique used for the measurement of chromatic dispersion in single mode fibers is employed to determine the dispersion of the integrated photonic filter.

The three main methods to measure the chromatic dispersion in optical fibers, which are recognized by the International Telecommunication Union (ITU) are [18]:

- Time-of-flight method
- Interferometric method
- Modulation Phase Shift (MPS) method

The time-of-flight method is also known as the pulse delay technique. This technique uses the time delay due to different group velocities of the optical pulses of different wavelengths propagating through the optical fiber to determine the chromatic dispersion. The pulses at the output of the fiber are detected by a fast photo-detector and recorded by a sampling oscilloscope. The time delays of the pulses with different wavelengths are recorded after propagation through a fiber of known length [3]. Chromatic dispersion is obtained by differentiating the group delay with respect to the wavelength. This method can measure large values of dispersion without requiring a reference signal and it is fast [17].

The interferometric method uses either a MZI or a Michelson interferometer with a white light source [3, 18]. One arm of the interferometer uses the test device/fiber and the other arm has a reference fiber with a known group delay or an adjustable air gap. The cross-correlation of test fiber beam and the reference beam determine the group delay of the fiber/device under test. This method is ideally suited for short fibers and has a very high group delay resolution of up to 0.1 ps.

In the modulation phase shift method, the intensity of a laser source is intensity modulated by an intensity modulator. This modulated signal is fed to the fiber/device under test. The phase of the reference signal is compared with the phase of the envelope at the output of the device/fiber under test to determine the group delay. The wavelength is swept during the measurement and chromatic dispersion is obtained by differentiating the group delay with respect to the wavelength. This technique has an accuracy of 0.02 ps/nm and has a resolution of group delay in the order of 0.1 ps. This technique works well for both long fibers and short devices such as FBGs and PICs. The sweeping of the wavelength makes this technique slow as compared to the other techniques. A variant of the phase shift method uses the modulation of both the amplitude and frequency of the laser signal. This method is called as differential modulation phase shift method [19].

5.3. Measurement Method

For the characterization of the parallel-serial dispersion compensating filters, the Modulation Phase Shift (MPS) method is used to measure the group delay response of the filter. This method measures the group delay response of a device by measuring the change in the phase of a sinusoidal RF modulation envelope as the wavelength is changed [1]. More details about the MPS are available at [2, 3].

MPS utilizes a tunable optical laser source. Modulation is impressed by using an external Mach-Zehnder modulator and recovered by an amplified optical receiver. The change of phase $\Delta\Phi$ is converted to an equivalent change in group delay $\Delta\tau$ according to following expression:

$$\Delta\tau_{(\Delta\lambda)} = \frac{\Delta\phi^0}{360^0} \cdot \frac{1}{f_m} \quad (5.1)$$

Here, $\Delta\Phi$ is the change in phase in degrees when the wavelength is varied; f_m is the RF modulation frequency; $\Delta\lambda$ is the incremental wavelength change and $\Delta\tau$ is the group delay being measured and has units of seconds.

Agilent 86038B Photonic Loss and Dispersion Analyzer (PDLA) is used to obtain the transmission and group delay of the parallel-serial filter. The F2F measurement is performed by using the tunable laser source of the PDLA. Later, the parallel-serial filter is placed between the input and the output fiber to determine the transmission and the group delay response. Figure 5.4 shows the block level representation of the measurement setup for transmission and GD characterization of the parallel-serial filter. For the characterization of the parallel-serial filter lensed fibers are used. The mode field diameter of the lensed fibers is around $3.3 \mu\text{m}$. This provides a good match between the mode field diameter for the coupling fibers and the waveguides which are $3.5 \mu\text{m}$ wide. As a result the coupling loss between the coupling fibers and waveguides is reduced.

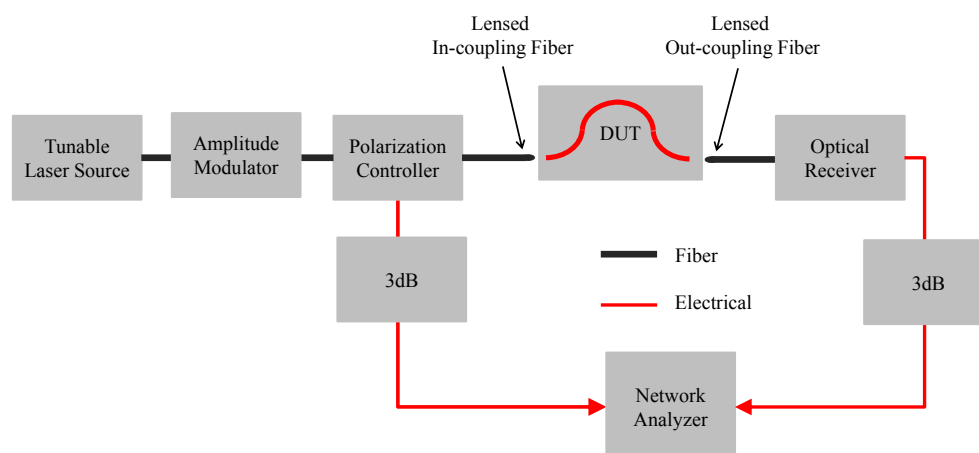


Figure 5.4: Block level representation of the measurement setup for transmission and GD characterization of the parallel-serial filter. Excluding the DUT, all the other components are embedded inside the PDLA.

It is important to optimize the settings of the PDLA to achieve reliable measurements especially for characterizing small sized PICs (PDLA is typically used for characterizing optical fibers). The appropriate settings for the PDLA are determined the amount of dispersion D delivered by a device, which is defined by:

$$D = \frac{\Delta\tau}{\Delta\lambda} \quad (5.2)$$

Here, D is the dispersion in ps/nm, $\Delta\tau$ and $\Delta\lambda$ are group delay and wavelength increment respectively. Combining equation (5.1) and (5.2) leads to:

$$\Delta\phi = 360 \cdot D \cdot \Delta\lambda \cdot f_m \quad (5.3)$$

Equation (5.3) explains that the amount of phase change $\Delta\Phi$ for an incremental wavelength change depends on the dispersion D , wavelength step $\Delta\lambda$, and the modulation frequency f_m .

In order to see the effect of phase noise, equation 5.3 can be written as:

$$\Delta\phi = 360 \cdot D \cdot \Delta\lambda \cdot f_m + \Delta\phi_{noise} \quad (5.4)$$

Equation (5.4) highlights that a decrease in the size of the wavelength increment $\Delta\lambda$ and/or RF modulation frequency f_m , the effect of phase noise will increase. An appropriate choice of wavelength increment and RF modulation frequency is required for accurate characterization of the parallel-serial filter. The typical settings used for the characterization of the parallel-serial filter are as follows.

Measurement Bandwidth	1540-1560 nm
Wavelength Increment ($\Delta\lambda$)	1 pm – 3 pm
RF Modulation Frequency	1100 MHz

By using these settings, a group delay resolution of ~ 1 ps (for $\Delta\lambda = 1$ pm) – ~ 3 ps (for $\Delta\lambda = 3$ pm) is achieved. This results in phase resolution $\Delta\phi$ of $\sim 0.4^\circ$ for 1 ps and $\sim 1.2^\circ$ for 3 ps. The parallel-serial filter is designed to compensate couple of hundreds of ps/nm of dispersion ($D = \Delta\tau / \Delta\lambda$), therefore, the above resolutions are sufficient to provide reliable measurements.

5.4. Device Preparation for Measurements

One of the key challenges in the characterization of SOI devices is the temperature dependence of Silicon. This requires that the measurements of the SOI filters are performed on a measurement setup that ensures constant temperature to prevent a shift

in the transfer function of the filter. The chips are normally placed on a constant temperature surface (sample holder), which is regulated by a temperature controller. Furthermore, the temperature of the measurement laboratory is also maintained at a level, which is lower than the temperature of the measurement setup so that the variations in the temperature do not influence the characteristics of the measured device. The measurements presented in this chapter are performed for laboratory temperature of 24 °C (with a variation of < 1°C) and the temperature of the sample holder (surface on which the chip is placed for measurement, see figure 5.8) is maintained at 35 °C.

The preparation of the device for measurement starts by mounting the SOI filter on an Aluminum carrier (chip carrier), which is later placed on another temperature controlled Aluminum surface (sample holder). To provide thermal conductivity between the SOI chip and the Aluminum chip carrier, commercially available thermally conductive glue is used. A flexible PCB is also mounted on the Aluminum chip carrier to provide an interface for the DC biasing of heaters. A schematic representation of a chip on an Aluminum carrier is shown in figure 5.5.

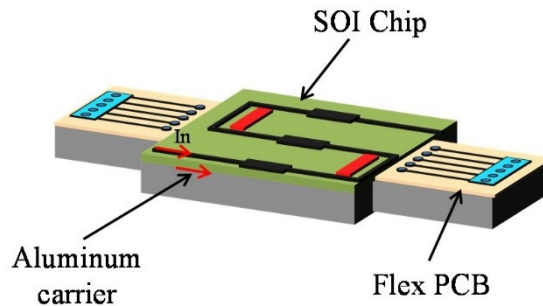


Figure 5.5: Schematic of the SOI chip mounted on an Aluminum carrier with an electrical PCB

The parallel-serial filters have metallic heaters, which are placed beside the delay lines. They act as the phase shifting elements and are based on the thermo-optic effect. Normally, contact needles are used for DC biasing of these phase shifters. To access more heaters, commercially available needle probe heads [4] are also used. Both approaches require careful handling, are bulky and require a lot of space on a measurement setup. One possibility is to wire-bond the heaters. For the characterization of the parallel-serial filter, wire-bonding of the heaters is done by using ultra-sonic wedge wire bonding using 20 μm aluminum wires. As highlighted in section 4.5, the fabricated devices are large in size, mainly due to the requirement of large bending radii. This requires long wire bonding from chip to the external PCB. The stability of the wire-bonds decreases with increase in the length. The wire-bonding is optimized to ensure long and stable wire bonding for the biasing of the heaters. The wire-bonded heaters are connected to a PCB, which is implemented by using flex PCB. This prevents a further increase in the size of the device and accounts for the limited place available to mount a chip on the chip holder of the measurement setup.

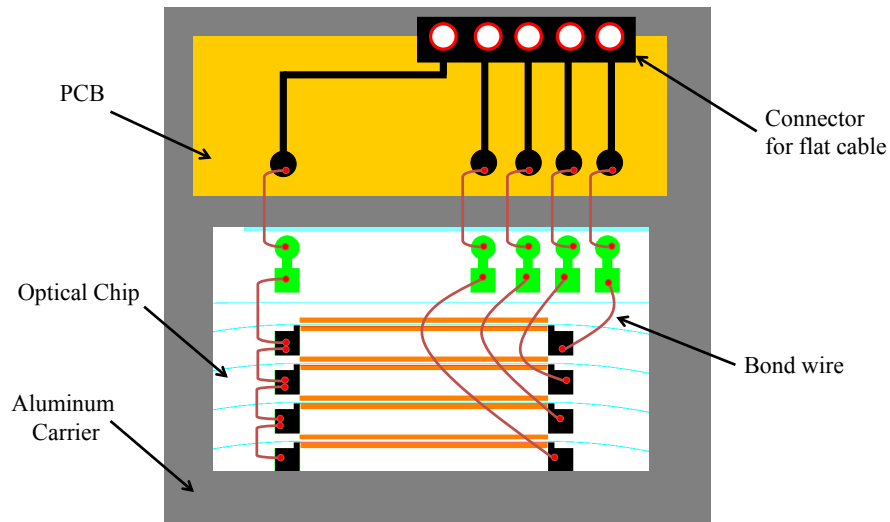


Figure 5.6: Interfacing heaters on SOI chip to the electrical PCB for DC biasing

The wire bonding of heaters with electrical PCB is schematically shown in figure 5.6. The process and steps involved in the mounting of an SOI chip on a carrier and its wire bonding to an electrical PCB for the biasing of on-chip heaters is shown in figure 5.7.

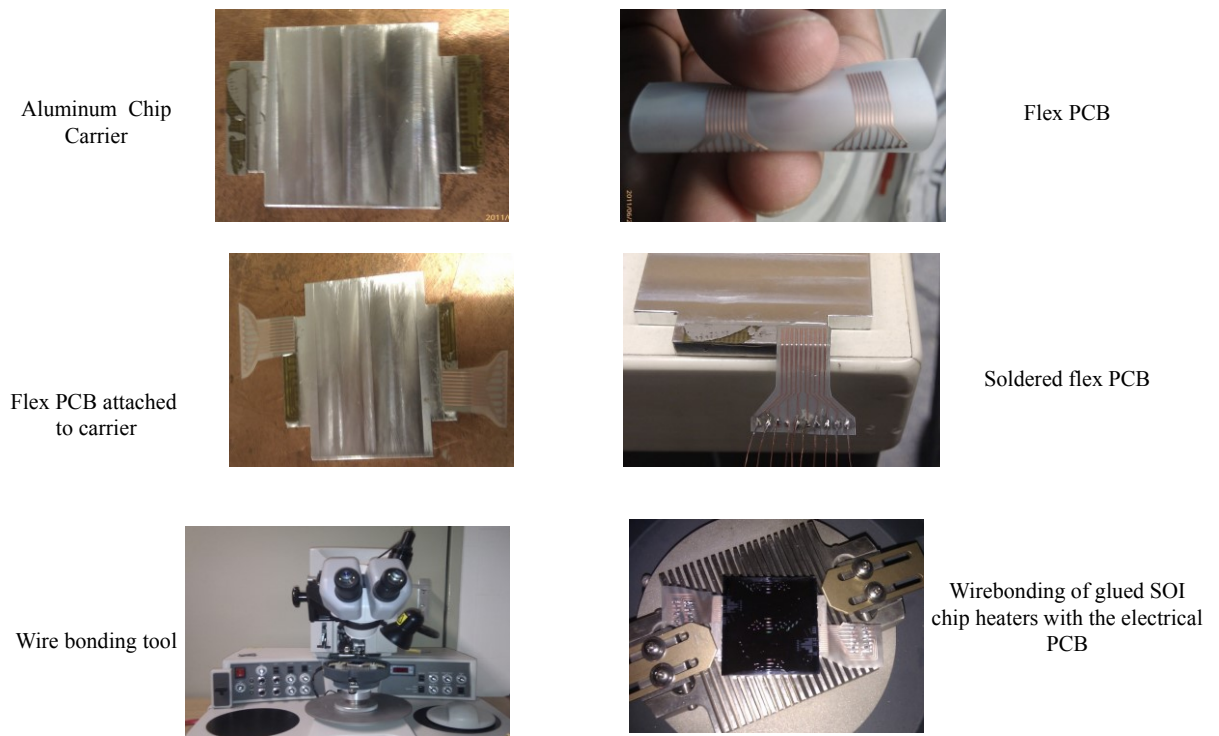


Figure 5.7: Steps involved in the preparation of SOI chip for measurement

Figure 5.8 shows an exemplary chip placed on the measurement setup for characterization.

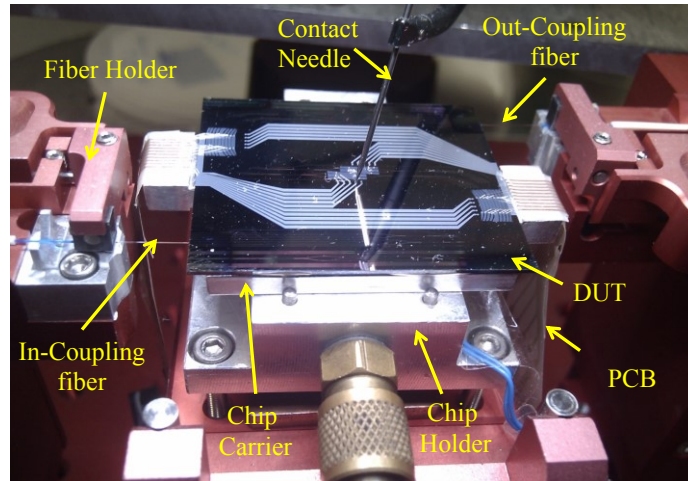


Figure 5.8: A prepared SOI chip placed on measurement setup for characterization

5.5. Single Stage Parallel-Serial Filter Characterization

The single stage parallel-serial filter lacks the functionality of a dispersion compensator due to its limited order. It is a 4-arm MZI and it has only 3 zeros ($R=3$). On the other hand, the realization and characterization of a single stage helps to provide an in-sight into the development of a full scale parallel-serial filter. The design parameters such as power requirement for phase shifting and optimum placement of heaters and trenches can be verified and further optimized before the full scale implementation of the device. Above all, the characterization of the single stage provides a good proof-of-concept to move towards full scale implementation of the parallel-serial filter.

Figure 5.9 shows the schematic representation of the 4-arm MZI (single stage of a 6th order parallel-serial filter). It comprises two 4-port MMI couplers, which are connected by delay lines with a unit delay $\tau=10$ ps for an $FSR = 100$ GHz. The first MMI coupler acts as a splitter and the second MMI coupler acts as a combiner. Phase shift by using thermo-optic effect is provided on the three delay lines to achieve a relative phase shift between the signal which is split by the first MMI coupler and delayed by the delay lines before recombination in the second MMI coupler.

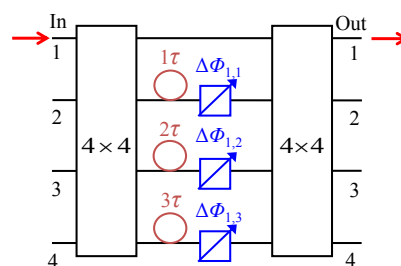


Figure 5.9: Schematic representation of a single stage (4-arm MZI) of a parallel-serial filter

5.5.1. Transmission and Group Delay Characterization

The transmission and group delay of the 4-arm MZI serving as a single stage of the parallel-serial filter is analyzed by using the measurement setup (see figure 5.4) and technique mentioned in section 5.3. The device is characterized for TE and TM polarizations. In this section, the results for only one of the polarization are presented and discussed. The effect of polarization on the device performance will be addressed in section 5.8. For measurement results shown in this section, the input signal is applied at port 1 of the first coupler and the output signal is received at port 1 of the second coupler.

Figure 5.10 shows the typical measurement result for transmission and group delay for a 4-arm MZI. In this case a phase shift of 170° is applied on the 30 ps delay line. For every *FSR*, the group delay has three peaks (one going up and two going down). These three peaks come from the interplay of the three group delay contributions from three zeros of a 4-arm MZI. The result shown in figure 5.10 is for a measurement which is performed over a bandwidth of 4 nm and has 5 *FSR*s. The device shows good uniformity in each *FSR* and small variation in the extinction ratio. The devices are designed for an *FSR* = 100 GHz, but the measured *FSR* is only 97 GHz. The reason for this variation can be attributed towards the variation in the thickness of the SOI wafer and difference in the assumed ($n_g=3.5$) and actual group index for the waveguides. It had later been measured by characterizing a 4-port MZI that the group index has a value of 3.6 for TE polarization and 3.599 for TM polarization.

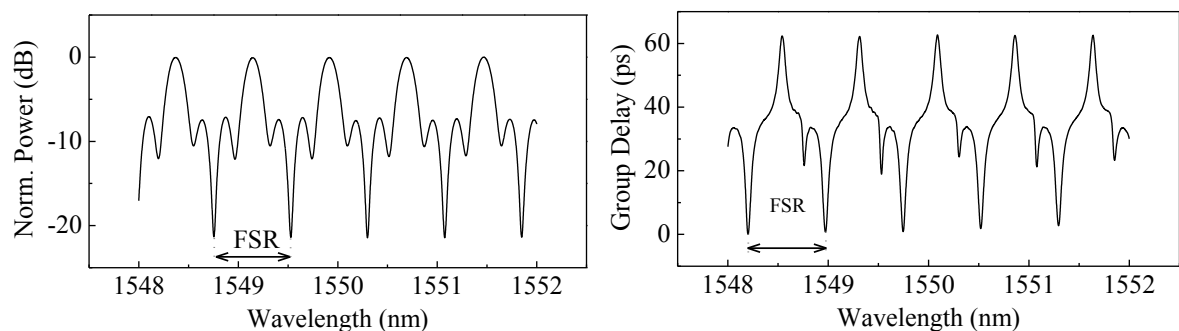


Figure 5.10: Measured Transmission (left) and Group delay (right) for the 4-arm MZI after phase tuning by using heaters on the delay lines

The ideal transmission and group delay response, which is obtained by using transfer matrices for ideal MMI couplers and delay lines is shown in figure 5.11 (top row). The intrinsic response, which is the response of the device without any phase shift, is different from the ideal transmission and group delay response. The main reasons for this variation are the non-optimum behavior of the MMI couplers in terms of their phase accuracy and imbalance. Also, the wavelength of the optical input signal (1550 nm) is much smaller than the length of the delay lines ($\sim 860 \mu\text{m}$). This means that a small

variation in the length of the delay line will result in a large deviation in the phase of the optical signal propagating along the delay line. For example, at 1550 nm a length variation of 100 nm in the delay lines will lead to a phase error of $\sim 23^\circ$, which is sufficient to make the response of the device to deviate from desired response. For example, figure 5.11 (bottom row) compares the transmission and group delay of an ideal 4-arm MZI (dotted-black) with the transmission and group delay for a 4-arm MZI, which has a phase error of 45° on the $1\tau=10$ ps (see figure 5.9) delay line (solid-red).

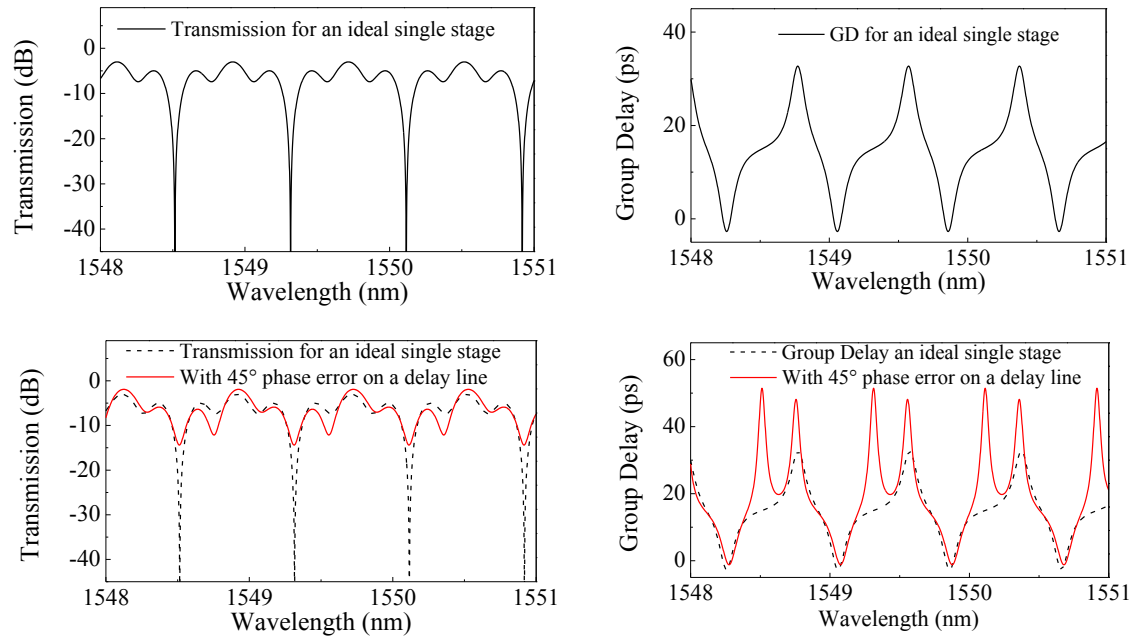


Figure 5.11: Top row shows the transmission and group delay for an ideal 4-arm MZI, Bottom row shows a comparison of the simulated transmission and group delay of the 4-arm MZI with and without phase error on the delay lines.

Similarly, a deviation in the coupling coefficients of the MMI couplers results in a deviation of the device performance. As mentioned in section 4.2, the images (output) of the MMI couplers have both magnitude and phase. Therefore, a deviation in either or both of them will result in the deviation of the device performance. This has been shown by the simulation result shown in figure 5.12, in which the coupling coefficient between input port 1 and output port 1 (first element of matrix in equation 3.32) of the input MMI coupler is changed from an ideal value of -6 dB to -7 dB. Similarly, it can be shown that a variation in the phase of the images of the MMI couplers leads to the variation in the response of the 4-arm MZI.

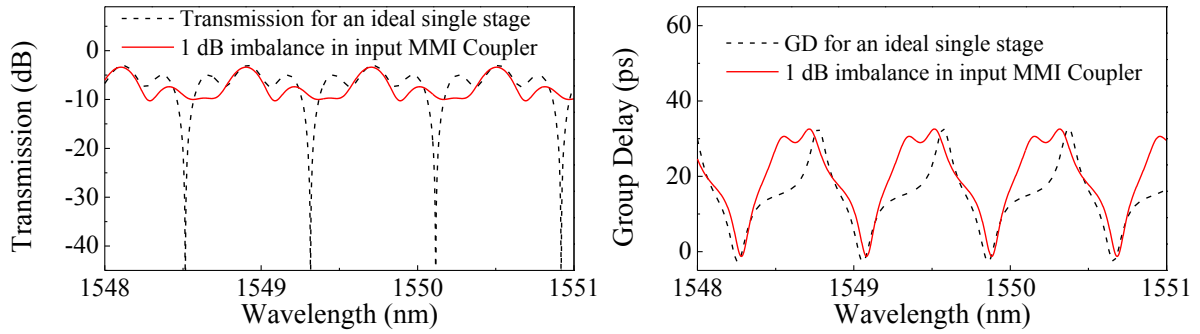


Figure 5.12: Deviation in the response of a 4-arm MZI due to variation in MMI coupler performance.

Phase errors on delay lines are less critical in undermining the performance of the filter because these errors can be compensated by using the heaters on the delay lines to heat the waveguides [5]. On the other hand, the coupling coefficients of the MMI couplers cannot be compensated. Therefore, the performance of the MMI couplers is a determining factor for the performance of the parallel-serial filter. A common consequence of the errors on delay lines and MMIs is the degradation of the extinction ratio of the transmission response [6].

For the fabricated devices, a very good agreement between the measurement result and simulation result is achieved by taking into account the imbalance in MMI couplers and phase errors on the delay lines and MMI couplers. For matching the measurement results with simulation, the imbalance and phase errors for the MMI couplers are kept within the characterized values of less than 0.7 dB and 5° respectively (see reference [7] and table 4.2 in chapter 4). The simulation is performed by the Transfer Matrix Method (TMM). In this method the transfer matrices of the MMI couplers and delay lines are multiplied to achieve the transfer function of the filter (see chapter 3). Figure 5.13 shows the good agreement between measured (solid-red) transmission (left) and group delay (right) for the fabricated device and the simulation result (dashed-black).

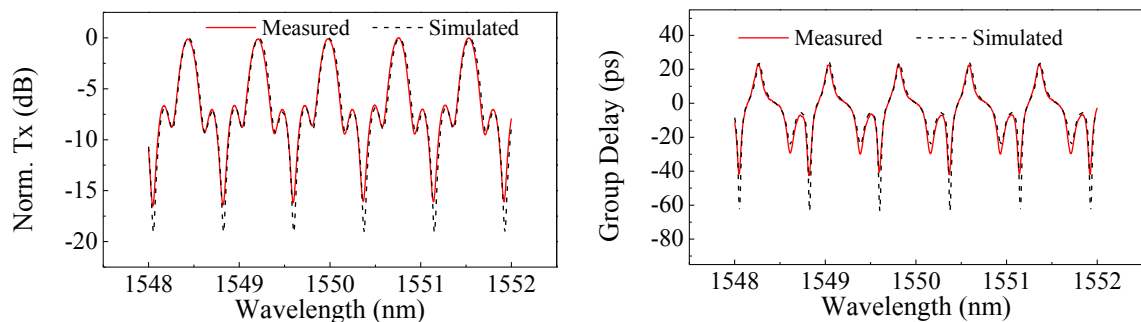


Figure 5.13: Measured vs. simulated transmission and group delay for the single stage of the parallel-serial filter

For an M-arm MZI to be used in the realization of a dispersion compensating filter, the phase on each delay line needs to be changed independently. A change in the phase on one delay line changes the relative phase relation for the other delay lines. If a phase

change on one delay line changes the phase on other delay lines then the required relative phase relation to tune a dispersion compensating filter using M-arm MZI becomes cumbersome. The thermo-optic effect to change the phase on the delay lines is used to tune the parallel-serial filters. Therefore, it is highly desirable to have minimal thermal cross-talk between the delay lines so that a phase change on one delay line does not influence the other delay lines. To quantify the amount of thermal cross-talk, a test heater (see figure 5.14) is placed at a distance comparable to the distance between the heated sections of the delay lines of a MZI. If there is thermal cross-talk then the effect of this test heater should produce a temperature change at the delay lines. This temperature change produces an undesired phase shift at the delay lines and changes the transfer function of the filter. Figure 5.14 shows the schematic used to test the thermal cross-talk between heaters.

To tune a dispersion compensator, the maximum phase change required on a delay line is not more than 2π . Therefore, a power which is larger than the power needed to bring 2π phase shift on a delay line is applied to the heater to quantify the thermal cross-talk for the worst case scenario. The effect of temperature rise produced by the test heater on the transmission and group delay has been measured. Since, all the outputs will be influenced therefore any output can be measured to see the influence. Figure 5.15 shows the transmission and group delay of the device for an input at port 1 and output at port 3 of the MZI. The measurement results are for a heater placed at $275\ \mu\text{m}$ from the delay line.

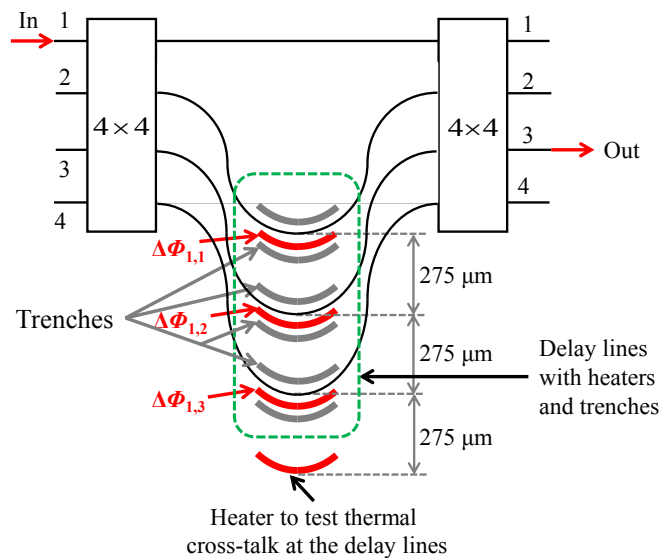


Figure 5.14: A test heater placed at a distance equal to the pitch of the delay lines ($275\ \mu\text{m}$) of a 4-port MZI to quantify the effect of thermal-cross talk

It is seen in Figure 5.15 that as the electrical power of the heater is increased from 0 mW to 255 mW, the transmission and the group delay of the MZI shifts along the wavelength axis, while the FSR has remained constant. The overall response for transmission and group delay has not changed with the increase in electrical power of the heater. This shift along wavelength axis means that the heater has increased the substrate

temperature. This increase has influenced the four delay lines equally and the relative phase for the four delay lines has not been influenced. A similar trend is seen for other input and output port combinations.

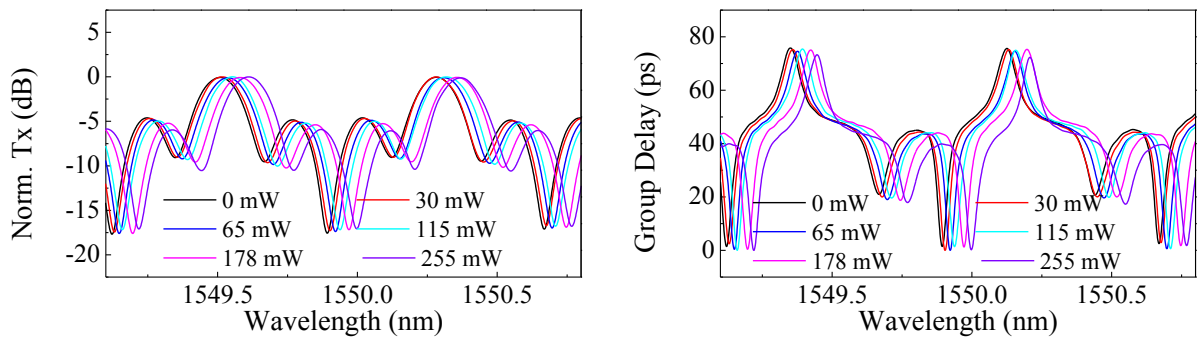


Figure 5.15: Dependence of thermal cross-talk between the delay lines on transmission (left) and group delay (right) for single stage of a parallel-serial filter shifts the transmission and group delay response of the filter.

In figure 5.16 the shift along the wavelength axis in the transmission and group delay response for the single stage of parallel-serial filter is plotted against the electrical power applied to the heater. At 255 mW a wavelength shift of 105 pm is recorded which is equivalent to a frequency shift of 13.25 GHz. To verify further that this shift is produced by the increase in the temperature of the substrate, a simple experiment has been performed in which the temperature of the holder for the parallel-serial filter is increased and the response of the filter is measured at different temperatures. A similar effect is observed as is observed for the case in which a heater at test heater at 275 μm from the delay lines is energized (see figure 5.15). The shift in the transmission response of the filter along the wavelength axis is shown in figure 5.17. Furthermore, it has been found that an increase in the temperature of substrate by 1K results in 82 pm of shift along the wavelength axis.

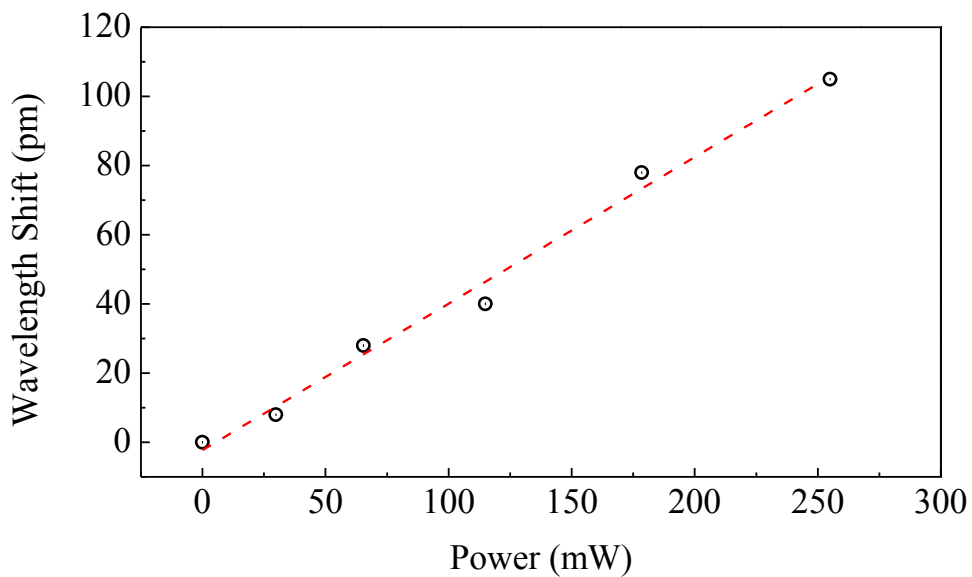


Figure 5.16: Wavelength shift in the transfer function for the single stage parallel-serial filter with an increase in the applied power on the heater.

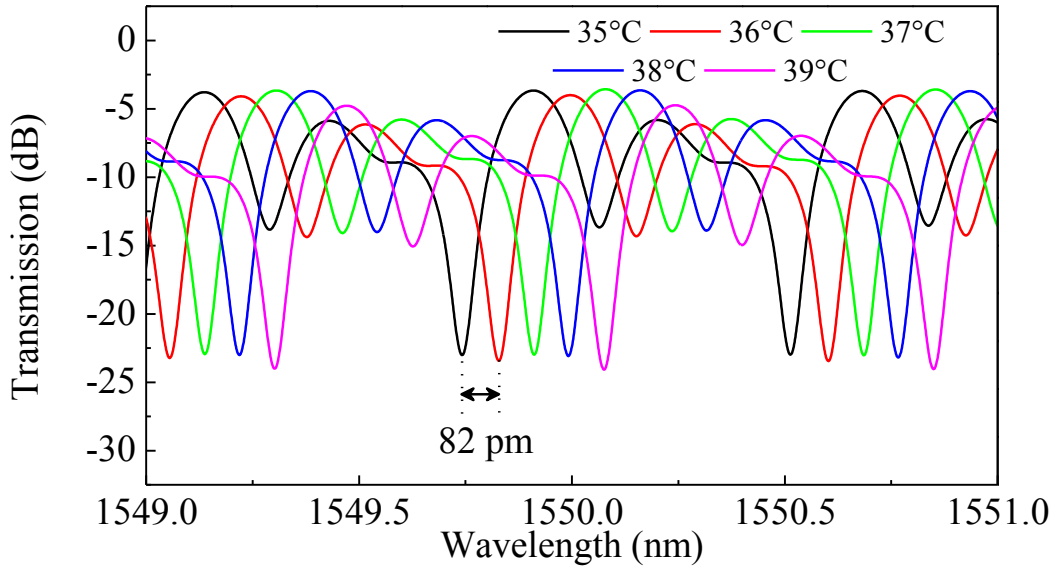


Figure 5.17: Shift in the transmission response of the single stage filter with an increase in the temperature of the chip holder

To further verify that the phase shift on one delay line does not introduce any undesired phase shift on the other delay lines, the measurement results for transmission and group delay for different phase values on the delay lines are compared with the simulation results. Approximately same value of phase shift on the delay lines was needed in simulation to get matching between the simulation and experiment. Figure 5.18 shows the measurement results for the transmission and the group delay (solid-red) when $\Delta\Phi_{1-1}=0^\circ$, $\Delta\Phi_{1-2}=172^\circ$ and $\Delta\Phi_{1-3}=80^\circ$ are introduced on the delay lines of 4-port MZI (see figure 5.14). Simulation results for transmission and group delay (dotted-black, in figure 5.18) has shown a good matching with the experimental results when $\Phi_{1-1}=0^\circ$, $\Phi_{1-2}=165^\circ$ and $\Phi_{1-3}=75^\circ$ are applied on the delay lines.

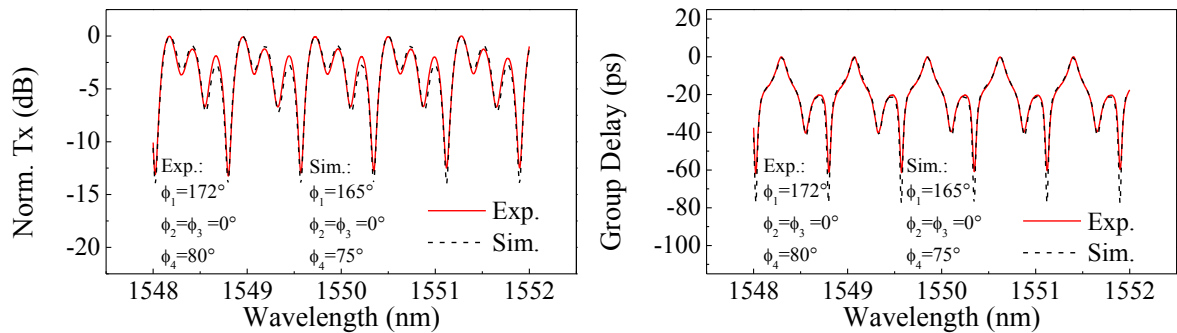


Figure 5.18: Comparison of Transmission (left) and group delay (right) with simulation (dashed-black) and measurement (solid-black) with phase shift on delay lines.

To further verify that the phase change on one delay line does not introduce any phase shift on the other delay lines, the phase Φ_{1-1} (see figure 5.14) is swept linearly. For every phase shift, transmission and group delay has been measured. It is found that by using approximately the same value of phase shift in the simulation, a good matching between simulation and measurement exist. A comparison of experimental phase shift and the phase shift needed to match the experimental result with simulation has been shown in Figure 5.19. In conclusion, it can be deduced that the thermal cross-talk between the

delay lines does not yield a significant additional phase shift on the neighboring delay lines.

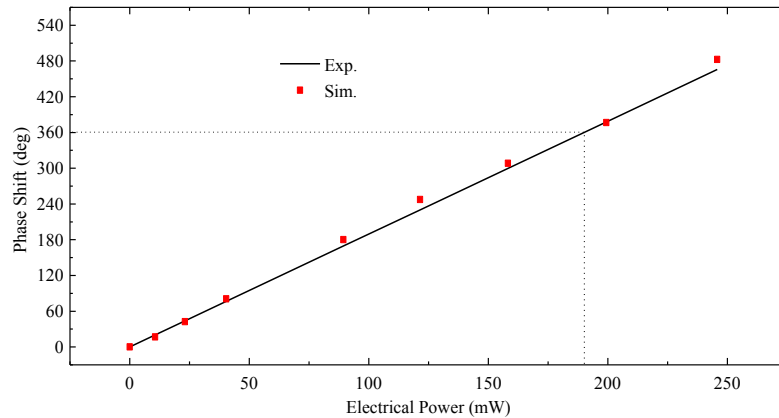


Figure 5.19: Comparison between experimental (Solid-black) and simulated (Red-Square) phase shift ϕ_{1-1} to match the simulated and experimental transmission and group delay for single stage of the parallel-serial filter (360° phase shift has required 180 mW).

After the preliminary testing of the single stage parallel serial filter, the device is tuned using the phase shifting elements. As expected due to the limited number of group delay contributions available in a single stage of the serial-parallel filter (only 3 in this case of 4×4 MZI with delay of 0, 10, 20 and 30 ps), it is not possible to achieve a perfectly linear group delay slope for a large bandwidth in each *FSR*. By increasing the number of stages one can obtain a larger number of group delay contributions, which can be adjusted by tuning phases on the delay lines of each stage. This leads to the interplay of these contributions in such a way that a linearly increasing or decreasing group delay can be achieved for larger bandwidth. Figure 5.20 shows the transmission and group delay behavior of a single-stage of a serial-parallel filter after tuning. The shaded parts show regions of approximately linear group delay for two different settings of the phase shifting elements.

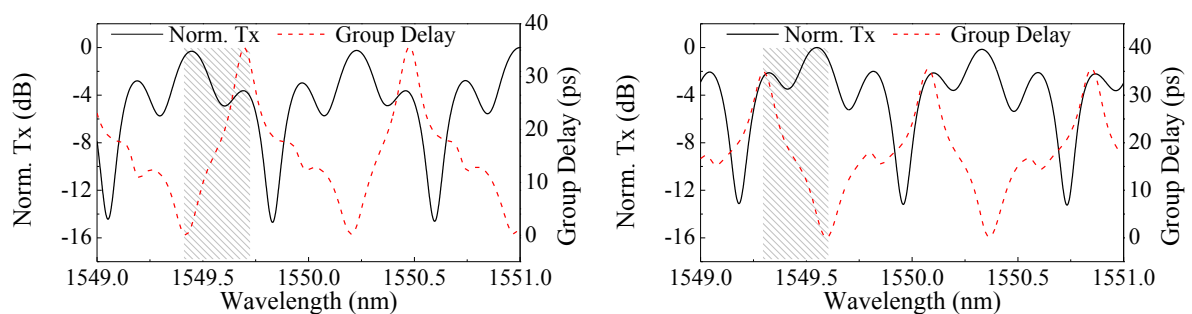


Figure 5.20: Single stage serial parallel filter tuned to nearly linear positive (left) and negative (right) group delay (dashed-red) and transmission (solid-black)

5.6. Two Stage Parallel-Serial Filter Characterization

By using the measurement method (section 5.3) and device preparation method (section 5.4), the two stage parallel-serial filter (parallel-serial filter with $R=6$, see figure 3.14) is characterized for transmission and group delay. The fabricated two stage parallel-serial filter is shown in figure 5.21 after mounting on the Aluminum carrier. The important sections such as the location of heaters, section of chip with anti-reflection coated (ARC) waveguides are shown in figure 5.21. It is important to mention that the region of chip with in- and out- coupling waveguides (dotted yellow region on top-right and bottom-left region in figure 5.21) has ARC. This allows that the heaters are easily accessible for contacting with wire-bonding. In figure 5.22, the wire bonded heaters are shown.

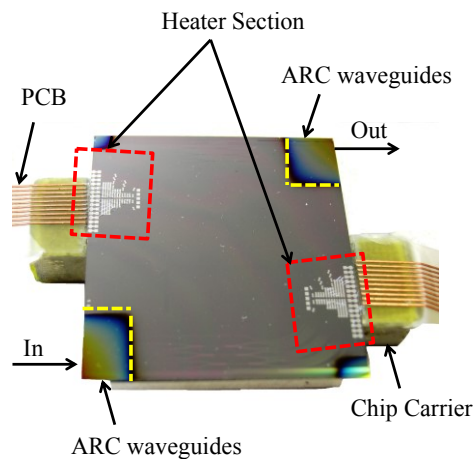


Figure 5.21: A two stage serial-parallel filter

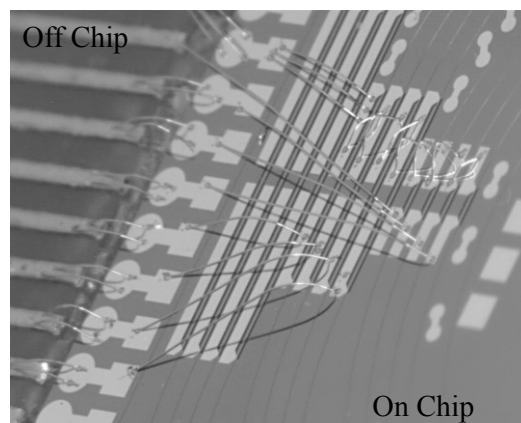


Figure 5.22: Wire-bonded heater for on-chip to off-chip interfacing of heaters

The two stage 6th order parallel-serial FIR filter for residual dispersion compensation is characterized for both polarizations. The discussion at this moment is limited to a single polarization (TE Polarization) only. The characterization of the waveguides on the chip with two stage parallel-serial filter has shown that the combination of lensed fibers and

ARC has limited the coupling loss to ~ 0.5 dB/facet. The waveguides have a typical loss of $0.2\text{--}0.3$ dB/cm. The total insertion loss excluding the coupling loss is ~ 6 dB. Roughly half of this loss is due to the waveguides and the remaining comes from the excess loss of the MMI couplers. The 6 dB insertion loss of the device considers the optical signal available at all 4 outputs of the last MMI coupler. The characterization of the two stage filter is presented in figure 5.23. The response in figure 5.23 is obtained by adjusting the phase on the delay lines in such a way that a linear group delay slope (shaded region in the group delay plot) is achieved for 0.35 nm (43.75 GHz) of the *FSR*. The measured *FSR* of the fabricated filter is 97 GHz. A comparison of the transmission and the group delay responses between the measured result (solid, red) and the calculation result (dotted, black) is also shown in Figure 5.23. The calculation result is obtained by using the transfer matrix method as has been done for the single stage parallel-serial filter. By suitable adjustment of the phase on the delay lines, it is possible to get various negative and positive slopes for the group delay. As an example, measured results (solid, red) and simulation results (dotted, black) for transmission and group delay for negative, no, and positive group delay slopes are shown in Figure 5.23(a)–(f) respectively.

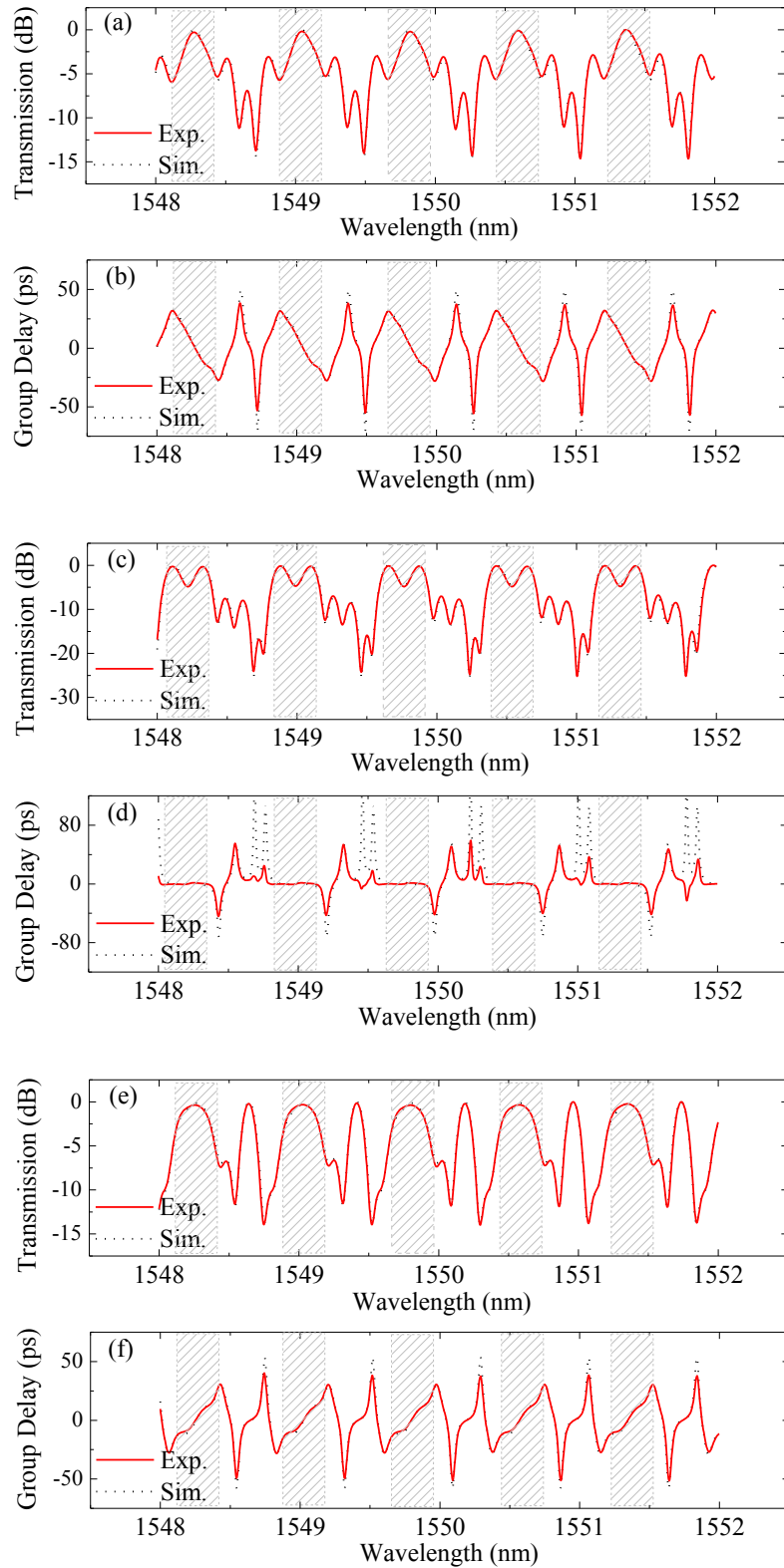


Figure 5.23: Measured (solid-red) transmission (a, c, e) and group delay (b, d, f) compared with the calculated (dotted-black) transmission and group delay for the two stage filter.

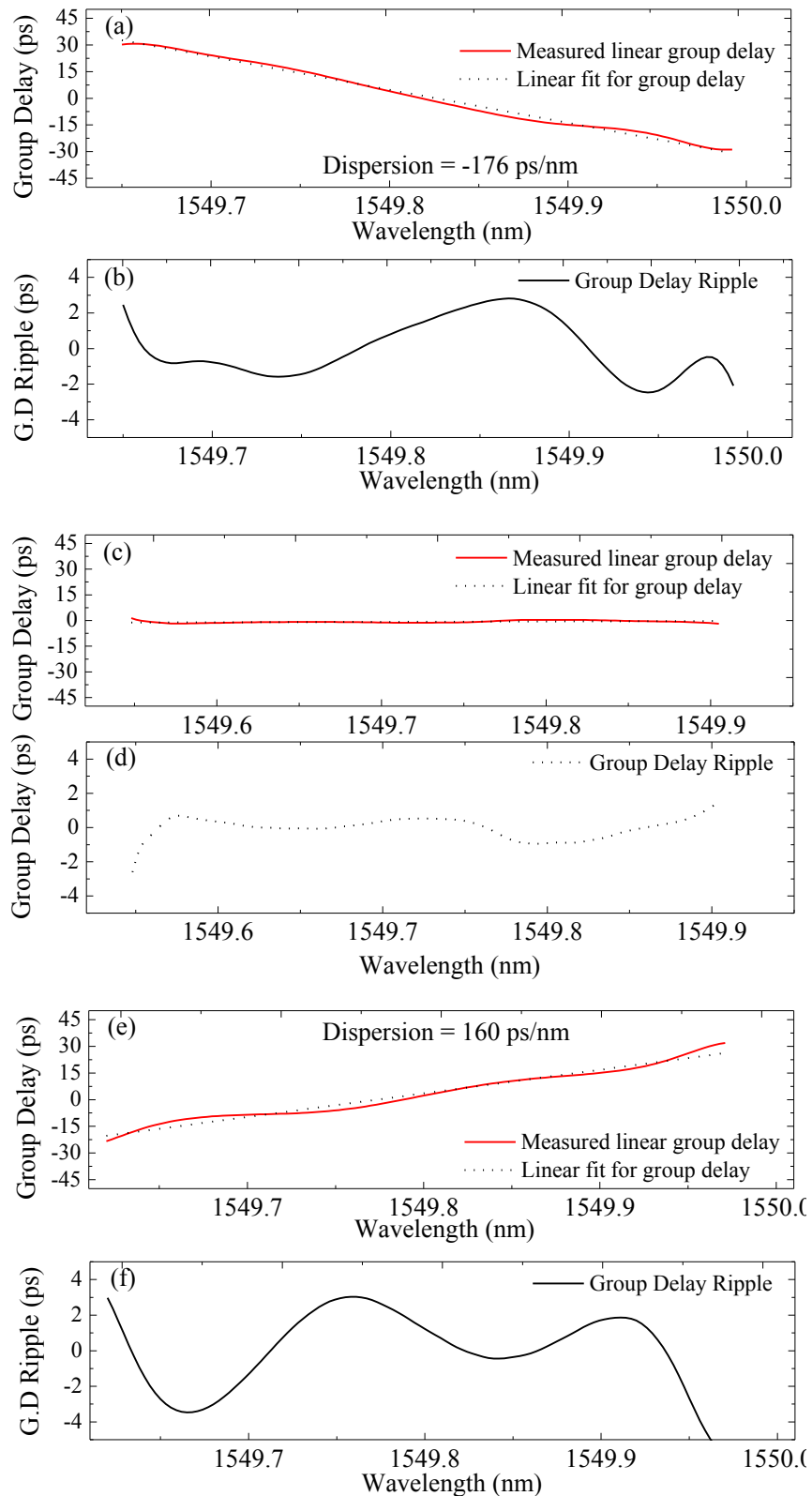


Figure 5.24: Linear fit (a, c, e) for the linear group delay slope and group delay ripple (b, d, e) in the region of linear group delay

In figure 5.23 (b), (d), and (f), the negative, zero, and positive group delay slopes correspond to a dispersion value of -176 ps/nm, 0, and +160 ps/nm, respectively. Figure 5.24 (a), (c), and (e) shows an enlarged version of the linear group delay of shaded

sections in figure 5.23 (b), (d), and (f). A good linear fit exists as shown by the black dotted line in figure 5.24 (a) (c), and (e). The group delay ripple, which is calculated by computing the difference between the measured group delay (solid-red curves in figure 5.24 (a), (c) and (e)) and the linear fit (dotted-black curves in figure 5.24 (a), (c) and (e)), in the region of linear group delay is only ± 3 ps as shown in figure 5.24 (b), (d), and (f). A small magnitude and short period of group delay ripple is also an important feature for a residual dispersion compensator. In [20] it has been shown that significant OSNR penalty, as high as 4 dB for NRZ OOK, occurs when the period of group delay ripple is comparable to the bit rate. For group delay ripples which have periods larger and smaller than the bit rate, the penalty the OSNR penalty reduces due to lack of phase matching between the signal pulse and scattered pulses, which are identical to signal pulses but with different amplitude, phase and delay with respect to the original pulse.

Tuning of the two stage filter from negative to zero to positive group delay slopes has shown 1 dB of variation in insertion loss. Figure 5.25 shows the tuned group delay slopes and their comparison with the calculation result for positive, zero and negative group delay slopes. Typical time constant for tuning the filter was in the range of few ms.

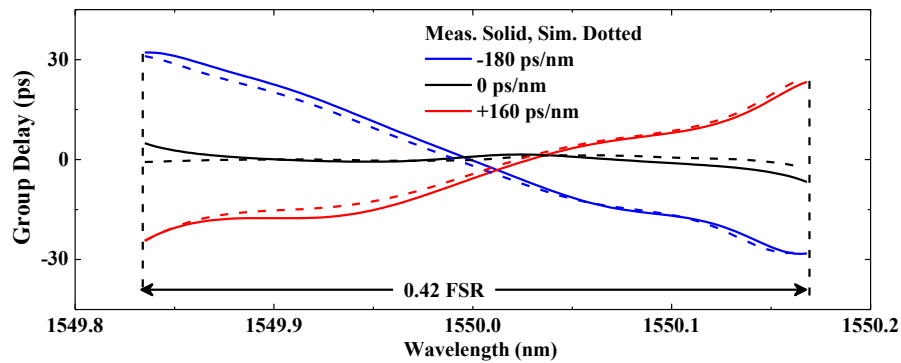


Figure 5.25: Measured (solid) and calculated (dotted) positive, zero and negative group delay slopes for the two stage filter (Filter FSR = 100 GHz)

The results presented in figure 5.23 show that the response of the filter is periodic, which is an important feature of a dispersion compensating filter so that it can compensate dispersion for multiple WDM channels simultaneously. Therefore, the characterization of the filter is performed over the whole C-band to check if the filter can compensate dispersion for all WDM channels in the C-band. As an example, figure 5.26 (a) and 5.26 (b) shows the tuned transmission and negative dispersion of the result shown in figure 5.24 (a) and figure 5.24 (b) for the 44 WDM channels in the C-band for a bandwidth of 35 nm from 1530 nm to 1565 nm. As shown in figure 5.26 (c), the filter has shown a variation of 18 ps/nm ranging from -162 ps/nm to -180 ps/nm. The maximum group delay ripple stays within ± 5 ps (see figure 5.26(d)). The variation in the GD bandwidth for the 44 WDM channel is limited only to 4 GHz and varies between 0.32 nm and 0.36 nm. The transmission response for the tuned filter has shown ~ 2 dB variation in the insertion loss over a bandwidth of 35 nm.

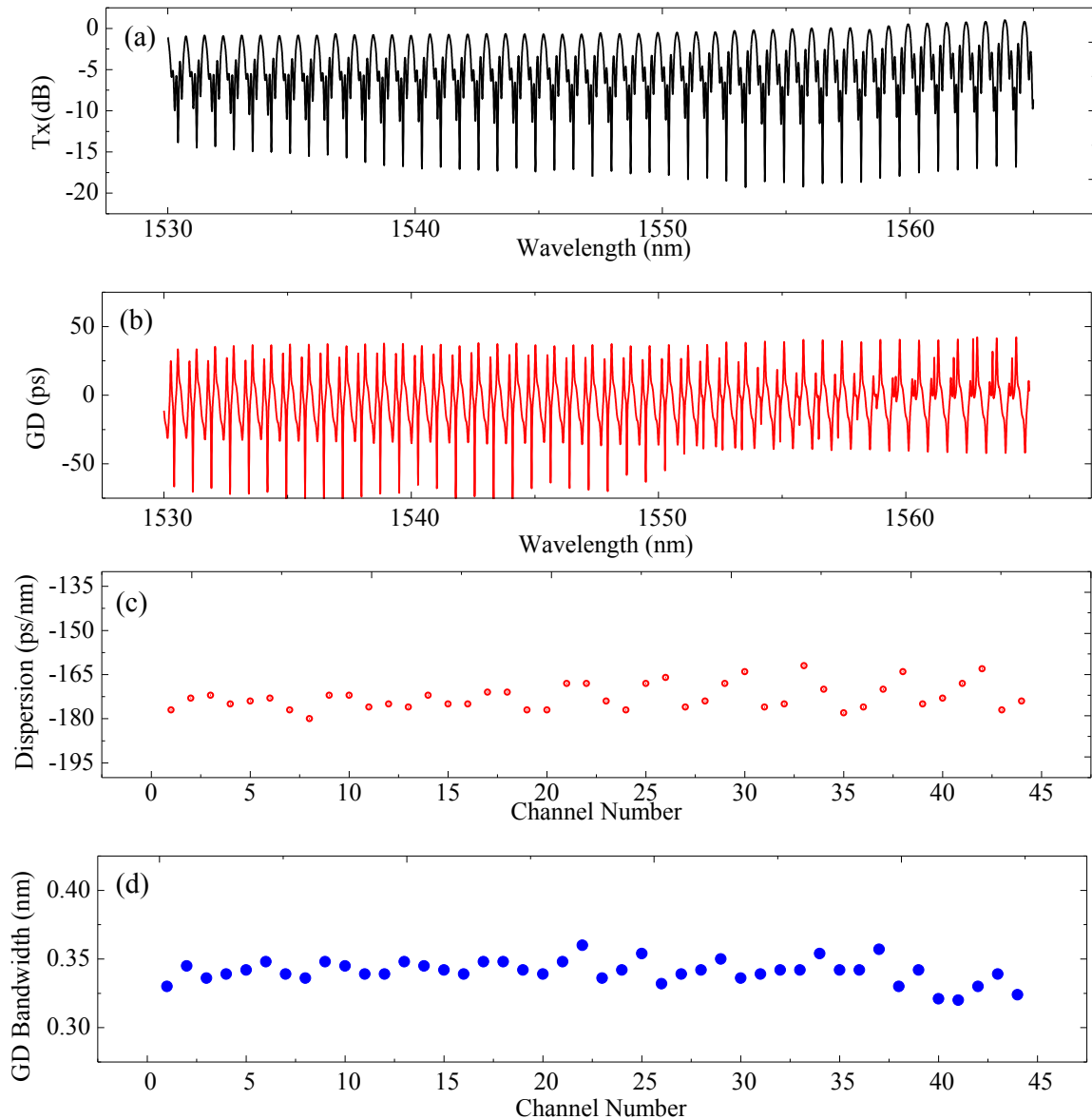


Figure 5.26: Transmission (a) for negative dispersion slope (b), variation in dispersion (c) and group delay bandwidth, which is the fraction of filter FSR with linear group delay slope (d) over the C-band for the two stage parallel-serial filter

To check the performance of the two stage filter as a dispersion compensating device, emulation is performed using VPI TransmissionMaker 8.7 [8]. Such emulation provides a good estimation about the performance of the device. The emulation setup is shown in figure 5.27. It comprises a transmitter, which uses Quadrature Phase Shift Keying (QPSK) as the modulation format. The transmitter operates at 28 Gbaud. The transmitted signal propagates through a 100 km long SSMF. The transmitted signal is divided into two arms. Fiber loss is fully compensated on both arms by using Erbium-Doped Fiber Amplifiers (EDFA). One arm acts as a reference and has a dispersion compensating fiber (DCF), which fully compensates the dispersion after propagation through SSMF. The other arm is used to analyze the two stage (6th order) parallel-serial filter performance as a residual dispersion compensator. In this arm, the length of DCF is varied so that it partially compensates the dispersion. The two-stage parallel-serial filter is used for the

residual dispersion compensation. On both arms, the optical signal-to-noise ratio (OSNR) was adjusted at the receiver to achieve a target symbol error rate of 10^{-3} . A coherent receiver with matched local oscillator is used for detection. Figure 5.28 (a) shows the constellation of a 28 Gbaud QPSK for a sequence of 2^{16} bits after transmission through the SSMF without compensation of residual chromatic dispersion. Figure 5.28 (b) shows the constellation after compensation of 176 ps/nm of residual fiber chromatic dispersion using two-stage parallel-serial filter. In Figure 5.29, the plot shows the OSNR penalty introduced by the dispersion compensating filter. OSNR penalty is determined by calculating the difference in required OSNR for a perfect dispersion compensator (reference arm in figure 5.27) and the required OSNR when dispersion is compensated with the parallel-serial filter (test arm in figure 5.27). For a dispersion value of -176 ps/nm produced by the parallel-serial filter, as shown by the measurement result in figure 5.24(b), the filter degrades the OSNR by only 0.34 dB. The OSNR penalty increases when there is an increase in the uncompensated residual dispersion. It approaches 1 dB when the filter is used to compensate 176 ± 64 ps/nm of residual dispersion for a target symbol error rate of 10^{-3} .

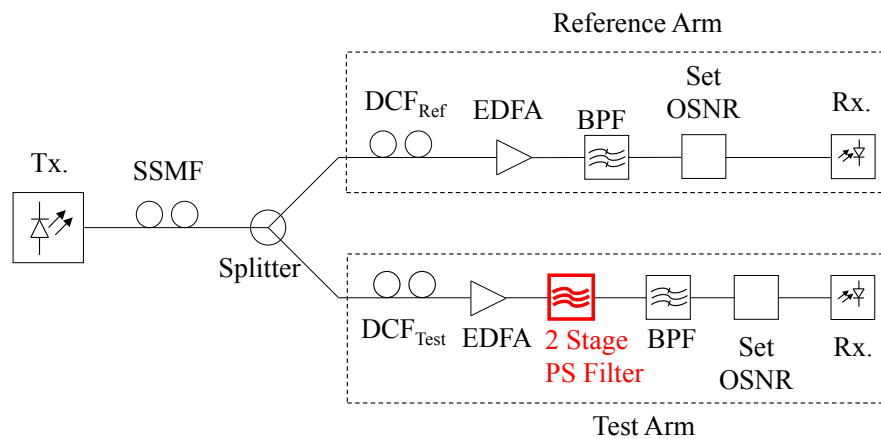


Figure 5.27: Emulation setup to test the performance of the two stage parallel-serial filter

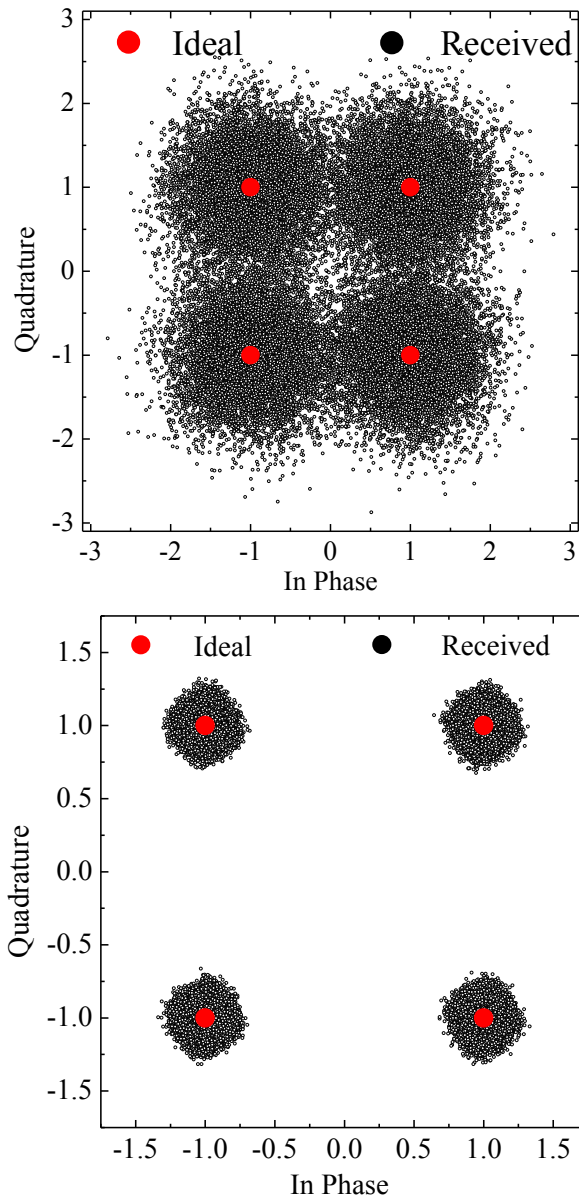


Figure 5.28: Constellation for 28 Gbaud QPSK after transmission through 100 km of SSMF (top) without compensation of +176 ps/nm residual dispersion and (bottom) after compensation of residual dispersion using two-stage parallel-serial filter

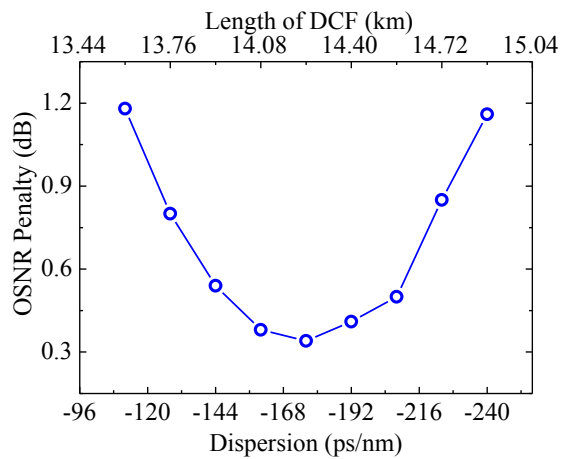


Figure 5.29: OSNR penalty for the two stage parallel-serial filter

5.7. Enhanced Two Stage Parallel-Serial Filter Characterization

The characterization for two stage parallel-serial filter has shown promising results but as shown by the measurement results in figure 20, the tuning range for the filter is limited and the filter has a 6dB transmission bandwidth of not more than 0.32 nm. As explained in section 3.9, this performance can be enhanced by replacing the middle MMI coupler of the two stage parallel-serial filter with a symmetric MZI. This symmetric MZI acts as a tunable coupler, whose coupling coefficients can be tuned by the changing the phase on the waveguides connecting the MMI couplers. The detailed principle of the tunable MMI coupler is already explained in [10]. Figure 27 shows the waveguide layout and the fabricated device.

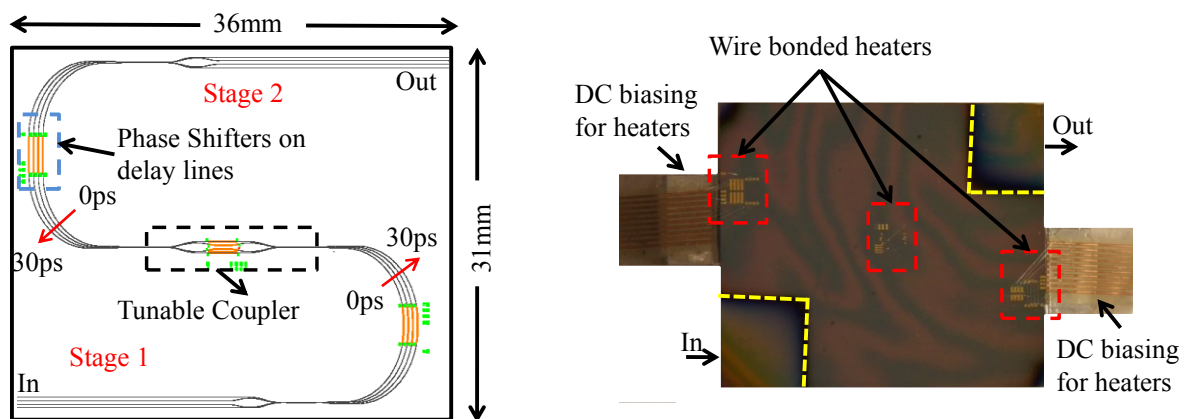


Figure 5.30: Waveguide layout (left) for the enhanced two stage filter and the fabricated device (right) with heaters shown in red-dashed regions and the anti-reflected coated waveguide facets in the yellow-dotted region

The characterization of the enhanced two stage filter is performed in the same way as explained earlier in section 5.3. The insertion loss for the filter is measured to be ~ 9 dB and it includes the waveguide loss, excess loss of the MMI couplers, coupling and reflection loss at the facets. To demonstrate the performance, the results for TM polarization, which is adjusted at the tip of the in-coupling fiber, are presented. By controlling the phase on each delay line for the MZIs and the tunable coupler, the filter can be tuned to deliver different group delay slopes. Both two stage parallel-serial filter (section 3.8) and enhanced two stage parallel-serial filter (section 3.9) are 6th order FIR filter with 6 zeros and 12 degrees-of-freedom. In both approaches, the six zeros of the filters can be adjusted to achieve a linear group delay slope for a certain fraction of the filter *FSR*. The tunable coupler of the enhanced two stage filter approach provides an increased control in placing the 6 complex zeros in the complex plane. Therefore, this

approach enables to achieve an almost “continuous tuning” of the filter for dispersion compensation (see section 3.9).

By phase adjustment, +90 ps/nm, +30 ps/nm, -95 ps/nm and -50 ps/nm dispersion over a bandwidth of more than 40 GHz is achieved. The maximum group delay ripple inside this area is less than 5 ps. In comparison to the two stage filter, this filter is more flexible in terms of tunability. The transmission and group delay bandwidth is 5 GHz more than the 40 GHz bandwidth delivered by the two stage filter. Figure 5.31 shows the measurement results for the transmission and group delay slopes for the enhanced two stage filter.

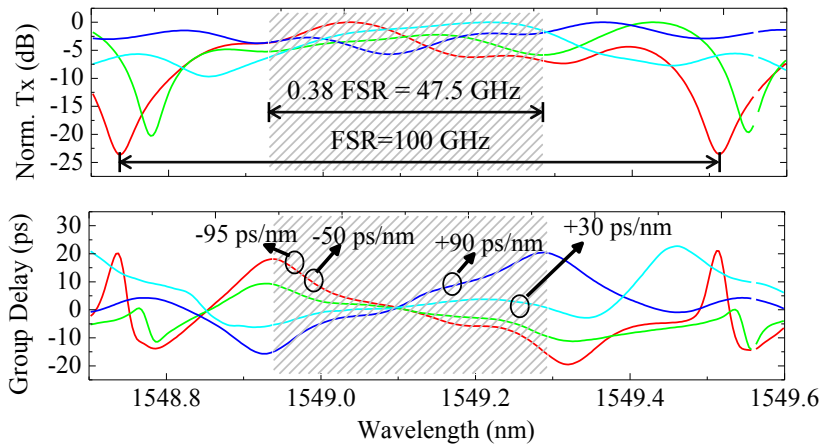


Figure 5.31: Characterization of the enhanced two stage filter (Filter $FSR=100$ GHz).

Emulation has been performed by using the measurement results shown in figure 5.31. The emulation is performed by the project partners in Helmut-Schmidt University (Hamburg-Germany) and results are presented in [11]. It has been shown that the dispersion tolerance of a 28 Gbaud QPSK transmission system can be enhanced from 218 ps/nm to 314 ps/nm. Dispersion tolerance is the amount of dispersion which can be tolerated without increasing the OSNR penalty beyond a certain threshold. OSNR penalty is the difference between the required OSNR for a perfectly dispersion compensated channel vs the required OSNR when a parallel-serial filter is used for dispersion compensation. By using the measurement results of figure 5.31, the QPSK transmission systems becomes 44% more tolerant to dispersion for a $BER = 10^{-3}$. A more detailed description about the emulation setup for enhanced dispersion tolerance in a QPSK transmission system is mentioned in [11].

5.8. Effect of Polarization

In section 5.5, 5.6 and 5.7, characterization of the parallel-serial filters for dispersion compensation for only one polarization has been shown. To apply a dispersion compensating filter in a real transmission system, the device has to have a polarization independent response. The polarization of the optical signal changes along the

propagation length and ideally it requires the dispersion compensating filter to have a polarization independent response.

The characterization of the parallel-serial filter has shown a Polarization Dependent Frequency Shift (PDFS), which is typical in SOI devices. PDFS originates due to the different effective indices for the TE and TM polarized light. This difference is commonly termed as birefringence and originates from the geometry of the waveguides. Simulations have shown that $3.5 \mu\text{m}$ wide rib waveguides in $4 \mu\text{m}$ SOI have an effective index which is different by $\sim 2.6 \times 10^{-4}$ for TE ($n_{\text{TE}} = 3.4768$, $n_{\text{TM}} = 3.47656$) and TM polarized light. This difference in effective index for the two polarization leads to a PDFS of 120 pm, which has been observed by characterizing the filter for TE and TM polarization. Figure 5.32 and Figure 5.33 show the measured transmission and group delay response for TE and TM polarization for the two stage parallel-serial filter tuned for positive (figure 5.32) and negative (figure 5.33) group delay slope. To show the similarity of the transmission and group delay response for the two polarizations, the PDFS has been removed in Figure 5.32 and Figure 5.33. The 120 pm PDFS shift for the two polarizations has been shown by the wavelength axis for TE (black) and wavelength axis for TM polarization (red). Due to this PDFS, the WDM channels will no longer be matched to the ITU-grid for both polarizations. When one polarization is matched to the ITU-grid specifications, the other will be shifted by 120 pm. This means that the center frequency of the WDM channel will no longer be matched to the center of the filter FSR. As a result, dispersion will not be completely compensated due to this off-set between the WDM channel center frequency and the filter FSR.

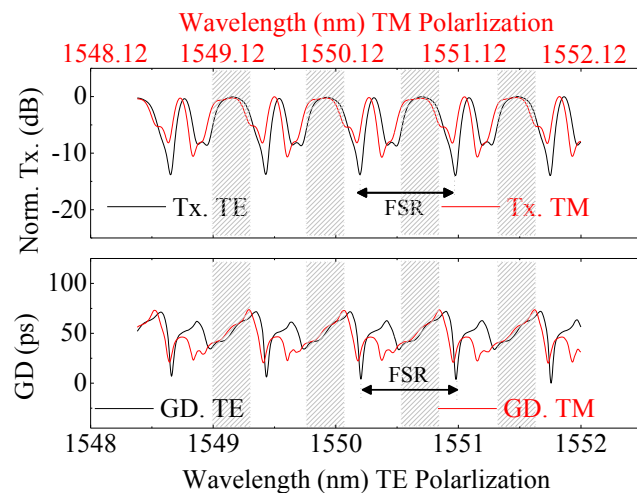


Figure 5.32: TE (solid-black) and TM (solid-red) characterization for the two stage parallel-serial filter when tuned for positive group delay slope. The PDFS is depicted by the 120pm shift between the top and bottom wavelength axis.

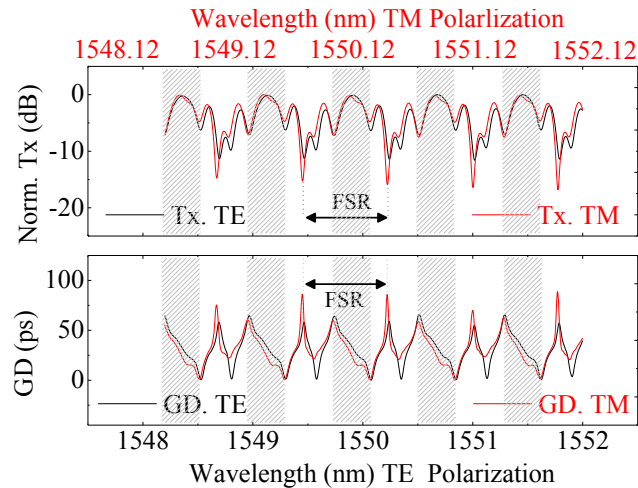


Figure 5.33: TE (solid-black) and TM (solid-red) characterization for the two stage parallel-serial filter when tuned for negative group delay slope. The PDFS is depicted by the 120pm shift between the top and bottom wavelength axis.

PDFS in SOI devices is a typical problem. Birefringence tuning techniques are employed to resolve this problem. These techniques are based on either modifying the geometry of the waveguide core [12] or by increasing the cross-section of the waveguides making such techniques impractical due to small fabrication tolerance. In [13], it has been shown that the PDFS can be compensated by stress-engineering of the waveguides. In this technique, the stress is induced in a waveguide by depositing a cladding layer of SiO₂ to compensate PDFS. Similar technique can be used for the compensation of modal birefringence for the parallel-serial filter. In the scope of this work, the birefringence for the fabricated devices has been compensated by depositing 700 nm of SiO₂ layer at 500°C in a PECVD system. The resulting transmission and group delay for the un-tuned two stage parallel-serial filter is shown in figure 5.34. A strong correlation exists between the transmission and group delay response for the two polarizations after the tuning of birefringence. Once the PDFS is removed, the tuned parallel-serial filter is capable for dispersion compensation in stage of the art polarization multiplexed QPSK transmission systems. The results shown in figure 5.34 are preliminary and more effort is required to optimize the process for the compensation of PDFS and tuning of the parallel-serial filter.

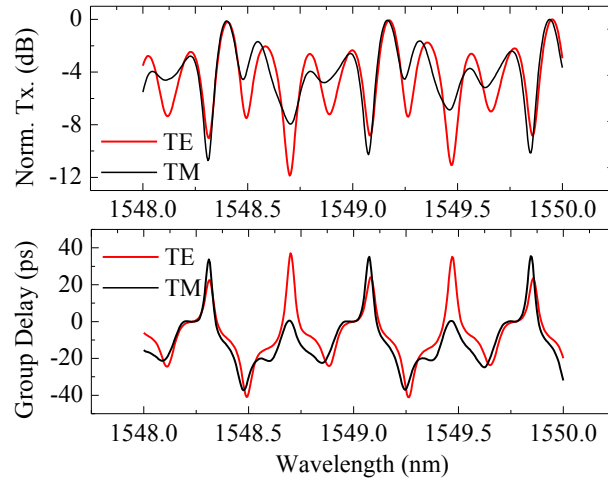


Figure 5.34: Birefringence tuned transmission (top) and group delay (bottom) for the TE (solid-red) and TM (solid-black) polarization for an un-tuned two stage parallel-serial filter

5.9. Transforming Integrated Micro-Optic Parallel-Serial Filter to Nano-photonic Parallel-Serial Filter

The large dimensions of the $4\ \mu\text{m}$ SOI implementation limit the co-integration of other photonic components. Therefore, an implementation with smaller footprint is highly desirable. This can be achieved with a nano-photonic implementation. In this section, the implementation and characterization of the single stage of the parallel-serial filter using nano-wire technology is addressed. It must be highlighted that this single stage (4-port MZI) of the parallel-serial filter should not be treated as a full scale dispersion compensator. The fabricated device should be treated as a test structure to verify that a nano-photonic implementation of the parallel-serial filter for residual dispersion compensator is possible.

The quality of results obtained from the single stage implementation in nano-wires can provide a good estimation and feasibility for implementing the parallel-serial filter in more compact and standard nano-wire technology of SOI system [14].

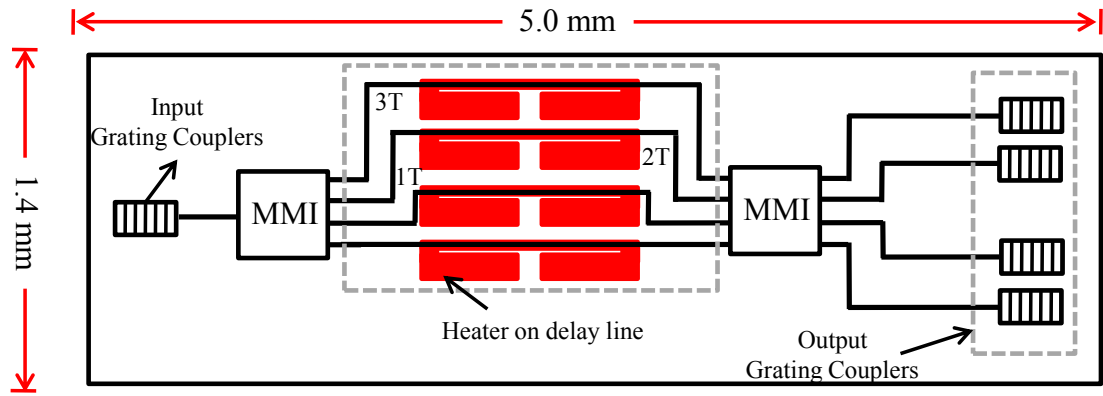


Figure 5.35: Mask layout of single stage parallel-serial filter for nano-photonic implementation

The waveguide layout of the single stage parallel-serial filter is shown in figure 5.35. For the fabrication 450 nm wide nano-wire waveguides, which are etched on SOI wafers with silicon and Buried Oxide (BOX) thickness of 220 nm and 2 μm respectively. 248 nm Deep Ultraviolet (DUV) lithography and decoupled plasma source etching is used for the structuring of nanowires, grating and MMI couplers. The fabricated waveguides have shown 2 dB/cm [15] of optical loss, which is 10 times higher as compared to the rib waveguides used in 4 μm SOI implementation of [16]. The in- and out-coupling of the optical signal is achieved by one-dimensional grating couplers. The phase shift of the optical signal after split operation in each stage of the filter is performed by using the thermo-optic effect induced phase shift on the delay lines, which is also used for the compensation of phase errors on the delay line introduced by fabrication errors. Aluminum heaters with 1 μm width and 700 nm thickness are deposited on top of the delay lines. A buffer oxide layer of 1.5 μm is used between the heaters and the waveguide to prevent optical losses due to absorption in metallic heaters. Figure 5.36 shows that the transmission and the group delay of the fabricated single stage of the parallel-serial filter does not require any tuning to deliver a good match between the ideal device and the fabricated device. The measured GD response for the fabricated device has three group delay peaks but the ideal result has only two. The third peak of the ideal result is not visible because it corresponds to a zero which lies on the unit circle and has infinitely deep and narrow peak. The results in figure 5.36 provide a very clear indication that the realization of parallel-serial filter in nano-technology is highly feasible as has already been demonstrated by the transformation of an O-OFDM demultiplexer from 4 μm SOI to CMOS compatible nano-wire based SOI technology [16]. Resulting implementation using nano-silicon photonic platform has a potential to provide compact filters enabling higher density of photonic integrated circuits on a single chip. Moreover such implementations are more power efficient as compared to the micro-silicon photonic implementations.

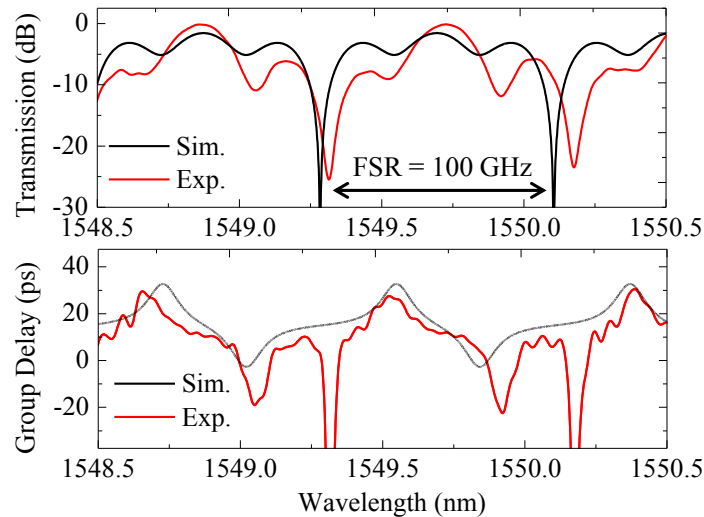


Figure 5.36: Transmission (top) and group delay (bottom) compared with ideal (solid-black) and measured (solid-red) for a nano-photonic implementation of a single stage parallel-serial filter

References:

- [1] Agilent 86038B Photonic Dispersion and Loss Analyzer User's Guide.
- [2] Costa, B.; Mazzoni, D.; Puleo, Mario; Vezzoni, Emilio, "Phase shift technique for the measurement of chromatic dispersion in optical fibers using LED's," *Quantum Electronics, IEEE Journal of*, vol.18, no.10, pp.1509,1515, Oct 1982.
- [3] Cohen, L.G., "Comparison of single-mode fiber dispersion measurement techniques," *Lightwave Technology, Journal of*, vol.3, no.5, pp.958,966, October 1985.
- [4] <http://www.ggb.com/wedge.html> accessed on 24.09.2013.
- [5] Hiroshi Kawashima, and Kazutaka Nara, "Wideband Tunable Dispersion Compensator Using a 25-Stage PLC-MZI", *Furukawa Review*, No. 35 2009.
- [6] L. Zimmermann, K. Voigt, G. Winzer, K. Petermann, "Towards silicon on insulator DQPSK demodulators" *Proc. Optical Fiber Communication Conference (OFC 2009)*, paper OThA4, San Diego, 2010.
- [7] Voigt, K.; Zimmermann, L.; Winzer, G.; Petermann, K., "SOI based 2×2 and 4×4 waveguide couplers - evolution from DPSK to DQPSK," *Group IV Photonics, 2008 5th IEEE International Conference on*, vol., no., pp.209,211, 17-19 Sept. 2008.
- [8] <http://www.vpi-photonics.com/TMOpticalSystems.php> accessed on 23.09.2013.
- [10] Lagali, N.S.; Paiam, M.R.; MacDonald, R.I., "Theory of variable-ratio power splitters using multimode interference couplers," *Photonics Technology Letters, IEEE*, vol.11, no.6, pp.665,667, June 1999.

- [11] S. Schwarz, A. Rahim, J. Bruns, K. Petermann, C. G. Schäffer, "Tunable Two-Stage 6th order FIR-Filter for Residual Dispersion Compensation " in ECOC 2013, September 2013.
- [12] L. Vivien, S. Laval, B. Dumont, S. Lardenois, A. Koster, and E. Cassan, "Polarization-independent single-mode rib waveguides on silicon-on-insulator for telecommunication wavelengths", *Opt. Commun.*, vol. 210, pp.43 -49 2002.
- [13] D. Xu, P. Cheben, D. Dalacu, A. Delâge, S. Janz, B. Lamontagne, M. Picard, and W. Ye, "Eliminating the birefringence in silicon-on-insulator ridge waveguides by use of cladding stress," *Opt. Lett.* 29, 2384-2386 (2004).
- [14] Abdul Rahim, Stefan Schwarz, Juergen Bruns, Karsten Voigt, Georg Winzer, Lars Zimmermann, Christian G. Schäffer and Klaus Petermann, " Silicon Photonic Implementation of a scalable OFDM Demultiplexer" accepted in *Photonics Technology Letters*.
- [15] H. Tian et al., "Fabrication of low-loss SOI nano-waveguides including BEOL processes for nonlinear applications" *Journal of the European Optical Society - Rapid publications*, 7 (2012).
- [16] A. Rahim et al., "Terabit Optical OFDM demultiplexer in Silicon Photonics", in *Optical Fiber Communication Conference/National Fiber Optic Engineers Conference 2013, OSA Technical Digest (online) (Optical Society of America, 2013)*, paper JTh2A.28.
- [17] Maran, J-N; Slavik, R.; LaRochelle, S.; Karasek, M., "Chromatic dispersion measurement using a multiwavelength frequency-shifted feedback fiber laser," *Instrumentation and Measurement, IEEE Transactions on* , vol.53, no.1, pp.67,71, Feb. 2004.
- [18] Thevenaz, L.; Pellaux, J. -p; Von der Weid, J.-P., "All-fiber interferometer for chromatic dispersion measurements," *Lightwave Technology, Journal of* , vol.6, no.1, pp.1,7, Jan 1988.
- [19] Ryu, S.; Horiuchi, Y.; Mochizuki, K., "Novel chromatic dispersion measurement method over continuous Gigahertz tuning range," *Lightwave Technology, Journal of* , vol.7, no.8, pp.1177,1180, Aug 1989.
- [20] Xiang Lu, Linn F. Mollenauer, Xing Wei, "Impact of group-delay ripple in transmission systems including phase-modulate formats", *Photonics Technology Letters*, Vol. 16, No. 1. Jan. 2004.

Conclusion and Research Forecast

The art of silicon photonics has shown tremendous progress in the last two decades. The high quality components, which are used as building blocks have demonstrated state-of-the-art modules. The progress of development in the field of silicon photonics is bound to deliver complete systems in near future by combing the modules developed in SOI.

In this work, a tunable residual dispersion compensator module in SOI is demonstrated. Such a device is highly desirable in present and future optical communication systems, which do not require any in-line dispersion management. For modern detection techniques, such as coherent detection, the electrical signal processing after the coherent detection accounts for the dispersion induced limit on information carrying capacity of an optical fiber. The extravagant increase for increased data rates, which is concurrently driven by mobility, video and cloud services, will soon face an electronic speed limit barrier. Optical solutions can come to a rescue. They can be merged with electronic schemes especially where electronics is handicapped. The residual dispersion compensating device presented in this work can be seen as a small signal processor which can be integrated on chip with the recently demonstrated coherent receivers [1,2] in SOI to deliver an integrated coherent optical receiver with optical signal processing functionality. This way the optical solutions can serve the electronic DSP for modern optical communication systems.

The implementation of the parallel-serial filter approach has proved a new filter concept, which is based on higher order MMI coupler and makes it novel. The use of higher order MMI coupler potentially leads to smaller footprints, when implemented on modern nano-wire based SOI technology [3]. Parallel-serial filter approach has shown that it can bring the benefits of both the serial lattice filter and fully parallel AWG based approach. The approach is not only limited to the compensation of residual dispersion compensation but other signal processing functions such as demultiplexer for an O-OFDM can also be implemented by taking an inspiration from parallel-serial filter approach [4]. The work presented here is the pioneer in terms of using higher order MMI couplers for signal processing filter applications.

The characterization of the two stage parallel-serial filter has shown lot of promising results in terms of very small group delay ripple of less than $< \pm 5$ ps over the whole C-band, good group delay bandwidth of at least 40 GHz and nice periodicity over the whole C-band with a variation of only 18 ps/nm in dispersion to compensate residual dispersion for multiple WDM channels. The architecture of the two stage filter had limited tuning range, which is improved by the enhanced two-stage implementation. The characterization has shown improved turning range and transmission and group delay bandwidth for the parallel-serial approach. Although, the birefringence for the realized SOI devices has not be compensated in this work but techniques have been

mentioned in literature and are available to solve this problem. If birefringence is mitigated then the characterization has shown that the realized devices parallel-serial filters can be used for both TE and TM polarization.

No real transmission experiment is performed to evaluate the performance of the realized filters but emulation is performed to forecast the performance of the filter. The emulation result has shown that the filter has a small OSNR penalty of ~ 0.3 dB to compensate residual dispersion of a 28 Gbaud QPSK signal.

Lastly, the nano-wire based implementation of the single stage of the parallel-serial filter has shown very promising results. They are very encouraging to implement the parallel-serial filter on nano-wire SOI platform, which will result in a much smaller footprint as compared to the micro-photonic implementation, which has been the focus of discussion in this work.

The main aim of this research was the design, fabrication and characterization of a residual dispersion compensating filter. This goal was successfully accomplished. During the course of this research work, various problems were resolved and some of them still need to be addressed.

To mention some of the outstanding problems, the first one is the mechanism to limit the thermal cross-talk between the delay lines. This cross-talk is probably impossible to be completely removed but efforts need to be made to minimize it to an extent that it does not interfere with the tuning of the filter. In the fabricated devices a large spacing between the heaters is maintained to minimize this cross-talk. To improve further, trenches have been etched which go even inside the substrate and the silicon slab is also removed to minimize lateral spread of heat. This has improved the thermal-cross talk but it can further be improved by developing isotropic etching of silicon substrate. A process for such isotropically etched substrate has been developed. But, a complete filter device with such trenches has not been measured and the improvement of thermal cross-talk has not yet been quantified.

The two and three stage filter devices have been characterized for both polarizations so that they can be used of PM-QPSK systems. The devices have shown good performance for both polarizations. The outstanding issues the birefringence of the devices, which results in a polarization dependent frequency shift of ~ 15 GHz. The most prominent technique to get rid of this problem is by using stress engineering of the waveguides. A similar technique has been adopted to resolve this problem. By using an oxide layer of 507 nm, the birefringence was removed but the optical losses for the device were enhanced probably due to increased excess loss of the MMI couplers, which may be attributed to deviation in the position of MMI images at the output of the MMI. More research effort needs to be made to resolve this problem.

During the course of this research work, the filter architecture for dispersion compensation has been modified (adapted) to work as a scalable DFT filter for the demultiplexing of O-OFDM signals. DFT filters that can demultiplex an O-OFDM super-

channel with a data rate of up to 1.2 Tb/s have been designed, fabricated and characterized. Moreover, the performance has been estimated by performing emulations. Potential for smaller footprint by using nano-photonic implementation is demonstrated by a nano-photonic implementation of an 8 channel DFT filter. The scalability of the DFT filter by using parallel-serial approach is demonstrated by implementing an 8 and 16 channel DFT filters. 16-channel DFT filter demonstrated by using parallel-serial approach is the highest order MMI based DFT filter demonstrated so far. A more detailed explanation is not part of this work but is available in [3–5].

References:

- [1] Y. Painchaud, M. Poulin, J. Gagné, and C. Paquet, "Ultra-compact Si-photonic DQPSK demodulator," in *Optical Fiber Communication Conference, OSA Technical Digest (Optical Society of America, 2012)*, paper OM3J.3.
- [2] M. Kroh, G. Unterbörsch, G. Tsianos, R. Ziegler, A. Steffan, H. Bach, J. Kreißl, R. Kunkel, G. Mekonnen, W. Rehbein, D. Schmidt, R. Ludwig, K. Petermann, J. Bruns, T. Mitze, K. Voigt, and L. Zimmermann, "Hybrid Integrated 40 Gb/s DPSK Receiver on SOI," in *Optical Fiber Communication Conference and National Fiber Optic Engineers Conference, OSA Technical Digest (CD) (Optical Society of America, 2009)*, paper OMK3.
- [3] Rahim, A.; Schwarz, S.; Bruns, J.; Voigt, K.; Winzer, G.; Zimmermann, L.; Schäffer, C.G.; Petermann, K., "Silicon Photonic Implementation of a Scalable O-OFDM Demultiplexer," *Photonics Technology Letters, IEEE*, vol.25, no.20, pp.1977,1980, Oct.15, 2013
- [4] Rahim, A.; Schwarz, S.; Bruns, J.; Schäffer, C.G.; Petermann, K., "Terabit optical OFDM demultiplexer in silicon photonics," *Optical Fiber Communication Conference and Exposition and the National Fiber Optic Engineers Conference (OFC/NFOEC), 2013*, vol., no., pp.1,3, 17-21 March 2013
- [5] Abdul Rahim et al., "16-Channel O-OFDM Demultiplexer in Silicon Photonics", accepted in OFC 2014.

Scientific Contributions

[Journal] Abdul Rahim et al., "Finite Impulse Response Filter Using 4-Port MMI Couplers for Residual Dispersion Compensation", in Journal of Lightwave Technology, Vol. 30, No. 7, April 2012.

[Journal] Stefan Schwarz, Abdul Rahim, Christian G. Schäffer, Juergen Bruns, Klaus Petermann, "Comparison of Phase Error Sensitivities of All-Optical Discrete Fourier Transforms for OFDM Demultiplexing", in Journal of Optical and Quantum Electronics, Vol. 45, No. 3, page 775-781, March 2013.

[Journal] Abdul Rahim et al., "Silicon Photonic Implementation of a scalable OFDM Demultiplexer", Photonics Technology Letters Vol.25, No.20, 1977-1980, Oct.15, 2013.

[Int. Conf.] Abdul Rahim et al., "16-Channel O-OFDM Demultiplexer in Silicon Photonics", accepted in OFC 2014.

[Intl. Conf.] Stefan Schwarz, Abdul Rahim, Juergen Bruns, Klaus Petermann, Christian G. Schäffer, "Tunable Two-Stage 6th order FIR-Filter for Residual Dispersion Compensation", in 39th European Conference on Optical Communication (ECOC), London, United Kingdom, 22-26 September 2013, P.2.12.

[Intl. Conf.] Abdul Rahim et al., "Terabit Optical OFDM demultiplexer in Silicon Photonics" in The Optical Fiber Communication Conference and Exposition (OFC), Anaheim, March 2013, JTh2A.28.

[Intl. Conf.] Stefan Schwarz, Abdul Rahim, Christian G. Schäffer, Juergen Bruns, Klaus Petermann, "Fully Adjustable Serial-Parallel FIR Filter for Compensation of Residual Chromatic Dispersion" in 38th European Conference on Optical Communication (ECOC), Amsterdam, Nederland, September 2012, We.1.A.1.

[Intl. Conf.] Abdul Rahim et al., "Tunable Residual Dispersion Compensator Using Generalized MZIs In Silicon-on-Insulator" in The Optical Fiber Communication Conference and Exposition (OFC), Los Angeles, March 2012, OTh4D.4

[Intl. Conf.] Abdul Rahim et al., "C-band Performance of a Novel Tunable Integrated Filter for Dispersion Compensation" in 16 European Conference on integrated optics and technical exhibition, Barcelona, May 2012.

[Intl. Conf.] Abdul Rahim et al., "FIR Filter Architecture for Tunable Optical Dispersion Compensation in Silicon Photonics" in Integrated Photonics Research, Silicon and Nanophotonics (IPRSN) Toronto, Canada June, 2011.

[Intl. Conf.] Stefan Schwarz, Abdul Rahim, Christian G. Schäffer, Juergen Bruns, Klaus Petermann, "All-Optical Discrete Fourier Transform for OFDM Demultiplexing and its Sensitivity to Phase Errors" in 12th International Conference on Numerical Simulation of Optoelectronic Devices, Shanghai, China, August 2012, ThC5.

[Intl. Conf.] Abdul Rahim et al., “Highly Scalable Integrated Discrete Fourier Transformation Filter in Silicon-on-Insulator for Next Generation WDM Systems” in CLEO Europe 2013, C1-1.2 Mon.

[Intl. Conf.] Stefan Schwarz, Abdul Rahim, Juergen Bruns, Klaus Petermann, Christian G. Schäffer, “ Scalable DFT demultiplexer for Terabit Optical OFDM Transmission” in Signal Processing in Photonics Communications (SPPCom 2013).

[Workshop] Stefan Schwarz, Abdul Rahim, Christian G. Schäffer, Juergen Bruns, Klaus Petermann, “Optical Planar OFDM Demultiplexer for Realtime Signal Processing” in Workshop der ITG-Fachgruppe 5.3.1 Modellierung photonischer Komponenten und Systeme, Universitaet Stuttgart, Stuttgart, Germany, Feb. 2013.

[Workshop] Abdul Rahim et al., “Novel Tunable Integrated Filter for Dispersion Compensation realized in Silicon (SOI)” in Symposium on Opto and Micro-electronic Devices and Circuits, SODC 2012, 16.-20.09. 2012, Hangzhou, China.

[Workshop] Abdul Rahim et al., “Optical Filter for Dispersion Compensation based on 4x4 MMI couplers in 4_μm Silicon on Insulator” in 2nd International Workshop on Tunable and Active Silicon Photonics, Berlin, Germany, September 2011.

[Workshop] Stefan Schwarz, Abdul Rahim, Juergen Bruns, Christian G. Schäffer, Klaus Petermann, “Tunable Finite Impulse Response Filter for Dispersion Compensation using Multi-Arm MZIs in SOI Technology” in IX. ITG-Workshop - Silicon Photonics, Nuernberg, May 2011.

[Workshop] Ivano Giunttoni and Abdul Rahim, “Integrated devices for compensation of chromatic dispersion based on Silicon-on-Insulator”, Workshop zu chromatischer Dispersion, Technische Universitaet, Dortmund, March 2010.

APPENDIX I

Fabrication Process for the parallel-serial filter devices

A brief summary of the fabrication process is presented in section 4.6. In this section, all the steps involved and parameters used in the fabrication process are outlined.

A	Process Steps	Waveguide Structuring
1	Cleaning	Cleaned with Distille water and dried iwth N ₂
2	Drying	200 °C; 30 min; Hotplat
3	Deposit HMDS	Deposit for 5 min 1 min; 120 °C Hot plate
4	Photoresist	Hoechst AZ 5214 E, 4000 rev./min Humidity in clean room: 56 % ; 66 %; 58% Clean room temperature: 21.2°C; 22.3°C; 22.7°C Wait for 30 minutes
5	Pre-bake	100 °C; 2 min on hot plate Wafer is slowly cooled
6	Exposure Maskalignment MA1006	Mask 008 / 10 (alignment distance 15 µm) Exposure time ~. 3.7 s
7	Developer	RohmHaas Developer 1:1 (Mixture at room temperature) Time for development 55-60
8	Inspection	Microscope
9	Inspection	Resist thickness with Dektak
10	UV-exposure	Whole wafer for 300 s with FLOOD-Program
B	<i>Process Step</i>	Silicon Etching
11	Plasma-Dip	in RIE (Reactive Ion Etching) t 1 min O ₂ 50 sccm; p 0.05 Torr; P 100 W; T 200 K
12	RIE-Etching	Required etch depth 1.7 µm Etch time = 30 to 35 SF ₆ 50 sccm; O ₂ 5.5 sccm;

		CHF3 3,4 sccm; p 0.022 Torr; P 50 W; T 200 K He 5.3 mbar
13	Inspection	Etch Depth with Dektak
14	Removal of Photoresist	AZ-Remover, 70 °C, 10 min US
15	Inspection	Microscope
16	Plasma Cleaning	60 min 400 W
17	Inspection	Microscope
18	Inspection	Dektak
C	<i>Process Step</i>	Heater Metallization
20	Cleaning	with Aceton und distilled water, dry with N ₂
21	Heating	200 °C; 30 min; Hot plate
22	Deposit HMDS	Deposit for 5 min 1 min; 120 °C Hot plate
23	Photoresist	Negative resisit N 1420 1000 rev/min Clean room temperature. = 22.2 °C / 22.4 °C / 22.3 °C / 22.8 °C Humidity = 47 % / 38 % / 45 % / 57 % Wait for 60 minutes
24	Pre-bake	100 °C, 2 min, Hot plate Wafer slowly cooled
25	Exposure and mask allignment	Maske: 09 / 12 → Hard contact, Exposure time: 23 s
26	Development	Developer ma-D 532S, Development time: ~180 s
27	Inspection	<i>Microscope</i>
28	Inspection	Dektak for resisit thickness
29	Post-bake	Flood exposure for 300 s
30	Vepor deposition-preperation	UNIVEX

31	Vapor Deposition	100 nm Aluminum
32	Ventilate	Remove Wafer
33	Lift-Off	1x in kept in Acetone over night + 1x with ultra sound and fresh acetone
34	Inspection	<i>Microscope</i>
35	Inspection	Dektak to measure metal thickness
E	<i>Process Step</i>	Metallization for contact pads
36	Wafer preparation	200 °C; 30 min; Hot plate
37	Deposit HMDS	Deposit for 5 min 1 min; 120 °C Hot plate
38	Photo-resist	Negative resist ma-N 440 4000 rev./min Room Temperature. = 21.0 °C / 23.1 °C Humidity = 53 % / 57 % 60 minutes wait after photo-resist
39	Pre-bake	5 min, Hot plate Wafer slowly cooled down
40	Exposure and mask alignment	Mask: 10 / 2010 →Hard Contact,
41	Development	Developer ma-D 532S, undiluted Development time ~ 140 to 180 s
42	Inspection	<i>Microscope</i>
43	Inspection	Dektak
44	Post-bake	FLOOD exposure for 300 s
45	Vapor Deposition Preparation	<i>UNIVEX</i> : 5x 30 s, 20 mA, Ar
46	Vapor Deposition	~ 500 nm Aluminum
47	Ventilate	
48	Lift-Off	1x in acetone overnight dip + 1x ultrasonic treatment in fresh Acetone
49	Inspection	Microscope
50	Inspection	Dektak
G	<i>Process Step</i>	Trech Etching

51	Cleaning	Cleaning with distilled water and dry with nitrogen
52	Heating	200 °C; 30 min; Hot plate
53	HMDS	Directly from hot plat for HMDS deposition for 5 min 1 min; 120 °C Hot plat
54	Photoresisit	Hoechst AZ 5214 E, 2000 rev./min Humidity 39 % // 59% // 53% Temperature of clean room 21.7 // 22.6 // 22.2°C Wiat for 45 minutes
55	Pre-bake	90 °C; 2 min; Hot plate Wafer cooled down slowly
56	Exposure and Mask allignment	Mask → 11 / 2012 → Hard kontakt- Program. Exposre time ~ 5.3 s
57	Development	RohmHaas Developer 1:1 t 60 s
58	Inspection	With microscope and Dektak
60	UV-Flood	300 s
H	<i>Prozcess Step</i>	1.Si _x N _y -Etching
61	Nitrid-Etching + Dip	in RIE with <i>Sophie</i> 194 nm CHF ₃ 25 sccm; O ₂ 5 sccm; p 0,050 Torr; P 150 W; T 288 K ~. 3 min t _{SOI 184} 3 min t _{SOI 185} / min
62	Inspection	Dektak
I	Prozessschritt	2.&3.Si- / 2.SiO _x - Etching
63	Plasma-Dip	in ICP O ₂ 60 sccm; p 1,6 Pa P _{ICP} 50 W P _{RIE} 3 W T 20 °C He 10 mbar t 30 s
64	ICP-Etching	in ICP 16 cyclic t _{SOI 184} 16 cyclic C ₄ F ₈ 60 sccm SF ₆ 60 sccm

		<p>T 20 °C p 2,0 Pa P_{ICP} 200 W P_{RIE} 5 W He 10 mbar t₁ 6 s t₂ 12 s</p>
65	Inspection	Dektak
66	2. Oxid-Etching	<p>in RIE with <i>Sophie</i> ~ 1 μm CHF₃ 25 sccm; Ar 25 sccm; p 0,025 Torr; P 150 W; T 288 K ca. 70 min t_{SOI 184} 70 min t_{SOI 185} 70 min</p>
67	Inspection	Dektak
68	ICP-Etching	<p>Etch depth required : ≥ 6 μm in ICP t_{Si} 20 cycles t_{SOI_184} 44 cycles C₄F₈ 60 sccm SF₆ 60 sccm T 20 °C p 2,0 Pa P_{ICP} 200 W P_{RIE} 5 W He 10 mbar t₁ 6 s t₂ 12 s</p>
69	Inspection	Dektak
70	Cleaning	Remove photo resisit
71	Inspection	Microscope
72	Cleaning	Plsama 60 min 400 W
73	Inspection	Microscope
74	Inspection	Dektak
J	Process Step	Dicing of SOI-Wafer
76	Cleaning	Distilled water and Nitrogen for drying
77	Prepeation 1	<p>30 min Hot plate 200 °C; direct in 5 min HMDS; 1 min Hot plate 120 °C Protection resist</p>

		Resist type: AZ 6632 Program 6: 2000 re/min 60 min to wait Hot plate: 2 min, 100 °C
78	Preparation 2	Stick the protection dicing plastic and wait for 2 hours minimum
79	Dicing	
80	Cleaning the chips	a) carefully remove dicing plastic tape b) in Acetone (up-side-down cleaning); c) Clean with Iso-propanol; d) Clean with iso-propanol; e) Clean with flowing distilled water; f) Dry with nitrogen
81	Inspection	
82	Transport	
84	Polishing	
85	Cleaning	
86	PECVD	Anti-Reflection Coating 208 °C 208 nm

The fundamental process has been developed by the clean room staff of HFT TU Berlin, which has been modified to the requirements of the work presented in this research.

APPENDIX II

Relationship of filter order R with maximum achievable dispersion D_{max}

The phase shift $\Delta\Phi$ and the delay length ΔL of the MZI are related by:

$$\Delta\phi = \beta \cdot \Delta L = n_g \cdot k \cdot \Delta L = n_g \cdot \frac{2\pi}{\lambda} \cdot \Delta L$$

The time delay $\Delta\tau_{MZI}$ introduced by the delay length ΔL given by:

$$\Delta\tau_{MZI} = \frac{\Delta L \cdot n_g}{c}$$

Equivalently,

$$\Delta\lambda_{FSR} = \frac{\lambda^2}{c} \cdot \frac{1}{\Delta\tau_{MZI}}$$

or

$$\Delta\tau_{MZI} = \frac{\lambda^2}{c} \cdot \frac{1}{\Delta\lambda_{FSR}}$$

For a filter with order R , the maximum delay between two spectral components of the signals is:

$$\Delta\tau_{max} = R \cdot \Delta\tau_{MZI}$$

The maximum for the 3dB bandwidth of the filter is $\Delta\lambda_{3dB} \equiv \Delta\lambda_{FSR}$

The maximum dispersion D_{max} that can be reached with the filter of order R is given by:

$$D_{max} = \frac{\Delta\tau_{max}}{\Delta\lambda_{3dB}} \cdot R = \frac{\Delta\tau_{MZI}}{\Delta\lambda_{3dB}} \cdot R = \frac{\lambda^2}{c} \cdot \frac{R}{\Delta\lambda_{FSR} \cdot \Delta\lambda_{3dB}}$$

From this one can get a measure to compare different filters:

$$D_{max} \cdot \Delta\lambda_{FSR} \cdot \Delta\lambda_{3dB} = \frac{\lambda^2}{c} \cdot R$$

or

$$D_{max} \cdot (\Delta\lambda_{3dB})^2 = \frac{\lambda^2}{c} \cdot R \cdot \left(\frac{\Delta\lambda_{3dB}}{\Delta\lambda_{FSR}} \right)$$